

University of Kentucky

UKnowledge

Theses and Dissertations--Chemical and
Materials Engineering

Chemical and Materials Engineering

2017

Synthesis and Energy Applications of Mesoporous Titania Thin Films

Syed Z. Islam

University of Kentucky, syedislam@uky.edu

Author ORCID Identifier:

<http://orcid.org/0000-0002-5149-8094>

Digital Object Identifier: <https://doi.org/10.13023/ETD.2017.081>

[Right click to open a feedback form in a new tab to let us know how this document benefits you.](#)

Recommended Citation

Islam, Syed Z., "Synthesis and Energy Applications of Mesoporous Titania Thin Films" (2017). *Theses and Dissertations--Chemical and Materials Engineering*. 73.

https://uknowledge.uky.edu/cme_etds/73

This Doctoral Dissertation is brought to you for free and open access by the Chemical and Materials Engineering at UKnowledge. It has been accepted for inclusion in Theses and Dissertations--Chemical and Materials Engineering by an authorized administrator of UKnowledge. For more information, please contact UKnowledge@lsv.uky.edu.

STUDENT AGREEMENT:

I represent that my thesis or dissertation and abstract are my original work. Proper attribution has been given to all outside sources. I understand that I am solely responsible for obtaining any needed copyright permissions. I have obtained needed written permission statement(s) from the owner(s) of each third-party copyrighted matter to be included in my work, allowing electronic distribution (if such use is not permitted by the fair use doctrine) which will be submitted to UKnowledge as Additional File.

I hereby grant to The University of Kentucky and its agents the irrevocable, non-exclusive, and royalty-free license to archive and make accessible my work in whole or in part in all forms of media, now or hereafter known. I agree that the document mentioned above may be made available immediately for worldwide access unless an embargo applies.

I retain all other ownership rights to the copyright of my work. I also retain the right to use in future works (such as articles or books) all or part of my work. I understand that I am free to register the copyright to my work.

REVIEW, APPROVAL AND ACCEPTANCE

The document mentioned above has been reviewed and accepted by the student's advisor, on behalf of the advisory committee, and by the Director of Graduate Studies (DGS), on behalf of the program; we verify that this is the final, approved version of the student's thesis including all changes required by the advisory committee. The undersigned agree to abide by the statements above.

Syed Z. Islam, Student

Dr. Stephen E. Rankin, Major Professor

Dr. Thomas D. Dziubla, Director of Graduate Studies

SYNTHESIS AND ENERGY APPLICATIONS OF MESOPOROUS TITANIA THIN
FILMS

DISSERTATION

A dissertation submitted in partial fulfillment of the
requirements for the degree of Doctor of Philosophy in the
College of Engineering
at the University of Kentucky

By
Syed Z. Islam

Lexington, Kentucky

Director: Dr. Stephen E. Rankin, Professor of Chemical Engineering

Lexington, Kentucky

2017

Copyright © Syed Z. Islam 2017

ABSTRACT OF DISSERTATION

SYNTHESIS AND ENERGY APPLICATIONS OF MESOPOROUS TITANIA THIN FILMS

The optical and electronic properties of TiO₂ thin films provide tremendous opportunities in several applications including photocatalysis, photovoltaics and photoconductors for energy production. Despite many attractive features of TiO₂, critical challenges include the innate inability of TiO₂ to absorb visible light and the fast recombination of photoexcited charge carriers. In this study, mesoporous TiO₂ thin films are modified by doping using hydrogen and nitrogen, and sensitization using graphene quantum dot sensitization.

For all of these modifiers, well-ordered mesoporous titania films were synthesized by surfactant templated sol-gel process. Two methods: hydrazine and plasma treatments have been developed for nitrogen and hydrogen doping in the mesoporous titania films for band gap reduction, visible light absorption and enhancement of photocatalytic activity. The hydrazine treatment in mesoporous titania thin films suggests that hydrazine induced doping is a promising approach to enable synergistic incorporation of N and Ti³⁺ into the lattice of surfactant-templated TiO₂ films and enhanced visible light photoactivity, but that the benefits are limited by gradual mesostructure deterioration. The plasma treated nitrogen doped mesoporous titania showed about 240 times higher photoactivity compared to undoped film in hydrogen production from photoelectrochemical water splitting under visible light illumination.

Plasma treated hydrogen doped mesoporous titania thin films has also been developed for enhancement of visible light absorption. Hydrogen treatment has been shown to turn titania (normally bright white) black, indicating vastly improved visible light absorption. The cause of the color change and its effectiveness for photocatalysis remain open questions. For the first time, we showed that a significant amount of hydrogen is incorporated in hydrogen plasma treated mesoporous titania films by neutron reflectometry measurements.

In addition to the intrinsic modification of titania by doping, graphene quantum dot sensitization in mesoporous titania film was also investigated for visible light photocatalysis. Graphene quantum dot sensitization and nitrogen doping of ordered mesoporous titania films showed synergistic effect in water splitting due to high surface area, band gap reduction, enhanced visible light absorption, and efficient charge separation and transport. This study suggests that plasma based doping and graphene quantum dot sensitization are promising strategies to reduce band gap and enhance visible light absorption of high surface area surfactant templated mesoporous titania films, leading to

superior visible-light driven photoelectrochemical hydrogen production. The results demonstrate the importance of designing and manipulating the energy band alignment in composite nanomaterials for fundamentally improving visible light absorption, charge separation and transport, and thereby photoelectrochemical properties.

KEYWORDS: mesoporous; titania thin films; nitrogen doping; hydrogen doping; photocatalysis; surfactant templated sol-gel

Syed Z. Islam

Student's Signature

4/14/2017

Date

SYNTHESIS AND ENERGY APPLICATIONS OF MESOPOROUS TITANIA THIN
FILMS

By

Syed Z. Islam

Stephen E. Rankin, PhD
Director of Dissertation

Thomas D. Dziubla, PhD
Director of Graduate Studies

Date: 4/14/2017

My father, *Syed Abdul Mannan* and my mother, *Mosammad Fazilotun nesa*

ACKNOWLEDGEMENTS

Praise be to God who has blessed me to take on this journey. I am grateful to everybody who have in one way or other contributed to this journey. The first and foremost, I would like to present my utmost gratefulness towards my PhD supervisor, Dr. Stephen E. Rankin, for his guidance and mentorship throughout my graduate study. The helps and supports that Dr. Rankin has provided with extraordinary patience during each step of this research could not be measured. His guidance throughout my graduate career has proven to be invaluable and his dedication to the education of his students is unparalleled. One of things I have joyed most working with him is the independence he has given me to work on my research, which will provide me with confidence in every endeavors in my life. He has been a great mentor and leader. I wish to have my future mentors as good as Dr. Rankin.

I would like to express my sincere thanks to all my dissertation committee members Dr. Barbara L. Knutson, Dr. Brad Berron and Dr. Doo-Young Kim for being accessible at any point in time. I thank the members for their comments about my proposed research during the early times of the proposal defense and yearly committee meetings, which helped to improve several of the experiments and analyses performed to complete this dissertation. Their questions, comments and suggestions regarding this research during those meetings really helped me think in different perspectives. I would like to acknowledge and show my deep appreciation to our collaborators Dr. Doo-Young Kim, a professor of Chemistry department at UK, Allen Reed and Namal Wanninayake from Dr. Kim's group for providing me with plasma system and graphene quantum dots. This research would be incomplete without their ingenious support. Other than that, the guidance from Dr. Doo-Young Kim was tremendously helpful in formulating my research. My sincerely appreciation goes to Dr. Barbara L. Knutson for her valuable suggestions and

guidance throughout my graduate study from course work to research. Also, her suggestions during our group meeting was really helpful. I would like to thank Dr. Brad Berron for taking the time to actively participate in my dissertation committee and provide valuable feedback during the proposal and yearly committee meetings.

I would like to thank Nicholas Briot and Dali Qian from the Electron Microscopy Facility for their help with SEM and TEM characterizations. I would also like to thank Mr. Jason Backus from Kentucky Geological Survey for help with XRD instrument. The help from Dr. Joseph W Strzalka at Argonne National Laboratory with analyzing our samples through GISAXS and GIWAXS is greatly appreciated. I really appreciate the opportunity my lab member, Suraj Nagpure gave me to work with him in Oak Ridge National Laboratory to perform neutron reflectivity under his allotted beam time. I would also like to thank Dr. James Browning at Oak Ridge National Laboratory for his help to analyze neutron reflectometry data. I thank Prof. Y.T. Cheng, Prof. Dibakar Bhattacharyya and Andrew Colburn, and Prof. Brad Berron and Ishan Fursule, Prof. Anne-Frances Miller and Dr. Rupam Sarma, and Prof. Vijay Singh and Sai Guduru for access and assistance with the XPS, zeta potential, contact angle measurements, oxygen measurement, and water oxidation using the Xe arc lamp, respectively. I would also like to thank all my previous and current lab members; specially Dr. Suvid Joshi, Dr. Ravinder Garlapalli, Dr. Saikat Das, Dr. Suraj Nagpure, Dr. Daniel M. Schlipf, Md. Arif Khan, Shanshan Zhou, Yuxin He and Mahsa Moradipour. Without their assistance in the lab it would not have been possible to complete this research successfully and in a timely manner, and would not have a great time in this graduate study. I would like to extend my gratitude to our departmental staff

Ms. Chelsea Hansing, Ms. Marlene Spurlock, Ms. Melissia Witt, Ms. Nancy Miller and Mr. Bruce Cole for being extremely efficient and supportive.

I acknowledge the financial support to accomplish this work from U.S. Department of Energy EPSCoR Implementation award supported by grant no. DE-FG02-07-ER46375 and National Science Foundation EPSCoR Research Infrastructure Initiative award supported by grant no. IIA-1355438. I am very grateful to Professor Dibakar Bhattacharyya for giving me funding from NSF EPSCoR. I acknowledge the Dissertation Enhancement Award from UK. I also acknowledge the Liquids Reflectometer facility at the Spallation Neutron Source, which is sponsored by the Scientific User Facilities Division, Office of Basic Energy Sciences, U.S. DOE (J.F.B., J.K.K.) and the GISAXS and GIWAXS facilities of the Advanced Photon Source, a U.S. Department of Energy (DOE) Office of Science User Facility operated for the DOE Office of Science by Argonne National Laboratory under Contract No. DE-AC02-06CH11357.

My sincerely gratitude goes to my former lab member and roommate, Saikat Das and present roommate, Riasad Azim Badhan for providing me a congenial atmosphere and their support at home. My special thanks go to all of my friends across the world, especially Rupam Sarma, Moushumi Sarma, Md. Arif Khan, Nirupam Aich, Md. Ariful Hoque and Md. Monir Uddin for support and friendship.

Lastly, I would like to acknowledge the most important persons in my life who are my mother, brothers, sisters, nieces and nephews for their perennial love and support throughout my entire life. I have deprived them from meeting me for last seven years. I am very sorry for that. Their unreturnable sacrifices have brought me here today.

TABLE OF CONTENTS

ACKNOWLEDGEMENTS.....	iii
TABLE OF CONTENTS.....	vi
LIST OF FIGURES	xi
LIST OF TABLES	xviii
Chapter 1. Introduction.....	1
1.1. Background and Motivation.....	1
1.2. Hydrogen production from water splitting.....	2
1.3. Titania as a Photocatalyst.....	4
1.4. Nanostructured Titania.....	5
1.5. Doping of Titania	6
1.6. Sensitization of Titania.....	8
1.7. Overview and Summary of the Dissertation	10
Chapter 2. Synthesis and Catalytic Applications of Non-metal Doped Mesoporous Titania	18
2.1 Summary	18
2.2. Introduction	19
2.2.1. Synthesis of mesoporous TiO ₂	25
2.2.2. Titanium Precursor Chemistry	26
2.2.3. Surfactant-templated Film Deposition	29
2.2.4. Surfactant/Titania Film Aging	32
2.2.5. Thermal Treatment.....	35
2.3. Nitrogen doping.....	37
2.3.1. Amines	38
2.3.2. Ammonia.....	40

2.3.3.	Hydrazine	41
2.3.4.	Plasma Doping	42
2.3.5.	Thiourea	43
2.3.6.	Urea.....	44
2.3.7.	Summary of Nitrogen Doped Mesoporous Titania.....	46
2.4.	Other non-metal doped mesoporous titania	49
2.4.1.	Hydrogenation.....	49
2.4.2.	Boron doping	50
2.4.3.	Carbon doping.....	51
2.4.4.	Fluorine doping.....	53
2.4.5.	Iodine doping	55
2.4.6.	Phosphorus doping.....	56
2.4.7.	Summary of Nonmetal Dopants other than Nitrogen	58
2.5.	Co-doping of non-metals.....	59
2.6.	Applications	63
2.6.1.	Water Splitting.....	63
2.6.2.	CO ₂ Reduction	67
2.7.	Future Directions.....	69
2.8.	Conclusion.....	71
Chapter 3. Hydrazine-based Synergistic Ti(III)/N Doping of Surfactant-Templated TiO ₂ Thin Films for Enhanced Visible Light Photocatalysis		85
3.1	Summary	85
3.2	Introduction	86
3.3.	Experimental	89
3.3.1.	Materials	89

3.3.2.	Synthesis of mesoporous titania films	90
3.3.3.	Characterization	91
3.3.4.	Photocatalytic testing	92
3.3.5.	Photoelectrochemical testing	93
3.4.	Results and discussion.....	93
3.5.	Conclusions	108
Chapter 4. N ₂ /Ar Plasma Induced Doping of Ordered Mesoporous TiO ₂ Thin Films for Visible Light Active Photocatalysis.....		
		120
4.1.	Summary	120
4.2.	Introduction	121
4.3.	Experimental	124
4.3.1.	Materials	124
4.3.2.	Synthesis of mesoporous titania films	124
4.3.3.	N ₂ /Ar Plasma treatment of mesoporous TiO ₂ film	125
4.3.4.	Characterization	125
4.3.5.	Photocatalytic measurement	126
4.4.	Results and discussion.....	127
4.5.	Conclusions	137
Chapter 5. Remarkable Enhancement of Photocatalytic Water Oxidation in N ₂ /Ar Plasma Treated, Mesoporous TiO ₂ Films.....		
		144
4.1.	Summary	144
5.2	Introduction	145
5.3	Experimental Section	149
5.3.1	Materials	149
5.3.2.	Synthesis of mesoporous titania films	149
5.3.3.	N ₂ /Ar plasma treatment of mesoporous TiO ₂ film	150

5.3.4.	Characterization	150
5.3.5.	Photoelectrochemical measurements	151
5.3.6.	Zeta potential (ζ) measurements	153
5.3.7.	Contact angle measurements.....	154
5.4.	Results and Discussion.....	154
5.5.	Conclusion.....	171
Chapter 6. Synergistic Effects of Graphene Quantum Dot Sensitization and Nitrogen Doping of Mesoporous TiO ₂ Films for Water Oxidation Photocatalysis		179
6.1.	Summary	179
6.2.	Introduction	180
6.3.	Experimental Section	183
6.3.1.	Materials	183
6.3.2.	Synthesis of mesoporous titania films	184
6.3.3.	N ₂ /Ar plasma treatment of mesoporous TiO ₂ film	185
6.3.4.	Synthesis of GQDs.....	185
6.3.5.	Attachment of GQDs to TiO ₂ and nitrogen doped TiO ₂	186
6.3.6.	Characterization	186
6.3.7.	Photoelectrochemical measurements	188
6.4.	Results and Discussion.....	189
6.5.	Conclusion.....	201
Chapter 7. Plasma Treated Hydrogen Doped Mesoporous Black TiO ₂ Thin Films for Water Oxidation Photocatalysis		214
7.1.	Summary	214
7.2.	Introduction	215
7.3.	Experimental Section	221
7.3.1.	Materials	221

7.3.2.	Synthesis of mesoporous titania films	221
7.3.3.	H ₂ Plasma Treatment	222
7.3.4.	Characterization	222
7.3.5.	Photoelectrochemical characterization	226
7.4.	Results and Discussion.....	227
7.5.	Conclusion.....	238
Chapter 8. Conclusions and Future Work.....		246
8.1.	Conclusions	246
8.2.	Future Work	251
APPENDIX.....		258
APPENDIX A Supporting Information of Chapter 3		258
APPENDIX B Supporting Information of Chapter 4		270
APPENDIX C Supporting Information of Chapter 5.		279
APPENDIX D Supporting Information of Chapter 6.		288
APPENDIX E Supporting Information of Chapter 7.		295
References.....		300
Vita.....		320

LIST OF FIGURES

Figure 1.1. Basic principle of the overall water-splitting reaction on a semiconductor photocatalyst. Adapted from ref. [70].	16
Figure 1.2. Band positions of several semiconductors in contact with aqueous electrolyte at pH 1. The lower edge of the conduction band (red colour) and upper edge of the valence band (green colour) are presented along with the band gap in electron volts. The energy scale is indicated in electron volts using the normal hydrogen electrode (NHE) as a reference. Note that the ordinate presents internal and not free energy. The free energy of an electron-hole pair is smaller than the band gap energy due to the translational entropy of the electrons and holes in the conduction and valence band, respectively. On the right side, the standard potentials of water redox couple are presented against the standard hydrogen electrode potential. Adapted from reference [14].	16
Figure 1.3. Schematic of band diagram of sensitization of titania by small band gap semiconductors.	17
Figure 2.1. Schematic representation of Kohn-Sham one-electron states and spin density plot of substitutionally doped anatase TiO ₂ . Reprinted with permission from ref [73]. Reprinted from Catalysis Today vol. 206, C. Di Valentin and G. Pacchioni, "Trends in non-metal doping of anatase TiO ₂ : B, C, N and F," pp. 12-18, Copyright (2013), with permission from Elsevier.	74
Figure 2.2. Computer-generated illustrations of typical mesoporous structures and mesophases. Clockwise from lower left are illustrated an Im3m cubic mesoporous material, o-HCP mesoporous film, parallel HCP mesoporous film, and lamellar mesophase where higher intensity (yellow and red) corresponds to a greater density of hydrophobic tails of the surfactant template.	74
Figure 2.3. Schematics of the important stages of the formation of ordered nanoporous metal oxide films by EISA: (a) The dip coating process in which surfactant micelles form and may begin to assemble due to evaporation, (b) the aging process after deposition in which films organize into an ordered mesophase, and (c) high-temperature aging during which organic templates are removed by oxidation, crystallization may occur but loss of mesostructural order can happen with increasing temperature and time. Part (a) is reproduce with permission from C.J. Brinker et al. [115], (b) shows the rise of intensity	

from a o-HCP mesophase in a TiO₂ film during aging, adapted from Nagpure et al.[103] and (c) shows the loss of intensity of the o-HCP mesophase during heating of a TiO₂ film at 600 °C, adapted from Das et al.[105] 75

Figure 2.4. Schematic of procedures for preparing mesoporous nitrogen-modified titania photocatalyst. Reprinted with permission from ref. [178]. Reprinted from Chemical Engineering Journal vol. 219, J. Fu et al., “Soft-chemical synthesis of mesoporous nitrogen-modified titania with superior photocatalytic performance under visible light irradiation,” pp. 155-161, Copyright (2013), with permission from Elsevier. 75

Figure 2.5. Methylene blue degradation reaction with undoped TiO₂ (0 min) film, N-TiO₂ films and without films (Photolysis): (a) Concentration profile (b) the plot of the first-order rate coefficient vs. plasma treatment time. Reprinted with permission from ref. [69]. Reprinted from Microporous and Mesoporous Materials vol. 220, S.Z. Islam et al., “N₂/Ar plasma induced doping of ordered mesoporous TiO₂ thin films for visible light active photocatalysis,” pp. 120-128, Copyright (2018), with permission from Elsevier. 76

Figure 2.6. Proposed photocatalytic mechanism over the C-TiO₂ samples. Reprinted with permission from ref. [47]. Reprinted from Applied Catalysis B vol. 115, Y. Zhang et al., “Ethanol supercritical route for fabricating bimodal carbon modified mesoporous TiO₂ with enhanced photocatalytic capability in degrading phenol,” pp. 236-244, Copyright (2012), with permission from Elsevier. 77

Figure 2.7. SEM images of F-mp-TiO₂ microspheres synthesized in (a) 0.1, (b) 0.3, (c) 0.5, (d) 0.8, and (e) 1.0% H₂SO₄ solution. Panel f and the insert of panel a are TEM images corresponding to hollow (e) and solid (a) microspheres, respectively. Reprinted with permission from ref. [227]. Reprinted with permission from Journal of the American Chemical Society vol. 130, J.H. Pan et al., “Self-etching reconstruction of hierarchically mesoporous F-TiO₂ hollow microspherical photocatalyst for concurrent membrane water purifications,” pp. 11256-7, Copyright (2008) American Chemical Society. 77

Figure 2.8. Schematic diagram for generation and transfer of charge carriers in F-TiO₂ under UV irradiation. Reprinted with permission from ref [229]. Reprinted with permission from The Journal of Physical Chemistry C vol. 113, J. Yu et al., “Enhancement of photocatalytic activity of mesoporous TiO₂ powders by hydrothermal surface fluorination treatment,” pp. 6743-6750, Copyright (2009) American Chemical Society. 78

Figure 2.9. The transformation of surface structures of B,N-TiO ₂ . Reprinted with permission from ref. [242]. Reprinted from Journal of Solid State Chemistry vol. 184, X. Zhou et al., “Effect of nitrogen-doping temperature on the structure and photocatalytic activity of the B,N-doped TiO ₂ ,” pp. 134-140, Copyright (2011) with permission from Elsevier.	78
Figure 2.10. Basic principle of the overall water-splitting reaction on a semiconductor photocatalyst. Adapted from ref. [70]......	79
Figure 2.11. Schematic illustrations of synthesis procedure for CNMT-x samples. Reprinted with permission from ref. [48]. Reprinted from International Journal of Hydrogen Energy vol. 38, S.-H. Liu and H.-R. Syu, “High visible-light photocatalytic hydrogen evolution of C,N-codoped mesoporous TiO ₂ nanoparticles prepared via an ionic-liquid-template approach,” pp. 13856-13865, Copyright (2013) with permission from Elsevier.	79
Figure 2.12. The mechanism of photocatalytic reduction of CO ₂ under visible light irradiation. Adapted from ref. [254].	80
Figure 3.1. Electron micrographs of the F127-templated TiO ₂ film after calcination and without hydrazine treatment: (a) SEM image of the top surface, (b) TEM image of material scraped from the glass substrate, and (c) XRD pattern of TiO ₂ film on the original substrate.	111
Figure 3.2. HRTEM image of undoped titania film.....	111
Figure 3.3. (a) UV-vis spectra of undoped TiO ₂ and Ti ³⁺ -N-TiO ₂ films prepared using different hydrazine treatment times (the inset shows an enlarged region in the visible wavelength range) and (b) band gap vs. hydrazine treatment time based on Tauc plot analysis.....	112
Figure 3.4. (a) High resolution N 1s XPS spectra, (b) XPS N 1s depth profile spectra for 5 h_Ti ³⁺ -N-TiO ₂ film, and (c) plot of nitrogen content from XPS depth profile vs. total Ar etching time at 1000 eV power.	113
Figure 3.5. XPS Ti 2p depth profile spectra of (a) undoped TiO ₂ films and (b) 5 h_Ti ³⁺ -N-TiO ₂ films.....	114

Figure 3.6. Methylene blue degradation kinetics with undoped TiO ₂ (0 h) films, Ti ³⁺ -N-TiO ₂ films, and solution without catalysis (Photolysis): (a) Concentration profile, and (b) pseudo-first order rate coefficient vs. hydrazine treatment time.	115
Figure 3.7. Plan view SEM images of (a) undoped TiO ₂ , (b) 5 h_Ti ³⁺ -N-TiO ₂ , (c) 10 h_Ti ³⁺ -N-TiO ₂ , and (d) 20 h_Ti ³⁺ -N-TiO ₂ films (Scale bar: 120 nm).....	116
Figure 3.8. Concentration profiles during methylene blue degradation with 10 h_Ti ³⁺ -N-TiO ₂ films showing (a) effect of calcination temperature of titania films, (b) effect of calcination time of titania films and (c) effect of light sources (BLED and UVLED)...	117
Figure 3.9. (a) Current density as a function of time for the water oxidation reaction with TiO ₂ and Ti ³⁺ -N-TiO ₂ films (The inset is an expansion of the region from 400 to 1800 s) and (b) Photocurrent per mass of undoped TiO ₂ and Ti ³⁺ -N-TiO ₂ films at 600 s as a function of hydrazine treatment time.	118
Figure 3.10. (a) Mott-Schottky plots for undoped TiO ₂ and Ti ³⁺ -N-TiO ₂ films, and (b) flat band potential and (c) charge carrier density of the films as a function of hydrazine treatment time.	119
Figure 4.1. Schematic of the plasma reactor used for nitrogen doping of TiO ₂ films. ..	139
Figure 4.2. Electron micrographs of the F127-templated TiO ₂ film after calcination and without plasma treatment: (a) SEM image of the top surface, (b) TEM image of material scraped from the glass substrate, (c) cross sectional bright-field STEM image and (d) XRD pattern of TiO ₂ film on the original substrate.	139
Figure 4.3. (a) UV-vis spectra of undoped TiO ₂ and N-TiO ₂ films prepared using different plasma treatment time (inset is a photograph of undoped TiO ₂ and 30 min_N-TiO ₂ film) and (b) Band gap vs. plasma treatment time based on analysis using Tauc plots.	140
Figure 4.4. (a) High resolution N 1s XPS spectra, (b) plot of surface N content from XPS vs. plasma treatment time, and (c) XPS N 1s depth profile for the 90 min_N-TiO ₂ sample.	141
Figure 4.5. Valence band XPS spectra (inset is the enlarged region near the band edge) of undoped TiO ₂ and N-TiO ₂ films.	142
Figure 4.6. Methylene blue degradation reaction with undoped TiO ₂ (0 min) film, N-TiO ₂ films and without films (Photolysis): (a) Concentration profile (b) the plot of the first-order rate coefficient vs. plasma treatment time.	143

Figure 4.7. SEM images of (a,b) undoped TiO ₂ , (c, d) 30 min_N-TiO ₂ and (e, f) 210 min_N-TiO ₂ films.	143
Figure 5.1. Schematic of the plasma reactor used for N ₂ /Ar plasma treatment of TiO ₂ films.	172
Figure 5.2. UV-vis absorption spectra of undoped and N-doped TiO ₂ films prepared with different nitrogen gas flow rate (0-100 sccm) in the plasma reactor at 70 torr. The inset shows photographs of the corresponding 0 sccm_N-TiO ₂ , 40 sccm_N-TiO ₂ , 60 sccm_N-TiO ₂ , 80 sccm_N-TiO ₂ and 100 sccm_N-TiO ₂ films (from left to right).	172
Figure 5.3. (a) High resolution N 1s XPS spectra, (b) plot of surface N content from XPS vs. nitrogen flow rate in the plasma reactor, (c) XPS N 1s depth profile for the 100 sccm_N-TiO ₂ sample and (d) high resolution Ti 2p XPS spectra.	173
Figure 5.4. Valence band XPS spectra of undoped TiO ₂ and N-TiO ₂ films.	173
Figure 5.5. SEM images of (a) 0 sccm_N-TiO ₂ , (b) 40 sccm_N-TiO ₂ , (C) 60 sccm_N-TiO ₂ , (d) 80 sccm_N-TiO ₂ and (e) 100 sccm_N-TiO ₂ films (Scale bar = 100 nm).	174
Figure 5.6. Zeta potential (ζ) of the undoped TiO ₂ and 100 sccm_N-TiO ₂ thin films as a function of pH.	174
Figure 5.7. The effect of plasma treatment conditions on photocatalytic current-time (i-t) profiles under halogen lamp illumination representing water oxidation reaction (a) with a gas pressure variation and (b) with a different N ₂ gas flow rate in the plasma reactor. .	175
Figure 5.8. Amperometric current-time profiles with 0 sccm_N-TiO ₂ (undoped) and 100 sccm_N-TiO ₂ films under the illumination of (a) Xe arc lamp with AM 1.5 G filter (b) UVLED, (c) BLED and (d) GLED.	176
Figure 5.9. Linear sweep voltammetric (LSV) curves recorded with 0 sccm_N-TiO ₂ (undoped) and 100 sccm_N-TiO ₂ films under the illumination of (a) Xe arc lamp with AM 1.5 G filter, (b) UVLED, (c) BLED and (d) GLED.	177
Figure 5.10. (a) Mott-Schottky plot and (b) Nyquist plot recorded for 0 sccm_N-TiO ₂ and 100 sccm_N-TiO ₂ films.	178
Figure 6.1. Synthesis steps of (a) graphene quantum dots, and (b) graphene quantum dot sensitized nitrogen doped mesoporous titania thin films.	204
Figure 6.2. (a). UV-VIS absorbance, (b). Fluorescence, (c) low resolution and high-resolution TEM images and (d) FTIR spectrum of graphene quantum dots.	205

Figure 6.3. UV-vis spectra of pure TiO ₂ , GQD/TiO ₂ , N-TiO ₂ and GQD/N-TiO ₂ films.	206
Figure 6.4. SEM images of (a) undoped TiO ₂ , (b) GQD/TiO ₂ , (c) N-TiO ₂ films and (d) GQD/N-TiO ₂ films.....	206
Figure 6.5. GISAXS patterns of (a) undoped TiO ₂ and (b) N-TiO ₂ films	207
Figure 6.6. (a) High resolution (a) C 1s and (b) N 1s XPS spectra of TiO ₂ , GQD/TiO ₂ , N-TiO ₂ and GQD/N-TiO ₂ films	208
Figure 6.7. Zeta potential (ζ) of the undoped TiO ₂ and GQD/TiO ₂ , N-TiO ₂ and GQD/N-TiO ₂ films as a function of pH.....	209
Figure 6.8. Amperometric current-time profiles with undoped TiO ₂ , GQD/TiO ₂ , N-TiO ₂ and GQD/N-TiO ₂ films under the illumination of (a) BLED and (b) halogen bulb.....	209
Figure 6.9. Linear sweep voltammetric (LSV) curves recorded with undoped TiO ₂ and GQD/TiO ₂ , N-TiO ₂ and GQD/N-TiO ₂ films under the illumination of (a) BLED and (b) Halogen bulb.....	210
Figure 6.10. Linear fit for the ln(R) vs time curve considering only the linear portion with (a) TiO ₂ , (b) GQD/TiO ₂ , (c) N-TiO ₂ and (d) GQD/N-TiO ₂ film.....	211
Figure 6.11. Nyquist plot recorded for TiO ₂ , N-TiO ₂ , GQD/TiO ₂ and GQD/N-TiO ₂ films	211
Figure 6.12. Energy band diagram for GQD/TiO ₂ and GQD/N-TiO ₂	212
Figure 7.1. Schematic of the plasma reactor used for H ₂ plasma treatment of TiO ₂ films.	240
Figure 7.2. UV-vis spectra of mesoporous undoped TiO ₂ and H-TiO ₂ films	240
Figure 7.3. SEM images of (a) undoped TiO ₂ and (b) H-TiO ₂ films.....	241
Figure 7.4. GISAXS patterns of (a) undoped TiO ₂ and (b) H-TiO ₂ films	242
Figure 7.5. GIWAXS line cut patterns of undoped TiO ₂ , H-TiO ₂ and anatase TiO ₂ (calcined at 600 °C for 60 min) films. Integrated line-cut profiles of x-ray intensity vs. q_y were computed from the 2D GIWAXS patterns along angular direction ($90^\circ < \phi < 180^\circ$) at a fixed range of q_y values using GIXSGUI package.	242
Figure 7.6. (a) Ti 2p and (b) O 1s high resolution XPS spectra of undoped TiO ₂ and H-TiO ₂ films.....	243
Figure 7.7. NR profile of H-doped mesoporous TiO ₂ film in air. The inset shows the scattering length density (SLD) profile of the fitted model.....	244

Figure 7.8. NR profile of undoped mesoporous TiO ₂ film in D ₂ O. The inset shows the scattering length density (SLD) profile of the fitted model.....	244
Figure 7.9. Zeta potential measurements of undoped TiO ₂ and H-TiO ₂ films	244
Figure 7.10. Photocurrent-time measurement with undoped TiO ₂ film and H-TiO ₂ films under (a) UVLED and (b) BLED light irradiation.....	245
Figure 7.11. Nyquist plot of TiO ₂ and H-TiO ₂ films (Inset shows enlarged plot).....	245
Figure 8.1. Preliminary test of masking with a fractured Si wafer for (a) H-doping and (b) N-doping. A line scan by XPS of the N-doped interface.....	256
Figure 8.2. XPS N1s spectra of N-TiO ₂ film prepared by masking some portions of the film (line scan was performed) (small scale).....	257
Figure 8.3. An untreated TiO ₂ film (left) compared to a dopamine treated TiO ₂ film (right).	257

LIST OF TABLES

Table 2.1. Synthesis method, dopant source, chemical, optical and photocatalytic properties of nitrogen doped mesoporous titania.....	81
Table 2.1. Synthesis method, dopant source, chemical, optical and photocatalytic properties of nitrogen doped mesoporous titania (Continued).	82
Table 2.2. Synthesis method, dopant source, chemical, optical and photocatalytic properties of non-metal doped mesoporous titania.....	83
Table 2.3. Synthesis method, dopant source, chemical, optical and photocatalytic properties of non-metal co-doped mp-TiO ₂	84
Table 6.1. Photoelectrochemical water oxidation performance of titania films in amperometric <i>i-t</i> measurements.....	212
Table 6.2. Photoelectrochemical water oxidation performance of titania films in linear sweep voltammetry measurements (currents are taken at 0.35 V vs. Ag/AgCl).....	212
Table 6.3. Charge recombination rate constants for TiO ₂ , GQD/TiO ₂ , N-TiO ₂ and GQD/N-TiO ₂ films in the transient photocurrent decay kinetics.....	213

Chapter 1. Introduction

1.1. Background and Motivation

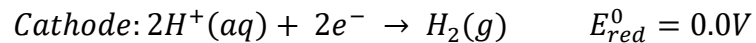
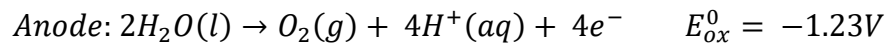
Recently, growing energy demand, depletion of fossil fuel and harmful effect of traditional energy sources on the global climate and environment have become profound concerns [1]. As time passes, both the global population and worldwide energy demand increase tremendously. For example, according to the United Nations forecasts, another 2.5 billion people are expected to be added to the present population of 6.5 billion by 2050 which will cause the energy demand to double over current demand [2, 3]. Even though the primary energy sources used currently are hydrocarbon-based fossil fuels with limited supply, they are causing serious environmental concerns such as climate change due to atmospheric CO₂ emission [4-8]. According to the U.S. Energy Information Administration, 1 billion barrels of oil were consumed every 12 days in 2011, which would result in 1 trillion pounds of CO₂ release to the atmosphere [9]. According to the prediction of the Intergovernmental Panel on Climate Change, the atmospheric CO₂ level could reach as high as 590 ppm by 2100, resulting in a 1.9 °C rise in global mean temperature [4, 10]. This temperature rise will have catastrophic consequences including sea level rise, flood and drought. Because of this, it has become a grand challenge to reduce atmospheric CO₂ levels while at the same time fulfilling the huge energy demanded for a high quality of life.

To tackle these global concerns, intensive research is going on to find clean and renewable energy sources. Renewable energy technologies including solar, hydro and wind power are all possible options to reduce the use of limited and climate change-inducing fossil fuels. However, all of these technologies are based on energy sources with variable intensity, and cannot be used directly for continuous electricity production at a single site.

Therefore, it is also pressing to find an efficient and economically viable technology for storable renewable energy so that it can be delivered on demand.

1.2. Hydrogen production from water splitting

Hydrogen has tremendous potential to become an environmentally-friendly fuel, in addition to its ever-growing demand in the petrochemical, refining, and semiconductor industries. Hydrogen is one of the greenest energy carriers, in that it produces only water when oxidized either by combustion or in a fuel cell. It also is a widely used raw material for chemical conversions and reduction reactions. However, production of hydrogen in required quantities at a competitive price has been a crucial and urgent challenge [11]. Hydrogen can be produced from water splitting using electrolysis by the following reactions.



The first reaction and second reaction are called the oxygen evolution reaction (OER) and hydrogen evolution reaction (HER), respectively. The standard potentials of the half reactions (E_{cell}^0) is -1.23V which is required to drive the reaction to split water into hydrogen and oxygen gases. However, a significantly larger potential must be applied for electrolysis to occur, usually well over 2 V in practice. The extra potential applied is called the overpotential, which contributes to direct electrolysis being energetically and financially costly.

To make the water splitting process feasible and cheap for industrial application, hydrogen can be produced by water splitting using a semiconductor photocatalyst with

sunlight as the required source of energy. The basic principle of the overall water-splitting reaction on a semiconductor photocatalyst is shown in Figure 1.1. There are two primary requirements for a semiconductor to be a water-splitting photocatalyst. First, the band gap of the semiconductor must be higher than the energy needed to split water. Second, band alignment is needed; the conduction band potential of the semiconductor must be more negative than the water reduction potential (H^+/H_2 , 0 V vs. NHE) and the highest level of valence band potential must be more positive than the water oxidation potential ($\text{O}_2/\text{H}_2\text{O}$, 1.23 V vs. NHE). The mechanism of hydrogen production by the water splitting reaction photocatalyzed by a semiconductor using sunlight is depicted in Figure 2 [12]. It is shown that electrons in the valence band of the semiconductor are excited by light of energy exceeding the band gap. The excited electrons are transferred into the conduction band of the semiconductor leaving holes (electron vacancies) in the valence band. The holes thus formed in the valence band oxidize H_2O to H^+ and O_2 . The newly formed H^+ reacts with the electrons excited in the conduction band of the semiconductor to form molecular hydrogen.

There are several semiconductor photocatalysts available for water splitting. Figure 2.2 shows the band positions for some of the most common metal oxide semiconductors in contact with aqueous electrolyte at pH 1. It can be seen that there are several semiconductors (such as GaAs_ with band gap small enough to absorb the most prominent, visible wavelengths of sunlight, and larger than the required energy for water splitting. However, the band positions of these semiconductors do not align with the water redox potential required for them to be used as photocatalysts for water splitting. On the other hand, there are other semiconductors such as CdS whose band gap is small enough to

absorb sunlight and larger than the potential required for water splitting, and whose band positions perfectly match with the water redox potentials. However, the challenge of using such semiconductors as a photocatalyst for water splitting is photocorrosion or instability in aqueous medium. Along with the small band gap and proper band alignment with the redox reaction potentials of water, stability of the photocatalyst in an aqueous medium is another challenge for industrial practice of photocatalytic water splitting. It has proven difficult to find a material which combines desirable band positions, a useful band gap, aqueous stability and a cost low enough for widespread application.

1.3. Titania as a Photocatalyst

Based on the general principles outlines above, titania fulfills all the primary requirements to be a potential photocatalyst for solar H₂ production. Since the first report of its use for hydrogen generation via the photocatalytic decomposition of water by Fujishima and Honda, [13] TiO₂ has attracted significant interest as a photocatalyst due to its favorable band edge positions which are well-matched with the redox potentials of water, CO₂ and a variety of organic compounds. TiO₂ is also attractive for this application because of its opto-electronic properties, which can be tuned by changing lattice defects or oxygen stoichiometry, its superior chemical stability and photocorrosion resistance, and its low cost [13-16]. These unique properties have enabled TiO₂ to be utilized in a wide range of applications including solar energy conversion, antimicrobial and self-cleaning surfaces, paint whiteners, ceramics, textiles, personal care products, and environmental catalysis [17-27].

Like many semiconductors, the photoactivity of TiO₂ originates from its ability to absorb light with energy greater than the band gap, which generates electrons and holes as

charge carriers by promoting electrons from the valence band to the conduction band [14]. This photocatalytic process involves a series of physical processes including light absorption, charge separation, charge migration, charge recombination and surface redox reactions [28]. The photogenerated charges can recombine and release their energy as light and heat, or these excited charges may reach the surface of titania and participate in reactions. The excited electrons have the potential to reduce oxygen molecules to produce superoxide radicals which are very reactive and participate in different reactions. On the other hand, if they reach the electrolyte interface either at titania or a counter electrode, holes are able to oxidize water to produce reactive hydroxyl radicals [29].

1.4. Nanostructured Titania

For the application of TiO_2 in photocatalysis, it is very important to control its morphology, nanostructure, and electronic properties to enhance the available surface area, light absorption, and effective charge carrier separation and transport [18, 30-32]. Further, to address the challenges of reducing recombination and increasing interfacial transport of photogenerated charge carriers, altering the atomic and nanoscale architecture of TiO_2 has become a major goal. Mesoporous TiO_2 offers a promising platform to address these challenges for a number of reasons that are beneficial for efficient photocatalysis [18, 33-35]. By using process variables to tune its morphology, nanostructure, and electronic properties, enhancements can be realized in the accessible surface area, light absorption, and effective charge carrier separation and transport in mesoporous TiO_2 [18, 30-32]. For instance, surfactant-induced templating provides excellent control over the pore size, pore orientation, interfacial structure and pore connectivity, which can be tuned to promote rapid diffusion of reactants to photocatalytic sites. Further, mesoporous TiO_2 offers a high

reactive surface area for photocatalysis and its thin walls provide a short distance for the transport of photogenerated charge carriers to the catalytic sites, thereby having the potential to suppress charge recombination processes [5, 15, 33, 34]. TiO₂ thin film can be prepared by an evaporation induced self-assembled (EISA) process using surfactant templating [36]. In this method, a substrate is dip coated in a solution of metal precursor, surfactants and solvent. A controlled amount of chemicals in the solution and definite synthesis conditions drive ordered micelle formation with the surfactants in the dip coated film. After removing the polymer, surfactant by calcining, the films are found with desired properties such as pore size, shape and their order. A detail discussion on the synthesis of mesoporous titania is provided in Chapter 2.

1.5. Doping of Titania

Despite many attractive features of TiO₂, the major challenges of its applications under natural solar light are its innate inability to absorb visible light, high rate of photogenerated charge carrier recombination, and low interfacial charge transfer rate of photogenerated charge carriers [17, 37]. The first challenge results from the wide band gap of TiO₂ (3.0-3.5 eV[38]), which allows the absorption of light mainly in the ultraviolet (UV) range, which corresponds to only 4-5% of the whole solar spectrum, while visible light constitutes 40% [39]. To reduce the intrinsic band gap of TiO₂, several strategies have been tested including the incorporation of either metallic (e.g. Fe and Ni) or non-metallic (e.g. C, F, N, S, P and B) atoms into the lattice of TiO₂ host materials [17, 23, 40-42]. Metal doping showed controversial photocatalytic activity results at both UV and visible wavelengths [43-46]. In addition, metal doping in titania can be complicated by thermal instability, increase of carrier-recombination centers, dopant insolubility, formation of

secondary phase or surface aggregation rather than substitution, phase transformation among the titania polymorphs, alteration of charge carrier diffusion length, narrow band bending etc. [47-49]. From this perspective, non-metal (H, B, C, N, F, S, P, and I) doping is thought to be a more viable strategy to reduce the band gap and enhance the visible light driven photocatalytic activity of titania. Increased visible light photocatalytic activity has been reported in non-metal doped titania. However, the exact chemical nature of the dopant species in titania and their roles for visible light absorption are not always clear [29].

Among non-metal dopants, nitrogen is one of the most effective elements to promote visible light photoactivity [17, 18, 50-52]. Due to its atomic size (comparable to oxygen), low ionization potential, and high stability, it is straightforward to introduce nitrogen into the titania lattice [29]. Effective band gap narrowing has been correlated with high amounts of dopants and strong interactions among the dopant energy states, valence and conduction bands [53]. Nitrogen atoms are known to occupy either interstitial sites (possibly with N-O bonding) or substitutional sites (replacement of O with N atoms) in TiO₂ [51]. Though interstitial nitrogen has been shown to increase visible light absorption, it does not reduce the band gap because it forms a discrete energy state between the valence band and conduction band, often referred to as a midgap state [54]. Most of the theoretical and experimental studies have shown that the predominant active form in doped TiO₂ is substitutional nitrogen which reduces the band gap and increases visible light absorption [17, 51, 54-57]. The reduced band gap is attributed to an upward shift of the edge of valence band due to the hybridization of the N 2p with the O 2p orbitals [17]. As a result, doped titania is able to absorb visible light due to the electrons excited from the localized N orbitals to the conduction band or to surface adsorbed O₂ [29]. In addition, it has been

reported that nitrogen doping increases the wettability of titania, resulting in better adsorption of polar reactant molecules [44, 58]. Different strategies of incorporating non-metal dopants, particularly nitrogen in titania, and resulting photocatalytic activities are discussed in details in Chapter 2.

1.6. Sensitization of Titania

In addition to the intrinsic modification of titania, sensitization is another route to help titania absorb visible light. Recently, utilization of tunable narrow band gap semiconductor quantum dots has drawn tremendous interest to sensitize wide band gap semiconductors such as metal oxides as alternative approaches to increase photoresponse [59]. Figure 1.3 shows a schematic of the sensitization mechanism of titania by small band gap semiconductors. Typically, small band gap semiconductors absorb visible light and electrons are excited from the valence band to the conduction band. When the conduction band potential of the small band gap semiconductors is more positive than that of the wide band gap semiconductors, the excited electrons from the conduction band of the small band gap semiconductors shift to the conduction band of the large band gap semiconductors where they participate in chemical reactions. Several semiconductor quantum dots including CdS, CdSe, CdTe and PbS with large extinction coefficient strongly absorb visible light, inject electrons into the conduction band of metal oxides such as TiO₂, and thereby contribute to increased solar energy conversion [59, 60]. However, the heterojunctions formed between these semiconductor quantum dots and wide band gap semiconductor photocatalysts are often inefficient because of the presence of surface traps in naked QDs which increase charge recombination [61]. Furthermore, these semiconductor quantum dots include toxic elements and are unstable due to photo-

oxidation leading to the photodegradation of their performances. For example, Pan et al. reported that CdS and CdSe sensitized TiO₂ nanotube arrays exhibit cycling instability due to serious photo-oxidation in a liquid medium under light irradiation [61].

As emerging quantum dots, graphene quantum dots (GQDs) are metal free and green sensitizers which are synthesized from carbon precursors. Pan et al. also showed that the GQD heterojunctions are superior to conventional semiconductor QDs in terms of visible-light catalytic activity, durability, and environmental friendliness [61]. Recently, graphene quantum dots (GQDs) have drawn tremendous attention due to their unique and novel properties. These include size-dependent band gaps due to strong quantum confinement and edge effects, excellent thermal and chemical stability, and environmentally friendly nature [62, 63]. GQDs are also water soluble which can enhance the water oxidation process. It has been found that making composites of GQDs and TiO₂ enhances the visible light absorption of TiO₂ due to charge transfer from GQDs to the conduction band of TiO₂ [62, 64-66]. Zhuo et al. demonstrated the design of TiO₂/GQD photocatalysts to harness the visible spectrum of sunlight based on the upconversion luminescence properties of GQDs. The efficacy of their photocatalytic ability was determined by degradation of methylene blue under visible light irradiation [62]. Williams et al. also demonstrated the feasibility of hot electron harvesting from GQDs to titania using time-resolved second harmonic generation, and found evidence for ultrafast electron injection from photoexcited GQDs to the conduction band of titania. In addition, titania with various morphologies including nanotubes, fibers and nanoparticles has been sensitized with GQDs [62, 64-68]. All of these GQDs-TiO₂ show high visible-light catalytic activity, long-term durability, and environmental friendliness.

1.7. Overview and Summary of the Dissertation

While mesoporous TiO₂ can be synthesized by different methods, it is challenging to incorporate dopants into the lattice of the material while maintaining an advantageous mesostructure. Normally, high-temperature heat treatment of TiO₂ in the presence of a dopant source is used to incorporate new elements into the titania lattice. High temperature treatment typically causes a decrease in pore size, surface area and pore accessibility by sintering and crystallization. Various strategies have been reported to introduce non-metal dopants into mesoporous TiO₂, but the properties of the doped mesoporous TiO₂ product are strongly dependent on the dopant source and strategy. The photocatalytic activity of the materials is closely related to its preparation method, so understanding the relationship between synthetic strategy, structure and performance is a key to moving towards highly efficient visible-light photocatalysis using mesoporous TiO₂ based materials.

This dissertation addresses the applications of mesoporous titania thin films synthesized via a surfactant templated sol-gel process. To address the challenge of using titania as a photocatalyst, the band gap of mesoporous titania thin films is reduced by modifying the valence band and the conduction band using nitrogen and hydrogen doping, respectively. For tuning the band gap, hydrazine and plasma treatments have been developed in this dissertation research. In addition to the intrinsic modification of titania, graphene quantum dot sensitized mesoporous titania thin films for visible light driven photocatalysis has been developed. All of the modified titania films were applied for photoelectrochemical water oxidation. This dissertation is organized into eight chapters including Chapter 1 (this chapter) which describes the general background of this

dissertation. The summaries of Chapter 2 to Chapter 7 are provided below. Lastly, the findings from this dissertation and future directions are provided in Chapter 8.

Chapter 2: This chapter provides a comprehensive literature review on non-metal doping in mesoporous TiO₂ and its effects on visible light driven photocatalytic performance for environmental and energy conversion applications. First, the general synthesis process of mesoporous TiO₂ are presented, with an eye towards how the evolution from precursor to final mesoporous structure can be influenced by the doping strategy. Following this, a comprehensive review is provided of non-metal dopant sources and doping strategies for mesoporous TiO₂. While fewer examples have been reported in literature, some examples of co-doping are discussed. A summary of photocatalytic performance enhancements by non-metal doping of mesoporous TiO₂ is provided. Finally, applications of the non-metal doped mesoporous TiO₂ are summarized in the fields of organic pollutant photocatalysis, hydrogen production from water splitting and CO₂ reduction. Finally, this review provides a summary of key achievements and directions in the non-metal doping of mesoporous TiO₂ and the extent of applications of these materials. This work was published in the journal *Inorganics* (Islam et al., *Inorganics*, 2017, 5(1), 15).

Chapter 3: In this chapter, we report the incorporation of Ti³⁺ and nitrogen atoms into surfactant-templated mesoporous TiO₂ thin films by hydrazine treatment. Cubic ordered mesoporous TiO₂ thin films were synthesized by templating films derived from TiCl₄ with triblock copolymer surfactant Pluronic F127. Then, the films were treated with hydrazine hydrate, followed by analysis of photocatalytic activity for methylene blue degradation as a test reaction. The photoelectrochemical performance of the doped films

were demonstrated using water oxidation under basic pH conditions with a visible light source. This study suggests that hydrazine induced doping is a promising approach to enable synergistic incorporation of N and Ti³⁺ into the lattice of surfactant-templated TiO₂ films for enhanced visible light photoactivity, but that the benefits are limited by gradual mesostructure deterioration. This chapter was published in *Materials Chemistry and Physics* (Islam et al., *Mater. Chem. Phys.*, **2016**, 182, 382-393).

Chapter 4: In this chapter, we report the incorporation of nitrogen into surfactant templated mesoporous TiO₂ films by N₂/Ar plasma treatments. The cubic ordered mesoporous TiO₂ thin films are treated with N₂/Ar plasma generated by a microwave-assisted chemical vapor deposition (CVD) system, followed by analysis of photocatalytic activity for methylene blue degradation as a test reaction. The optical absorbance and photocatalytic activity of nitrogen doped TiO₂ films are correlated with the duration of N₂/Ar plasma treatments. The doped films showed about six times higher performance than undoped titania films in the photocatalytic degradation of methylene blue under visible-light illumination. This study suggests that the plasma-based doping approach is very effective for incorporation of heteroatoms into mesoporous titania films while maintaining their nanostructure.

The work in this chapter was performed in collaboration with the research group of Dr. Doo-Young Kim from the Chemistry department at the University of Kentucky. My contributions are the synthesis and characterization of the mesoporous titania thin films, and photocatalytic activity tests. Allen Reed performed the plasma treatment of the films for nitrogen doping. This work was published in *Microporous and Mesoporous Materials* (Islam et al., *Microporous Mesoporous Mater.*, **2016**, 220, 120-128).

Chapter 5: This study explores the water oxidation using nitrogen doped, ordered mesoporous TiO₂ thin films under visible light irradiation. In our previous chapter, we demonstrated enhanced photocatalytic activity for dye degradation of mesoporous TiO₂ films by treating them with N₂/argon plasma [69]. In this chapter, we report even more substantial effects for photocatalytic water oxidation under visible light using mesoporous TiO₂ films treated with N₂/argon plasma. Cubic ordered mesoporous titania films were treated with microwave-generated N₂/Ar plasma. The effects of plasma treatment conditions such as gas pressure and nitrogen flow rate on the ultimate photocatalytic performance were studied along with the effects of light sources with different wavelengths. Photocatalytic activities of plasma-treated TiO₂ mesoporous films were studied by chronoamperometry, linear sweep voltammetry and electrochemical impedance spectroscopy. The results show exceptional improvements (over 200 times at certain wavelengths) in photocatalytic water oxidation under both UV and visible light compared with prior reports due to the amorphous, high surface area nature of the surfactant templated mesoporous titania. These results suggest that these materials may be a promising platform for “disorder engineering” of photoelectrocatalysis.

This project was performed in collaboration with the research group of Dr. Doo-Young Kim from the Chemistry Department at the University of Kentucky. My contributions are the synthesis and characterization of mesoporous titania thin films and photocatalytic activity tests, Allen Reed performed plasma treatment of the films for nitrogen doping, and Namal Wanninayake conducted zeta potential and contact angle measurements. This work was published in *Journal of Physical Chemistry C* (Islam et al., *J. Phys. Chem. C*, **2016**, 120(26), 14069-14081).

Chapter 6: In this work, we report the first example of GQD sensitized, nitrogen doped mesoporous titania for photoelectrochemical water oxidation. The cubic ordered mesoporous titania films were treated with nitrogen/argon plasma for nitrogen doping. The graphene quantum dots were synthesized by chemical oxidation of carbon nano-onions. Finally, GQDs were attached to the nitrogen doped titania films by a hydrothermal method. The graphene quantum dot sensitized titania films show synergistic enhancement when combined with plasma-based doping for photoelectrochemical water oxidation.

This project was performed in collaboration with the research group of Dr. Doo-Young Kim from Chemistry department at the University of Kentucky. My contributions are the synthesis and characterization of the mesoporous titania thin films and photocatalytic activity tests, Allen Reed performed the plasma treatment of the films for hydrogenation, and Namal Wanninayake synthesized and attached GQDs on titania films, conducted zeta potential and contact angle measurements. A manuscript on graphene quantum dot sensitized and nitrogen doped titania is in preparation for submission.

Chapter 7: This study investigates the presence of hydrogen in hydrogen plasma treated black mesoporous titania thin films for visible light driven photocatalytic water oxidation. Hydrogen treatment has been shown to turn titania from bright white to black, indicating vastly improved visible light absorption. The cause of the color change and its effectiveness for photocatalysis remain open questions. For the first time, we showed that a significant amount of hydrogen is incorporated in hydrogen plasma treated mesoporous titania films using neutron reflectometry measurements. Photocatalytic activities of hydrogen plasma-treated mesoporous TiO₂ films are studied by photoelectrochemical

water oxidation under both UV and visible light irradiation. A manuscript on hydrogen plasma treated titania films is ready for short-term submission.

This project was performed in collaboration with the research group of Dr. Doo-Young Kim from the Chemistry Department at the University of Kentucky. My contributions are the synthesis and characterization of mesoporous titania thin films and photocatalytic activity tests, Allen Reed conducted plasma treatment of the films for hydrogenation, and Namal Wanninayake conducted the zeta potential and contact angle measurements. A manuscript on hydrogen plasma doping of mesoporous titania films is ready for short-term for submission.

Figures of Chapter 1

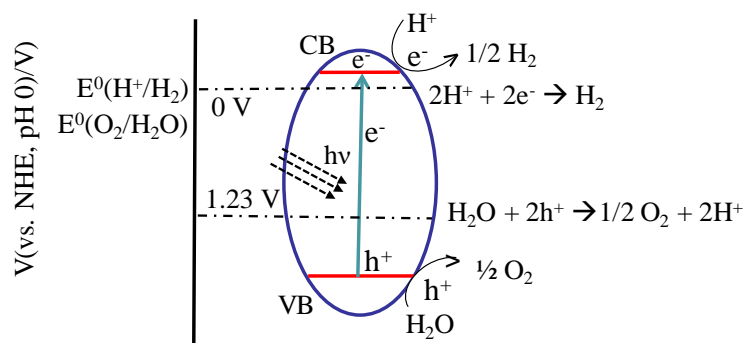


Figure 1.1. Basic principle of the overall water-splitting reaction on a semiconductor photocatalyst. Adapted from ref. [70].

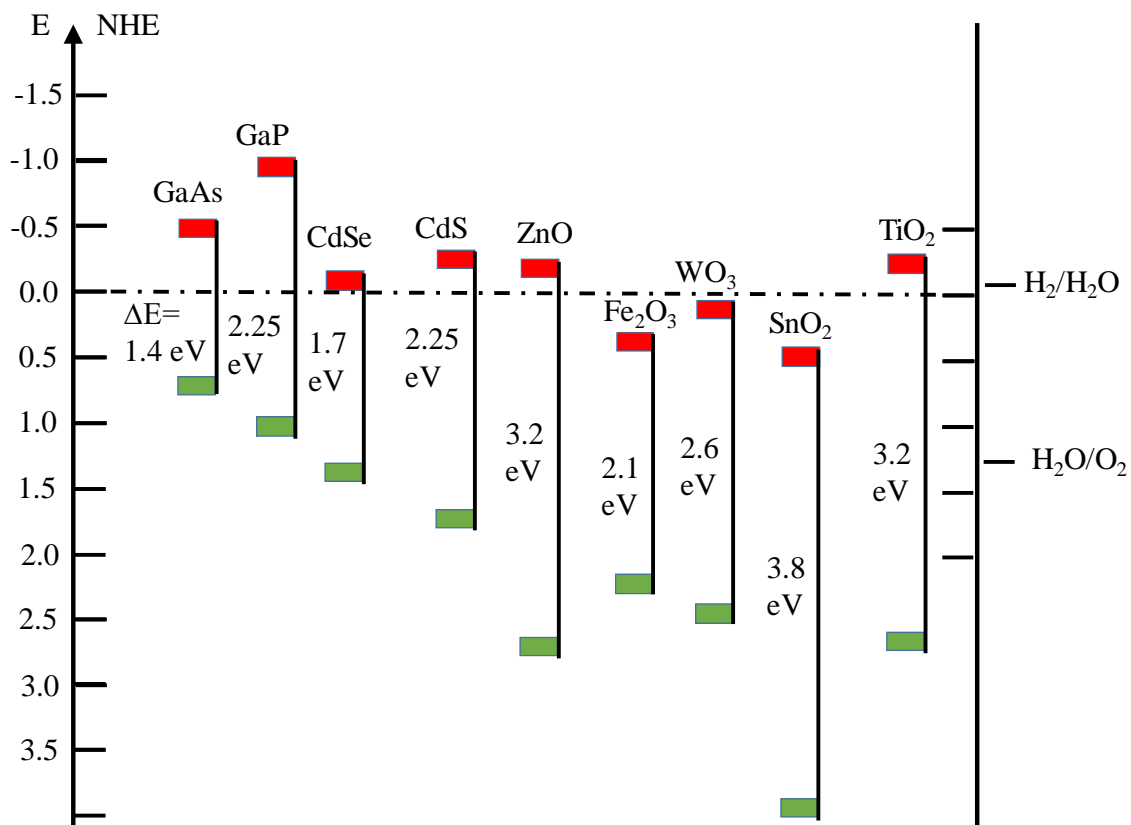


Figure 1.2. Band positions of several semiconductors in contact with aqueous electrolyte at pH 1. The lower edge of the conduction band (red colour) and upper edge of the valence band (green colour) are presented along with the band gap in electron volts. The energy scale is indicated in electron volts using the normal hydrogen electrode (NHE) as a reference. Note that the ordinate presents internal and not free energy. The free energy of an electron–hole pair is smaller than the band gap energy due to the translational entropy

of the electrons and holes in the conduction and valence band, respectively. On the right side, the standard potentials of water redox couple are presented against the standard hydrogen electrode potential. Adapted from reference [14].

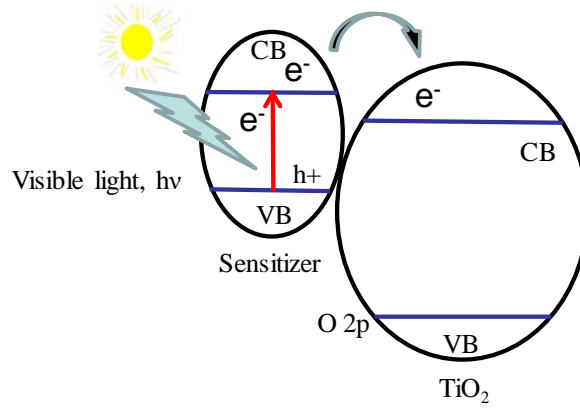


Figure 1.3. Schematic of band diagram of sensitization of titania by small band gap semiconductors.

Chapter 2. Synthesis and Catalytic Applications of Non-metal Doped Mesoporous Titania

Reproduced with permission from Islam, S. Z., Nagpure, S., Kim, D. Y., Rankin, S. E., *Inorganics*, 2017, 5(1), 15.

2.1 Summary

Mesoporous titania (mp-TiO₂) has drawn tremendous attention for diverse applications due to its high surface area, interfacial structure and tunable combination of pore size, pore orientation, wall thickness, and pore connectivity. Its pore structure facilitates rapid diffusion of reactants and charge carriers to the photocatalytically active interface of TiO₂. However, because the large band gap of TiO₂ limits its ability to utilize visible light, non-metal doping has been extensively studied to tune the energy levels of TiO₂. While first-principles calculations support the efficacy of this approach, it is challenging to efficiently introduce active non-metal dopants into the lattice of TiO₂. This review surveys recent advances in the preparation of mp-TiO₂ and their doping with non-metal atoms. Different doping strategies and dopant sources are discussed. Further, co-doping with combinations of non-metal dopants are discussed as strategies to reduce the band gap, improve photogenerated charge separation, and enhance visible light absorption. The improvements resulting from each doping strategy is discussed in light of potential changes in mesoporous architecture, dopant composition and chemical state, extent of band gap reduction, and improvement in photocatalytic activities. Finally, potential applications of non-metal doped mp-TiO₂ are explored in water splitting, CO₂ reduction and environmental remediation with visible light.

2.2. Introduction

TiO₂ (titania) is one of the most extensively studied semiconductor photocatalysts due to its potential to help overcome the worldwide energy shortage while also counteracting issues of climate change and environmental contamination [70-72]. Since the first report of its use for hydrogen generation via the photocatalytic decomposition of water by Fujishima and Honda, [13] TiO₂ has attracted significant interest as a photocatalyst due to its favorable band edge positions which are well-matched with the redox potentials of water, CO₂ and a variety of organic compounds. TiO₂ is also attractive for this application because of its opto-electronic properties, which can be tuned by changing lattice defects or oxygen stoichiometry, its superior chemical stability and photocorrosion resistance, and its low cost [13-16]. These unique properties have enabled TiO₂ to be utilized in a wide range of applications including solar energy conversion, antimicrobial and self-cleaning surfaces, paint whiteners, ceramics, textiles, personal care products, and environmental catalysis [17-27].

Like many semiconductors, the photoactivity of TiO₂ originates from its ability to absorb light with energy greater than the band gap, which generates electrons and holes as charge carriers by promoting electrons from the valence band to the conduction band [14]. This photocatalytic process involves a series of physical processes including light absorption, charge separation, charge migration, charge recombination and surface redox reactions [28]. The photogenerated charges can recombine and release their energy as light and heat, or these excited charges may reach the surface of titania and participate in reactions. The excited electrons have the potential to reduce oxygen molecules to produce superoxide radicals which are very reactive and participate in different reactions. On the

other hand, if they reach the electrolyte interface either at titania or a counter electrode, holes are able to oxidize water to produce reactive hydroxyl radicals [29].

Despite many attractive features of TiO₂, the major challenges of its applications under natural solar light are its innate inability to absorb visible light, high rate of photogenerated charge carrier recombination, and low interfacial charge transfer rate of photogenerated charge carriers [17, 37]. The first challenge results from the wide band gap of TiO₂ (3.0-3.5 eV[38]), which allows the absorption of light mainly in the ultraviolet (UV) range, which corresponds to only 4-5% of the whole solar spectrum, while visible light constitutes 40% [39]. To reduce the intrinsic band gap of TiO₂, several strategies have been tested including the incorporation of either metallic (e.g. Fe and Ni) or non-metallic (e.g. C, F, N, S, P and B) atoms into the lattice of TiO₂ host materials [17, 23, 40-42]. Metal doping showed controversial photocatalytic activity results at both UV and visible wavelengths [43-46]. In addition, metal doping in titania can be complicated by thermal instability, increase of carrier-recombination centers, dopant insolubility, formation of secondary phase or surface aggregation rather than substitution, phase transformation among the titania polymorphs, alteration of charge carrier diffusion length, narrow band bending etc. [47-49]. From this perspective, non-metal (H, B, C, N, F, S, P, and I) doping is thought to be a more viable strategy to reduce band gap and enhance the visible light driven photocatalytic activity of titania. Increased visible light photocatalytic activity has been reported in non-metal doped titania. However, the exact chemical nature of the dopant species in titania and their roles for visible light absorption are not always clear [29].

Among non-metal dopants, nitrogen is one of the most effective elements to promote visible light photoactivity [17, 18, 50-52]. Due to its atomic size (comparable to

oxygen), low ionization potential, and high stability, it is straightforward to introduce nitrogen into the titania lattice [29]. Effective band gap narrowing has been correlated with high amounts of dopants and strong interactions among the dopant energy states, valence and conduction bands [53]. Nitrogen atoms are known to occupy either interstitial sites (possibly with N-O bonding) or substitutional sites (replacement of O with N atoms) in TiO₂ [51]. Though interstitial nitrogen has been shown to increase visible light absorption, it does not reduce the band gap because it forms a discrete energy state between the valence band and conduction band, often referred to as a midgap state [54]. Most of the theoretical and experimental studies have shown that the predominant active form in doped TiO₂ is substitutional nitrogen which reduces the band gap and increases visible light absorption [17, 51, 54-57]. The reduced band gap is attributed to an upward shift of the edge of valence band due to the hybridization of the N 2p with the O 2p orbitals [17]. As a result, doped titania is able to absorb visible light due to the electrons excited from the localized N orbitals to the conduction band or to surface adsorbed O₂ [29]. In addition, it has been reported that nitrogen doping increases the wettability of titania, resulting in better adsorption of polar reactant molecules [44, 58].

Other non-metal elements such as H, B, C, F, I, S and P have also been doped into TiO₂ and visible light driven photocatalytic activity was observed as a result [73, 74]. Valentin et al. performed density functional theory (DFT) calculations to investigate the effects on the electronic structure of replacing lattice O atoms with B, C, N, or F dopants, or to include the same atoms in interstitial positions [73]. As Figure 2.1 shows, the energy states associated with substitutional non-metal dopants fall in between the valence and conduction bands of TiO₂. Relative to the valence band, the energy level of the bands

introduced by doping increases with decreasing electronegativity. N-doping introduces an energy state just above the valence band whereas B gives states high in the band gap. Since fluorine is very electronegative, it has introduced states below the O 2p valence band and leads to the formation of Ti^{3+} ions due to charge compensation. In contrast, interstitial doping led to a combination of energy levels above and below the valence band for B and C. Without donating any electron to the host lattice, N was predicted to form a direct bond with a lattice O atom to create a non-photoactive interstitial doping site.

To further improve the visible light driven photocatalytic activity of TiO_2 , binary and ternary co-doping of two non-metal elements such as N-B and N-C has been studied [29, 75-85]. Synergistic effects of the co-doping were observed in many cases, although the complexity of the parameter space makes it difficult to draw general conclusions about doping effects. In addition to band gap reduction and visible light absorption, adding non-metal elements into TiO_2 may have effects on the microstructure of the material, depending on the route of introduction. In one example, boron doped TiO_2 particles were found to have reduced size resulting in higher surface area and suppressed phase transformation, and improves photogenerated charge separation, which contribute to the photocatalytic performance of titania significantly [86].

While significant positive effects of doping TiO_2 have been reported, from an application and commercial point of view, the photocatalytic performance of TiO_2 must be further enhanced. To address the challenges of reducing recombination and increasing interfacial transport of photogenerated charge carriers, altering the atomic and nanoscale architecture of TiO_2 has become a major goal. Mesoporous TiO_2 offers a promising platform to address these challenges for a number of reasons that are beneficial for efficient

photocatalysis [18, 33-35]. By using process variables to tune its morphology, nanostructure, and electronic properties, enhancements can be realized in the accessible surface area, light absorption, and effective charge carrier separation and transport in mp-TiO₂ [18, 30-32]. For instance, surfactant-induced templating provides excellent control over the pore size, pore orientation, interfacial structure and pore connectivity, which can be tuned to promote rapid diffusion of reactants to photocatalytic sites. Further, mp-TiO₂ films offers a high reactive surface area for photocatalysis and their thin walls provide a short distance for the transport of photogenerated charge carriers to the catalytic sites, thereby having the potential to suppress charge recombination processes [5, 15, 33, 34].

While mp-TiO₂ can be synthesized by different methods, it is challenging to incorporate dopants into the lattice of the material while maintaining an advantageous mesostructure and crystal phase. Normally, high-temperature heat treatment of TiO₂ in the presence of a dopant source is used to incorporate new elements into the titania lattice. High temperature treatment typically causes a decrease in pore size, surface area and pore accessibility by sintering and crystallization. Various strategies have been reported to introduce non-metal dopants into mp-TiO₂, but the properties of the doped mp-TiO₂ product are strongly dependent on the dopant source and strategy. For instance, we recently reported that plasma treatment of mp-TiO₂ introduces a high level of substitutional nitrogen into the lattice, whereas methods based on chemical precursors are more prone to generating interstitial nitrogen [69]. The photocatalytic activity of the materials is closely related to its preparation method, so understanding the relationship between synthetic strategy, structure and performance is a key to moving towards highly efficient visible-light photocatalysis using mp-TiO₂ based materials.

There have been a number of reviews published addressing the synthesis of mp-TiO₂ and its broad range of applications [87-90] so we will begin with just a brief overview of some of the most relevant strategies. In 2011, Ismail et al. published a review article on mp-TiO₂ photocatalysts [41] that provides an overview of the preparation and characterization of mp-TiO₂ and incorporation of noble metals nanoparticles, transition metal ions, and non-metal dopants. The characteristics of the mesoporous materials and their activity and mechanisms of photocatalysis are discussed. A recent short review by Zhou et al. addresses the effects of the mesoporous structure, crystallinity, surface area, and pore size of TiO₂ on its photocatalytic performance [91], with a short overview of modifications of mp-TiO₂ using doping and composite materials. While doping has been included to some extent, the primary focus of all the reviews mentioned here was the synthesis and characterization of the mp-TiO₂. Considering the intense interest in visible-light photocatalysis using inexpensive materials, there is room for a review addressing primarily doping strategies and their outcomes.

This article will focus specifically on non-metal doping strategies in mp-TiO₂ and recent advances in understanding their effects on visible light driven photocatalytic performance for environmental and energy conversion systems. First, the general synthesis process of mp-TiO₂ will be presented, with an eye towards how the evolution from precursor to final mesoporous structure can be influenced by the doping strategy. Following this, a comprehensive review will be provided of non-metal dopant sources and doping strategies for mp-TiO₂. While fewer examples have been reported in literature, some examples of co-doping will be discussed. A summary of photocatalytic performance enhancements by non-metal doping of mp-TiO₂ will be provided. Finally, applications of

the non-metal doped mp-TiO₂ will be summarized in the fields of organic pollutant photocatalysis, hydrogen production from water splitting and CO₂ reduction. Although this area of research is very broad, this review will provide a summary of key achievements and directions in the non-metal doping of mp-TiO₂ and the extent of applications of these materials.

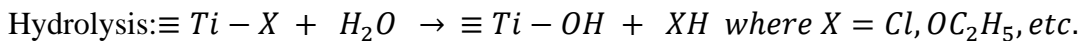
2.2.1. Synthesis of mesoporous TiO₂

Surfactant-templated synthesis of ordered mp-TiO₂ was first reported by Antonelli and Ying in 1995 [92]. Since then, different mesoporous structures of TiO₂ have been synthesized including 2D hexagonal, 3D cubic and lamellar using methods including sol-gel, hydrothermal, solvothermal, microwave, and sonochemical methods [69, 93-106]. A variety of morphologies have also been reported due to the interplay between mesostructure nucleation, orientation of mesophases at the surface of surfactant/precursor aggregates, and growth of organic/titania composites. Of all forms, thin mp-TiO₂ films are highly relevant to photoelectrocatalysis both for practical reasons (they can readily be deposited onto electrodes) and because they provide fundamental insight into the interplay of composition, processing, and surface chemistry. For instance, in our group we have prepared mp-TiO₂ thin films using Pluronic triblock copolymer surfactants with cubic mesostructure [69] and orthogonally oriented 2D hexagonally close packed (o-HCP) cylindrical nanopores [103-105] using the evaporation induced self-assembly (EISA) technique by manipulating process conditions. Figure 2.2 shows computer-generated illustrations of typical mesoporous structures and mesophases such as Im3m cubic mesoporous material, o-HCP mesoporous film, parallel HCP mesoporous film, and

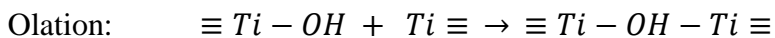
lamellar mesophase where higher intensity (yellow and red) corresponds to a greater density of hydrophobic tails of the surfactant template.

2.2.2. *Titanium Precursor Chemistry*

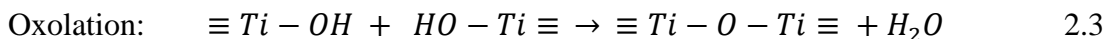
Most of the doped TiO₂ materials to be discussed are prepared by precipitation or sol-gel processes based on “bottom-up” growth using molecular precursors. This process proceeds by hydrolytic polycondensation of titanium precursors (most often alkoxides or chlorides) in the presence of reactivity modifiers, solvents and organic templates. The process begins with hydrolysis, which is the formation of Ti-OH moieties by the substitution reaction of water with Ti-Cl or Ti-OR groups (Equation 2.1). After being “activated” this way, precursors undergo condensation reactions to generate Ti-OH-Ti bonds by olation (Equation 2.2), or Ti-O-Ti by oxolation (Equation 2.3). Livage et al. provided an excellent overview of the sol-gel chemistry of transition metal precursors [107] and described the dependence of hydrolysis reaction mechanism of metal ions on several factors including the electron affinities, sizes and the charges of metal ions and alkoxy groups; and the number of alkoxy groups. Because titanium has a high partial charge and a preferred coordination number greater than its valence, Ti precursors tend to be quite reactive towards hydrolysis. The high reactivity of transition metal oxides can be reduced by adding complexing ligands (such as acetylacetonate) [108] or increasing acid concentration [109].



2.1



2.2



Kim et al. [110] proposed two kinds of mechanisms for the hydrolysis of titanium alkoxides. One is an associative mechanism, in which the entering group forms a complex with the metal first, then a detectable intermediate of expanded coordination number is formed. The other mechanism is an interchange associative (Ia) mechanism in which the transition state is reached mostly through formation of the bond with the entering group. In this mechanism, the bond weakening of the leaving group also takes place in the course of reaching the transition state. An associative (A) mechanism is most appropriate to describe the hydrolysis of Ti(OEt)₄, whereas the transition states for the hydrolysis for Ti(OⁿPr)₄ and Ti(OⁿBu)₄ are reached through the interchange associative (Ia) mechanism. Henry et al. [111] studied the mechanistic aspects of the hydrolysis and condensation of titanium alkoxides complexed by tripodal ligands and found that bridging positions for OR groups are sites of preferential attack for substitution by OH and/or OX groups and the basic structure of the Ti₄O₁₆ core can be conserved upon hydrolysis and can be used as a building block for building complexes of higher nuclearity. Sanchez and coworkers [112] studied the role of water in the hydrolysis reaction in the presence of Pluronic surfactants and found that during anhydrous or low water conditions, there are strong Ti-polymer interactions which hinder the assembly of the template, leading to a final wormlike structure. In contrast, a high water / high acid environment hinders Ti-polymer interactions, which allows the micelles to assemble into well-ordered mesoporous structures.

There are two main pathways for the preparation of ordered mp-TiO₂, soft and hard templating. The soft templating method usually proceeds by a co-assembly process of the

precursors (silica, metal oxides, polymers, *etc.*) and surfactant templates [89, 113]. Since the success in the synthesis of ordered mesoporous silica, this methodology has been extended to transition metal oxide analogues. Since the soft-templating method is based on the co-assembly of reacting metal oxide precursors with surfactants in a dried film, the chemistry of the precursors needs to be understood and controlled to give the best chance of producing a desired film. As noted above, titania precursors (e.g. titanium (IV) ethoxide and titanium tetrachloride) are more reactive than silica precursors such as tetraethoxysilane, which can lead to rapid precipitation under uncontrolled conditions. Thus, titania precursors can be very difficult to work with if care is not taken in the design of the synthesis procedure.

In their synthesis, Antonelli and Ying [92] used acetylacetone to decrease the hydrolysis and condensation rate of titanates to permit assembly of well-ordered materials by interactions with the phosphate head groups of a tetradecylphosphate surfactant aqueous solution. However, a significant amount of phosphorus remained after the surfactant template was removed leading to relatively low photocatalytic activity. In 1999, Antonelli et al. reported the synthesis of nonphosphated mp-TiO₂ by using dodecylamine as the template combined with a dry aging technique [114]. However, the materials did not have high thermal stability for catalytic applications. Also, developing new methods of controlling the hydrolysis and polymerization of titania precursors was essential to be able to obtain high mesostructural regularity over large domains. The EISA method of Brinker and coworkers offers such an opportunity. The method was initially reported to prepare mesoporous silica thin films,[115] but was almost immediately realized as the most

efficient strategy to synthesize mp-TiO₂. Figure 2.3 shows the schematics of the important stages of the formation of ordered nanoporous metal oxide films by EISA.

2.2.3. Surfactant-templated Film Deposition

Figure 2.3a shows the dip coating process in which surfactant micelles form and may begin to assemble due to evaporation adapted from Brinker et al. [115]. In EISA, films are prepared by dip coating of substrates from a solution containing inorganic precursors, surfactant and solvent accompanied by rapid evaporation of volatile solvents (ethanol and water) to drive the formation of an ordered mesoporous structure. One important advantage of EISA for the preparation of mesoporous transition metal based thin films is that the pH can initially be adjusted to stabilize the coating sol and allow gradual assembly of an ordered mesostructure after coating. In order to inhibit rapid oligation and condensation of the titania precursors to allow self-assembly to occur, protons (H⁺ ions) have been used as inhibitors [109]. Although ligands such as acetylacetonate can also be used to reduce the reactivity of metal alkoxides, they can interfere in the interactions between titanium species and surfactants, so H⁺ is a more widely used inhibitor in the synthesis of surfactant templated mp-TiO₂ films [116-119]. Using a highly acidic sol prevents uncontrolled condensation of transition metal precursors, which allows slow formation of the inorganic network within the liquid crystal mesophase formed after coating. Gradual elimination of the acid by evaporation provides a way to control the polymerization of the inorganic components while allowing a fully cured inorganic network to form [120].

In addition to precursor chemistry, the choice of structure directing agent has a vital influence over the final mesostructure formed in surfactant-templated titania films [116, 121]. For example, using titanium isopropoxide as inorganic precursor, films with an

columnar 2D hexagonal close packed (HCP) mesostructure were reported using the Pluronic surfactant P123 (a triblock copolymer with average formula $\text{EO}_{20}\text{PO}_{70}\text{EO}_{20}$, where EO is ethylene oxide and PO is propylene oxide), while cubic mesostructured films were obtained with Pluronic F127 ($\text{EO}_{106}\text{PO}_{70}\text{EO}_{10}$) [122]. In addition to the template itself, the molar ratio (M) of structure directing agent to the titania precursor also influences the type of mesostructure formed [33, 116, 121]. Changing M changes, the amount of inorganic precursor associated with the hydrated PEO head groups and the number density of micelles formed after coating. In other words, M changes the packing parameter (P) of the micelles, which is defined as $P=V_0/(A_e \cdot L_0)$, where V_0 is the surfactant tail volume, A_e is the equilibrium area per molecule at the aggregate interface and L_0 is the surfactant tail length.[123] The most direct effect of decreasing M should be to increase A_e (since more polar components are present to interact with and expand the surfactant headgroups), which is expected to favor aggregates with higher curvature such as cylinders ($P=1/2$) and then spheres ($P=1/3$).

Films with cubic, hexagonal and lamellar phase can be obtained by varying M . Crepaldi et al. [33] synthesized mp- TiO_2 films using TiCl_4 as titania precursor using various surfactants and found that for P123, titania films with 2D HCP mesophase are obtained for M of 0.05-0.09 and lamellar mesophase for higher values of M . With F127 as template, a cubic phase is obtained for M values of 0.003-0.006, and 2D HCP for M between 0.008-0.01. In a slightly different but consistent approach, Alberius et al. [116] showed that the final mesophases in surfactant-templated materials can often be predicted based on the volume fraction of surfactant (Φ), which is defined as the ratio of the volume of surfactant in the dried film to the volume of the nonvolatile (polar) components in the

final film. They predicted based on the observed phase behavior of P123 in water that for titania films synthesized using P123 as the surfactant and titanium ethoxide [Ti(OEt)₄] as the titania precursor, the mesophase should be cubic, 2D HCP or lamellar for Φ in the ranges from 29%-36%, 38%-55% and 61%-75% respectively. Wu et al. [124] reported the synthesis of titania films using P123 and Ti(OEt)₄ for M ratios between 0.006 and 0.012, which is expected to correspond to Φ in the range from 26% to 41% [124]. The mesostructure should vary from 2D HCP, to a cubic mesophase, to a disordered micellar solution sequentially, as the molar ratio (M) decreases from 0.0122 to 0.01, 0.008 and 0.006 according to Alberius et al. [116]. However, Wu et al. [124] found for a P123 to Ti ratio as low as 0.006, a stable well-ordered mesostructure is still obtained, which is similar to the results obtained by Crepaldi et al. [33] and unlike Alberius et al. [116]. This might be because the formation mechanism of the mp-TiO₂-based thin films is influenced by many factors besides the templates and precursor volume fractions, including aging temperature, aging time, relative humidity of atmosphere, [33, 125] the acidity of the solution, [33, 125] etc.

In addition to the type of mesophase, its orientation can be important for many applications. By analogy with surface chemistry strategies used to orient block copolymer films [126-131], the Rankin group has reported the synthesis of mp-TiO₂ thin films with orthogonally tilted HCP (o-HCP) cylindrical nanopores using EISA with P123 as structure directing agent and titanium(IV) ethoxide as titania precursor [104, 132]. The hypothesis underlying this approach is that orthogonal alignment of the HCP mesophase can be achieved in EISA-derived ceramic film by modifying the substrate surface so that it interacts equally with both blocks of the P123 template, making it chemically “neutral”

towards the template surfactant. Monte Carlo simulations [133, 134] have shown that this is the expected outcome for mixtures of surfactants and small molecules, and not just for neat block copolymers [130]. A related epitaxial orientation procedure was demonstrated by Tolbert and coworkers, where HCP film was cast onto a cubic template film to induce orthogonal alignment [135].

2.2.4. Surfactant/Titania Film Aging

In addition to surface modification, the synthesis procedure for o-HCP TiO₂ films includes aging after coating in a refrigerator at 4 °C under high relative humidity (approx. 94%). The objectives of using a low temperature are to slow titanium precursor condensation and to provide a driving force for mesophase formation, similar to the subambient temperatures used by Alberius et al. [116]. Even though this aging procedure has been found to be an essential part of o-HCP TiO₂ film formation, little is known about the o-HCP mesostructure formation mechanism other than what has been inferred by characterization of the films before and after calcination [104]. Grosso et al. analyzed the mechanisms involved in the formation of 2D-hexagonal templated SiO₂ and TiO₂ mesostructured films during dip coating using Brij-58 as surfactant and found that the self-assembly leads to the formation of organized phase at the final stage of the drying process and involves the formation of an intermediate disorganized phase [136]. The disorder to order transition takes place on the order of 2-3 minutes after the start of coating for TiO₂ under the conditions studied. Other reports have shown that for dip-coated thin films, the mesostructure generally forms through a disorder-to-order transition which may involve intermediate hybrid mesophases that are related to the concentration gradient [137-139].

Recently, Nagpure et al. [103] reported an *in-situ* GISAXS investigation of low-temperature aging in oriented surfactant-mesostructured titania thin films and found that the o-HCP structure is the first ordered mesophase formed, and it emerges slowly by a disorder-order transition consistent with the tunable steady state (TSS) proposed for highly acidic TiO₂ sols [140, 141]. Figure 2.3b shows the aging process after deposition in which films organize into an ordered mesophase. [103]. The slow mesophase formation and long TSS may also be accentuated by the use of P123 as a template [142]. Other studies that showed the formation of vertically oriented cylindrical channels by transformation of a cubic phase and merging of the pores normal to the film also showed diffraction spots consistent with the cubic phase prior to thermal treatment [143-145]. However, the results obtained by Nagpure et al. [103] are consistent with the hypothesis underlying the work of Koganti et al. [132] that vertical channels simply form due to reorientation of the HCP phase in response to the modification of the surface of the substrate with a chemically neutral crosslinked P123 layer. A perfectly o-HCP structure follows 2D growth mechanism with nucleation at the start of the process, whereas films with mixed pore orientation follow 2D growth with continuous nucleation. They also studied the effects of aging temperature on mesostructure orientation and found that for the film aging at 4 °C, a very well-ordered, accessible porous structure was observed everywhere indicating orthogonal alignment of the cylindrical micelles. When a film was aged at 23 °C, randomly oriented parallel stripes were observed everywhere at the top surface of the film, indicating that the cylindrical micelles were arranged parallel to the substrate but with no preferred in-plane orientation. Significant thermotropic behavior occurs in Pluronics because of changes in the hydrophilicity of the PPO blocks at around 15-20 °C. For films aged at 4 °C, the "contrast"

between hydrophobic PPO and hydrophilic PEO is expected to be small and the polymer may find hydrophilic surfaces to be "neutral" [146] even though specific interactions with titanium precursors still drive mesophase formation. This would be expected to promote orthogonal alignment of the mesophase during low temperature aging. On the other hand, at 23 °C, PPO becomes hydrophobic and the usual contrast mechanisms return.

After deposition of the sol on glass substrates, the relative humidity (RH) of the environment in which these films are aged have been shown to play a vital role in mesostructure development. A highly humid environment is important during the aging of these films to slow down the evaporation of the water from the films (to provide sufficient time for reorientation and ordering of the mesostructure) and also to permit the mesoscopic ordering of the surfactant [117, 119, 147-149]. Crepaldi et al. [33] provided a thorough discussion of the complete synthesis and characterization procedures to obtain ordered mp-TiO₂ films. They discussed all important chemical and processing parameters important for reproducible construction of mp-TiO₂ thin films and explained that humidity during aging determines the water content in the coatings. This water content determines the fluidity of deposited coating and the possibility of occurrence of the disorder-to-order transition. The continuous exchange of water between the film and the atmosphere during the first hour of aging after deposition allows the condensation of the organic framework around micellar aggregates and controls the final mesophase. Jang et al. [125] study the effects of pH of the coating sol as well as the humidity of the curing environment on the mesostructure of titania films obtained. They suggest an optimum pH (~ -0.6) and humidity (~ 80% RH) values to synthesize highly organized mp-TiO₂ films. In much of the work in the Rankin group, high humidity (~ 94%) has been used to slow the condensation of

inorganic precursor, and it is possible that this also plays a role in promoting o-HCP mesostructured formation.[103]

2.2.5. Thermal Treatment

Calcination of titania film after aging removes surfactant molecules, stabilizes the coating, causes structural contraction and induces anatase crystallization from the initially amorphous titania structure formed during the sol-gel process [33]. These mp-TiO₂ films are stable up to a certain level of thermal treatment, but as the time and temperature used for calcination increase, they begin to lose mesopore order. This is because high temperatures allow diffusion and sintering of atoms in the initial amorphous structure, and also induce the nucleation and growth of anatase nanocrystallites, which can destroy mesopore ordering due to extensive atomic rearrangement and modification of the oxidation state of the titanium by redox reactions [118]. Kirsch et al. [117] studied the crystallization kinetics of mp-TiO₂ thin films using in-situ x-ray diffraction and suggested based on the measured activation energies for the two processes that short calcination times at high temperatures are better to produce crystalline films with minimal loss of mesoporous order. However, the exact time and temperature required vary for different synthesis procedures, and the effects of pore orientation on crystallization vs. mesostructured loss remain open questions.

Das et al. [150] investigated the effects of pore orientation on the mesostructural stability for HCP nanopores of titania and found that films with pores oriented orthogonal to the substrate at the top surface retain their long-range pore order at higher calcination temperatures (500 °C or more) compared to films with pores oriented parallel to the substrate. with mixed orientation (mixture of parallel and orthogonal orientation) as shown

in Figure 2.3c. This difference was ascribed to greater resistance to anisotropic stress during heating of the orthogonally oriented pores, and titania crystallite nucleation at the top surface of the films with orthogonally oriented pores. Consequently, the activation energy and entropy for mesostructure loss of o-HCP TiO₂ films was found to be greater than that for films with mixed orientation (mixture of parallel and orthogonal orientation) [105]. Nearly perfect orthogonal orientation contributes to the larger activation energy by supporting the anisotropic stresses that develops orthogonal to the films during annealing.

While progress has been made at understanding the rates and mechanisms of crystallization vs. mesostructured loss in soft-templated films, the loss of the template by oxidation at relatively low temperatures (< 400 °C) presents challenges in forming a mesoporous crystalline material. Hard templating may provide an alternative by using mesoporous solids as hard templates in which the growth of the precursor to a new material is restricted to the surface, cages, channels, or substrate of a hard template. The three main steps in the hard templating approach consist of (i) precursor infiltration inside mesopores of the template; (ii) conversion of the precursor into the target product in the mesopores; and (iii) removal of the mesoporous template [90]. As compared with the soft-templating method, the hard-templating method is less straightforward because of the need to selectively remove the hard template. Also, it is not easy to completely fill up the voids of mesoporous templates with titanium precursors because of their strong tendency to precipitate and crystallize into bulk oxide phases directly in aqueous media [107]. However, this synthesis strategy avoids the need to control cooperative assembly and possible mesostructured loss during heating, thus making it attractive for the synthesis of ordered mp-TiO₂ with high thermal stability and crystallinity. Lee et al. [151] synthesized

thermally stable mp-TiO₂ with a hierarchical 4-5 nm mesopore / 50 nm macropore structure via replication of citric acid-templated mesoporous silica as a hard template. Yue et al. [152] fabricated mesoporous rutile TiO₂ (which forms at a higher temperature than anatase TiO₂) by using SBA-15 and KIT-6 mesoporous silica particles as hard templates and Ti(NO₃)₄ solution as a precursor. The reaction temperature and concentration of HNO₃ in the used precursor had significant effects on the crystallization of TiO₂. Zhang et al. [153] reported the synthesis of mesoporous crystalline anatase TiO₂ with KIT-6 as the hard template and titanium alkoxides as the precursors. It was found that the precursor/template ratios, calcination temperatures and immersion time in NaOH solution for the removal of the hard template are the three key synthetic parameters that play important roles in the formation of crystalline porous TiO₂.

2.3. Nitrogen doping

Non-metal doping in mp-TiO₂ has the potential to extend its light absorption from UV to visible wavelengths. Hydrogen, boron, carbon, nitrogen, fluorine, iodine, sulfur and phosphorus have been used in this capacity, but nitrogen has been studied most extensively. Until now, various approaches to incorporate nitrogen atoms into titania have been reported, such as doping during film sputtering [154], annealing under ammonia gas [20], ion implantation [155, 156], hydrazine treatment [157, 158], urea treatment [159-161], treatment of sol-gel titania with nitrogen-containing organics [162], electrochemical processing [163], chemical vapor deposition [164], and plasma techniques [19, 21, 50, 165-172]. Most of the above doping methods require high temperature treatment and complicated or expensive equipment. Therefore, those doping methods are difficult to apply in mp-TiO₂ due to risk of losing mesostructure at the doping conditions. For example,

nitrogen doping in mp-TiO₂ by heating in the presence of nitrogen sources is not feasible. Because high temperature is required to dissociate molecular nitrogen to atomic nitrogen or nitrogen radicals, the mesostructure and crystal phase of titania cannot be easily maintained. In addition, higher temperature treatment of titania forms oxygen vacancy which works as a recombination center for the photogenerated charge carriers resulting in lower photocatalytic activity [35]. It is necessary to use simple, low-temperature methods for doping nitrogen in mp-TiO₂. In many approaches, a nitrogen precursor is added into the titania precursor solution in sol-gel, hydrothermal and solvothermal methods. Several nitrogen sources such as urea, thiourea, nitric acid, and hydrazine have been used for doping in mp-TiO₂. While many nitrogen sources are available, not all of them can be used in all synthesis conditions. For instance, when mp-TiO₂ is synthesized in acidic medium, a nitrogen source which makes the precursor solution basic cannot be used. For example, acidic solutions to prepare surfactant-templated mp-TiO₂ thin films to stabilize low-molecular weight titanate [69]. In this case, hydrazine cannot be added in the precursor solution because the increase in pH will induce titania precipitation. In this section, we will discuss nitrogen doping of mp-TiO₂ using several nitrogen sources and synthesis approaches.

2.3.1. Amines

Amines have been widely used as sources of nitrogen for doping in mp-TiO₂ [173-181]. Nassoko et al. synthesized nitrogen doped mp-TiO₂ (N-mp-TiO₂) nanoparticles by a sol-gel method using ethylene-diaminetetraacetic acid as both a soft template and a source of nitrogen [175]. The resulting N-mp-TiO₂ nanoparticles showed enhanced rhodamine B degradation under visible light irradiation. Cheng et al. reported the preparation of

mesoporous, nitrogen-doped dual phase titanate/titania by a low-temperature one-pot process in the presence of triethylamine [176]. The N-doped titanate/titania showed efficacy in visible-light phenol degradation. Fu et al. prepared N-mp-TiO₂ using an exfoliation-reassembly strategy where ethylamine caused delamination of layered titanate and acted as a source of nitrogen [178]. Figure 2.4 shows a schematic illustration of the exfoliation-reassembly technique for the synthesis of N-mp-TiO₂. In this method, the layered protonic titanate sheets are delaminated by ethylamine followed by reassembling with positively charged titania colloid nanoparticles leading to formation of randomly aggregated hybrid with porous structure. Nitrogen was incorporated into titania from the decomposition of ethylamine during calcination. In the photocatalytic degradation of methyl orange, the N-mp-TiO₂ prepared this way showed much higher photocatalytic performance at visible wavelengths compared to commercial P25 or pristine titanate. This improvement in photocatalytic activity was ascribed to the porosity, visible light absorption, and especially the effective separation of photogenerated charge carriers in the modified material.

Wanqin et al. reported the preparation of nanocrystalline N-mp-TiO₂ using ultrasonic irradiation with ethylenediamine (C₂H₄(NH₂)₂) as a source of nitrogen [180]. They proposed that ethylenediamine might form N radicals from its decomposition under elevated temperature and pressure produced by acoustic cavitation, which are able to easily dope TiO₂. The band gap was reduced from 3.3 eV to 2.98 eV by this approach, and the N-mp-TiO₂ degraded 58% of dimethyl phthalate in 5 h whereas undoped TiO₂ did not show significant degradation. Hu et al. prepared ordered arrays of N-mp-TiO₂ spheres using dual templating with a combination of inverse opal templating with PMMA (hard templating)

and surfactant templating with P123 (soft-templating) [182]. Tetramethylammonium hydroxide was used as a source of nitrogen. The N-mp-TiO₂ spheres showed enhanced rhodamine B degradation compared to nonporous N-TiO₂ spheres and undoped mp-TiO₂ spheres under visible light illumination. The high photocatalytic activity of the doped mp-TiO₂ spheres was attributed to N-doping, abundant ordered mesopores and optical effects of the opal structure.

2.3.2. Ammonia

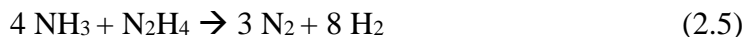
In addition to organic amines, ammonia has been used as a source of nitrogen to prepare N-mp-TiO₂ [35, 182-185]. Hou et al. reported the preparation of nanocrystalline N-mp-TiO₂ from an alkoxide precursors and concentrated ammonia solution as a source of nitrogen [184]. Joshi et al. synthesized N-mp-TiO₂ by templating with chitosan, which also served as nitrogen source along with ammonium hydroxide [185]. The resulting N-mp-TiO₂ showed enhanced methyl orange degradation under visible light illumination. Li et al. prepared N-mp-TiO₂ spheres by a hydrothermal method with CTAB and ammonia as template and nitrogen source, respectively. Varying ratios of ammonia: Ti were used to give N-mp-TiO₂ spheres containing about 1.31% of nitrogen (vs. 0.17% for nonporous N-TiO₂ spheres). A higher level of doping was found in the mesoporous spheres because of homogeneous doping facilitated by ammonia uptake into the mesopores. Due to greater, more homogeneous doping, the N-mp-TiO₂ spheres showed the greatest degree of degradation of rhodamine B under a 1000 W tungsten halogen lamp (>420 nm). The degradation of rhodamine B was found to be 100%, 50%, 35%, and 20% for N-mp-TiO₂, nonporous N-TiO₂, mp-TiO₂, and solid TiO₂ spheres, respectively. The enhanced photocatalytic activity of N-mp-TiO₂ spheres is attributed to combination of N-doping and

mesopore structure. The maximum photocatalytic activity was found with a 0.5 molar ratio of ammonia to TiO₂. The surface area of the materials was reduced by the use of more ammonia, which decreased the photocatalytic activity of the samples. In addition, excessive nitrogen might cause the formation of recombination centers for photogenerated electrons and holes.

2.3.3. *Hydrazine*

Hydrazine has also been tested as a potential source of nitrogen in N-mp-TiO₂. Along with nitrogen, titanium (Ti³⁺) introduced into the TiO₂ due to reduction by in situ hydrogen generation is expected to create an energy state below the conduction band of TiO₂ which further reduces the band gap [74, 158, 186-193]. This Ti³⁺ state in TiO₂ might improve not only light absorption but also charge transport. For instance, Zuo et al. prepared a self-doped (Ti³⁺) TiO₂ photocatalyst and demonstrated its use for hydrogen production under visible light [186]. More recently, Ti³⁺ doped TiO₂ prepared by hydrazine reduction has been reported [158]. When TiO₂ is reduced by any reducing agent, Ti³⁺ is expected to be formed along with oxygen vacancies. However, with hydrazine (N₂H₄), titania is expected to be co-doped with both Ti³⁺ and N and is therefore to synergistically absorb more visible light and potentially be a more effective redox catalyst than TiO₂ doped with either species alone. Aman et al. explored this concept using Ti³⁺ and N-mp-TiO₂ nanoparticles for enhanced photocatalytic activity under visible light [157]. The Ti³⁺/N-mp-TiO₂ showed higher photocatalytic reduction of selenium to metallic Se⁰ under visible light illumination compared to undoped TiO₂.

When hydrazine is decomposed under heat treatment, ammonia, nitrogen and hydrogen gases are formed as by Equation 2.4 and 2.5.



This in-situ formed ammonia and nitrogen (and possibly unstable radical species) act as sources of nitrogen for doping [157]. Selvam et al. prepared N-mp-TiO₂ particles by wet impregnation with hydrazine [194]. The N-mp-TiO₂ particles were used for the conversion of azoxybenzene to amines or 2-phenylindazoles with methanol using a 365 nm medium-pressure mercury lamp. In addition to introducing N and Ti³⁺, hydrazine increased the surface area from 74 to 134 m²/g due to hydrazine decomposition [157, 194]. The yield of 4,4'-azoxyanisole by catalytic reductive cleavage on N-mp-TiO₂ (95.7 %) in methanol under UV (365 nm) light illumination is higher than that on undoped mp-TiO₂ (60.3%) and P25 (50.6%). These results show that both high surface area and nitrogen doping contributed in the higher photocatalytic activity of the N-mp-TiO₂.

2.3.4. Plasma Doping

Plasma treatment is an efficient method to introduce nitrogen into the titania lattice [19, 21, 50, 165-172]. Among available doping approaches, plasma-assisted doping has several critical advantages, such as: (i) effectively incorporating heteroatoms into the TiO₂ host by providing reactive dopant species, and (ii) being conducted at relatively low temperature so that the nanostructure of TiO₂ is maintained. Recently, we have reported the incorporation of nitrogen into surfactant templated cubic ordered mp-TiO₂ thin films by N₂/Ar plasma treatments [69, 195]. About 2-3 atomic % substitutional nitrogen was found in the doped films and the nitrogen was found to be uniformly distributed through the depth of the films. XPS and optical characterization results suggest that the band gap of TiO₂ films was reduced from 3.5 eV (in undoped TiO₂ films) down to a minimum of 3.0

eV after the plasma treatment. Photocatalytic degradation tests with methylene blue demonstrated a significant enhancement in photocatalytic activity of the N-TiO₂ films over undoped TiO₂ films under visible-light illumination (455 nm LED) as shown in concentration profile in Figure 2.5. The N-TiO₂ prepared by 150 min plasma treatment showed the best photocatalytic performance, with the determined rate coefficient of 0.24 h⁻¹, roughly 6 times greater than that of undoped TiO₂ films. This enhancement in photocatalytic activity is qualitatively similar to prior studies of nitrogen doping in nanostructured titania but significantly greater in magnitude than the 2-3 times enhancement reported by Liu et al [167]. This photocatalytic improvement is attributed to the combination of the efficient N₂/Ar plasma-induced doping approach with the well-defined high surface area found in surfactant-templated mp-TiO₂ thin films. The present study showed that plasma-induced doping enables the efficient incorporation of heteroatoms into the TiO₂ films while maintaining their mesoporous structure, thereby leading to the significant enhancement of visible-light photoactivity. The coating and plasma based process presented here has several advantages over competing synthetic strategies, as it can be scaled to continuous film production and to deposition of the films onto other substrates for photoelectrocatalytic applications.

2.3.5. Thiourea

Thiourea has also been used as a nitrogen source for the doping of mp-TiO₂ [18, 196, 197]. Soni et al. reported the preparation of N-mp-TiO₂ films via evaporation induced self-assembly using P123 as a template and thiourea as a source of nitrogen [18]. The films showed the thickness of 73 nm, 211 nm, 385 nm and 695 nm by multiple coating and contained 0.9, 1.7, 4.8 and 8.3 at.% of interstitial nitrogen in the films, respectively. It is

not clear why nitrogen content increases with the film thickness formed by multilayer film deposition. While 73 nm thick N-TiO₂ films degraded about 10% methylene blue in 18 hours, undoped TiO₂ did not show any degradation in the photocatalytic degradation test under visible light of 442 nm illumination. N-TiO₂ of 695 nm thickness showed the best response which is complete degradation of methylene blue in 18 hours. That indicates that 695 nm thick N-TiO₂ films exhibited about 10 times higher rate compared to 73 nm thick N-TiO₂ films, which is due to the increased surface area in the thicker films. The same research group used the N-mp-TiO₂ thin films for visible light induced bactericidal activity on Gram-positive bacteria (*Bacillus amyloliquifaciens*) [197]. An electron paramagnetic resonance study of the N-mp-TiO₂ powders produced using thiourea by this group showed that several paramagnetic species associated with oxygen radicals after calcination at 400 °C, while nitrogen centers appear after calcination at temperature as high as 500 °C [196]. Interestingly, since it contains nitrogen, carbon and sulfur, different authors claimed that thiourea modified mp-TiO₂ contains different dopants and combinations of dopants including B/N/S co-doped mp-TiO₂ which will be discussed in later sections [75, 198-201].

2.3.6. Urea

Urea is a common source of nitrogen for doping in mp-TiO₂ since it is readily available and easy to introduce into TiO₂ precursor sol or solid TiO₂ using a urea solution [37, 85, 202-211]. In addition to being a nitrogen source, urea can contribute to forming mesopores in titania by generation of CO₂ gas bubbles during its decomposition (Equation 2.6) [37, 205]. For instance, the surface area of mp-TiO₂ prepared using urea was reported in one procedure to be 154 m²/g, but only 101 m²/g in mp-TiO₂ prepared using a similar method without urea [205].



Chi et al. synthesized N-mp-TiO₂ by a solvothermal method using urea as both a source of nitrogen and mesopore former [205]. The nitrogen content in the N-mp-TiO₂ was 0.81 at%. The N-mp-TiO₂ degraded about 38% of methylene blue whereas undoped mp-TiO₂ degraded only about 20% under visible light illumination, indicating a 2.1 times increase in photoactivity upon nitrogen doping. Shao et al. reported the preparation of hierarchical mesoporous-macroporous N-TiO₂ by thermal treatment of the hierarchical TiO₂ with urea solution [207]. The band gap was reduced from 3.14 to 2.48 eV after N-doping. XPS and FT-IR spectra confirmed the formation of Ti–N bonds in the meso-macroporous N- TiO₂. The first-order photocatalytic degradation of Rhodamine B under visible light illumination was increased from $3.7 \times 10^{-3} \text{ min}^{-1}$ to $5.3 \times 10^{-3} \text{ min}^{-1}$ due to N-doping. This enhancement in the photocatalytic performance was due to the incorporation of nitrogen into the titania lattice and the presence of the hierarchical meso/macroporous structure. Recently, N-mp-TiO₂ was prepared using a urea-assisted solvothermal method at mild temperature [202]. The band gap was reduced from 3.16 eV to 3.02 eV upon nitrogen doping. In photocatalytic oxidation of acetic acid in 60 min under solar simulator, N-mp-TiO₂ showed about 1.55 times higher performance compared to undoped TiO₂. Notably, the properties such as the band gap, chemical state of nitrogen and enhancement in photocatalytic activity of N-mp-TiO₂ are very different based on the preparation methods even when urea was used as the nitrogen source. To help to understand the reason for this variability, Sreethawong et al. prepared nanocrystalline N-mp-TiO₂ and studied the urea decomposition process in conjunction with XRD characterization [212]. A mechanism was proposed based on the appearance of biuret and cyanuric acid along with anatase titania

as observed by XRD. The biuret and cyanuric acid form at about 150-250 °C and 190-350 °C temperature, respectively.

2.3.7. Summary of Nitrogen Doped Mesoporous Titania

A summary of synthesis methods, pore directing agents, dopant sources, N 1s binding energy in doped TiO₂, the band gap before and after doping, specific surface area, compounds used for photocatalytic testing, and photocatalytic enhancement found in the N-mp-TiO₂ from various literature is presented in Table 2.1. The photocatalytic tests were performed under visible light in all cases, although the light source varied. Typical organic compounds used for photocatalytic test are methylene blue (MB), methyl orange (MO), and rhodamine B (Rh B). It is difficult to compare results of different studies directly due to variations in testing conditions including the preparation method of the photocatalyst, light sources, light intensities, excitation wavelengths, organic compound chosen for photocatalytic testing, catalyst amount, reactor geometry, etc.

For the sake of comparison, the enhancement is defined by the rate of reaction using doped mp-TiO₂ divided by the rate of reaction using undoped mp-TiO₂. When there was no photocatalytic test using undoped titania, the enhancement could not be defined. Most of the literature did not report directly the rate coefficient for degradation of the organic compounds, in which case the reaction is assumed to be pseudo-first order to determine the photocatalytic enhancement. The enhancement is calculated ratio of the maximum photodegradation occurring over a certain reaction duration by the doped mp-TiO₂ to the photodegradation by the undoped mp-TiO₂. The reported specific surface area is for undoped TiO₂. If the surface area of undoped titania is not given, the surface area of doped

titania is reported in Table 2.1. The content of dopants are in atomic percentage unless otherwise noted.

From Table 2.1, it is observed that in most cases, urea gives about 1 at.% N. N-mp-TiO₂ prepared using urea showed about a 0.1-0.2 eV bandgap reduction. Only one study was performed using nitrogen plasma-treated mp-TiO₂. The nitrogen content and band gap reduction in the resulting N-mp-TiO₂ were 3.2 at.% and 0.48 eV, respectively. The N-mp-TiO₂ prepared using ethylenediamine showed the largest band gap reduction of 2.2 eV. However, this band gap reduction is not from a primary absorption edge shift but from formation of a new absorption edge in the visible region [173]. Typically, the binding energies of nitrogen in N-TiO₂ are in the range of 396 - 404 eV [6, 43, 47]. Two types of nitrogen atoms were assigned in titania: (i) substitutional nitrogen with a binding energy of 396 eV, and (ii) interstitial nitrogen with a binding energy of 400 eV. The XPS peak at 396-397 eV is for substitutional nitrogen because it indicates Ti-N bonding [48]. The binding energy at around 400 eV is due to the interstitial nitrogen incorporated through various N-O-Ti species. From Table 2.1, it is seen that most of the nitrogen is interstitial in the N-TiO₂, which forms mid-gap states between the valence band and conduction bands. On the other hand, very few methods produce N-mp-TiO₂ containing substitutional nitrogen which is responsible for band gap reduction. In some cases, authors deconvoluted the N 1s XPS peak and showed both interstitial and substitutional nitrogen. Only N-TiO₂ prepared by supercritical CO₂ drying method and nitrogen plasma explicitly showed substitutional nitrogen [69, 206]. In terms of photocatalytic enhancement, all N-mp-TiO₂ materials showed higher visible-light activity compared to undoped titania. Of all

approaches, N-mp-TiO₂ prepared using nitrogen plasma and amines give the greatest enhancement.

Cong et al. performed an comparison of N-mp-TiO₂ prepared using a microemulsion-hydrothermal method with triethylamine, urea, thiourea, or hydrazine hydrate as nitrogen source and Triton X-100 and 1-hexanol as structure directing agents [49]. All of the N-mp-TiO₂ catalysts exhibited higher photoactivity compared to undoped titania and P25 for rhodamine B degradation under visible light irradiation. The N-TiO₂ prepared with triethylamine showed the highest photocatalytic activity and thiourea showed the lowest. The photocatalytic activity increased with nitrogen content. That was correlated with the band gap reduction and enhancement in visible light absorption. Nitrogen doping could also inhibit charge recombination resulting in increased photocatalytic activity as found by photoluminescence measurements. The results from this study is also in agreement with the other studies that N-mp-TiO₂ prepared with amines as a nitrogen source showed higher photocatalytic performance than those prepared with other sources, as shown in Table 2.1.

2.4. Other non-metal doped mesoporous titania

2.4.1. Hydrogenation

Hydrogen doping is a potential strategy to reduce the band gap of TiO₂ by introducing electronic states below the conduction band [74]. In addition to band gap reduction, hydrogenation of TiO₂ been shown to increase its conductivity and subsequently its capacitance [213]. Upon hydrogenation, titania becomes black and can absorb light over a wide wavelength range [15, 214-217]. It has been speculated that hydrogenation introduces surface functional groups which also allow for Faradaic reactions to take place [213]. Hydrogenation in titania leads to Ti³⁺ formation or oxygen vacancy.

Zhou et al. reported the preparation of hydrogenated mp-TiO₂ (H-mp-TiO₂) with 5-10 nm pores [218]. The nanoporous titania was formed in situ on titanium flakes by electrodeposition followed by annealing in a 1:4 H₂/Ar atmosphere. Oxygen vacancy and hydroxyl groups formed on the surface of TiO₂ due to the hydrogenation. The H-mp-TiO₂ showed a capacitance of 1.05 mFcm⁻¹ at the scanning rate of 100 mVs⁻¹, which is 14-fold higher than that of pure TiO₂. This capacitance enhancement was attributed to the nanoporous architecture which provides easy access of the surface to liquid electrolyte, more active sites for ion binding and charge separation, and improvement in electrical conductivity. Muhammad et al. reported reduced mp-TiO₂ thin films prepared by evaporation induced self-assembly using F127 as a pore template followed by heat treatment under a hydrogen environment [219]. The transparent titania thin films turned black upon heat treatment. However, no evidence of forming Ti³⁺ was provided. The band gap did not change after hydrogenation, but the H-mp-TiO₂ films were used for photoelectrocatalytic water oxidation at 0.6 V vs. Ag/AgCl in 1 M NaOH solution under a

150 W Xenon lamp-based solar simulator. The hydrogenated films showed about 11 times higher photocurrent compared to pure films. This enhancement was attributed to the oxygen vacancy formation during the heat treatment under the flow of hydrogen gas.

2.4.2. Boron doping

As noted above, other non-metals than nitrogen have been used in an effort to enhance the visible light absorption in titania. Boron doped mp-TiO₂ (B-mp-TiO₂) was prepared by a sol-gel process using boric acid as a boron source [86]. Different concentrations of boron ranging from 0.25 to 9.0 (wt%) was used in the precursor solution to obtain B-mp-TiO₂ with different loadings. The surface area of samples prepared with 2% and 5% of boron were 104 and 100 m²/g, respectively, which were higher than other samples. At this concentration of boron, aggregation of particles was reduced resulting in higher surface area. On the other hand, agglomerates were fused together to form comparatively larger irregular grains in pure TiO₂ and 9% B-mp-TiO₂ resulting in lower surface area. This suggests that the presence of boron significantly affects the particle size and surface area. Despite the incorporation of boron as B-O-Ti species, the band gap of TiO₂ was not reduced upon boron doping. The photocatalytic activity of the boron doped titania were tested for the degradation of pharmaceutical contaminant metoprolol using a Xe lamp solar simulator. Among all the samples, the highest degradation (70%) was obtained for the sample with 5% B whereas undoped TiO₂ removed 48% of metoprolol after 180 min of treatment. Further increase in boron concentration (9%) reduced the photocatalytic performance. At this percentage of B, a level of maximum saturation at the particle surface is reached and an excessive amount of boron occupied active sites of the catalyst, inhibiting the radiation absorption of TiO₂ particles. The observed photocatalytic

enhancement was attributed to the high surface area, mesoporous structure, formation of Ti(III), introduction of boron as a B–O–Ti species and uniformity in particle size with 5% B.

2.4.3. Carbon doping

Doping with carbon atoms has been found to increase visible light absorption and photocatalytic activity of titania. The carbon dopants can form a new energy state in between the valence band and conduction band of titania as shown in Figure 2.1 [73, 220]. In addition, carbon doping increases the photocatalytic activity of titania by decreasing the recombination rate of photogenerated electron-hole pair where carbon works as an electron scavenger [220]. Furthermore, carbon doping increases the conductivity of titania and it improves the charge transfer from the bulk to the surface sites where charge carriers participate in reactions [44]. Several studies have been reported on carbon doped mp-TiO₂ (C-mp-TiO₂) [220-225]. C-mp-TiO₂ films were synthesized by a sol-gel process combined with hydrothermal treatment using glucose as a source of carbon and a structure-directing agent [220]. In this method, titania particles prepared from Ti(OBu)₄ and glucose were hydrothermally treated in an autoclave containing a glass substrate to make C-mp-TiO₂ films. XPS showed peak at 282.4 eV for Ti-C along with other peaks at 284.8, 286.2 and 288.6 eV for adventitious elemental C or residual carbon from the precursor. These results indicated that substitutional carbon was incorporated into titania lattice by replacing oxygen by forming O-Ti-C bond. Photoluminescence showed that electron-hole recombination is reduced due to carbon doping. The C-doped mp-TiO₂ films also exhibited higher photocatalytic degradation of Brilliant Red X-3B under both UV and visible light irradiation compared with that of the smooth TiO₂ film and a P25 film. The degradation

rate coefficients of the doped films were enhanced 2.4 times under UV light and 3.6 times under visible light irradiation compared with the undoped film. High surface area, enhanced visible light absorption and lower charge carrier recombination due to carbon doping contributed to this higher photocatalytic activity of C-mp-TiO₂ films. Another important feature of this study was repeated cycling, in which it was found that C-mp-TiO₂ showed a 3% decrease in UV photocatalytic activity after 5 cycles whereas undoped titania showed a 16% decrease. That indicates C-doped titania is more stable than undoped titania.

Zhang et al. prepared bimodal C-mp-TiO₂ in supercritical ethanol from tetrabutyl titanate and raw rice [47]. The mixed precursor solution was heated at varying temperatures (all supercritical) and treated at varying temperatures. In the carbon doped mp-TiO₂, carbon was proposed to play dual roles as a dopant in the titania lattice and a photosensitizer at the surface of titania. Sensitization was proposed to come from nanosized carbon at the surface of the material, which accepts photogenerated electrons from titania to reduce charge carrier recombination. Although authors call this sensitization, it is basically a charge separator or electron sink since carbon doped titania itself is absorbing the light. The mesostructure was developed due to the ethanol supercritical treatment. The surface area of titania increased from 138 m²/g to 160 m²/g upon doping, which suggests that carbon doping prohibited the aggregation of nanoparticles. From XPS spectra, peaks for carbon were found at 284.9, 285.8, 288.2 and 288.6 eV. The peak at 284.9 eV is for adventitious elemental carbon whereas peaks at 285.8 and 288.6 eV are assigned to the oxygen bound species C-O and C=O, respectively. The incorporated carbon in the titania lattice showed a peak at 288.2 eV. Phenol degradation under visible light has demonstrated that the carbon doped mp-TiO₂ performed much higher activity compared to undoped titania. The optimal

sample was C-mp-TiO₂ prepared at 260 °C giving a pseudo-first order rate coefficient for phenol degradation of 0.452 min⁻¹. Excessive carbon was left on the 250 °C treated titania surface, which inhibited the transfer of the photo-generated electrons from the sensitizer layer (outer carbon layer) to the TiO₂. On the other hand, the sample treated at 270 °C showed lower activity because of a low content of carbon, higher band gap and lower surface area. In order to identify the contribution from carbon doping and sensitization, the best performed sample prepared first at 260 °C temperature was further heat treated and it was found that the sample treated at the lowest temperature (300 °C) showed the lowest band gap (2.7 eV) and highest photocatalytic activity (0.526 min⁻¹). Treatment at 300 °C was proposed to enhance crystallinity, and hence photoactivity. However, at 400 °C and higher, the sample might lose carbon and widen band gap resulting in lower photoactivity. These results suggest that the activity contribution from the carbon sensitization is about three times that coming from the promotion effect of carbon doped in the titania lattice. Such synergistic effect of the lower band gap induced by the carbon doped into the titania crystal lattice and photosensitizing resulting from the hybridized carbon grafted on the titania surface played a significant role in the photocatalytic degradation of phenol as shown in Figure 2.6.

2.4.4. Fluorine doping

Studies have been carried out on fluorine doping in mp-TiO₂ to improve its photocatalytic performance [226-230]. Pan et al. reported the preparation of fluoride doped mp-TiO₂ (F-mp-TiO₂) hollow microspherical photocatalyst for membrane-based water purification [227]. F-mp-TiO₂ microspheres were synthesized by hydrothermal treatment of TiF₄ in a H₂SO₄ aqueous solution which acts as an acid source to promote HF etching.

This etching governed the aggregation of hydrolyzed TiO₂ primary particles and the formation of porous microspheres depending on the concentration of H₂SO₄ (0.1% to 1.0% by mass). H₂SO₄ with 1.0% concentration provided monodispersed mesoporous hollow F-TiO₂ microspheres with abundant cavities and nanopores. The Figure 2.7 shows the SEM of mesopore formation at different H₂SO₄ concentration and TEM images of F-mp-TiO₂ hollow microspheres. XPS spectrum revealed only one peak for F⁻ at 684.3 eV which is associated with physically adsorbed anions on the surface of TiO₂ microspheres. It has been reported that OH[·] Radicals are more mobile in F-TiO₂ surface than pure TiO₂, which accelerates the photocatalytic degradation of organic pollutants [231]. F-mp-TiO₂ microspheres were more efficient in the absorption of visible light compared to P25, which was attributed to light scattering inside the core and mesopores. In the methylene blue photocatalytic degradation under UV light, the F-mp-TiO₂ hollow microspheres showed about 93% degradation compared with 88% for P25 over the same time interval. This enhancement was attributed to the accessible mesopore channel, improved light harvesting capabilities and surface fluorination.

Along with enhancing the production of free OH[·] radicals and reduction of the recombination of photogenerated electrons and holes due to the strong electron-withdrawing ability of the surface fluoride, it was shown that F⁻ ions suppress the crystallization of the brookite phase, catalyze the phase transformation of brookite to anatase, and enhance the growth of anatase crystallites [229]. F-mp-TiO₂ powders were prepared by a hydrothermal method from NH₄HF₂-H₂O-C₂H₅OH mixed solution with tetrabutylorthotitanate (Ti(CC₄H₉)₄, TBOT)) as precursor. XPS showed fluorine in the form of surface adsorbed F⁻ and the UV-vis absorption edge remained unchanged while

slight visible light absorption was increased due to surface fluorination. The photocatalytic decomposition of acetone under UV illumination was used to test the activity of F-mp-TiO₂ powders. The rate constant for F-mp-TiO₂ powders is about 0.0175 min⁻¹ which is about 2.8 times higher than pure TiO₂. This enhancement in photoactivity is due to the strong electron-withdrawing ability of the surface ≡Ti-F groups of F-TiO₂ powders, which reduces the recombination of photogenerated electrons and holes, and enhances the formation of free OH· radicals as shown in Figure 2.8. All the above studies suggest that the improvement in photocatalytic activity of F-mp-TiO₂ tested under UV irradiation is due to efficient charge separation but not band gap reduction.

2.4.5. Iodine doping

Iodine doping in titania can enhance visible light absorption and iodine acts as an electron acceptor to reduce charge carrier recombination [232]. Liu et al. prepared visible light active iodine doped mp-TiO₂ (I-mp-TiO₂) with a bicrystalline framework by a hydrothermal method using Ti[OCH(CH₃)₂]₄, P123, and iodic acid as precursor, pore directing agent, and iodine source, respectively [233]. Iodine doped titania was also synthesized without the use of a block copolymer as a template. The resulting titania had a mix of anatase and rutile crystal structure. The photocatalytic activity of the I-mp-TiO₂ was demonstrated by MB degradation under visible light. The degradation with I-mp-TiO₂ was about 85% in 240 min whereas the I-TiO₂ and P25 showed about 55% and 15%, respectively. The superiority of the I-mp-TiO₂ is attributed to the large surface area, mesoporous structure, high crystallinity, bicrystalline framework, and higher visible light absorbance due to iodine doping. Qian et al. reported the synthesis of polyvinyl alcohol [PVA]-iodine complex doped mp-TiO₂ (PIT) and iodine doped TiO₂ (IT) by hydrothermal

method using tetrabutyl titanate as precursor, potassium iodate and iodine as iodine sources [232]. A smaller particle size of PIT was obtained with PVA additive because the polymer helped to disperse particles and control the size of the titania. PIT prepared with calcination at 200 °C contained the maximum observed iodine content of 0.62%. Further increasing calcination temperature resulted in reduction of both surface area and iodine content. The lowest band gap of IT and PIT were 1.93 eV and 1.38 eV, respectively. In MB degradation under a 100 W halogen lamp for 1 hour, the PIT nanoparticles showed the maximum degradation of 90.2%, whereas it was only 80% and 9% with IT and P25, respectively. Photoluminescence spectra obtained using terephthalic acid as a probe molecule revealed the production of large amount of OH· radicals on the surface of the photocatalysts. The photocatalytic enhancement of the PIT is due to the higher visible light absorption, less aggregated particles, and synergy produced by carbon doped from PVA. The thermal stability of iodine in PIT was also improved due to the use of PVA.

2.4.6. Phosphorus doping

Phosphorus has been doped in mp-TiO₂ to improve its photocatalytic activity [234-238]. Yu et al. prepared a surfactant-templated phosphorus doped mp-TiO₂ (P-mp-TiO₂) using phosphoric acid as a source of phosphorus [235]. It was found that the specific surface area of the materials decreased with increasing calcination temperature. The specific surface area of P-mp-TiO₂ calcined at 400 °C was 301 m²/g compared with 137 m²/g for pure mp-TiO₂. The XRD data showed that the crystallite size increased in the pure mp-TiO₂, which caused the collapse of mesoporous structure, resulting in lower surface area. In contrast, the crystallite size did not change much with calcination temperature in the P-mp-TiO₂ indicating the inhibition of anatase grain growth. Undoped titania exhibited

mesoporosity loss due to condensation of Ti-OH from the as-prepared material, while H₃PO₄ promoted the formation of more completely condensed walls without mesopore loss by providing repulsion between grains. XPS showed a P 2p peak at 133.8 eV in P-mp-TiO₂ which indicates phosphorus pentavalent oxidation state (P⁵⁺). This indicates the absence of Ti-P since the binding energy of Ti-P is 128.6 eV. Pentane oxidation was used to demonstrate the photocatalytic activity of P-mp-TiO₂. The UV-vis spectroscopy measurement showed that the band gap of TiO₂ increased from 3.10 eV to 3.17 eV in P-mp-TiO₂. This blue shift in light absorption upon phosphorus doping is attributed to the reduced crystallinity of the P-mp-TiO₂. P-mp-TiO₂ calcined at 500 °C showed the highest pentane oxidation rate of about 8.5 ppm min⁻¹g⁻¹ whereas it was only 6 ppm min⁻¹g⁻¹ with pure mp-TiO₂. The higher photocatalytic activity of P-mp-TiO₂ was explained by the extended band gap energy which provided a more powerful redox ability, large surface area, and the existence of Ti ions in tetrahedral coordination.

Fan et al. studied the role of phosphorus in the synthesis of P-mp-TiO₂ prepared by EISA [236]. As noted above, incorporation of phosphorus is of benefit to improving the thermal stability and enhancing the surface area of mp-TiO₂ by constraining the growth of anatase crystallites. UV-vis spectra showed no change after phosphorus doping, and XPS revealed pentavalent phosphorous (P⁵⁺) consistent with amorphous titanium phosphate embedded into the nanocrystalline TiO₂. P-mp-TiO₂ exhibited higher photocatalytic degradation of gas phase acetaldehyde compared to pure mp-TiO₂ and P25 under 300-W Xe arc lamp due to the enhanced surface area upon phosphorus doping. The optimum amount of phosphorus was obtained from the balance between the increased surface area, and the formation of recombination centers for photogenerated charge carriers.

Guo et al. reported the synthesis P-mp-TiO₂ hydrothermal and sol-gel methods [234]. The P-mp-TiO₂ showed high photocatalytic activity in MB degradation under Xe lamp irradiation due to the mesoporous structure and large specific surface area. The above studies suggest that phosphorus doping showed improved photocatalytic activity of mp-TiO₂ due to the inhibition of crystal growth and maintaining high-surface area mesostructure, but not improvement in visible light absorption. Basically, phosphorus might not present in the lattice of mp-TiO₂ as a dopant and it has a favorable mesopore structure effect.

2.4.7. Summary of Nonmetal Dopants other than Nitrogen

Table 2.2 summarizes the synthesis methods, pore directing agents, dopant sources, relevant XPS binding energies, band gaps before and after doping, specific surface areas, compounds used for photocatalytic testing, and photocatalytic enhancement found in titania doped with non-metals other than N. As discussed above, C, B, F, I and P have been used to enhance visible light absorption and visible light driven photocatalytic activity of titania by various mechanisms. All the non-metal doped mp-TiO₂ showed higher photocatalytic performance compared to either undoped mp-TiO₂ or doped nonporous titania. Contributions to improved photocatalytic activity of titania include better visible light absorption due to bandgap reduction and optical effects, efficient charge separation, suppressing phase transformation, controlling crystal growth, and inhibiting photogenerated charge carrier recombination.

2.5. Co-doping of non-metals

Overall, non-metal doping in mp-TiO₂ has been shown to have a variety of effects including extending the absorption edge into the visible-light region, improving the separation efficiency of photogenerated electron–hole pairs and thus enhancing visible light driven photocatalytic activity. Further progress in the utilization of solar energy has increased in recent years. Since different dopant elements form energy states at different positions between the valence and conduction band of titania, co-doping has been hypothesized to induce synergistic enhancements in photocatalytic activity of TiO₂. In addition, co-doping may help to reduce charge recombination by compensating for charge vacancies formed by nitrogen doping alone. Co-doping of mp-TiO₂ to improve visible light photoactivity has been accomplished with N/B [239-242], N/C [48, 243], N/F [79, 209, 244, 245], N/P [85], N/S [198, 199, 201, 244, 246, 247], I/S [248] and N/S/C [75, 200].

B/N co-doping in mp-TiO₂ has been shown in several reports to give enhanced visible light photoactivity [239-242]. Liu et al. showed synergistic effects of B/N co-doping of mp-TiO₂ prepared using P123 as a template in visible light photocatalytic degradation of rhodamine B [76]. B dopant (with XPS binding energy of 191.5 eV) was incorporated by hydrothermal processing and N dopant by thermal treatment under ammonia. The presence of O–Ti–B bonds contributed to the visible light absorption, and a new O-Ti-B-N structure that formed on the surface of the mp-TiO₂ enhanced the separation and transfer of photogenerated charge carriers. In addition, the presence of boron stabilized the structure, including the crystal size and specific surface area, relative to undoped titania during the nitrogen doping process. All these factors contributed to much higher visible light driven photocatalytic activity of B/N-mp-TiO₂ compared to B-mp-TiO₂ and N-mp-

TiO₂ alone. Zhou et al. studied the effect of nitrogen doping temperature of B/N-doped TiO₂ by boron doping first and subsequently nitrogen doping in NH₃ at variable temperatures. The B/N-TiO₂ showed synergistic effect in the photocatalytic activity demonstrated by methyl orange degradation under visible light irradiation. Boron and nitrogen can both be incorporated either interstitially or substitutionally and the Ti-O-B-N structure plays a vital role in visible-wavelength photocatalytic activity. Figure 2.9 shows a schematic of the transformation of surface structures of B/N-TiO₂ at different calcination temperatures. At low temperature, the main dopants are Ti-O-N or Ti-O-N and Ti-O-B bonds, whereas the Ti-O-B-N structure becomes unstable at higher temperature and Ti-B and Ti-N bonds are formed. The optimal nitrogen doping temperature was 550 °C while further increasing the calcination temperature formed oxygen vacancies and Ti³⁺ species, resulting in the decrease of photocatalytic activity in visible light.

/NF co-doped mp-TiO₂ has been shown to exhibit enhanced visible light adsorption and photoactivity [79, 209, 244, 245]. Nitrogen and fluorine co-doping provides synergistic effects compared with single element doping. Preparation of F/N-mp-TiO₂ microsphere by a solvothermal method has been reported using urea as a nitrogen source and ammonium fluoride as a fluorine source [209]. The band gaps of TiO₂, F-TiO₂, N-TiO₂ and F/N-TiO₂ were 3.02, 2.95, 2.8 and 2.74 eV, respectively. The contents of F and N were 1.9 at.% and 0.57 at.%, respectively. The photocatalytic activity of the doped titania was evaluated by the acid orange 7 degradation under visible light. The percentages of degradation after 5 h were 10%, 15%, 20%, 48% and 55% for P25, TiO₂, N-mp-TiO₂, F-mp-TiO₂ and F/N-mp-TiO₂, respectively. Fluorine doping contributed to the photocatalytic performance enhancement in different ways such as band gap narrowing, inhibition of the

transformation from anatase to rutile and increasing the concentration of OH[·] radicals in the solution which reduces the charge carrier recombination. In addition, fluorine doping formed surface acid sites which is beneficial for adsorption of reactant molecules and act as electron acceptors. High surface area, mesostructure and a synergistic effect of N and F co-doping improved photocatalytic activity of N/F-mp-TiO₂ microspheres.

P/N doping can also enhance visible light driven photocatalytic activity and thermal stability of mp-TiO₂ [85]. Shao et al. synthesized P/N-mp-TiO₂ by direct phosphorylation from phosphoric acid followed by nitridation with urea solution [85]. The band gap of the N/P-mp-TiO₂ is narrower than either N- or P-doped titania. Rhodamine B degradation was carried out using the co-doped titania under visible light illumination with a 40-W tungsten bulb. The pseudo-first order degradation rate coefficient of rhodamine B for P/N-mp-TiO₂ is $4.9 \times 10^{-3} \text{ min}^{-1}$, which is much higher than that of P-mp-TiO₂, N-mp-TiO₂ and mp-TiO₂.

Tri-element co-doping of mp-TiO₂ provides even more opportunities to enhance visible light driven photocatalytic activity but has been studied less frequently due to the complexities of such systems [75, 200]. The band gap is proposed to be narrowed by mixing the O 2p with C 2p, N 2p and S 3p orbitals. El-Sheikh et al. reported the preparation of S/N/C-mp-TiO₂ by sol-gel process using P123 as a template and thiourea as a precursor [75]. The titania is comprised of both anatase and brookite phases. The prepared photocatalysts were applied for the degradation of microcystin-LR under a 15 W fluorescent lamp. The S/N/C-mp-TiO₂ performed 100% degradation with a pseudo first order rate coefficient of 0.0095 min^{-1} which is about 11.5 times higher compared to pure TiO₂. This higher activity of the S-N-C-mp-TiO₂ is attributed to the mesostructure,

trielement co-doping, crystallinity of titania and conductivity obtained due to carbon doping.

Table 2.3 summarizes the synthesis methods, pore directing agents, dopant sources, XPS binding energy of relevant dopants, band gaps before and after doping, specific surface area, compounds used for photocatalytic testing, and photocatalytic enhancement found in the non-metal co-doped mp-TiO₂. All reported co-doped TiO₂ materials had band gaps below 3.0 eV. Visible-light photocatalytic activity was achieved using both single non-metal dopants and co-doping of mp-TiO₂. However, it appears that the enhancement in photocatalytic activity of the co-doped mp-TiO₂ is consistently higher compared to single-element doping, as shown in Tables 2.1 and 2.2, due to the synergistic effects of co-doping.

2.6. Applications

Due to its combination of optoelectronic activity, high surface area, mesostructure and controllable morphology, mp-TiO₂ has many potential applications including in sensors, photocatalytic decomposition of organic compounds, solar hydrogen production by water splitting, photovoltaics, photocatalytic CO₂ reduction, lithium ion batteries, and supercapacitors. Non-metal doping of mp-TiO₂ further can have benefits for all of these applications. From the literature review, it shows that extensive study on making visible light active titania has been performed and tested their photocatalytic performance by the decoloration and degradation of organic compounds such as methylene blue, methyl orange and rhodamine B. However, very few studies were carried out to apply the developed materials in the energy fields. The following sections review what has been reported regarding the application of non-metal doped mp-TiO₂ in photocatalytic water splitting and CO₂ reduction. The benefits of non-metal doping for sensor, battery, and capacitor applications are probably related more to conductivity changes rather than optical and surface chemical changes, and are beyond the scope of this review.

2.6.1. Water Splitting

Molecular hydrogen is considered to be one of the best alternative green energy sources to renewably fulfill increasing global energy demands. Hydrogen can be produced with solar energy by water splitting using a semiconductor photocatalyst. There are two primary requirements for the semiconductor to be a water-splitting photocatalyst. First, the band gap of the semiconductor must be higher than the energy needed to split water. Second, band alignment is needed; the conduction band potential of the semiconductor must be more negative than the water reduction potential (H⁺/H₂, 0 V vs. NHE) and the

highest level of valence band potential must be more positive than the water oxidation potential ($\text{O}_2/\text{H}_2\text{O}$, 1.23 V vs. NHE). Titania fulfills these requirements, and thus has potential to be a photocatalyst for solar H_2 production. Figure 2.10 summarizes how titania has the capability of both oxidizing water to O_2 by holes generated during photoexcitation, and reducing water by excited electrons to produce H_2 .

Hartmann et al. showed the effectiveness of sol-gel derived mp-TiO₂ in the water splitting reaction, but its large bandgap limits visible light absorption [249]. To improve in hydrogen production from water splitting using visible light, non-metal elements have been doped into mp-TiO₂ [48, 174, 203, 212, 250, 251]. First, Sreethawong et al. prepared N-mp-TiO₂ and assemblies of TiO₂ nanocrystals [212]. Mp-TiO₂ was synthesized by a sol-gel method using laurylamine hydrochloride as a structure-directing agent, and nitrogen was doped in titania by calcination using urea. The activities of the materials were tested by photocatalytic H_2 production from aqueous methanol solution under 300 W Xe arc lamp with a wavelength longer than 400 nm using a UV cut-off glass filter. The N-mp-TiO₂ showed a maximum hydrogen production rate of about $6.5 \mu\text{lh}^{-1}$ whereas it is at most about $4.5 \mu\text{lh}^{-1}$ for N-doped commercial titania, which demonstrated the importance of the mesoporous structure of the photocatalyst. In 2009, the same research group investigated the effect of Pt loading in N-mp-TiO₂ on the photocatalytic hydrogen production from water splitting under visible light irradiation [250]. Various amounts of Pt were loaded on to the N-mp-TiO₂ from hydrogen hexachlorophatinate (IV) hexahydrate aqueous solution via the incipient wetness impregnation method. Hydrogen was produced from water splitting in an aqueous methanol solution in a closed system under 300 W Xe arc lamp with a wavelength longer than 400 nm using a UV cut-off glass filter, where methanol was used

as a sacrificial electron donor. The Pt loaded N-mp-TiO₂ produced more hydrogen compared to only N-mp-TiO₂. The hydrogen production increases with the Pt loading. The maximal production of hydrogen was about 27 μlh^{-1} using 1.3 wt.% Pt loaded nitrogen doped titania, which is about 4.5 times higher than that of N-mp-TiO₂. The improvement of hydrogen production upon Pt loading is due to the effect of electron trapping by Pt metal on the surface of titania. The excited electrons on the conduction band of titania are moved to the Pt metal surface which locally traps the electrons and increases the charge carrier lifetime, and then they participate in the water reduction to produce hydrogen. In the meantime, the methanol consumes the photogenerated holes in the valence band of titania, which inhibits the undesired photogenerated charge recombination. This efficient charge separation by Pt resulted in the improved hydrogen production from water splitting. Increase in loading Pt more than 1.3 wt.% decreased the hydrogen production due to increased Pt agglomeration, excessive coverage of the titania surface by the Pt nanoparticles and increased probability of charge recombination by the excess electrons on the Pt surface. In the next year, Fang et al also showed the efficacy of Pt loading in N/S-mp-TiO₂ in water splitting [251]. The co-doped samples were prepared by controlled thermal decomposition of a single source, ammonium titanyl sulfate ((NH₄)₂TiO(SO₄)₂). Following preparation, Pt was loaded into the TiO₂ mesopores via incipient wetness. The doped titania showed high photocatalytic methyl orange degradation whereas P25 did not show any detectable degradation under visible light irradiation. The UV-vis spectroscopy data showed that the band gap of the N/S-mp-TiO₂ is 3.2 eV which indicates that the doping did not reduce the band gap but instead formed isolated energy states in the band gap of titania. The N-mp-TiO₂ contained Brønsted acid sites arising from covalently bound sulfate

groups from the precursor which also helped with MO degradation. The optimum amounts of Pt were 1 wt% and 0.1 wt.% for broad spectrum and visible light, respectively. The Pt loaded N-mp-TiO₂ produced 740 $\mu\text{mol h}^{-1}\text{g}^{-1}$ and 3.49 $\mu\text{mol h}^{-1}\text{g}^{-1}$ hydrogen from aqueous solution of methanol under broad spectrum and visible ($\lambda > 400$ nm) illumination, respectively. The hydrogen production rate without Pt loading were 20.4 $\mu\text{mol h}^{-1}\text{g}^{-1}$ and 1.82 $\mu\text{mol h}^{-1}\text{g}^{-1}$ under broad spectrum and visible ($\lambda > 400$ nm) illumination, respectively.

Recently, Liu et al. prepared N-mp-TiO₂ nanoparticles by EISA method [203]. The mp-TiO₂ was doped with nitrogen using urea to introduce 3.46 at.% nitrogen. In the photocatalytic water splitting from an aqueous solution containing methanol under visible light illumination (450 W Xe lamp with cutoff filter ≥ 450 nm), they found that N-mp-TiO₂ showed about seven times higher hydrogen generation rate (14.9 $\mu\text{mol g}^{-1}\text{h}^{-1}$) compared to undoped titania. This enhancement was attributed to the high surface area of mp-TiO₂ as well as N-doping.

Liu et al. reported the preparation of C/N-mp-TiO₂ nanoparticles via EISA method using an ionic liquid [48]. The ionic liquid (1-ethyl-3-methylimidazolium chloride, [C₂mim][Cl]) provided a source of carbon and nitrogen, and served as a template for pore formation. Figure 2.11 shows a schematic illustration of the synthesis of C/N-mp-TiO₂. The positively charged titania prepared from Ti isopropoxide co-assemble with [C₂mim][Cl] aggregates followed by calcination to generate C/N-mp-TiO₂. Mp-TiO₂ nanoparticles doped only with carbon were prepared using F127. The surface areas obtained from [C₂mim][Cl] and F127 were 101 m²/g and 54 m²/g, respectively. The nitrogen content and band gap of the C/N-mp-TiO₂ nanoparticles were 1.75 at.% and 2.92 eV, respectively. Both doped and undoped titania showed carbon peaks in XPS spectra. No

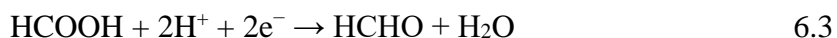
peak for Ti-C at 281 eV was observed, indicating that substitutional C atoms may not have been incorporated. Photocatalytic hydrogen generation rates from water with methanol as a sacrificial reagent under 450 W Xe lamp for P25, C-mp-TiO₂ and best performing C/N-mp-TiO₂ nanoparticles were 2.2, 7.8 and 81.8 $\mu\text{mol g}^{-1}\text{h}^{-1}$, respectively. This superior photocatalytic activity is attributed to the high surface area, and synergistic effects of carbon and nitrogen co-doping. In addition, the small particle size found in mp-TiO₂ helped reduce charge recombination, which contributed to the improved water splitting performance.

Recently, our group has reported surfactant templated mp-TiO₂ films treated with N₂/argon plasma studied for ultraviolet and visible light induced photocatalytic water splitting activity [195]. The effect of light sources on PEC performance was explored using UV (365 nm), blue (455 nm) and green (530 nm) LEDs. N-TiO₂ films showed 242x and 240x enhancement of photocurrent, compared to undoped TiO₂ films under UV (365 nm) and blue LED (455 nm) irradiation, respectively. The N-doped films also showed overall enhancement of up to 70x and 92x with a broad spectrum Xe arc lamp and halogen bulb, respectively, and photocatalytic activity even with green LED illumination, compared to no measurable activity without doping. This study showed that plasma-induced doping of sol-gel materials enables the efficient incorporation of heteroatoms into disordered metal oxide nanostructures, thereby leading to remarkable enhancement in visible-light driven photoelectrochemical water splitting.

2.6.2. CO₂ Reduction

Recently, depletion of fossil fuels and climate change due to CO₂ emission have become profound concerns [1]. To tackle these global concerns, intensive research is

ongoing to find clean and renewable energy sources and reduce CO₂ emissions. TiO₂ can address these concerns through its use for CO₂ conversion to fuel since its conduction band potential is more negative than the reduction potential of CO₂. Fuels such as formic acid, formaldehyde, methyl alcohol, and methane can be formed by the reduction of CO₂ [252, 253]. A multistep reaction (Equations (6.1)–(6.5)) process for CO₂ reduction has been suggested based on the products (HCOOH, HCHO, CH₃OH and CH₄) [253].



In this mechanism, consumption of CO₂ leads to formation of several different products depending on the photocatalyst and co-catalyst used. Only one article reports the application of non-metal-doped mp-TiO₂ in CO₂ reduction [254]. Mengyu et al. reported the synthesis of silver-loaded, nitrogen-doped TiO₂/SBA-15 mesoporous catalysts through a solvothermal method using titanium n-butoxide, carboxylate-modified SBA-15, urea, and silver nitrate as TiO₂ precursor, support, and nitrogen and Ag sources, respectively [254]. The mesoporous SBA-15 support was loaded with anatase N-TiO₂ and Ag. Ag served as an effective electron trap to prevent fast recombination of photogenerated charge carriers, and at the same time, visible light absorption was enhanced by silver nanoparticles due to a surface plasmon resonance effect. Both substitutional and interstitial nitrogen were found in the doped titania. In the CO₂ reduction reaction, the catalyst produced 45.7 μmol·g⁻¹·h⁻¹

methanol. The improvement of methanol production upon Ag loading is due to the effect of electron trapping by Ag metal on the surface of titania as illustrated in Figure 12. The excited electrons formed in the conduction band of titania are injected to Ag nanoparticles where they participate in CO₂ reduction to produce carbon radicals. In the meantime, water is oxidized by photogenerated holes to form OH· radicals. These radicals ultimately form methanol. The enhanced visible light driven activity was attributed to the synergistic effect of N-doping and Ag nanoparticle loading over TiO₂. Though many publications have reported the synthesis of non-metal doped mp-TiO₂ and demonstrated its photocatalytic activity by degrading different compounds, a significant opportunity still exists to explore and develop these materials for CO₂ reduction to produce fuels.

2.7. Future Directions

Intensive studies have been carried out on the synthesis of mp-TiO₂ and its non-metal doping for environment and energy applications. Although significant progress has been made in terms of band gap reduction, visible light absorption, and increasing the surface area of titania by various treatments, there is still significant room for development of these materials for photocatalysis and photovoltaics. Some of the remaining questions to be addressed are whether the mesopores are fully accessible, whether the dopants are distributed uniformly, whether the dopants are only on the surface of titania incorporated into the bulk of the material, and how the crystal structure of the matrix affects performance. The performance of the materials can be improved by better designing its mesostructure. For instance, the lifetime of charge carriers can be increased by making materials with thin pore walls and increasing the surface/volume (bulk) ratio of titania, which will help to inhibit photogenerated charge recombination. Since the mesopores of

titania particles may not be fully accessible due to aggregation of the particles, well-ordered mp-TiO₂ films might be promising materials to enhance pores accessibility for separation of products and reactants. The activity can be further improved by making thick multilayer films to optimize light absorption vs. reactant and charge carrier diffusion in the materials. It is essential to understand the charge transfer dynamics among dopants, mp-TiO₂ and reactants molecule to further improve the photocatalytic performance of non-metal doped mp-TiO₂.

In addition to non-metal dopants themselves, there is room to better understand metal co-catalysts. Noble metals act as passive sinks for electrons to promote the interfacial charge transfer process and enhance the quantum efficiency of photocatalytic system [44, 255-257]. In addition, metal nanoparticles show plasmonic effects and provide hot electrons into the conduction band of titania. Incorporation of noble metal nanoparticles such as Pt, Au, Ag, Cu onto non-metal doped mp-TiO₂ would benefit from further exploration. Furthermore, the fabrication of non-metal doped mp-TiO₂ composites with other narrow band gap semiconductor materials or quantum dots that act as sensitizers will open the door to understanding synergistic effect of doping and sensitization for further improving photocatalytic activity. Although great progress has been made in the development of the materials in terms of functionality and visible light absorption for applications in degradation of organic pollutants, few reports are available regarding their application in H₂O splitting, CO₂ reduction and energy storage applications such as in lithium ion batteries. Finally, study on long term stability and deactivation of the non-metal doped mp-TiO₂ are necessary for their development for commercial use.

2.8. Conclusion

Mesoporous TiO₂ presents opportunities for use in a number of applications due to combining a favorable morphology (accessible pores, high surface area, well-defined mesostructure, tunable pore size and shape, and thin pore walls) with innate optoelectronic activity. It is of particular interest for high-volume applications because of its low cost and environmentally benign nature. These unique properties make it highly promising in environmental, energy conversion and storage applications. To overcome its limitation in visible light absorption due to its wide band gap, mp-TiO₂ has been doped with several non-metal elements in an effort to enhance the visible light driven photocatalytic activity. Although significant progress has been made in last few years, incorporation of non-metal dopants into the mp-TiO₂ lattice while controlling its phase and mesostructure remains a challenge.

In this review, we have discussed the synthesis of mp-TiO₂, different doping methods and dopant sources. Its applications in environmental pollutant degradation, H₂O splitting to produce hydrogen gas, and CO₂ reduction to fuel were discussed. Among several non-metal dopants and modifiers that have been investigated (H, C, B, N, F, I, S, and P), the most promising and most studied one is nitrogen. The most common approaches to materials synthesis for this purpose are based on liquid-phase methods (hydrothermal or solvothermal) where the buildup of the material from molecular precursors provides opportunities to introduce dopants during its formation (in solution or during heat treatment steps). Typical nitrogen sources are ammonia, urea, thiourea, amine, hydrazine, and nitrogen plasma. Successfully producing doped titania for photocatalytic applications involves a tradeoff between maintaining the favorable morphology of the material (high

specific surface area, controlled pore morphology, crystalline phase, etc.) while selecting doping source and method that effectively introduces dopants at a high enough level and in the appropriate chemical state for band gap reduction, visible light absorption, control of charge carrier recombination, and ultimately, enhancement in photocatalytic activity. Because of the tradeoff between loss of mesostructure due to harsh temperature/ chemical conditions and the introduction of dopants, there is usually an optimum calcination temperature and dopant composition to give a favorable combination of titania phase, mesostructure, doping level, surface area, physical and chemical state to slow charge carrier recombination.

While the major contribution of nitrogen doping was to enhance visible light absorption, the other non-metal dopants mostly contribute to photocatalytic activity in other ways such as inhibiting crystal growth and phase transformations, retaining mesostructure, increasing surface area, and providing sites for efficient charge separation. Although the mechanisms vary with dopant, the literature contains many examples in which the visible light activity of mp-TiO₂ has been increased by on to order of several times by incorporating all of the non-metal dopants included in this review. Despite these improvements, there is still significant opportunity to continue to increase the photocatalytic activity of titania by orders of magnitude by judiciously selecting the synthesis method and doping strategy. For example, our group recently showed that two orders of magnitude increases in photocatalytic activity can be achieved by combining a sol-gel approach to forming disordered mp-TiO₂, and using N₂/Ar plasms to introduce a high level of substitutional nitrogen under mild conditions. Preventing rapid crystallization into anatase TiO₂ seems to be important to accomplishing this high level of enhancement.

Other groups have also begun to explore combining multiple mechanisms of visible light enhancement by co-doping mp-TiO₂ with more than one non-metal dopant. In many reported examples, co-doped materials exhibit greater enhancement in visible light photocatalytic activity than titania doped with single elements due to the synergistic effects of the co-doping.

Most of the investigations of photocatalytic activity of non-metal doped mp-TiO₂ employ colored organic dyes such as methylene blue, methyl orange and rhodamine B. These are useful for establishing baseline levels of enhancement and are of direct interest for the use of titania in environmental remediation and water treatment. Fewer studies have been performed on the application of non-metal doped mp-TiO₂ in H₂O splitting, and CO₂ reduction, but these are potentially important areas for application of titania due to the alignment of its valence and conduction bands with the relevant electrochemical potentials required for these reactions. Significant enhancements in these reactions have been made through non-metal doping of titania, including a recent report of 240 times enhancement in the rate of photoelectrochemical water oxidation in N₂/Ar plasma doped mp-TiO₂ films. Although this review summarizes significant enhancements in visible-light photoactivity, further improvements in visible light absorption, separation of photogenerated charge carriers, and charge transfer to reactants will be necessary for widespread use of titania in practical photocatalytic applications. Future directions to improve the efficiency of the non-metal doped mp-TiO₂ will include designing stable mesostructures with highly accessible pores, making composite with noble metal electron sinks and semiconductor sensitizers, and better understanding bottlenecks in energy conversion and storage systems limiting the commercialization of these materials.

Figures of Chapter 2

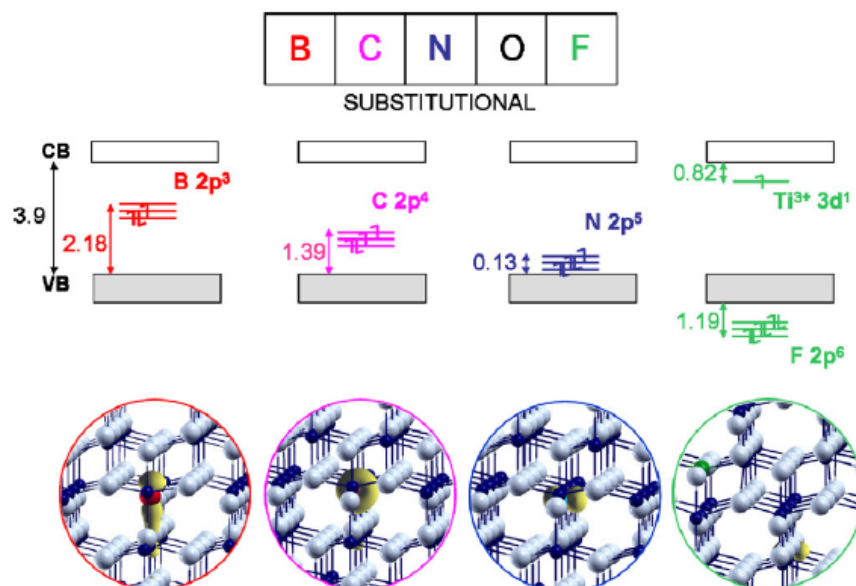


Figure 2.1. Schematic representation of Kohn-Sham one-electron states and spin density plot of substitutionally doped anatase TiO_2 . Reprinted with permission from ref [73]. Reprinted from *Catalysis Today* vol. 206, C. Di Valentin and G. Pacchioni, “Trends in non-metal doping of anatase TiO_2 : B, C, N and F,” pp. 12-18, Copyright (2013), with permission from Elsevier.

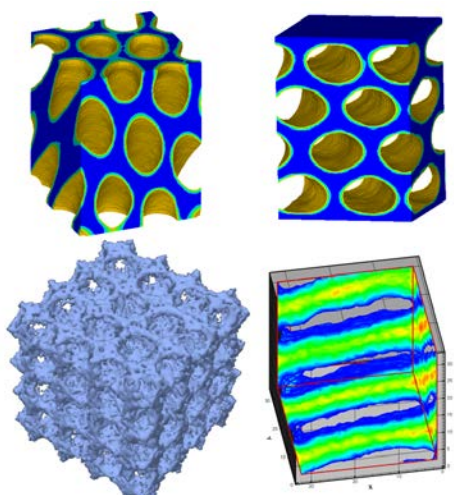


Figure 2.2. Computer-generated illustrations of typical mesoporous structures and mesophases. Clockwise from lower left are illustrated an $\text{Im}\bar{3}\text{m}$ cubic mesoporous material, o-HCP mesoporous film, parallel HCP mesoporous film, and lamellar mesophase

where higher intensity (yellow and red) corresponds to a greater density of hydrophobic tails of the surfactant template.

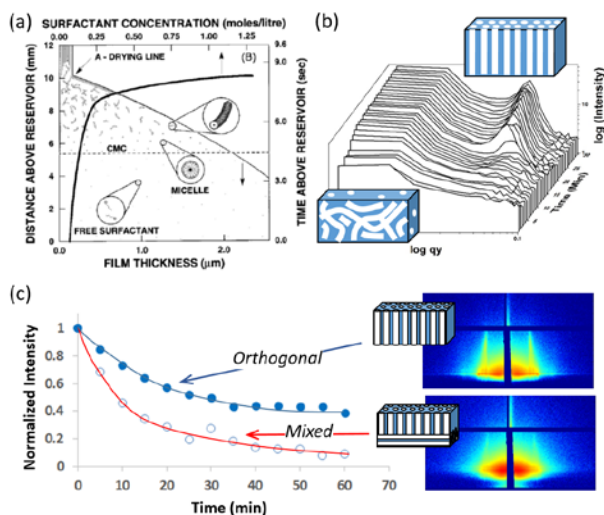


Figure 2.3. Schematics of the important stages of the formation of ordered nanoporous metal oxide films by EISA: (a) The dip coating process in which surfactant micelles form and may begin to assemble due to evaporation, (b) the aging process after deposition in which films organize into an ordered mesophase, and (c) high-temperature aging during which organic templates are removed by oxidation, crystallization may occur but loss of mesostructural order can happen with increasing temperature and time. Part (a) is reproduce with permission from C.J. Brinker et al. [115], (b) shows the rise of intensity from a o-HCP mesophase in a TiO₂ film during aging, adapted from Nagpure et al.[103] and (c) shows the loss of intensity of the o-HCP mesophase during heating of a TiO₂ film at 600 °C, adapted from Das et al.[105]

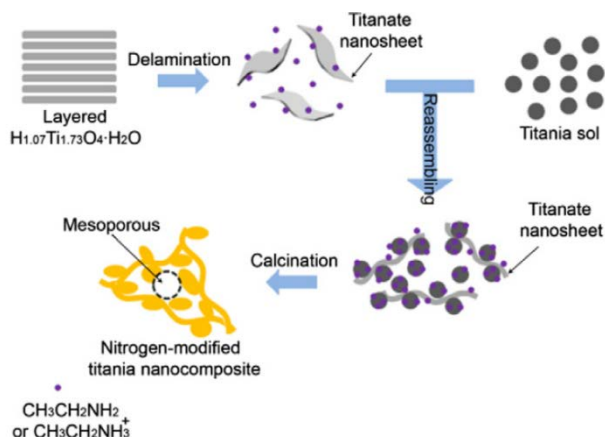


Figure 2.4. Schematic of procedures for preparing mesoporous nitrogen-modified titania photocatalyst. Reprinted with permission from ref. [178]. Reprinted from Chemical Engineering Journal vol. 219, J. Fu et al., “Soft-chemical synthesis of mesoporous

nitrogen-modified titania with superior photocatalytic performance under visible light irradiation,” pp. 155-161, Copyright (2013), with permission from Elsevier.

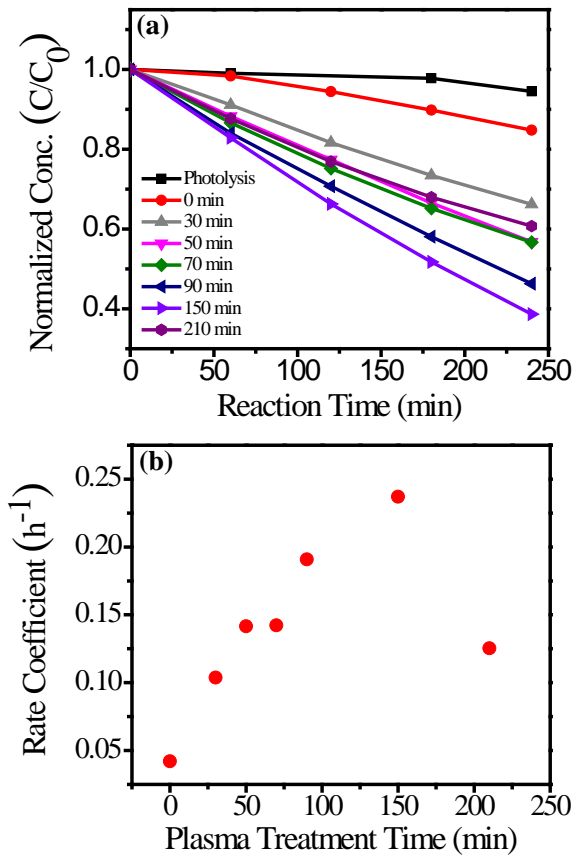


Figure 2.5. Methylene blue degradation reaction with undoped TiO_2 (0 min) film, N- TiO_2 films and without films (Photolysis): (a) Concentration profile (b) the plot of the first-order rate coefficient vs. plasma treatment time. Reprinted with permission from ref. [69]. Reprinted from Microporous and Mesoporous Materials vol. 220, S.Z. Islam et al., “ N_2/Ar plasma induced doping of ordered mesoporous TiO_2 thin films for visible light active photocatalysis,” pp. 120-128, Copyright (2018), with permission from Elsevier.

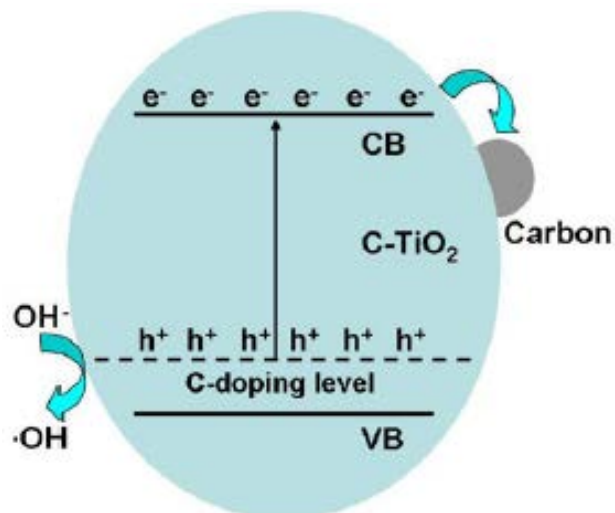


Figure 2.6. Proposed photocatalytic mechanism over the C-TiO₂ samples. Reprinted with permission from ref. [47]. Reprinted from Applied Catalysis B vol. 115, Y. Zhang et al., “Ethanol supercritical route for fabricating bimodal carbon modified mesoporous TiO₂ with enhanced photocatalytic capability in degrading phenol,” pp. 236-244, Copyright (2012), with permission from Elsevier.

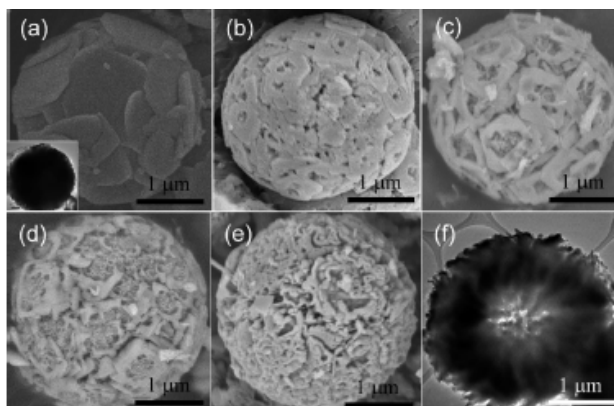


Figure 2.7. SEM images of F-mp-TiO₂ microspheres synthesized in (a) 0.1, (b) 0.3, (c) 0.5, (d) 0.8, and (e) 1.0% H₂SO₄ solution. Panel f and the insert of panel a are TEM images corresponding to hollow (e) and solid (a) microspheres, respectively. Reprinted with permission from ref. [227]. Reprinted with permission from Journal of the American Chemical Society vol. 130, J.H. Pan et al., “Self-etching reconstruction of hierarchically mesoporous F-TiO₂ hollow microspherical photocatalyst for concurrent membrane water purifications,” pp. 11256-7, Copyright (2008) American Chemical Society.

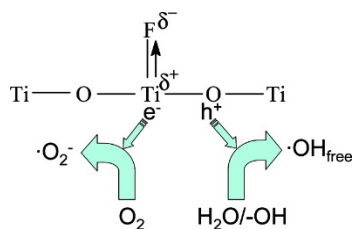


Figure 2.8. Schematic diagram for generation and transfer of charge carriers in F-TiO₂ under UV irradiation. Reprinted with permission from ref [229]. Reprinted with permission from The Journal of Physical Chemistry C vol. 113, J. Yu et al., “Enhancement of photocatalytic activity of mesoporous TiO₂ powders by hydrothermal surface fluorination treatment,” pp. 6743-6750, Copyright (2009) American Chemical Society.

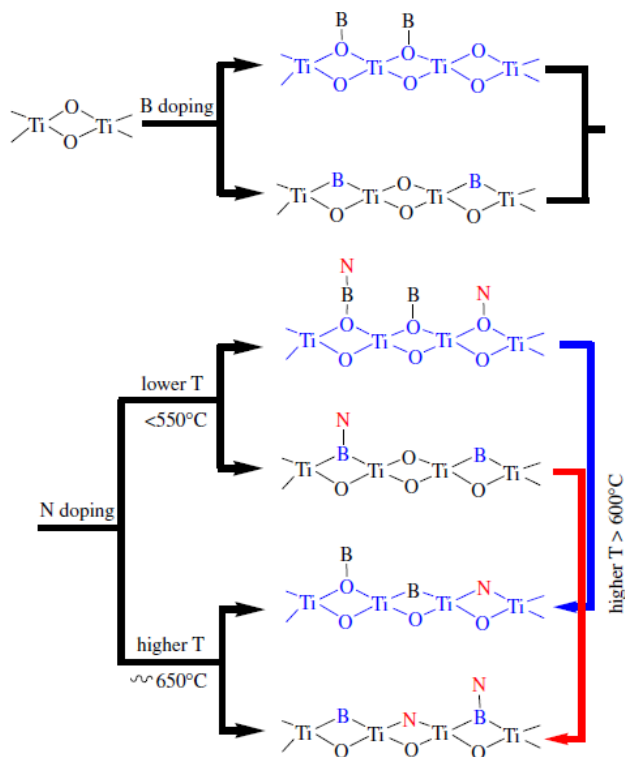


Figure 2.9. The transformation of surface structures of B,N-TiO₂. Reprinted with permission from ref. [242]. Reprinted from Journal of Solid State Chemistry vol. 184, X. Zhou et al., “Effect of nitrogen-doping temperature on the structure and photocatalytic activity of the B,N-doped TiO₂,” pp. 134-140, Copyright (2011) with permission from Elsevier.

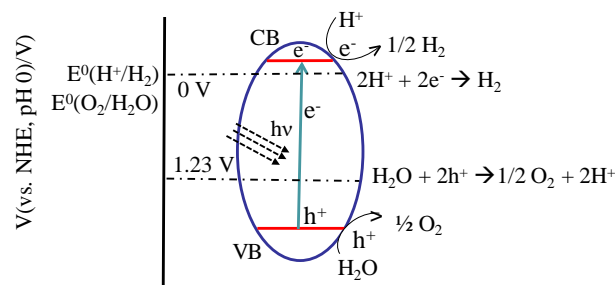


Figure 2.10. Basic principle of the overall water-splitting reaction on a semiconductor photocatalyst. Adapted from ref. [70].

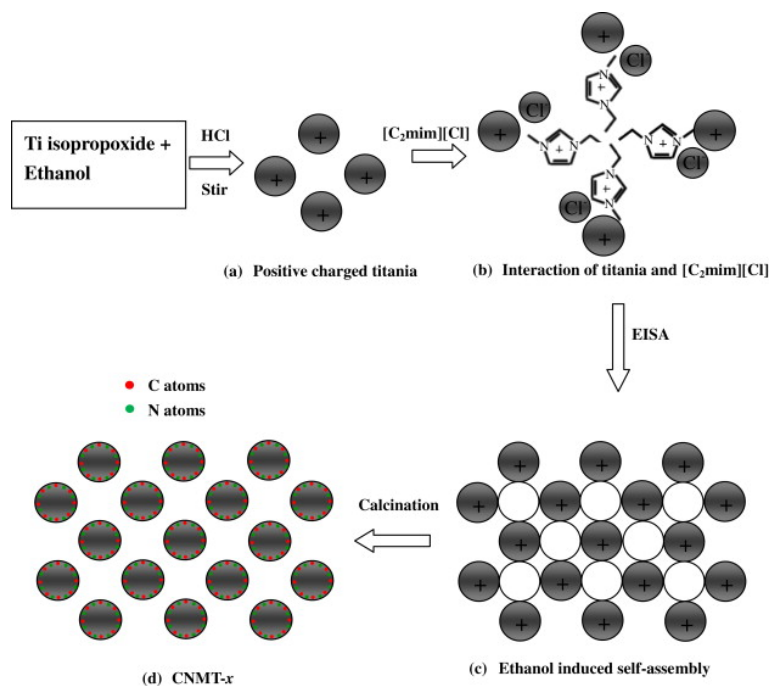


Figure 2.11. Schematic illustrations of synthesis procedure for CNMT-x samples. Reprinted with permission from ref. [48]. Reprinted from International Journal of Hydrogen Energy vol. 38, S.-H. Liu and H.-R. Syu, “High visible-light photocatalytic hydrogen evolution of C,N-codoped mesoporous TiO₂ nanoparticles prepared via an ionic-liquid-template approach,” pp. 13856-13865, Copyright (2013) with permission from Elsevier.

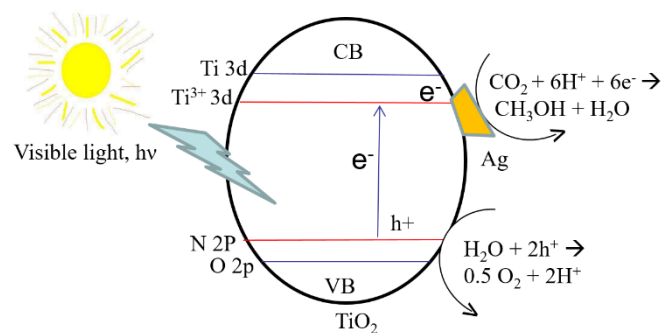


Figure 2.12. The mechanism of photocatalytic reduction of CO₂ under visible light irradiation. Adapted from ref. [254].

Table 2.1. Synthesis method, dopant source, chemical, optical and photocatalytic properties of nitrogen doped mesoporous titania.

Method	Template	N Source	N Comp (at. %)	Binding Energy (eV)	Initial BG (eV)	Final BG (eV)	S _{BET} (m ² /g)	Test Compound	Enhancement	Ref.
Solvothermal	Free	Urea	1.43	400	3.14	3.09	121	Rh B	1.43	[207]
Solvothermal	Free	Urea	-	399.5	3.16	3.02	23.6	Acetic Acid	1.54	[202]
EISA	F127	Urea	3.46	398.8	-	-	67	Water Splitting	2.37	[203]
Solvothermal	Urea	Urea	0.8	399.5	-	-	154	MB	3.1	[205]
Supercritical CO ₂ drying	-	Urea	-	396	3.1	1.92	116	-	-	[206]
Homogeneous precipitation	-	Urea	0.91	395.4, 401.5	-	-	89	MB	3	[208]
Sol-gel	PAM+PEG	Urea	0.6	397, 398.8, 402.4	2.9	2.75	110	MO	3	[210]
Sol-gel	Laurylamine hydrochloride	Urea	26.2 wt.%	400.8	3.2	3.1	110.3	Water Splitting	1.44	[250]
Sol-gel	F127	N ₂ plasma	3.2	396	3.5	3.02	143	MB	6	[69]
Exfoliation-reassembly	-	Ethylamine	-	399.8	-	-	217	MO	9	[178]
Solvothermal	F127	Ethylenediamine	4.1 wt.%	398.6	3.1	2.2	180.2	MB	-	[173]
Sol-gel	EDTA	EDTA	-	-	3.1	2.29	72.46	Rh B	1.5	[175]
Sol-gel	Triethylamine	Triethylamine	4	401.6	-	-	180	Phenol	7.5	[176]
Sol-gel		Triethanolamine	1.09	397, 399.9	-	-	70.5	MB		[177]

Table 2.1. Synthesis method, dopant source, chemical, optical and photocatalytic properties of nitrogen doped mesoporous titania (Continued).

Method	Template	Dopant Source	Dopant Comp (at.%)	XPS Binding Energy (eV)	Initial BG (eV)	Final BG (eV)	S _{BET} (m ² /g)	Test compounds	Enhancement	Ref.
Sol-gel reverse micelle	TritonX100	Na ₂ EDTA	6 wt.%	-	3.13	3.06	58	MB	4	[179]
Solvothermal	F127	Ethylenediamine	0.13 (N/Ti)	399.5, 401.4	3.32	2.98	185.4	Dimethyl Phthalate	2	[180]
Hydrothermal	P123	Triethylamine	-	399	-	-	150	Rh B	3.3	[174]
Hydrothermal	CTAB	Ammonia solution	1.31	399.5, 400.6, 401.5	-	-	83.1	Rh B	5	[183]
Sol-gel	P123	Tetramethylammonium hydroxide	-	400	-	-	105	Rh B	4	[182]
Sol-gel	Chitosan	Chitosan and NH ₄ OH	0.72 mass%	394.2, 400.9	-	2.65	132.26	MO	2	[185]
EISA	F127	NH ₃ gas	-	395.9	-	-	173 m ² /cm ³	MB	1.47	[35]
Wet Impregnation	Hydrazine Hydrate	Hydrazine Hydrate	-	398.1	-	-	74	Azoxybenzene	-	[194]

Table 2.2. Synthesis method, dopant source, chemical, optical and photocatalytic properties of non-metal doped mesoporous titania.

Method	Template	Dopant Source	Dopant Comp (at.%)	XPS Binding Energy (eV)	Initial BG (eV)	Final BG (eV)	S _{BET} (m ² /g)	Test compounds	Enhancement	Ref.
Sol-gel plus hydrothermal	Glucose	Glucose	C	282.4, 284.8, 286.2, 288.6	-	-	190	Reactive Brilliant X-3B	3.6	[220]
Solvothermal	Free	Rice	C	284.9, 285.8, 288.2, 288.6	3.1	2.04	138	MO	25.8	[47]
Hydrothermal	Free	TiF ₄	0.16 at. Conc. (F/Ti)	684.3	-	-	21.6	MB	1.06	[227]
Hydrothermal	-	NH ₄ HF ₂ -H ₂ O-C ₂ H ₅ OH	0.5 (at. F/Ti)	684	-	-	196.6	Acetone	3	[229]
Hydrothermal	P123	Iodic acid	5.2 (I)	624.5	-	-	157	MB	5.6	[233]
Hydrothermal	Polyvinyl alcohol	KI and I ₂	0.62 (I)	-	-	1.39	190.22 (doped)	MB		[232]
Sol-gel	-	Boric acid	17.8 (B)	192	3.05	3.04	68.11	Metoprolol	1.45	[86]
Sol-gel	P123	Phosphoric acid	14 (at. P/Ti)	-	3.1	3.17	-	Pentane	1.42	[235]
Hydrothermal and sol-gel	-	Phosphoric acid						MB		[234]

Table 2.3. Synthesis method, dopant source, chemical, optical and photocatalytic properties of non-metal co-doped mp-TiO₂.

Method	Template	Dopant Source	Dopant Comp (at. %)	XPS Binding Energy (eV)	Initial BG (eV)	Final BG (eV)	S _{BET} (m ² /g)	Test compounds	Enhancement	Ref.
Sol-gel	P123	Thiourea	1.41 (N), 2.33 (S), C	399.7, 401.8		2.9	85.1	Cyanotoxin microcystin-LR	11.5	[75]
Sol-gel	CTAB	Thiourea	-	396, 399.2, 284.6, 288.2, 165, 169	-	-	123.8	Reactive Brilliant Red X-3B	5	[200]
EISA	[C2mim][Cl] doped/F127 unodped	[C2mim][Cl]	1.75 (N), C	398.2, 400.2	3.1	2.98	54	Water splitting	10.5	[48]
EISA	F127	Thiourea	0.044 (N/O), 0.048 (S/O)	400.2, 396, 168.5	-	2.38	105	MO	18	[201]
Sol-gel	PAM and PEG	Urea (N), Boric acid (B)	1.78 (N), 1.23 (B)	400.5, 192.1	3.18	2.78	121.6	MB	3	[240]
Solvothermal	Thiourea	Thiourea	0.62 (N), 0.35 (S)	168.6, 169.7, 395.9, 399.7	-	-	29.11	MB	1.23	[198]
Hydrothermal	-	Thiourea	1.1 (N), 1.1 (S)	395.2, 396.9, 400.1, 168.9, 170.3	-	-	22.8 (doped)	Potassium ethyl xanthate	-	[199]
Solvothermal	-	Urea, Ammonium Fluoride	0.57 (N), 1.9 (F)	683.7-684.6, 688-688.6, 399.1, 400.1	3.02	2.74	36	Acid Orange 7	5.5	[209]

Chapter 3. Hydrazine-based Synergistic Ti(III)/N Doping of Surfactant-Templated TiO₂ Thin Films for Enhanced Visible Light Photocatalysis

Reproduced with permission from Islam, S. Z., Rankin, E. S., *Materials Chemistry and Physics*, 2016, 182, 382-393.

3.1 Summary

This study reports the preparation of titanium (Ti³⁺) and nitrogen co-doped cubic ordered mesoporous TiO₂ thin films using N₂H₄ treatment. The resulting co-doped TiO₂ (Ti³⁺-N-TiO₂) thin films show significant enhancements in visible light absorption and photocatalytic activity. Cubic ordered mesoporous TiO₂ thin films were prepared via a sol-gel method with Pluronic F127 as the pore template. After brief calcination, the TiO₂ films were dipped into hydrazine hydrate which acts both as a nitrogen source and as a reducing agent, followed by heating at low temperature (90 °C). The hydrazine treatment period was varied from 5 – 20 hours to obtain different degrees of reduction and nitrogen doping. X-ray photoelectron spectroscopy (XPS) analyses and UV-vis absorbance spectra of Ti³⁺-N-TiO₂ films indicate that the incorporated N atoms and Ti³⁺ reduce the band gap of TiO₂ and thus enhance the absorption of visible light. The corresponding visible light photocatalytic activity of Ti³⁺-N-TiO₂ films was determined from the photocatalytic degradation of methylene blue under visible light illumination (at 455 nm). The Ti³⁺-N-TiO₂ films prepared with 10 hours of treatment show the optimum photocatalytic activity, with a pseudo-first order rate coefficient of 0.12 h⁻¹, which is 3 times greater than that of undoped TiO₂ films. Calcination temperature and time were varied prior to hydrazine treatment to confirm that a brief calcination at low temperature (10 min at 350 °C) gave the best photochemical activity. In photoelectrochemical water oxidation using a 455 nm LED, the Ti³⁺-N-TiO₂ films prepared with 10 hours of N₂H₄ treatment show about 4 times the

photocurrent compared to undoped TiO₂ films. The present study suggests that hydrazine induced doping is a promising approach to enable synergistic incorporation of N and Ti³⁺ into the lattice of surfactant-templated TiO₂ films and enhanced visible light photoactivity, but that the benefits are limited by gradual mesostructure deterioration.

3.2 Introduction

Directly harvesting solar energy remains a promising approach to meet the increasing demand for clean and sustainable fuels and energy [22, 28, 158]. Since Fujishima and Honda first demonstrated its use for hydrogen generation from photocatalytic water splitting, TiO₂ has attracted much attention for solar energy harvesting due to its high photostability, low cost, and high availability [13, 29, 157, 189]. These unique properties have enabled TiO₂ to be utilized in a wide range of applications including solar energy conversion, antimicrobial surfaces, whiteners in paint, ceramics, glass, textiles, sunscreen, medicine, and organic pollutant degradation for environmental remediation [17-25, 69, 105, 192, 258]. The primary challenge of using TiO₂ for solar energy conversion is its high band gap [17]. The ultraviolet light that titania can absorb represents only 5% of the solar spectrum, whereas visible light constitutes about 47% [7]. A known strategy to overcome this limitation is to dope titania with nonmetal and metal dopants to introduce new electron energy levels, reduce the band gap, and allow the material to absorb visible light [17, 29, 40, 259]. Common nonmetal dopants include C, F, N, S, P and B [17]. Among the nonmetal dopants, nitrogen is the most effective dopant due to its comparable atomic size to oxygen, low ionization potential, and high stability [18, 29, 39, 79, 178, 180, 181, 194, 202, 203, 210, 211, 258, 260-262]. The mechanism of nitrogen doping is thought to be band gap reduction via the formation of a new energy state

above the valence band of titania by mixing the $2p$ orbital of the nonmetal dopant with the O $2p$ orbital [17, 263].

Along with nitrogen, titanium (Ti^{3+}) introduced into the TiO_2 lattice can create an energy state below the conduction band of titania which further reduces the band gap [74, 158, 186-193]. This Ti^{3+} state in TiO_2 improves not only light absorption but also charge transport. For instance, Zuo et al. prepared a self-doped (Ti^{3+}) TiO_2 photocatalyst and demonstrated its use for hydrogen production under visible light [186]. More recently, Ti^{3+} doped TiO_2 prepared by hydrazine reduction has been reported [158]. When TiO_2 is reduced by any reducing agent, Ti^{3+} is expected to be formed along with oxygen vacancies. However, with hydrazine (N_2H_4), titania is expected to be co-doped with both Ti^{3+} and N and is therefore to synergistically absorb more visible light and potentially be a more effective redox catalyst than TiO_2 doped with either species alone. Aman et al. explored this concept using Ti^{3+} and nitrogen doped TiO_2 nanoparticles for enhanced photocatalytic activity under visible light [157].

In addition to enhancing the optical absorption of TiO_2 , it is very important to control the morphology and the nanostructure of TiO_2 photocatalysts, which significantly impacts photocatalytic performance. Ordered nanostructured TiO_2 thin films prepared by surfactant templating are considered to be very effective structures for photocatalytic applications [18]. First, surfactant templating offers excellent control over the structure and morphology of the films such as tunable pore size, pore orientation, interfacial structure and pore connectivity. The pore structure facilitates the fast diffusion of reactants to the photocatalytic reaction sites of TiO_2 films. Second, the mesoporous structure of the TiO_2 films offers a high reactive surface area available for photocatalysis. Third, the sidewalls

of mesoporous TiO₂ films are thin and comparable to the diffusion length of photogenerated holes and electrons, thereby suppressing charge recombination processes [5, 33]. Here, cubic ordered mesoporous TiO₂ thin films are prepared using evaporation induced self-assembly with TiCl₄ and triblock copolymer surfactant Pluronic F127 as a template. Although mesoporous titania films have been reported for photoelectrolysis, those films had discontinuous, disordered pores and high wall thickness [264, 265]. In contrast, the pores of our mesoporous titania thin films are continuous, ordered with cubic symmetry and surrounded by thin walls. The thin walls in these films are expected to provide better charge transport and separation for photocatalysis. At the same time, the continuous, ordered pore space is expected to facilitate rapid diffusion of reactants to the surface and products away so that the entire thickness of the film can be utilized for reaction.

In the present study, we report the incorporation of Ti³⁺ and nitrogen atoms into surfactant-templated mesoporous TiO₂ thin films by hydrazine treatment. All prior studies of Ti³⁺ and N co-doping by hydrazine treatment used TiO₂ powders, nonporous films, nanowires or anodized nanotube arrays [49, 157, 158, 188-190, 194, 266-271]. We hypothesize that surfactant templated mesoporous TiO₂ films have several advantages over TiO₂ nanotubes. First, mesoporous titania films have smaller pores and thinner pore walls (both 10 nm or less) than titania nanotubes which should result in higher surface areas and lower charge recombination rates [33]. Moreover, surfactant templated mesoporous titania films can be prepared on any substrate whereas anodized nanotubes can only be prepared on Ti foil or substrates amenable to thin film vapor deposition. The incorporation of Ti³⁺ and nitrogen using a single source, hydrazine, along with the development of the well-

defined high surface area found in surfactant-templated ordered mesoporous TiO₂ thin films, are expected to result in a material exhibiting greatly enhanced visible-light absorption and photocatalytic activity. Because the films are formed *de novo* from a molecular precursor, they are expected to be more susceptible to doping, reduction, and structural modification than more fully crystalline materials available in other forms. To test this hypothesis, cubic ordered mesoporous TiO₂ thin films were synthesized by templating films derived from TiCl₄ with triblock copolymer surfactant Pluronic F127. Then, the films were treated with hydrazine hydrate, followed by analysis of photocatalytic activity for methylene blue degradation as a test reaction. Further, the optical absorbance and photocatalytic activity of Ti³⁺-N-TiO₂ films were correlated with the duration of hydrazine treatment. To understand the importance of the thermal treatment prior to hydrazine modification, the effects of calcination temperature and time of the titania films on the photocatalytic activity of hydrazine-treated titania films were studied. Finally, the photoelectrochemical performance of the doped films was demonstrated using water oxidation under basic pH conditions with a visible light source.

3.3. Experimental

3.3.1. Materials

Anhydrous ethanol (99.99%, 200 proof, Absolute, Anhydrous, ACS/USP Grade, Pharmco Aaper), F127 (triblock copolymer with average structure HO-(CH₂CH₂O)₁₀₀(CH₂CHCH₃O)₆₅(CH₂CH₂O)₁₀₀H, M_n = 12,500 Da, Sigma-Aldrich), titanium tetrachloride (tech grade, 99.9%, Sigma-Aldrich), deionized ultrafiltered (DIUF) water (Fisher Scientific), colloidal graphite (Ted Pella, inc.), N₂H₄·H₂O, 80% (Hydrazine, 51%) (Fisher Scientific), methylene blue hydrate (Sigma Aldrich), Nochromix powder

(Fisher Scientific), and concentrated sulfuric acid (Certified ACS Plus, Fisher Scientific) were all used as received.

3.3.2. Synthesis of mesoporous titania films

Nochromix solution, prepared according to the directions of the supplier, was used for the cleaning of borosilicate glass slides (Fisher Scientific). Sol preparation was begun by preparing a solution of 0.67 g of surfactant F127 in ethanol (18.43g). TiCl_4 (1.12 ml) was added to the previously prepared F127 solution in a nitrogen-filled glove bag. The solution was stirred for 10 min to allow for chloride / ethoxy exchange to take place. 1.8 g of deionized water was then added to the solution slowly. The solution was stirred again for 10 minutes. In-situ HCl is formed from the reaction between TiCl_4 and H_2O . This HCl makes the solution acidic which helps to control the condensation reaction and allow the formation of continuous films. The cleaned glass slides were dip coated using a home built system at a rate of 6 cm/min from this solution to prepare the TiO_2 films, followed by aging in a highly humid environment (RH ~ 94%) in a refrigerator at a temperature of 4 °C for 2 h. The high RH environment was provided by placing the slides in a sealed box with two beakers containing water. Aging at high humidity and low temperature helps to promote ordered mesostructure formation, transformation and orientation by slowing the condensation of the precursor and controlling evaporation of the solvent. Immediately after aging, TiO_2 films were calcined in a muffle furnace (Vulcan 3-550) for 10 minutes at 350 °C. The temperature of the furnace was increased to 350 °C at a ramp of 25 °C/min but the calcined TiO_2 films were cooled rapidly after 10 minutes at the final temperature. Rapid transfer directly from the refrigerator to the furnace was carried out to avoid moisture condensation on the surface of the films [272].

For titanium reduction and nitrogen doping, a film was dipped into a hydrazine hydrate solution ($\text{N}_2\text{H}_4 \cdot \text{H}_2\text{O}$ (80%)) deep enough to cover the titania film for 1 hour at room temperature. Then, the film was removed from the solution and heated at 90 °C for different periods (5, 10, 15 and 20 hours) in a closed 50 mL polypropylene centrifuge tube with a 1 ml reservoir of $\text{N}_2\text{H}_4 \cdot \text{H}_2\text{O}$ (80%) in its conical shaped bottom. The excess liquid hydrazine was present to prevent rapid evaporation of N_2H_4 from the films but did not come into direct contact with the slides during heating. After treatment the film was heated at 90 °C for 10 minutes after being taken out of the centrifuge tube to remove the adsorbed water and hydrazine. The untreated TiO_2 sample and the TiO_2 samples treated for 5, 10, 15, and 20 hours are denoted as undoped TiO_2 , and $x \text{ h_Ti}^{3+}\text{-N-TiO}_2$, where x is the duration of hydrazine treatment.

3.3.3. Characterization

For the imaging of nanoporous structure, scanning electron microscope (SEM) characterization was performed using a Hitachi S-900 at 6 kV. SEM samples were prepared by cutting the glass slide to the desired shape using a glass cutter and then mounting the sample exactly at the center of a SEM stub coated with carbon tape. The samples were aged at 120 °C overnight (~12 h). A Helios Nanolab 660 (FEI) was used for cross sectional sample preparation and STEM imaging. TEM was performed using an ultra-high resolution JEOL 2200FS. Low angle XRD analysis was performed using a Bruker-AXS D8 DISCOVER diffractometer to determine the degree of mesostructural ordering. Films were scanned at 0.25 °/min in 2θ increments of 0.02° from 1° to 4°. The optical absorbance of the samples was obtained with an UV-vis absorption spectrometer (Ocean Optics, DT-MINI-2-GS). The measurement was carried out by placing the films at an angle of ~45°

relative to the incident beam. X-ray photoelectron spectroscopic (XPS) analysis was conducted using a ThermoScientific K-Alpha photoelectron spectrometer using monochromatic Al K- α radiation with photon energy of 1486.6 eV. Before performing the experiment, the samples were cleaned with ethanol to remove dust from their surface.

3.3.4. Photocatalytic testing

The photocatalytic activity of the Ti³⁺-N-TiO₂ film was evaluated by monitoring the photo-degradation of methylene blue (MB). A photograph of the experimental set-up is shown in Appendix A Figure A.1. A blue LED (BLED) with wavelength of 455 nm and an ultraviolet LED (UVLED) with wavelength of 365 nm (Thorlabs) were used as the light sources. Power densities of the UVLED and BLED were measured with a power energy meter (standard photodiode power sensor, Si, Thorlabs) to be 6 mW/cm² and 22.5 mW/cm², respectively. The spectra of the UVLED and BLED reproduced from Thorlabs are given in Appendix A Figure A.2. A cylindrical beaker was used as the reactor. The top of the beaker was covered with parafilm to avoid the evaporation of water. In each experiment, the solution volume and the initial concentration of MB were 25 ml and 1×10⁻⁵ M, respectively. The area of mesoporous TiO₂ films illuminated by the light source was ~15 cm². The distance between the light source and the reactor was 1 cm. Before illumination, the solution was stirred for 30 minutes in the dark so that MB could be adsorbed onto the pore surface. The solution was continuously stirred using a magnetic stirrer throughout the experiment. The change in MB concentration was determined by periodically taking a 2 mL sample and measuring the optical absorbance at 664 nm using a spectrophotometer (Ocean Optics DT-MINI-2-GS). The sample was returned to the reactor after each measurement.

3.3.5. Photoelectrochemical testing

For photoelectrochemical (PEC) testing, TiO₂ and Ti³⁺-N-TiO₂ films were prepared on fluorine-doped tin oxide (FTO) slides. Prior to dip coating, the FTO slides were cleaned with deionized water, acetone and isopropanol followed by UV-ozone treatment for 20 minutes to remove any organic contaminants. The water oxidation reaction was performed to evaluate the Ti³⁺-N-TiO₂ film for photoelectrochemical performance in a photoelectrochemical system with a three electrode potentiostat (model CHI660D, CH Instruments, Inc.). TiO₂ films, platinum and Ag/AgCl were used as working, counter and reference electrodes, respectively. A glass cell was used as a reactor. KOH of 1 M concentration was used as the electrolyte. All three electrodes were kept in the reactor. The light source was a blue LED (ThorLabs) with 455 nm wavelength and 22.5 mW/cm² intensity. Current-time measurements were carried out using undoped TiO₂ and Ti³⁺-N-TiO₂ films with an applied potential of 0.4 V vs. the Ag/AgCl reference electrode. The light was turned on and off every 300 seconds periodically to obtain the light and dark currents. This experiment was performed for 1800 seconds.

Electrochemical impedance spectroscopy measurements were carried out using the same potentiostat and electrolyte solution used for photoelectrochemical measurement. The measurement was performed at 1 Hz frequency in the dark. The potential was varied between -1.5 V and -0.3 V (vs Ag/AgCl).

3.4. Results and discussion

The structure and surface morphology of the TiO₂ films were characterized by SEM as shown in Figure 3.1(a). Nanopores are clearly visible on the top surface of the film. The average pore diameter and wall thickness of the TiO₂ films are around 7 nm and 5.5 nm,

respectively. The TEM image in Figure 3.1(b) also clearly shows the presence of pores throughout the film. The arrangement of the pores is consistent with a cubic array of interconnected globular mesopores [33]. The cross-sectional bright field STEM image (Appendix A Figure A.3) also shows that the cubic array of pores extends across the thickness of ~ 80 nm thick films. Figure 3.1(c) shows the XRD pattern of the TiO₂ film, which corroborates that the mesoporous titania films have an ordered pore structure. A single XRD reflection was observed at $2\theta = 2.26^\circ$ which corresponds to a d-spacing value of 3.9 nm. Assuming that the mesostructure is oriented so that the SEM image gives the (110) d-spacing, this peak corresponds to the (420) plane parallel to the substrate for a body-centered cubic mesophase (*Im3m* space group), but this may be a different peak because of contraction normal to the film. Since the pore size found from SEM images is almost three times of the d-spacing, the reflection in Figure 3.1(c) is definitely a higher order XRD diffraction peak, indicating that a well-ordered structure is present. Wide angle XRD ($2\theta > 10^\circ$) was performed to investigate the phase of the mesoporous TiO₂ film but the films were found to be x-ray amorphous.

To identify the crystalline phase in the titania films, high-resolution TEM (HRTEM) and selected area electron diffraction (SAED) were performed. In a representative HRTEM image (Figure 3.2), a large amount of amorphous phase is observed. However, the film also contains dispersed nanocrystals with a size of about 2 nm. Appendix A Figure A.4 shows an enlarged HRTEM image of a nanocrystal in the film. The lattice fringe is 0.245 nm, which is consistent with anatase (103) or (004) d-spacing [273]. In addition to the direct visualization by HRTEM, the SAED pattern from the same sample (Appendix A Figure A.5) was collected but showed only a diffuse ring rather than

any bright diffraction spot, probably due to the small amount of nanocrystals embedded in an amorphous matrix.

Figure 3.3 presents the optical absorbance and the estimated band gap of hydrazine treated TiO₂ films. The UV-vis spectra indicate that the primary absorption feature associated with the band gap of the material shifts towards the visible wavelength range upon hydrazine treatment. In addition, modification of the films causes enhancement of absorbance in the range from 350-700 nm, along with enhancement of ultraviolet absorption. This enhancement in the absorbance is due to the reduction and nitrogen doping of the film. Enlarged spectra of the Ti³⁺-N-TiO₂ films in the visible light region are shown in the inset of Figure 3.3 (a). The inset reveals that the absorbance tail is extended towards longer wavelengths as the duration of hydrazine treatment increases. The absorbance of the 10 h_Ti³⁺-N-TiO₂, 15 h_Ti³⁺-N-TiO₂ and 20 h_Ti³⁺-N-TiO₂ films are almost the same up to 550 nm. However, the 15 h_Ti³⁺-N-TiO₂ and 20 h_Ti³⁺-N-TiO₂ films showed a new band in the range of 550-700 nm. This suggests that the films treated for more than 10 hours may exhibit an enhanced photo-response at long wavelengths.

In order to determine the band gap of the undoped TiO₂ and Ti³⁺-N-TiO₂ films, Tauc plots were drawn (Appendix A Figure A.6). To do this, $(\alpha h\nu)^{1/2}$ vs. $h\nu$ was plotted where α is the absorption coefficient and $h\nu$ is the photon energy. The absorption coefficients were calculated from the absorbance divided by the film thickness from Appendix A Figure A.3. The band gap was estimated by extrapolating the linear portion of the Tauc plot to the x-axis where the value of $(\alpha h\nu)^{1/2}$ approaches zero [274]. The relation between band gap and hydrazine treatment duration is shown in Figure 3.3(b) and clearly shows an effect of hydrazine treatment on the band gap of Ti³⁺-N-TiO₂. The band gap of

undoped TiO₂ film is 3.5 eV, which is consistent with an amorphous / nanocrystalline structure (wide angle XRD revealed no discernable reflections from crystalline phases). All of the doped films showed a band gap between 3.30 and 3.40 eV. Though the band gap of all the doped films are almost same, localized midgap states might be formed in the doped films treated for longer time, and specific surface sites could be generated representing catalytically active arrangements of Ti, N and O. This might be the reason for higher absorbance across the visible region of the Ti³⁺-N-TiO₂ films treated for increasing times.

XPS was used to determine the nitrogen content and chemical state of undoped TiO₂ and 5 h_Ti³⁺-N-TiO₂ films. As shown in Figure 3.4(a), XPS surface scanning shows a peak with high intensity at ca. 400 eV for 5 h_Ti³⁺-N-TiO₂ films whereas no peak was found for undoped TiO₂ films. The composition of nitrogen in 5 h_Ti³⁺-N-TiO₂ films was measured using the XPS peaks of Ti, O and N to be 2.32 atomic %. Several authors reported that the binding energy of nitrogen in TiO₂ are in the range of 396 - 404 eV [274-276]. There are two types of nitrogen found in doped titania - (i) substitutional doping with a binding energy of 396 eV, and (ii) interstitial doping with binding energy of about 400 eV [17]. The XPS peak at 400 eV is due to N-N, N-O, or Ti-O-N bonding whereas direct Ti-N bonding gives rise to a binding energy of 396 eV [190]. Compared to other hydrazine based studies, our hydrazine treated Ti³⁺-N-TiO₂ films showed significantly higher nitrogen content. For instance, Sun et al. reported about 0.2% nitrogen species in N-TiO₂ synthesized using hydrazine as the nitrogen source [188]. That might be because our amorphous/nanocrystalline surfactant templated TiO₂ films were formed *de novo* from a molecular precursor, which is expected to enhance nitrogen incorporation and hydrazine

reduction compared to more fully crystalline materials available in other forms. Depth profiling was performed inside the films using argon ion etching for 10 etching intervals of 5 seconds each at 1000 eV energy. Figure 3.4(b) shows that N 1s peaks are found at both 400 eV and 396 eV, which implies that both interstitial and substitutional nitrogen are present in the 5 h-Ti³⁺-N-TiO₂ film. Nitrogen is found throughout the film, but a higher amount of nitrogen is found at the film surface, as shown in Figure 3.4(c). This might be due to the combined nitrogen from doping and adsorbed species from the atmosphere. The fraction of substitutional nitrogen increases with increasing etching depth within the film, suggesting that N₂H₄ creates interstitial N/O species near the surface but still is able to introduce nitrogen into the matrix of the films throughout their depth. The etching depth of TiO₂ film has been estimated by comparing with the standard etching rate of Ta₂O₃. According to the XPS instrument documentation, the etching rate for Ta₂O₃ is 1.05 nm/s for the same potential (1000 eV) used for TiO₂ film etching. Since the TiO₂ film is also a metal oxide as Ta₂O₃, it is assumed that the etching rate of TiO₂ will be similar, suggesting a total etched depth of 47 nm.

Figures 3.5(a) and 3.5(b) show the XPS spectra in the Ti 2p range during 1000 eV Ar etching depth profiling of undoped TiO₂ and 5 h-Ti³⁺-N-TiO₂ films, respectively. The spectra have two obvious peaks at ca. 458.8 eV and 464.5 eV associated with the Ti 2p_{3/2} and Ti 2p_{1/2} orbitals, respectively in both undoped TiO₂ and 5 h-Ti³⁺-N-TiO₂ films [157]. A shoulder at about 457 eV was found to the right of the peak at 458.8 eV for both undoped TiO₂ and 5 h-Ti³⁺-N-TiO₂ films. This shoulder is associated with the Ti³⁺ state [157]. It is possible that Ti³⁺ is observed in both films because of partial reduction due to Ar etching. However, the relative peak intensity and width of the Ti³⁺ shoulder of 5 h-Ti³⁺-N-TiO₂ are

visibly higher than those of undoped TiO₂ film. This indicates that 5 h Ti³⁺-N-TiO₂ films have more reduced Ti³⁺ compared to undoped TiO₂ films. A direct comparison of the XPS spectra of undoped and doped TiO₂ films has been made to more clearly compare the Ti³⁺ peaks within the film. Appendix A Figure A.7(a) shows the XPS Ti 2p depth profile spectra of the undoped TiO₂ and 5 h Ti³⁺-N-TiO₂ films after 45 s of etching. Though the absolute intensity of the shoulder for Ti³⁺ in the 5 h Ti³⁺-N-TiO₂ film is a little higher than that for the undoped TiO₂ film, the relative intensity of Ti³⁺ in the 5 h Ti³⁺-N-TiO₂ film is much higher compared to the peak intensity of Ti³⁺ in the undoped TiO₂ film. Peak fitting was performed to deconvolute the contributions of Ti 2p_{1/2}, Ti 2p_{2/3} and Ti³⁺ in the Ti 2p spectrum. Appendix A Figure A.7(b) and (c) show the peak fitting of the XPS Ti 2p spectra (after 45 s of etching). The relative contribution of Ti³⁺ in the undoped TiO₂ and 5 h Ti³⁺-N-TiO₂ film are 11.3% and 23.2%, respectively. While Ar ion etching may introduce some reduced titanium, this indicates that the doped film has significantly more Ti³⁺ compared to an undoped titania films after 45 s of etching.

Aman et al. also observed a shoulder at 457 eV for Ti³⁺ state in addition to the original peak at 459.7 eV in hydrazine treated TiO₂. They suggested that the Ti³⁺ formation is mostly due to the hydrazine reduction [157]. Mao et al. prepared reduced titania by hydrazine treatment but could not detect Ti³⁺ in the hydrazine reduced TiO₂ using XPS analysis [158]. They used electron paramagnetic resonance (EPR) to show the presence of Ti³⁺. Several studies also used EPR to determine the presence of Ti³⁺ in hydrazine treated TiO₂ [158, 188, 267, 268]. However, due to the limited quantity of material present in these films, EPR analysis was not possible.

The characterization above established that hydrazine treatment leads to increases in nitrogen content, Ti^{3+} doping and visible light absorption. The visible light driven photocatalytic activity of Ti^{3+} -N- TiO_2 films was assessed by monitoring photocatalytic degradation of methylene blue (MB) and compared with that of undoped TiO_2 films. Prior to each photocatalytic measurement, the TiO_2 films were immersed in MB-containing solution for at least 30 min, in order to make sure that the adsorption of MB onto the surface of mesoporous TiO_2 films became saturated. MB adsorption reached equilibrium in 30 min, as shown in the representative long-time adsorption study in Appendix A Figure A.8(a). For photocatalytic measurements, the MB-containing solution was exposed to a blue LED light (peak wavelength 455 nm) to measure photocatalytic activity over the course of 4 hours. Figure 3.6(a) shows the photocatalytic results normalized using the absorbance at the time that illumination with the LED began, and with the time scale set to zero at the beginning of illumination. The curves clearly show enhanced photocatalytic activity of Ti^{3+} -N- TiO_2 films compared to the undoped TiO_2 film. Insignificant degradation was found without TiO_2 films (direct photolysis of MB). The photocatalytic degradation results of MB with undoped TiO_2 film and Ti^{3+} -N- TiO_2 films clearly showed that the photocatalytic activity of Ti^{3+} -N- TiO_2 gradually increased in proportion to the duration of hydrazine treatment from 0 to 10 hours.

The kinetics of photocatalytic degradation reaction rates were quantified by fitting the decay of MB concentration with the pseudo-first order rate equation: $C=C_0*\exp(-kt)$, where k = the rate coefficient. Appendix A Figure A.8(b) shows that all experiments display very good linear fits between $\ln(C/C_0)$ and t , thus indicating that first order kinetics are appropriate in this case. The rate coefficients are plotted as a function of hydrazine

treatment time in Figure 3.6(b). The rate coefficients increase with increasing hydrazine treatment until 10 hours. This correlates with the increase in visible light absorbance, and decrease in band gap found above. The 10 h Ti^{3+} -N-TiO₂ films showed the maximum rate coefficient of 0.12 h⁻¹, which was nearly 3 times greater than for undoped TiO₂ film. Based on the film thickness (80 nm), structure (from SEM) and illuminated area, this corresponds roughly to a rate coefficient of ~85 min⁻¹/(g catalyst). The increase in photocatalytic activity after hydrazine treatment could be attributed to the enhancement of the visible light absorbance due to a combination of nitrogen doping and titanium reduction to Ti^{3+} , facilitated by the nanocrystalline mesoporous architecture. The enhancement observed here is comparable to the results reported in a previous studies. For instance, Selvam et al. prepared N-doped TiO₂ by a wet method using hydrazine. The N-TiO₂ showed 70 % nitrobenzene conversion (5 h photoirradiation) whereas untreated TiO₂ showed 60 % conversion (6 h photoirradiation) under 365 nm mercury lamp irradiation, which represents a 1.6× increase in activity (assuming 1st order kinetics) [269]. Xu et al. observed about 4× enhancement in X-3B dye solution degradation under visible light irradiation (MVL 210 source) for TiO₂ nanotubes after the samples were hydrazine treated [189]. In another study, Sun et al. prepared Ti^{3+} and N co-doped titania particles by hydrazine treatment. In the 4-chlorophenol degradation under 250 W Xe lamp irradiation, the first order rate constant for doped titania was 0.002 min⁻¹ whereas undoped titania did not show any significant photodegradation [188]. It is difficult to compare our results directly with the literature due to the use of different light sources with different intensity and catalyst amount, but the effects of hydrazine treatment appear to be comparable or better than in prior reports.

While hydrazine treatment helps titania in visible light driven photocatalytic activity, excessive exposure to hydrazine negatively affected its photocatalytic performance. For instance, 20 h_Ti³⁺-N-TiO₂ films showed a rate coefficient of 0.054 h⁻¹, which was much lower than that for the 10 h_Ti³⁺-N-TiO₂ films. The photocatalytic performance of the 10 h_Ti³⁺-N-TiO₂, 15 h_Ti³⁺-N-TiO₂, and 20 h_Ti³⁺-N-TiO₂ films are not proportional with the UV-vis spectroscopy measurement as they exhibited about the same absorbance at 455 nm wavelength (Figure 3.3(a)). Since the reaction rate strongly depends on the available surface area of the film and the network connectivity, deterioration of the porous network might explain the decline in activity with long exposure to hydrazine (and water vapor). The mesostructure of the Ti³⁺-N-TiO₂ films was investigated by SEM as shown in Figure 3.7. More high resolution SEM images are provided in Appendix A Figure A.9. The pore wall thickness increased and pore size decreased due to the coarsening during the long time hydrazine treatment. These effects cause pore constriction and partial pore blocking. The coarsening increases with the hydrazine treatment period. After 20 hours of the treatment, the film almost lost accessibility of the pores completely at the scale visible by SEM. This structural deterioration caused a decrease in available surface area, which would explain the decrease in photocatalytic activity. Thus, the photocatalytic performance of the Ti³⁺-N-TiO₂ films displays a tradeoff between increasing absorbance due to doping and reduction, and decreasing surface area due to coarsening of the mesostructure. The reduction of surface area most likely dominates over the increase in visible light absorbance in the 15 h_Ti³⁺-N-TiO₂ and 20 h_Ti³⁺-N-TiO₂ films which causes the decrease in photocatalytic activity in the MB degradation reaction.

The effect of calcination temperature of the titania films on the photocatalytic activities of the 10 h Ti^{3+} -N-TiO₂ films was studied by methylene blue degradation using BLED illumination. First, three titania films were prepared using 10 min of calcination in air at 350 °C, 400 °C and 450 °C. Then, all the films were hydrazine treated for 10 h. The concentration profiles in Figure 3.8(a) shows that the degradation of MB is highest for the film calcined at 350 °C, and decreases with increasing temperature. Fitting a first-order kinetic model to the concentration profiles (Appendix A Figure A.10 (a)) yields rate coefficients for films calcined at 350 °C, 400 °C and 450 °C of 0.12 h⁻¹, 0.102 h⁻¹ and 0.09 h⁻¹, respectively. The trend probably reflects a tradeoff between crystallization during calcination and nitrogen doping / reduction during hydrazine treatment. At 350 °C, the films are likely to be least crystalline, and therefore most easily doped and reduced by species derived by hydrazine decomposition. Although increasing the calcination temperature would be expected to enhance the activity of the titania itself due to crystallization, it reduces the ease with which hydrazine modification of the matrix occurs, and the photocatalytic activity under visible illumination is reduced.

The effect of calcination time of the titania films on the photocatalytic activities of the 10 h Ti^{3+} -N-TiO₂ films was also studied by methylene blue degradation under BLED illumination. Three titania films were prepared with calcination in air at 350 °C for 10 min, 60 min and 120 min, followed by 10 h of hydrazine treatment. The concentration profiles in Figure 3.8(b) shows that the degradation of the MB in this series is fastest for the film calcined for 10 min, and decreases with longer calcination. Fitting a first-order kinetic model to the concentration profiles (Appendix A Figure A.10(b)) yields rate coefficients for 10 min, 60 min and 120 min calcined films of 0.12 h⁻¹, 0.064 h⁻¹ and 0.052 h⁻¹,

respectively. Longer calcination than the baseline 10 min used to decompose the pore template would be expected to induce greater crystallization of the titania, along with the possibility of pore sintering. Both effects would reduce the effectiveness of matrix modification by hydrazine treatment. Thus, consistent with the hypothesis that the disordered nature of sol-gel titania aids in hydrazine-based doping, brief (10 min), low temperature (350 °C) calcination is found to give the best photocatalytic activity for films with 10 h hydrazine treatment.

Further, methylene blue degradation was performed with titania films calcined at 350 °C for 10 min to test their photocatalytic activity under UVLED illumination. The 10 h-Ti³⁺-N-TiO₂ films showed higher photoactivity compared to the undoped TiO₂ film under both UVLED and BLED illumination as shown in Figure 3.8(c). The sample and wavelength are indicated in the legend as (hydrazine treatment time) (LED type), for example 10 h_BLED indicating 10 h hydrazine treatment and BLED illumination. Fitting the concentration profiles (Appendix A Figure A.10(c)) gives rate constants for 0 h_BLED, 10 h_BLED, 0 h_UVLED and 10 h_UVLED films of 0.042 h⁻¹, 0.12 h⁻¹, 0.231 h⁻¹, and 0.243 h⁻¹, respectively. The photoactivities of both undoped and doped films under UVLED illumination are much higher than under BLED illumination. In addition, the hydrazine treated titania films showed a higher degradation rate than undoped titania films illumination at both wavelengths. According to previous studies, nitrogen doping does not improve photocatalytic activity under UV light irradiation, and may actually deteriorate UV photoactivity [261, 274, 277]. The reason that UV photoactivity is not lost in the Ti³⁺-N-TiO₂ films here is due to efficient reduction and nitrogen doping of the titania matrix of

the amorphous sol-gel TiO₂. Efficient doping combined with advantageous mesoporous TiO₂ structure seems to enable efficient charge separation and transport.

To alleviate concerns over visible enhancement arising from sensitization by MB and to show the versatility of the doped films, photoelectrochemical (PEC) activity measurements were conducted in a three-electrode system to evaluate the water oxidation performance of the doped films as a photoanode. The current-time curves for the undoped TiO₂ and Ti³⁺-N-TiO₂ films are presented in Figure 3.9(a). The inset in Figure 3.9(a) presents the enlarged region from 400 to 1800 s of the current-time plot. The initial currents for the doped films are significantly higher than the undoped TiO₂ film. The current increases with increasing hydrazine treatment period. However, the current decreases with time for all of the doped films. Ti³⁺ may be oxidized during the current-time experiment resulting in decreasing current.

For comparison of the photoelectrochemical performance of the doped films, the photocurrent was separated from the total current. The current vs. time data for all dark periods was fit with a single fourth order polynomial (Appendix A Figure A.11) and this function subtracted from the total current to give the photocurrent. Appendix A Figure A.12 shows the photocurrent as a function of time for the undoped and Ti³⁺-N-TiO₂ films. It is clear that the photocurrent of the Ti³⁺-N-TiO₂ films is higher than undoped TiO₂ films. The specific photocurrent was calculated from the photocurrent density divided by the mass per area (2.29×10^{-5} g/cm² calculated using 80 nm film thickness, and pore diameter and wall thickness from the SEM imaging). The specific photocurrent of undoped TiO₂ and Ti³⁺-N-TiO₂ films at 600 s (the start of the second illuminated period) are plotted as a function of hydrazine treatment time in Figure 3.9(b). The 10 h_ Ti³⁺-N-TiO₂ films showed

the maximum photocurrent which is about 4 times as high as for undoped TiO₂ films. The photocurrent for the film after 20 hours of hydrazine treatment is lower than for the film treated for 10 hours. This is consistent with the maximum in photocatalytic activity for MB degradation at 10 hours of hydrazine treatment and can be explained by the mesostructure deterioration for more than 10 hours of hydrazine treatment as shown in Figure 3.7. The enhancement in water oxidation of this study surpasses the results reported in previous studies. For instance, Xu et al. prepared hydrazine treated titania nanotubes and found 2× enhancement in photoelectrochemical performance compared to undoped titania nanotubes in water oxidation under a halogen lamp [189]. Mao et al. also showed less than 2× photocurrent enhancement in water oxidation under a solar simulator for hydrazine TiO₂ nanotubes compared to undoped TiO₂ nanotubes [158]. The greater enhancement found here may be a result of the ease with which the initially amorphous sol-gel titania film is doped by N₂H₄ treatment. The absolute current density of our titania film is relatively small compared to the current density of some other titania materials reported in literature [278]. This is because the films have low thickness (80 nm) and the BLED source has low energy density. It is difficult to make absolute comparison of the photocurrents obtained from photoelectrochemical water oxidation across different measurement systems in the literature because of differences in several factors including light source, wavelength and intensity; catalyst amount; addition of various reagents (e. g. hole scavengers); addition of co-catalysts (e.g. metal nanoparticles); electrolyte pH; and applied potential. The specific photocurrent per gram of our doped mesoporous titania was estimated to be on the scale of mA, which is quite significant considering the low intensity of the BLED source. The absolute photocurrent of our mesoporous titania thin films can be further improved by

preparing thicker films using a layer-by-layer deposition technique to be reported in a future contribution.

The electronic properties of the films and the film /electrolyte interface were investigated by electrochemical impedance spectroscopy (EIS) for undoped TiO₂ and Ti³⁺-N-TiO₂ films. Mott-Schottky plots were prepared using data from the EIS measurement as shown in Figure 3.10(a). The positive slope of the Mott-Schottky plot indicates that (as expected) TiO₂ is an n-type semiconductor [158, 279]. The flat band potential (E_{fb}) was estimated by extrapolating the linear portion of the Mott-Schottky plot to the horizontal axis as shown in Appendix A Figure A.13. Figure 3.10(b) shows that E_{fb} of Ti³⁺-N-TiO₂ films decreases monotonically as a function of hydrazine treatment duration. E_{fb} represents the edge of the conduction band of TiO₂ since it is an n-type semiconductor, [280-284] so Figure 3.10(b) suggests that a new energy band for the Ti³⁺ state might be formed just below the conduction band of TiO₂ due to the reduction by hydrazine. The Ti³⁺ state formation increases with the increasing hydrazine treatment time resulting in decreasing E_{fb} . This EIS measurement is consistent with the photocatalytic and photoelectrochemical results in that the photoactivity increases as E_{fb} of TiO₂ decreases due to hydrazine treatment. The downward shift of the edge of the conduction band is also in agreement with the band gap reduction of the Ti³⁺-N-TiO₂ films estimated from optical measurement. It has suggested that nitrogen doping reduces E_{fb} [281, 282, 285], but Spadavecchia et al. demonstrated both experimentally and theoretically that nitrogen doping alone does not change E_{fb} [280]. Therefore, the observed change in E_{fb} is most likely caused by reduction due to the use of hydrazine as a source of nitrogen doping.

In an n-type semiconductor (TiO₂), electrons are the majority charge carriers. The charge carrier density (N_D) can be calculated from the slope of the linear portion of a Mott-Schottky plot using Equation 3.1 (the Mott-Schottky equation):

$$\frac{1}{C^2} = \left(\frac{2}{q\epsilon\epsilon_0 N_D} \right) \left(E - E_{fb} - \frac{\kappa T}{q} \right) \quad (3.1)$$

where C is the areal capacitance of the space charge layer, q the elementary charge (1.6×10^{-19} C), ϵ_0 the vacuum permittivity (8.85×10^{-14} Fcm⁻¹), ϵ the dielectric constant of the studied semiconductor, E_{fb} the flat band potential, E the applied external bias, κ Boltzmann's constant, and T the absolute temperature.

The dielectric constant is assumed to be 41 for TiO₂ [281]. The calculated value of N_D in the undoped mesoporous TiO₂ film is 9×10^{19} cm⁻³. Treatment with N₂H₄ caused a decrease in N_D for 5 and 10 hours of treatment (Figure 3.10(c)), but N_D increased to 9.62×10^{19} cm⁻³ in the film treated for 20 hours. Since N₂H₄ is both a strong reducing agent and a nitrogen source, treatment introduces both Ti³⁺ electron donors (tending to increase N_D) [158] and nitrogen atom electron acceptors (tending to decrease N_D) [280, 285]. The balance of the two determined the net change in N_D , and excessive nitrogen doping has been suggested to convert Ti³⁺ to Ti⁴⁺ species [280]. Figure 3.10(c) shows that introduction of acceptors dominates the properties of the 5 h_Ti³⁺-N-TiO₂ and 10 h_Ti³⁺-N-TiO₂ films resulting in lower N_D compared to undoped TiO₂ film. On the other hand, the increase in N_D in the 20 h_Ti³⁺-N-TiO₂ film suggests that prolonged treatment with hydrazine results in a net introduction of more Ti³⁺ compared to nitrogen. Hanzu et al. reported a reduction in N_D from 6.7×10^{20} cm⁻³ in undoped TiO₂ nanotubes to 3.9×10^{20} cm⁻³ upon nitrogen doping [280]. Mao et al. reported that N_D increased from 6.9×10^{18} cm⁻³ in titania nanowires to 8.54×10^{19} cm⁻³ after 24 hours of N₂H₄ treatment [158]. The results found here are

consistent with these two observations if we conclude that nitrogen introduction dominates N_D at short times and titanium reduction takes over the electronic properties of the films at long treatment times.

3.5. Conclusions

Titanium (Ti^{3+}) and nitrogen co-doped cubic ordered mesoporous TiO_2 thin films were prepared by hydrazine treatment and tested for photocatalysis under visible light illumination. The cubic ordered mesoporous TiO_2 thin films were prepared by a surfactant templated sol-gel method followed by hydrazine treatment in a closed vessel to allow long-term exposure to hydrazine from the vapor phase. Both interstitial and substitutional nitrogen were found inside of the doped films whereas no nitrogen was found in the undoped TiO_2 film. XPS and optical characterization suggest that the band gap of TiO_2 films was reduced from 3.5 eV (in undoped TiO_2 films due to their amorphous / nanocrystalline structure) down to a minimum of 3.3 eV after the hydrazine treatment. While this band gap reduction does not bring the primary absorption into the visible wavelength range, enhanced visible light absorption was found in an absorbance tail that extended well into the visible wavelength range, most likely due to the formation of localized absorbers that may function as catalytic sites at the surface of the mesoporous titania.

Photocatalytic degradation tests with methylene blue (MB) demonstrated a significant enhancement in photocatalytic activity of the Ti^{3+} -N- TiO_2 films over undoped TiO_2 films under visible-light illumination. A 455 nm LED was used as a representative visible light source for the experiment because this wavelength is not absorbed by MB. The Ti^{3+} -N- TiO_2 film prepared by 10 hours of hydrazine treatment showed the optimal

photocatalytic performance, with the determined rate coefficient of 0.12 h^{-1} , roughly 3 times greater than that of undoped TiO_2 films. Based on the film thickness, structure and illuminated area, this corresponds to a rate coefficient of $\sim 85 \text{ min}^{-1}/(\text{g catalyst})$. To confirm that the high level of photocatalytic enhancement observed here can be attributed to the use of disordered sol-gel TiO_2 , the effects of increasing calcination temperature and time were observed. Both were found to decrease photocatalytic activity, showing that $350 \text{ }^\circ\text{C}$ and 10 min are the optimum calcination conditions for introducing visible-light photocatalytic activity by hydrazine treatment in these films. The enhancement in photoactivity of the film was confirmed by measuring photoelectrochemical (PEC) water oxidation. The Ti^{3+} -N- TiO_2 films prepared with 10 hours of hydrazine treatment also showed optimal performance in the PEC experiments, roughly four times the photocurrent of undoped TiO_2 films. This study thus demonstrates the effectiveness of hydrazine treatment as a source of Ti^{3+} and N dopant for mesoporous TiO_2 thin films prepared by surfactant templating. Treatment with hydrazine leads to improved photocatalytic and photoelectrochemical performance, but is balanced by gradual coarsening of the titania mesostructure due to exposure to hydrazine and water vapor during treatment.

Figures of Chapter 3

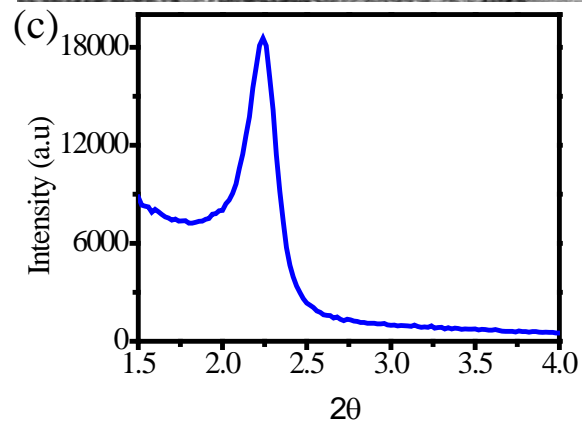
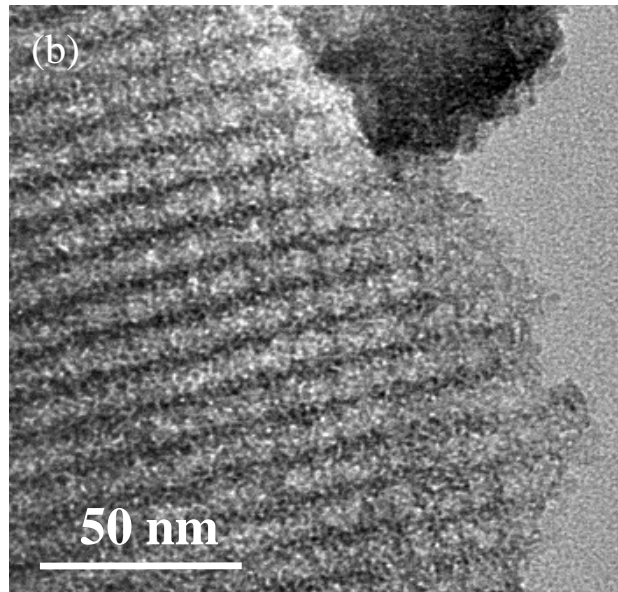
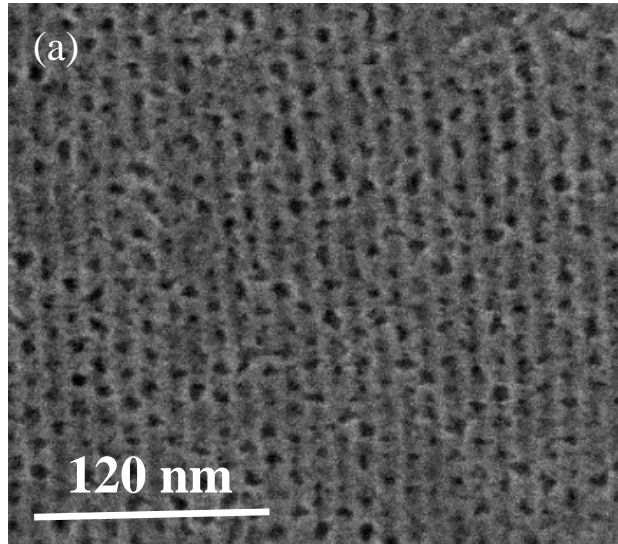


Figure 3.1. Electron micrographs of the F127-templated TiO₂ film after calcination and without hydrazine treatment: (a) SEM image of the top surface, (b) TEM image of material scraped from the glass substrate, and (c) XRD pattern of TiO₂ film on the original substrate.

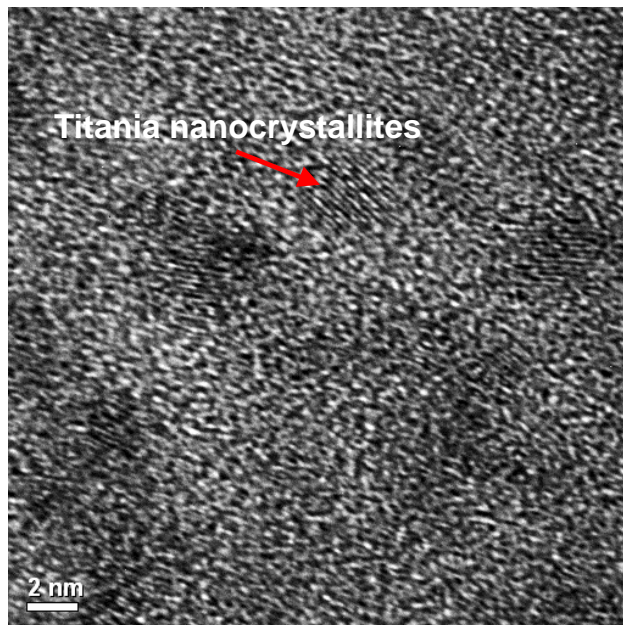


Figure 3.2. HRTEM image of undoped titania film.

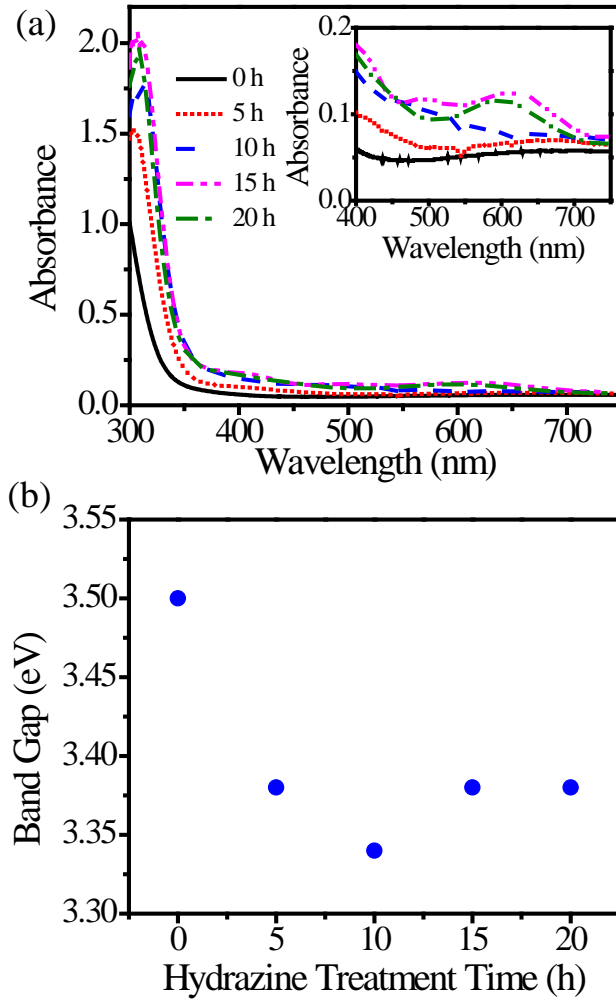


Figure 3.3. (a) UV-vis spectra of undoped TiO₂ and Ti³⁺-N-TiO₂ films prepared using different hydrazine treatment times (the inset shows an enlarged region in the visible wavelength range) and (b) band gap vs. hydrazine treatment time based on Tauc plot analysis.

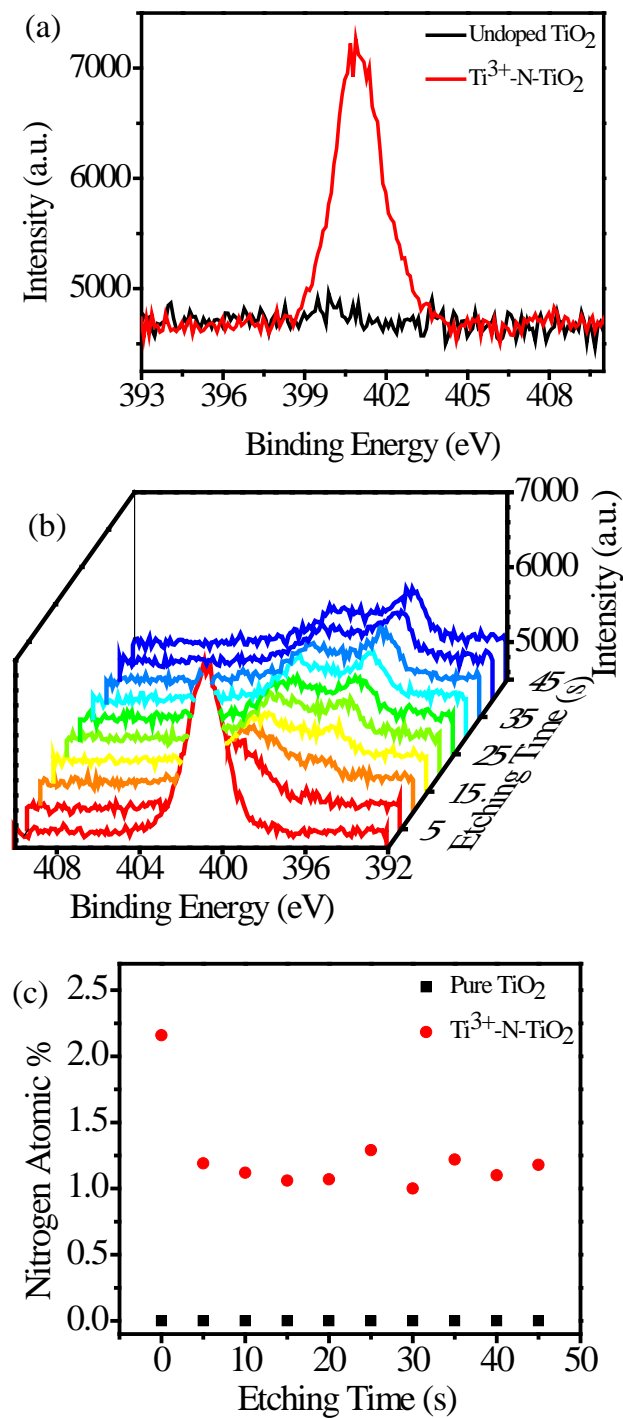


Figure 3.4. (a) High resolution N 1s XPS spectra, (b) XPS N 1s depth profile spectra for 5 h Ti³⁺-N-TiO₂ film, and (c) plot of nitrogen content from XPS depth profile vs. total Ar etching time at 1000 eV power.

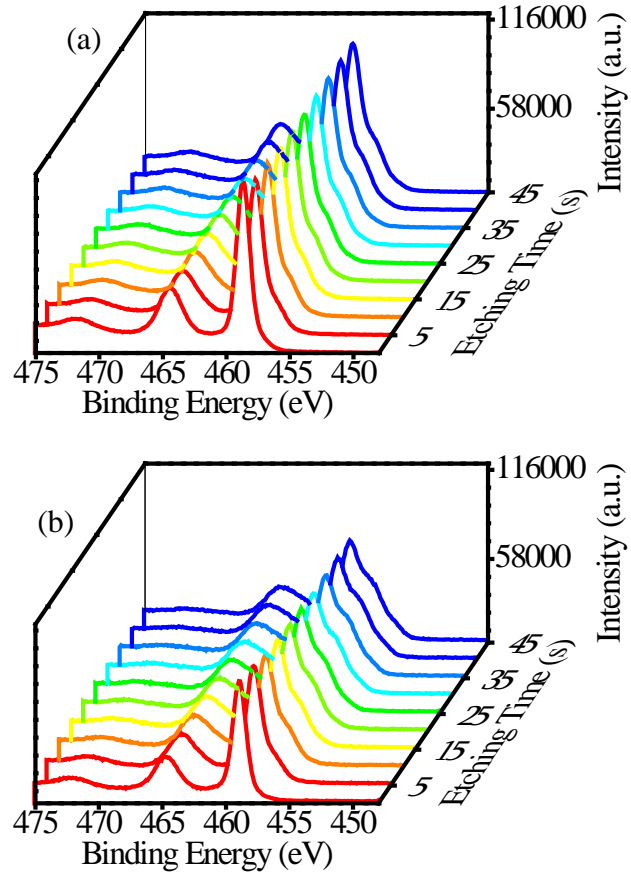


Figure 3.5. XPS Ti 2p depth profile spectra of (a) undoped TiO₂ films and (b) 5 h-Ti³⁺-N-TiO₂ films.

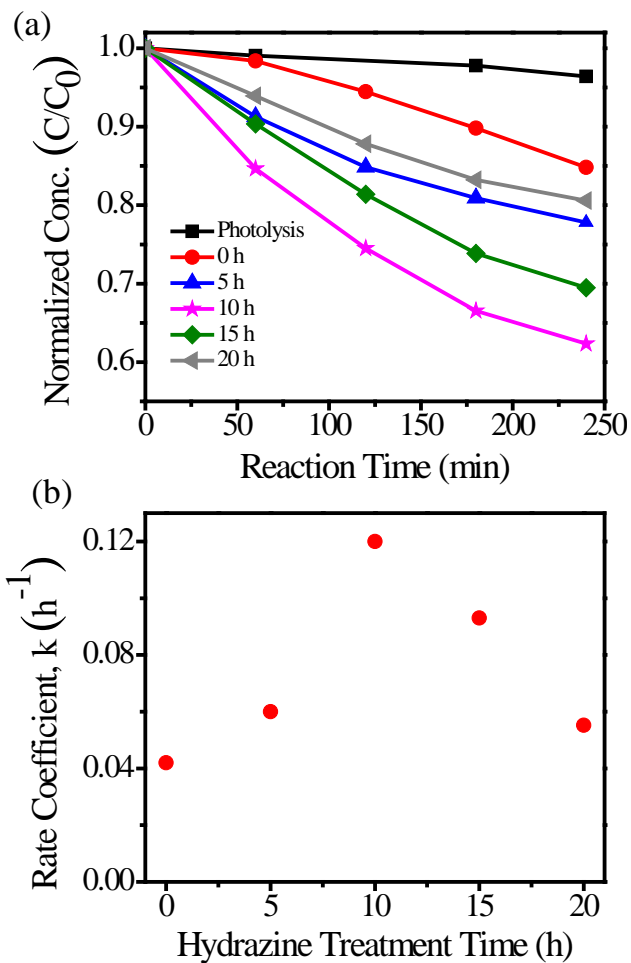


Figure 3.6. Methylene blue degradation kinetics with undoped TiO_2 (0 h) films, Ti^{3+} -N- TiO_2 films, and solution without catalysis (Photolysis): (a) Concentration profile, and (b) pseudo-first order rate coefficient vs. hydrazine treatment time.

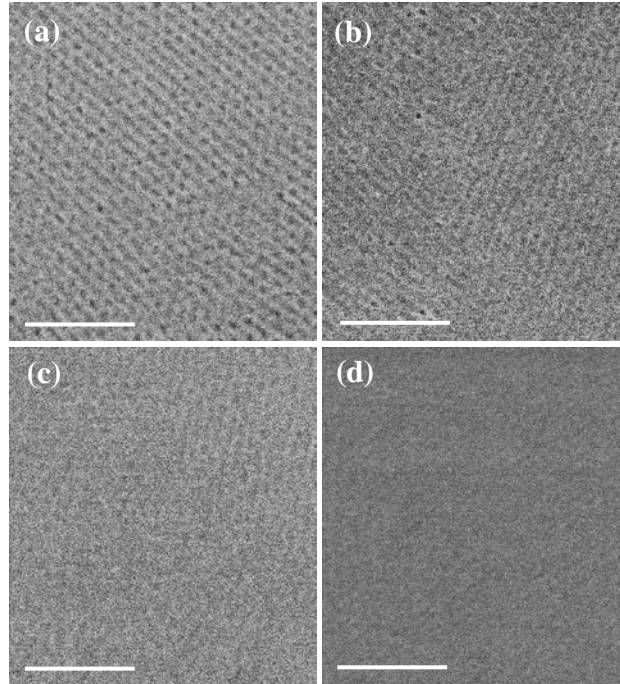


Figure 3.7. Plan view SEM images of (a) undoped TiO₂, (b) 5 h Ti³⁺-N-TiO₂, (c) 10 h Ti³⁺-N-TiO₂, and (d) 20 h Ti³⁺-N-TiO₂ films (Scale bar: 120 nm).

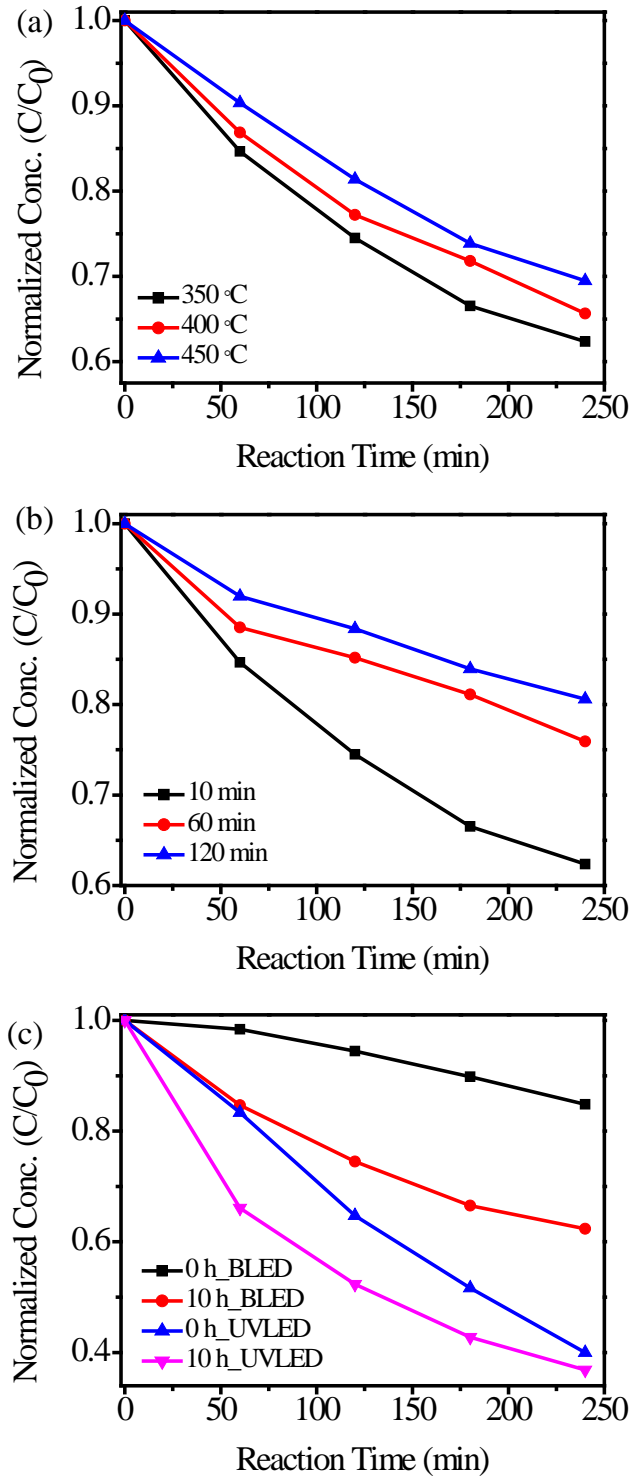


Figure 3.8. Concentration profiles during methylene blue degradation with 10 h Ti^{3+} -N- TiO_2 films showing (a) effect of calcination temperature of titania films, (b) effect of calcination time of titania films and (c) effect of light sources (BLED and UVLED).

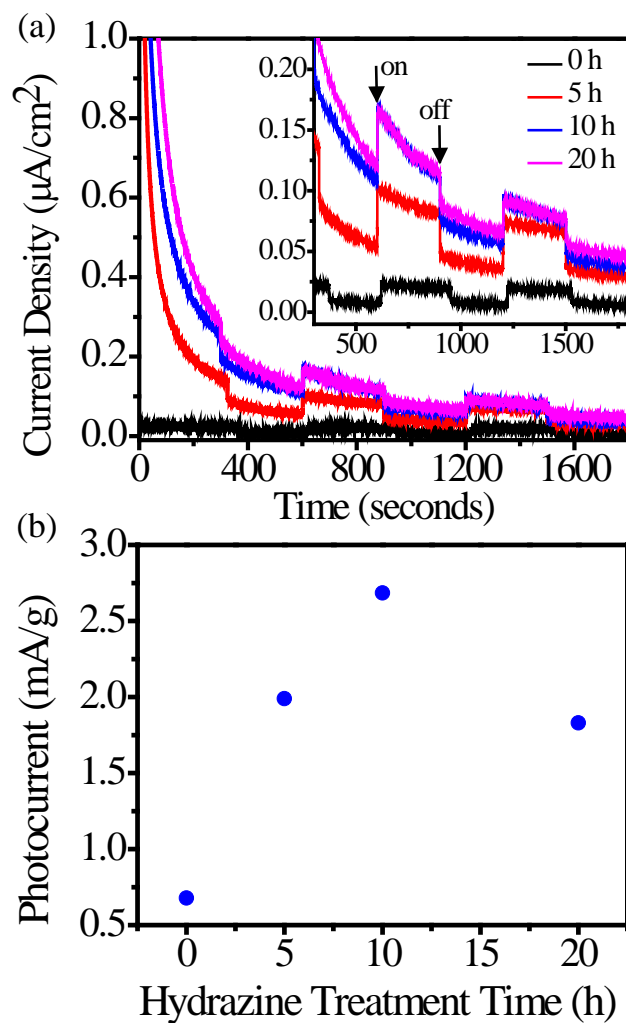


Figure 3.9. (a) Current density as a function of time for the water oxidation reaction with TiO_2 and $\text{Ti}^{3+}\text{-N-TiO}_2$ films (The inset is an expansion of the region from 400 to 1800 s) and (b) Photocurrent per mass of undoped TiO_2 and $\text{Ti}^{3+}\text{-N-TiO}_2$ films at 600 s as a function of hydrazine treatment time.

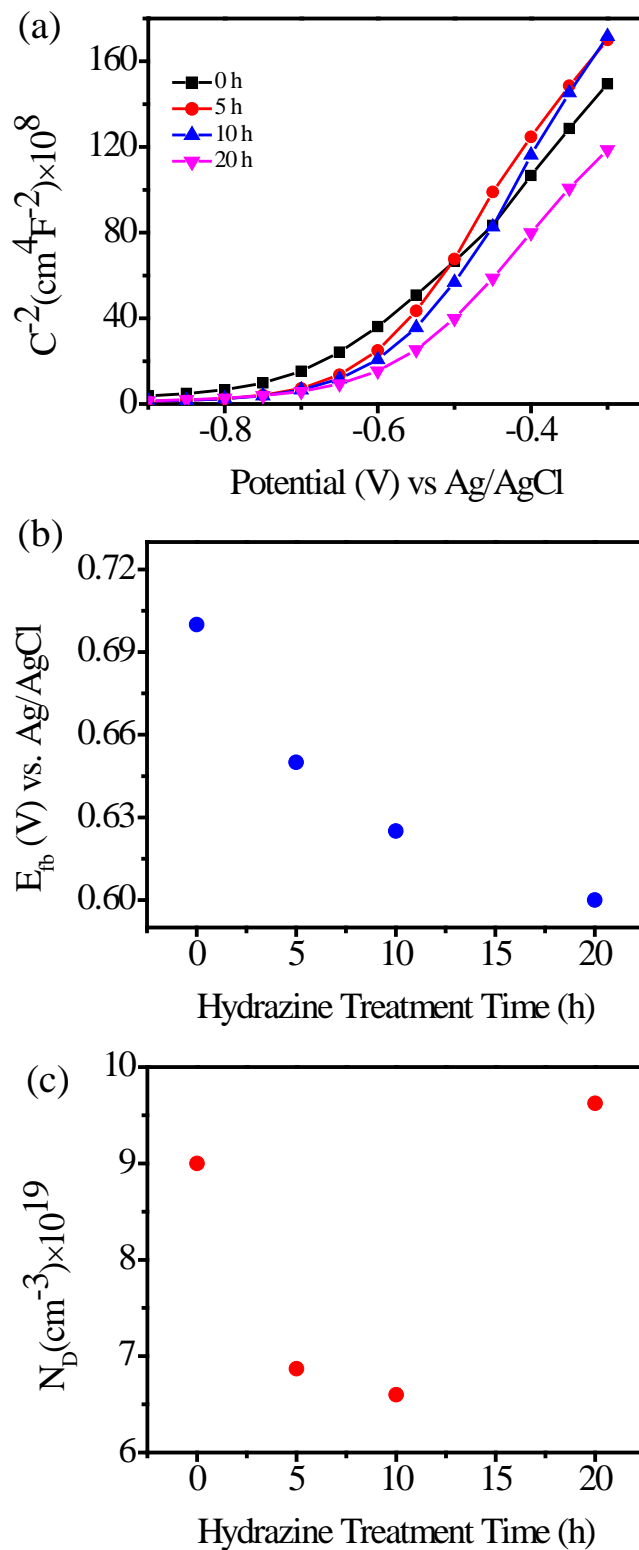


Figure 3.10. (a) Mott-Schottky plots for undoped TiO₂ and Ti³⁺-N-TiO₂ films, and (b) flat band potential and (c) charge carrier density of the films as a function of hydrazine treatment time.

Chapter 4. N₂/Ar Plasma Induced Doping of Ordered Mesoporous TiO₂ Thin Films for Visible Light Active Photocatalysis

Reproduced with permission from Islam, S. Z., Reed, D. A., Kim, D. Y., Rankin, S. E., *Microporous and Mesoporous Materials*, 2016, 220, 120-128.

4.1. Summary

This study reports the rapid and effective nitrogen doping of ordered, mesoporous TiO₂ thin films using nitrogen/argon (N₂/Ar) plasma. The resulting nitrogen-doped TiO₂ (N-TiO₂) films show a significant enhancement in both visible light absorption and photocatalytic activity. The cubic ordered mesoporous TiO₂ thin films are prepared via a sol-gel method using titanium tetrachloride (TiCl₄) as precursor and triblock copolymer Pluronic F127 as the template. Following brief calcination, the TiO₂ films are treated with N₂/Ar plasma under controlled conditions of reactive gas pressure, microwave power, and plasma exposure duration. To vary the degree of nitrogen doping, the plasma exposure time varied from zero up to 210 min. The nitrogen content of the films increases with plasma exposure duration, up to over 3 at% N. X-ray photoelectron spectroscopic (XPS) analyses and UV-vis absorbance spectra of N-TiO₂ films indicate that the incorporated N atoms reduce the band gap of TiO₂ and thus enhance the absorption of visible light. Finally, the visible-light photocatalytic activity of N-TiO₂ films is determined from the photocatalytic degradation of methylene blue under visible-light illumination (with a 455 nm LED). The N-TiO₂ films prepared by 150 min treatment show the optimum photocatalytic activity with a pseudo-first order rate coefficient of 0.24 h⁻¹, which is six times greater than that of undoped TiO₂ films. Treatment for excessive time (e.g. 210 min) leads to a decline in photocatalytic activity due to coarsening of the porous structure. The present study suggests that plasma-induced doping is a promising approach to enable the

efficient incorporation of heteroatoms into surfactant-templated TiO₂ thin films while maintaining their nanostructures, thereby leading to the significant enhancement of visible-light photoactivity.

4.2. Introduction

Since Fujishima first reported H₂ generation by splitting water with a TiO₂ photocatalyst, TiO₂ has attracted much attention due to many advantageous properties including its low cost, high availability, chemical stability, and excellent optoelectronic properties [1-4]. These unique properties have enabled titania to be utilized in a wide range of applications including solar energy conversion, antimicrobial agents, whiteners in paint, ceramics, textiles, personal care products, and catalysts for environmental remediation [4-12].

Despite many attractive features of TiO₂, one critical challenge is the innate inability of TiO₂ to absorb visible light [5]. The wide band gap of TiO₂ allows the absorption of solar light mainly in the ultraviolet (UV) range, which corresponds to only 8% of the whole solar spectrum, while visible light constitutes 47% [3]. To reduce the intrinsic band gap of TiO₂, several strategies have been tested including the incorporation of either metallic (e.g. Fe and Ni) or non-metallic (e.g. C, F, N, S, P and B) atoms into the lattice of TiO₂ host materials [3, 5, 11, 13, 14]. Among these dopants, nitrogen is one of the most effective elements to promote visible light photoactivity [5, 6, 15]. The classic hypothesis for the effect of bulk N-doping is that replacement of oxygen atoms with nitrogen atoms induces the addition of N2p energy states slightly above valence band, leading to a reduction in the band gap, thus enabling TiO₂ to absorb light in the visible range [5].

Until now, various approaches to incorporate nitrogen atoms have been reported, such as doping during film sputtering [16], annealing under ammonia gas [8], ion implantation [17, 18], hydrazine treatment [19, 20], urea treatment [21-23], treatment of sol-gel titania with nitrogen-containing organics [24], electrochemical processing [25], chemical vapor deposition [26], and plasma techniques [7, 9, 15, 27-34]. Among these approaches, plasma-assisted doping has several critical advantages over other methods, such as: (i) effectively incorporating heteroatoms into the TiO₂ host by providing reactive dopant species, and (ii) being conducted at relatively low temperature so that the nanostructure of TiO₂ is maintained.

In addition to the challenging issue associated with the optical absorbance of TiO₂, the morphology and the nanostructure of TiO₂ photocatalysts are important factors to determine their photocatalytic performance. Among many available TiO₂ nanostructures, surfactant-templated mesoporous TiO₂ thin films offer several advantages [6]. First, surfactant templating provides excellent control over the structure and morphology of the films such as tunable pore size, pore orientation, interfacial structure, and pore connectivity, which facilitate the fast diffusion of reactants to the photocatalytic reaction sites of TiO₂ films. Second, the mesoporous structure of the TiO₂ films offers a high reactive surface area available for photocatalysis. Third, the sidewalls of mesoporous TiO₂ films are thin and comparable to the diffusion length of photogenerated holes and electrons, thereby having the potential to suppress charge carrier recombination processes [35, 36].

In the present study, we report for the first time the incorporation of nitrogen into mesoporous TiO₂ films by N₂/Ar plasma treatments. All prior studies of N-doping by plasma treatment used TiO₂ powders, nonporous films, or anodized nanotube arrays [7, 9,

15, 27-34]. However, surfactant templated mesoporous TiO₂ films have several advantages over TiO₂ nanotubes. Mesoporous titania film have smaller pores and thinner pore walls (both on the order of 10 nm or less) than titania nanotubes (22-110 nm pore diameters and 7-34 nm thick walls) which results higher surface areas and lower charge recombination in mesoporous titania films [9, 28, 36]. Moreover, surfactant templated mesoporous titania films can be prepared on any substrate whereas anodized nanotubes can only be prepared on Ti foil or substrates amenable to thin film vapor deposition. Finally, the initial amorphous structure of surfactant-templated TiO₂ films may have photocatalytic advantages based on recent reports that surface defects enhance visible light absorption and charge carrier separation [37, 38], and is expected to enhance the incorporation of plasma-generated nitrogen species. The hypothesis of this work is that by combining the efficient N₂/Ar plasma-induced doping approach with the well-defined high surface area found in surfactant-templated mesoporous TiO₂ thin films, significant enhancement of visible light absorbance and visible light photo-activity will be achieved. To test this hypothesis, cubic ordered mesoporous TiO₂ thin films will be synthesized by templating films derived from TiCl₄ with Pluronic F127. Then, the films will be treated with N₂/Ar plasma generated by a microwave-assisted chemical vapor deposition (CVD) system, followed by analysis of photocatalytic activity for methylene blue degradation as a test reaction. If the hypothesis is correct, the optical absorbance and photocatalytic activity of N-TiO₂ films are expected to be correlated with the duration of N₂/Ar plasma treatments.

4.3. Experimental

4.3.1. Materials

Anhydrous ethanol (200 proof, Pharmco Aaper), F127 (triblock copolymer with average structure $\text{HO}-(\text{CH}_2\text{CH}_2\text{O})_{100}(\text{CH}_2\text{CHCH}_3\text{O})_{65}(\text{CH}_2\text{CH}_2\text{O})_{100}\text{H}$, $M_n = 12,500$ Da, Sigma-Aldrich), titanium tetrachloride (tech grade, Sigma-Aldrich), deionized ultrafiltered (DIUF) water (Fisher Scientific), colloidal graphite (Ted Pella, Inc.), methylene blue hydrate (Sigma Aldrich), Nochromix powder (Fisher Scientific), and concentrated sulfuric acid (Fisher Scientific) were all used as received.

4.3.2. Synthesis of mesoporous titania films

Nochromix solution, prepared according to the directions of the supplier, was used to clean borosilicate glass slides (Fisher Scientific). Sol preparation was begun by preparing a solution of 0.67 g of F127 in ethanol (18.43g). TiCl_4 (1.12 ml) was added to the previously prepared F127 solution in a nitrogen-filled glove bag. The solution was stirred for 10 min to allow for chloride / ethoxy exchange to take place and then 1.8 g of deionized water was added into the solution slowly. The solution was stirred again for 10 minutes. The cleaned glass slides were dip coated using a home built system at a rate of 6 cm/min from this solution to prepare the TiO_2 films, followed by aging in a highly humid environment (RH ~ 94%) in a refrigerator at a temperature of 4 °C for 2 h. The high RH environment was provided by placing the slides in a sealed box with two beakers containing DIUF water. Immediately after aging, TiO_2 films were calcined in a muffle furnace (Vulcan 3-550) for 10 minutes at 350 °C. The temperature of the furnace was increased to 350 °C at a ramp of 25 °C/min and the calcined TiO_2 films were cooled rapidly in air after 10 minutes at the final temperature. Rapid transfer directly from the refrigerator

to the furnace was carried out to avoid moisture condensation on the surface of the films [39].

4.3.3. *N₂/Ar Plasma treatment of mesoporous TiO₂ film*

A microwave-assisted plasma CVD system (Seki Diamond Systems, AX5010) was used for the nitrogen doping of TiO₂ films. The schematic diagram of this plasma system is shown in Figure 4.1. The TiO₂ sample was placed on a Mo sample stage and the chamber was evacuated. Once a base pressure of 60 mTorr was established, the chamber was purged with Ar gas at a flow rate of 100 sccm for 10 min. After 10 min, the pressure was brought to 15 Torr and an Ar plasma was ignited using 300 W microwave power (2.45 GHz). Immediately upon plasma ignition, N₂ gas was introduced at a rate of 40 sccm. The pressure was brought to 60 Torr and the power to 450 W where it remained through the rest of the treatment process. Plasma treatment duration was varied from 30 min to 210 min. After the treatment, the TiO₂ films were cooled in a 250 Torr N₂ atmosphere for 60 min prior to being removed from the chamber. The untreated TiO₂ sample and the TiO₂ samples treated for 30, 50, 70, 90, 150 and 210 min are denoted as undoped TiO₂ and *x* min_N-TiO₂, where *x* is the duration of plasma treatment.

4.3.4. *Characterization*

Thermaogravimetric analysis (TGA) was performed using a TA-SDT-Q600 simultaneous TGA/DSC instrument (TA Instruments). First, the TiO₂ films were dip coated and aged for 2 hours at 4 °C (RH ~ 94 %). Then the aged films were kept in oven at 100 °C overnight to remove solvents and water. Before the measurement, films were scratched from the substrate with a razor blade to generate a powder. TGA measurements were performed at various ramp rates under an air atmosphere. For imaging of the

mesoporous structure, scanning electron microscope (SEM) characterization was performed using a Hitachi S-900 at 6 kV. SEM samples were prepared by cutting the glass slide to the desired shape using a glass cutter and then mounting the sample exactly at the center of a SEM stub coated with carbon tape. The samples were aged at 120 °C overnight (~12 h). A Helios Nanolab 660 (FEI) was used for cross sectional sample preparation and STEM imaging. The thicknesses of the TiO₂ films were measured using a profilometer (Dektak 6M manufactured by Veeco). TEM was performed using an ultra-high resolution JEOL 2200FS. Low angle XRD analysis was performed using a Bruker-AXS D8 Discover diffractometer to determine the degree of mesostructural ordering. Films were scanned at 0.5 °/min in 2 θ increments of 0.02° from 1° to 4°. The optical absorbance of the samples was obtained with an UV-vis absorption spectrometer (Ocean Optics, DT-MINI-2-GS). The measurement was carried out by placing the films at an angle of ~45° relative to the incident beam. X-ray photoelectron spectroscopic (XPS) analysis was conducted using a ThermoScientific K-Alpha photoelectron spectrometer using monochromatic Al K- α radiation with photon energy of 1486.6 eV. Before performing the experiment, the samples were cleaned with ethanol to remove dust from their surface.

4.3.5. Photocatalytic measurement

The photocatalytic activity of the N-TiO₂ film was evaluated by monitoring the photo-degradation of methylene blue (MB). A photograph of the experimental set-up is shown in Appendix A Figure A.1. A blue LED with wavelength of 455 nm (Thorlabs) was used as the light source. The spectrum of the blue LED reproduced from Thorlabs is given in Appendix A Figure A.2b. A cylindrical beaker was used as the reactor. The top of the beaker was covered with parafilm to avoid the evaporation of water. In each experiment,

the solution volume and the initial concentration of MB were 25 ml and 1×10^{-5} M, respectively. The area of mesoporous TiO₂ films illuminated by the light source was ~ 15 cm². The distance between the light source and the reactor was 1 cm. Before illumination, the solution was stirred for 30 minutes in the dark so that MB could be adsorbed onto the pore surface. The solution was continuously stirred using a magnetic stirrer throughout the experiment. The change in MB concentration was determined by periodically taking a 2 mL sample and measuring the optical absorbance at 664 nm using a spectrophotometer (Ocean Optics DT-MINI-2-GS). The sample was returned to the reactor after each measurement.

4.4. Results and discussion

As a first characterization step, TGA measurements were performed to confirm that calcination at 350 °C leads to complete removal of the template. The TGA temperature program consisted of a ramp from 50 °C to 350 °C followed by isothermal heating for 10 min and a second ramp from 350 °C to 450 °C. Two ramp rates (25 °C/min to mimic calcination conditions and a more typical TGA rate of 5 °C/min) were used for two samples. The TGA profiles are presented in Appendix B Figure B.1. Most of the weight loss of the samples occurred near 300 °C and is associated with decomposition of F127. A small amount of additional weight loss was observed during isothermal heating at 350 °C temperature. The weight remaining after isothermal heating at 350 °C for 10 min was 49.7 % for samples heated at both 25 °C/min and 5 °C/min. This suggests that there is no residual carbon due to rapid calcination at 350 °C. Upon heating to higher temperature (350 to 450 °C), a steady loss of mass at a constant rate is observed which is due to loss of water

during coarsening of the TiO₂ films. This same rate of mass loss with heating was observed up to temperatures as high as 1000 °C (data not shown).

The structure and surface morphology of the TiO₂ films after calcination were characterized by SEM as shown in Figure 4.2(a). Nanopores are clearly visible on the top surface of the film. The average pore diameter and wall thickness of the TiO₂ films are around 7 nm and 5.5 nm, respectively. The TEM image in Figure 4.2(b) also clearly shows the presence of pores throughout the film. The arrangement of the pores is consistent with a cubic array of interconnected globular mesopores as reported for these synthesis conditions by Crepaldi et al. [36]. The cross-sectional bright field STEM image (Figure 4.2(c)) also shows that the cubic array of pores extends across the thickness of the films. A variety of globular ordered mesostructured oxides exist ($Im\bar{3}m$, $Fm\bar{3}m$, $Pm\bar{3}n$ and $P63/mmc$) that differ in the packing of their micelle templates, but since $Im\bar{3}m$ cubic is the only reported TiO₂ structure synthesized with F127 [40] and it is consistent with the micrographs, this is assumed to be the mesophase. The film thickness estimated from the cross-sectional STEM image is ~ 80 nm. To investigate the variation of film thicknesses arising from dip coating, the thickness was also measured at four different points in the film by profilometry to be 98 ± 16 nm. This thickness agrees reasonably well with the thickness measured from the STEM image assuming slight contraction due to cross sectioning and imaging. Figure 4.2(d) shows the XRD pattern of the TiO₂ film, which indicates that the mesoporous titania films have an ordered pore structure consistent with the electron micrographs. A single XRD reflection was observed at $2\theta = 2.24^\circ$ which corresponds to a d-spacing value of 3.9 nm. Assuming that the mesostructure is oriented so that the SEM image gives the (110) d-spacing, this peak corresponds to the (420) plane

parallel to the substrate for a body-centered cubic mesophase ($I\bar{m}\bar{3}m$ space group). However, contraction is expected normal to the film during calcination and drying (and is suggested by the appearance of Figure 4.2(c)), so a clear assignment cannot be made from one diffraction peak. In any event, since the pore size found from SEM images is almost three times of the d-spacing, the reflection in Figure 4.2(d) is certainly a higher order XRD diffraction peak, indicating that a well-ordered structure is present. Wide angle XRD was performed to investigate the phase of the mesoporous TiO_2 film. No XRD diffraction peak was observed before or after plasma treatment. This indicates that the mesoporous TiO_2 films are x-ray amorphous (most likely nanocrystalline based on studies of similar films by Das et al. [41]).

Figure 4.3 presents the optical absorbance and the estimated band gap of plasma-treated TiO_2 films. As shown in the inset of Figure 4.3a, the transparent TiO_2 film becomes yellowish after treatment with N_2/Ar plasma, indicating a profound effect on its optical response in the visible range. UV-vis absorbance spectra of N- TiO_2 films revealed the enhancement of absorbance primarily in the range from 350-550 nm, along with enhancement of ultraviolet absorption. The enhancement of visible and UV absorption is consistent with the incorporation of nitrogen atoms into the TiO_2 framework [42]. A closer look at the UV-vis spectra in Figure 4.3a reveals that the tail of absorbance is extended towards longer wavelengths as the duration of plasma treatment increases. In order to determine the band gap of the undoped TiO_2 and N- TiO_2 films, Tauc plots were drawn as shown in Appendix B Figure B.2. To do this, $(\alpha h\nu)^{1/2}$ vs. $h\nu$ was plotted where α is the absorption coefficient and $h\nu$ is the energy of photon. The absorption coefficients were calculated from the absorbance divided by the film thickness. The band gap was estimated

by extrapolating the linear portion of the Tauc plot to the x-axis where the value of $(\alpha h\nu)^{1/2}$ approaches zero [43]. The band gap of the undoped TiO₂ film is 3.5 eV. Generally, the band gap of crystalline anatase titania is 3.2 eV. However, the amorphous / nanocrystalline nature of our TiO₂ films gives a band gap larger than that of anatase TiO₂ [44]. The relation between band gap and plasma treatment duration is shown in Figure 4.3(b) and clearly shows an effect of plasma treatment on the band gap of N-TiO₂. While the band gap of undoped TiO₂ film is 3.5 eV, it decreases with plasma exposure for N-TiO₂ before starting to plateau at ~3.0 eV for the 150 min_N-TiO₂ film. The 90 min_N-TiO₂ film is an outlier from this general trend but still shows a reduced band gap relative to the undoped film. Surprisingly, long term exposure of the film to plasma reduced the visible light absorption of the 210 min_N-TiO₂ film. This may be because long plasma treatment begins to induce coarsening and mesostructure loss which, due to a reduction in interfacial area and growth of crystallites, lead to a loss of catalytic surface sites which act as light absorbers. A negative effect of excessive nitrogen plasma treatment on visible light absorption of TiO₂ was also reported by Jinlong et al. [15]. Compared to other doping methods, our plasma treated N-TiO₂ showed considerably larger reduction of band gap. For example, Selvam et al. prepared N-doped TiO₂ by a wet method using hydrazine hydrate and reported a 0.22 eV band gap reduction [45]. Recently, Siuzdak et al. synthesized N-TiO₂ by an electrochemical method using solutions with different nitrogen sources including amines (diethylenetriamine – DETA, trimethylamine – TEA, and ethylenediamine – EDA) and urea(U). The band gap reductions were found to be 0.4 eV (N-TiO₂-TEA), 0.37 eV (N-TiO₂-DETA), 0.14 eV (N-TiO₂-DETA) and 0.12 eV (N-TiO₂-U) [46].

The elemental compositions and chemical nature of N-doped TiO₂ films vs. undoped TiO₂ film were probed by XPS analyses. Representative survey XPS spectra are presented in Appendix B Figure B.3(a). The high resolution N1s spectra of N-TiO₂ films prepared with different treatment extents are shown in Figure 4.4(a). N-TiO₂ films showed a peak at ca. 397 eV indicating the presence of nitrogen atoms, whereas no peak was detected in undoped TiO₂ films. The peak intensity increased with the duration of plasma treatment. Previous researchers reported that the binding energies of nitrogen in N-TiO₂ are in the range of 396 - 404 eV [6, 43, 47]. Two types of nitrogen atoms were assigned in titania - (i) substitutional nitrogen with a binding energy of 396 eV, and (ii) interstitial nitrogen with a binding energy of 400 eV. The substitutional XPS peak at 396 eV is significant because it indicates Ti-N bonding [48]. Our results are consistent with reported literature that nitrogen plasma treatment induces mainly substitutional nitrogen doping into titania [5, 9, 33]. Asahi et al. reported that substitutional nitrogen is critical for visible light photoactivity of nitrogen doped TiO₂ [5]. The content of nitrogen atoms in N-TiO₂ films determined by XPS analysis is shown in Figure 4.4(b). The content of N atoms generally increases with exposure time and varies from 2-3 at%, up to a maximum content of N of 3.2 at% for the 90 min_N-TiO₂ film. The depth profile of nitrogen atoms in the 90 min_N-TiO₂ film was measured by XPS integrated with Argon ion etching (5 seconds per level in 10 levels using 1000 eV energy). As shown in Figure 4.4(c), the content of nitrogen atoms was uniform throughout the film. This uniformity may result from the mesoporous nature of the sample, which allows rapid diffusion of reactive nitrogen species from the plasma. Compared to other doping methods, our plasma treated N-TiO₂ showed significantly higher nitrogen content. For instance, Li et al. prepared nitrogen doped mesoporous titania

particles by hydrothermal process using ammonia as a nitrogen source. They reported at most 1.31 at.% interstitial nitrogen [49]. Sun et al. reported about 0.2 at.% nitrogen species in N-TiO₂ synthesized using hydrazine hydrate as the nitrogen source [50]. The XPS peaks for Ti 2p orbitals of undoped TiO₂ and 90 min_N-TiO₂ films are presented in Appendix B Figure B.3(b). The Ti 2p_{3/2} XPS peaks are observed at 458.2 eV and 457.7 eV in undoped TiO₂ and 90 min_N-TiO₂ films, respectively. The lowering of binding energy by 0.5 eV after nitrogen plasma treatment is attributed to the different electronic interaction of Ti with nitrogen because of the higher electronegativity of nitrogen compared to oxygen, and is another indication of direct Ti-N interactions [51-54].

Along with core-level study of N-TiO₂ films, the valence band XPS can help in understanding the doping mechanism [54, 55]. The valence band spectra of undoped TiO₂ and N-TiO₂ films are shown in Figure 4.5. The valence band edge for each film was estimated by linear extrapolation of the peaks to the baseline. Both undoped TiO₂ and N-TiO₂ films display typical VB density of state characteristics of TiO₂, with the edge of the maximum energy at about 2.1 eV for undoped TiO₂ [54]. A red shift is observed in the valence band edges with N-doping, which increases as the duration of plasma treatment gets longer. The valence band edge of the 90 min_N-TiO₂ film exhibited the maximum red shift of ~0.75 eV. This shift is consistent with previous reports on nitrogen-doped TiO₂ [55] as well as the band gap results from Tauc analysis (Figure 4.3(b)).

The visible light driven photocatalytic activity of nitrogen-doped TiO₂ films was assessed by monitoring photocatalytic degradation of methylene blue (MB) and compared with that of undoped TiO₂ films. Prior to each photocatalytic measurement, the TiO₂ films were immersed in MB-containing solution for at least 30 min, in order to make sure that

the adsorption of MB onto the surface of mesoporous TiO₂ films became saturated. MB becomes fully adsorbed in 30 min, as shown in the representative long-time adsorption study in Appendix B Figure B.4(a). This confirms that the mesoporous TiO₂ film is exposed to a constant concentration of MB after equilibration. For photocatalytic measurements, the MB-containing solution was exposed to a blue LED light (peak wavelength 455 nm) to measure photocatalytic activity for 4 h. Figure 4.6(a) shows the photocatalytic results normalized using the absorbance at the time that illumination with the LED began, and with the time scale set to zero at the beginning of illumination. The curves clearly show enhanced photocatalytic activity of N-TiO₂ films compared to the undoped TiO₂ film. Insignificant degradation was found without TiO₂ films (direct photolysis of MB). The photocatalytic degradation results of MB with undoped TiO₂ film and N-TiO₂ films clearly showed that the photocatalytic activity of N-TiO₂ gradually increased in proportion to the duration of plasma treatment (from 0 min to 150 min).

The activity of undoped TiO₂ films may seem surprising since the blue LED provides photons with energy below the bandgap, but since MB exhibits minimal absorbance at 455 nm, sensitization by MB is not likely to be the cause. To confirm this, photoelectrochemical water splitting experiments were performed using various light sources for undoped TiO₂ films (prepared according to the procedure above) on FTO-coated glass slides. Not surprisingly, the results (Appendix B Figure B.5) show the greatest photocurrent with a UV (365 nm) LED, followed by a solar simulator. However, the blue (455 nm) LED still exhibits photocurrent. Since no MB or any other dye is present during this experiment, this shows that photocatalytic activity in the undoped TiO₂ films at 455 nm is not a result of MB sensitization. In contrast, lower-energy light from a green (530

nm) LED does not induce any photocurrent in the undoped TiO₂ films. The sub-band gap photoactivity in the undoped films may result from surface defects in the amorphous / nanocrystalline films, which have been demonstrated in recent reports on nanocrystalline rutile and thin nanotubes to result in enhancements in visible-light activity of undoped TiO₂ by reducing the band gap and enhancing charge carrier separation [37, 38].

The kinetics of photocatalytic degradation reaction rates were determined by fitting the decay of MB concentration with the pseudo-first order rate equation: $C=C_0*\exp(-kt)$, where k = the rate coefficient. Appendix B Figure B.4(b) shows that all experiments display very good linear fits between $\ln(C/C_0)$ and t , thus indicating that first order kinetics are appropriate in this case. The rate coefficients are plotted as a function of plasma treatment time in Figure 4.6(b). The rate coefficients increase with increasing plasma treatment until 150 min. This correlates with the increase in nitrogen doping, increase in visible light absorbance, and decrease in band gap found above. The N-TiO₂ films prepared with 150 min plasma treatment showed the maximum rate coefficient of 0.24 h⁻¹, which was nearly 6 times greater than for undoped TiO₂ film. Based on the film thickness (98 nm), structure (body centered cubic pore array with 7 nm pore diameter and 5.5 nm wall thickness, see Appendix B Figure B.6) and illuminated area (15 cm²), an order of magnitude estimate of the specific rate coefficient can be made as ~110 min⁻¹/(g catalyst).

The enhancement of this study greatly surpasses the results reported in the previous study by Liu et al. where only 2-3 times enhancement was observed for TiO₂ nanotubes after the samples were plasma treated [29]. Compared to other doping methods, our plasma treated N-TiO₂ showed significantly higher enhancement in photoactivity. For instance, Siuzdak et al. reported that after 2 h xenon lamp illumination, the degradation of methylene

blue reached 27, 37, 38, 49, and 52% for pure TiO₂, N-TiO₂-TEA, N-TiO₂-EDA, N-TiO₂-U and N-TiO₂-DETA, respectively which represents at most a 2.3× increase in activity (assuming 1st order kinetics) [46]. Selvam et al. prepared N-doped TiO₂ by a wet method using hydrazine hydrate. The N-TiO₂ showed 70 % nitrobenzene conversion (5 h photoirradiation) whereas untreated TiO₂ showed 60 % conversion (6 h photoirradiation) under 365 nm mercury lamp irradiation, which represents a 1.6× increase in activity (assuming 1st order kinetics) [45]. In another study, Li et al. prepared nitrogen doped mesoporous titania particles by a hydrothermal method using ammonia. The N-TiO₂ showed at most a 1.7× improvement in degradation rate of Rhodamine B compared to undoped TiO₂ under 1000 W tungsten halogen bulb illumination with a UV filter [49]. However, it is difficult to compare our results directly with the literature due to the use of different light sources, different intensities and catalyst amounts. For instance, we used a single wavelength LED (455 nm wavelength) whereas most of the literature used a light source of broad spectrum and high intensity. Nevertheless, the maximum relative improvement in rate of MB degradation under comparable visible light illumination found here (6×) exceeds all previous reports of N-doping effects. We propose that the reason for this exceptional enhancement may lie in the use of amorphous / nanocrystalline TiO₂, which readily incorporates substitutional nitrogen and may also be able to easily form highly active surface sites.

While nitrogen plasma treatment helps titania in visible light driven photocatalytic activity, excessive exposure to the plasma negatively affected its photocatalytic performance. For instance, N-TiO₂ films prepared with 210 min treatment showed a rate coefficient of 0.13 h⁻¹, which was much lower than that for the sample prepared with 150

min plasma treatment. The reduced photocatalytic performance of the 210 min_N-TiO₂ film might be due to its lower visible light absorption as previously shown in Figure 4.3(a). In addition, since the reaction rate strongly depends on the available surface area of the film and the network connectivity, the deterioration of porous network might explain the decline in activity with long exposure to plasma. The mesostructure of the N-TiO₂ films was investigated by SEM as shown in Figure 4.7.

No significant structural change was found for 30 min of plasma treatment (Figure 4.7c/d). However, the pore structure was observed to be deteriorated in the films which were treated for 210 min (Figure 4.7e/f). The pores were fused with each other due to the effects of sintering, either because of defects caused by excessive nitrogen doping or because of the temperature reached during plasma exposure. Appendix B Figure B.7 shows more SEM images of varying magnification for 210 min_N-TiO₂ samples taken at different spots on the films. Fast Fourier transforms (FFT) were performed on the SEM images of undoped TiO₂ and 210 min_N-TiO₂ films using ImageJ software as shown in Appendix B Figure B.8. Ordered bright spots for ordered pores are found for the undoped TiO₂ film, whereas the 210 min_N-TiO₂ film shows a more diffuse ring with weak spots. This indicates a loss of long-range pore order in the 210 min_N-TiO₂ film. XRD was performed to further investigate the pore order in the 210 min_N-TiO₂ sample. Appendix B Figure B.9 shows XRD patterns of undoped TiO₂ and 210 min_N-TiO₂ films. No significant peak intensity was observed in the XRD pattern for 210 min_N-TiO₂ film, again showing that excessive plasma treatment of the film leads to a loss of long-range mesopore order.

We estimated the surface area reduction due to plasma treatment using analysis of SEM images with the particle analyzer tool in ImageJ. An image of undoped TiO₂ and

another of 210 min_N-TiO₂ films were used for the analysis. The SEM images before and after image processing by ImageJ are shown in Appendix B Figure B.10, along with details of the method. The calculated specific surface area of the undoped TiO₂ film is 143 m²/g which is consistent with the value (about 150 m²/g) reported by Crepaldi et al. for F127 templated mesoporous titania thin films [36]. The calculated specific surface area of 210 min_N-TiO₂ films is 117 m²/g. Thus, the specific surface area has been reduced by 18 % due to plasma treatment. This surface area reduction, along with the reduction in visible light absorption due to a loss of surface catalytic sites explains the reduction in photocatalytic activity in the 210 min_N-TiO₂ films. Huang et al. also reported the surface area reduction of titania by plasma treatment due to a sintering effect [32]. On the other hand, Ishihara et al. reported that excessive nitrogen plasma treatment causes surface defects in titania nanotubes resulting in lower photocatalytic performance [9]. Based on the UV-vis measurement, SEM results and previous literature, the observed deterioration of photocatalytic activity in 210 min_N-TiO₂ can be attributed to the lower visible light absorption, reduction of active surface area due to the sintering of TiO₂ films or the generation of surface defects causing the recombination of charge carriers. Regardless of the mechanism, the coarsening of the film with longest plasma exposure suggests the possibility for optimization of plasma exposure conditions in the future to balance doping rate with heating and structural changes.

4.5. Conclusions

Nitrogen-doped, cubic ordered mesoporous TiO₂ thin films were successfully prepared by N₂/Argon plasma treatment and tested for photocatalysis under visible light irradiation. Cubic ordered mesoporous TiO₂ thin films were prepared by a surfactant

templated sol-gel method followed by nitrogen plasma treatment. About 2-3 at% substitutional nitrogen was found in the doped films and the nitrogen was found to be uniformly distributed through the depth of the films. XPS and optical characterization results suggest that the band gap of TiO₂ films was reduced from 3.5 eV (in undoped TiO₂ films) down to a minimum of 3.0 eV after the plasma treatment. In addition, enhanced visible light absorption was found in an absorbance tail that extended well into the visible wavelength range. Photocatalytic degradation tests with methylene blue demonstrated a significant enhancement in photocatalytic activity of the N-TiO₂ films over undoped TiO₂ films under visible-light illumination. The N-TiO₂ prepared by 150 min plasma treatment showed the best photocatalytic performance, with the determined rate coefficient of 0.24 h⁻¹, roughly 6 times greater than that of undoped TiO₂ films. This enhancement in photocatalytic activity is qualitatively similar to prior studies of nitrogen doping in nanostructured titania but significantly greater in magnitude than the 2-3 times enhancement reported by Liu et al [29]. The present study shows that, as hypothesized, plasma-induced doping enables the efficient incorporation of heteroatoms into the TiO₂ films while maintaining their mesoporous structure, thereby leading to the significant enhancement of visible-light photoactivity. The coating and plasma based process presented here has many advantages over competing synthetic strategies, as it can be scaled to continuous film production and to deposition of the films onto other substrates for photoelectrocatalytic applications, which will be explored in future reports.

Figures of Chapter 4

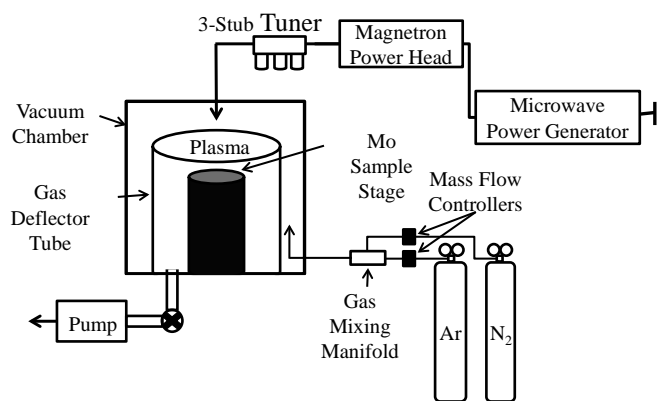


Figure 4.1. Schematic of the plasma reactor used for nitrogen doping of TiO₂ films.

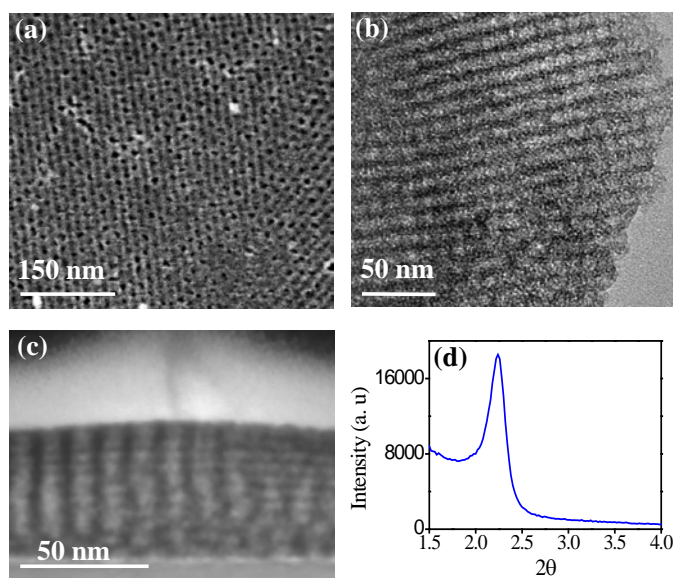


Figure 4.2. Electron micrographs of the F127-templated TiO₂ film after calcination and without plasma treatment: (a) SEM image of the top surface, (b) TEM image of material scraped from the glass substrate, (c) cross sectional bright-field STEM image and (d) XRD pattern of TiO₂ film on the original substrate.

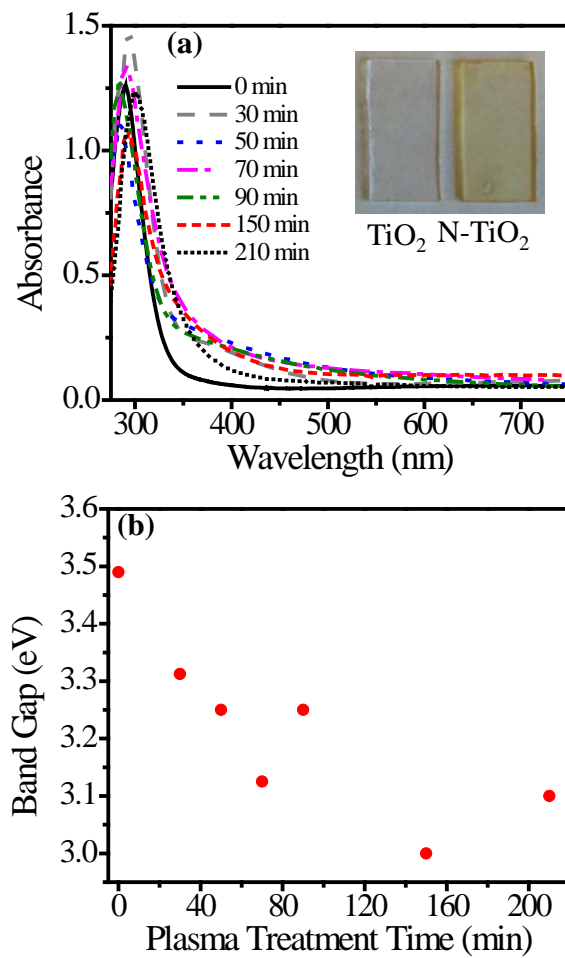


Figure 4.3. (a) UV-vis spectra of undoped TiO₂ and N-TiO₂ films prepared using different plasma treatment time (inset is a photograph of undoped TiO₂ and 30 min_N-TiO₂ film) and (b) Band gap vs. plasma treatment time based on analysis using Tauc plots.

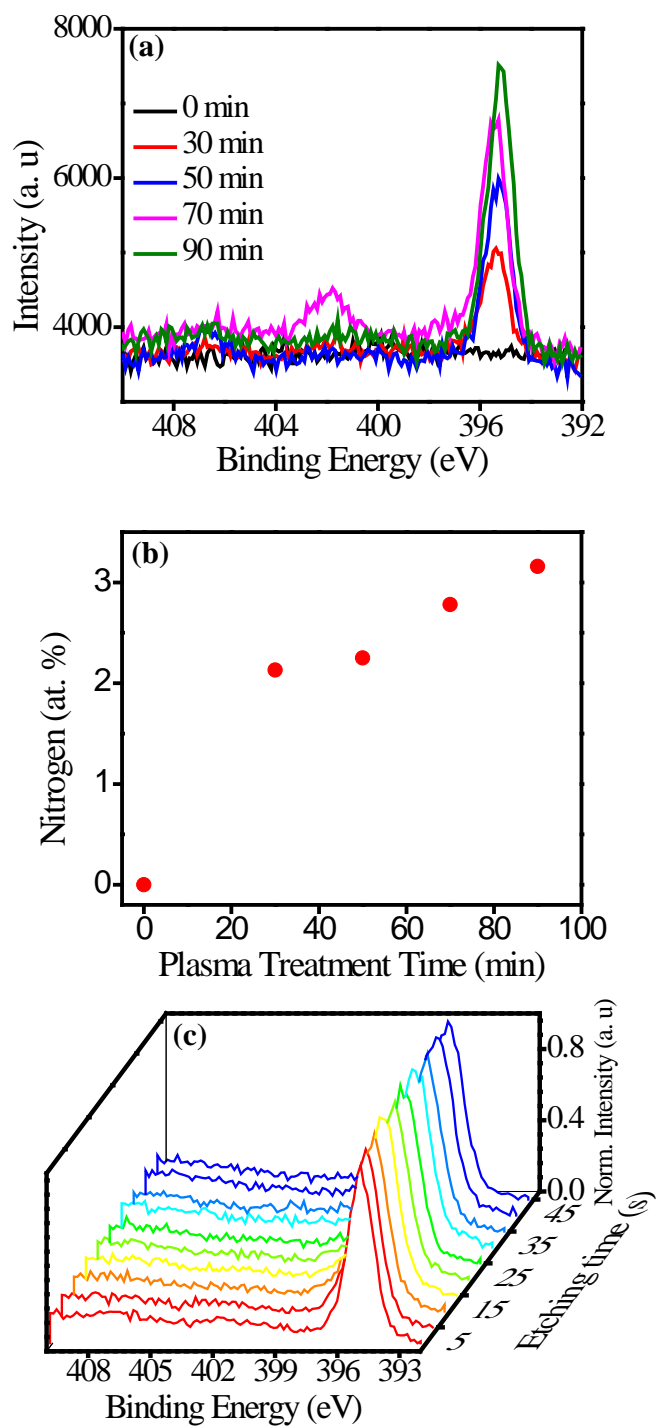


Figure 4.4. (a) High resolution N 1s XPS spectra, (b) plot of surface N content from XPS vs. plasma treatment time, and (c) XPS N 1s depth profile for the 90 min_N-TiO₂ sample.

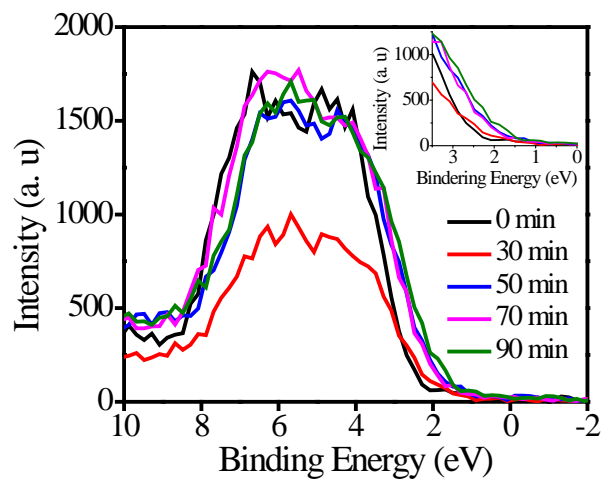


Figure 4.5. Valence band XPS spectra (inset is the enlarged region near the band edge) of undoped TiO₂ and N-TiO₂ films.

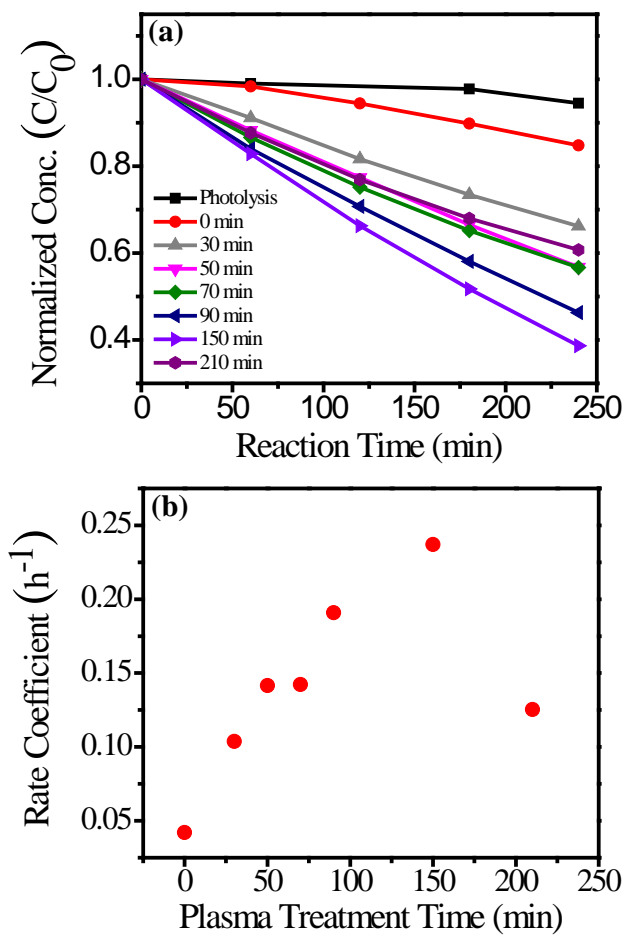


Figure 4.6. Methylene blue degradation reaction with undoped TiO₂ (0 min) film, N-TiO₂ films and without films (Photolysis): (a) Concentration profile (b) the plot of the first-order rate coefficient vs. plasma treatment time.

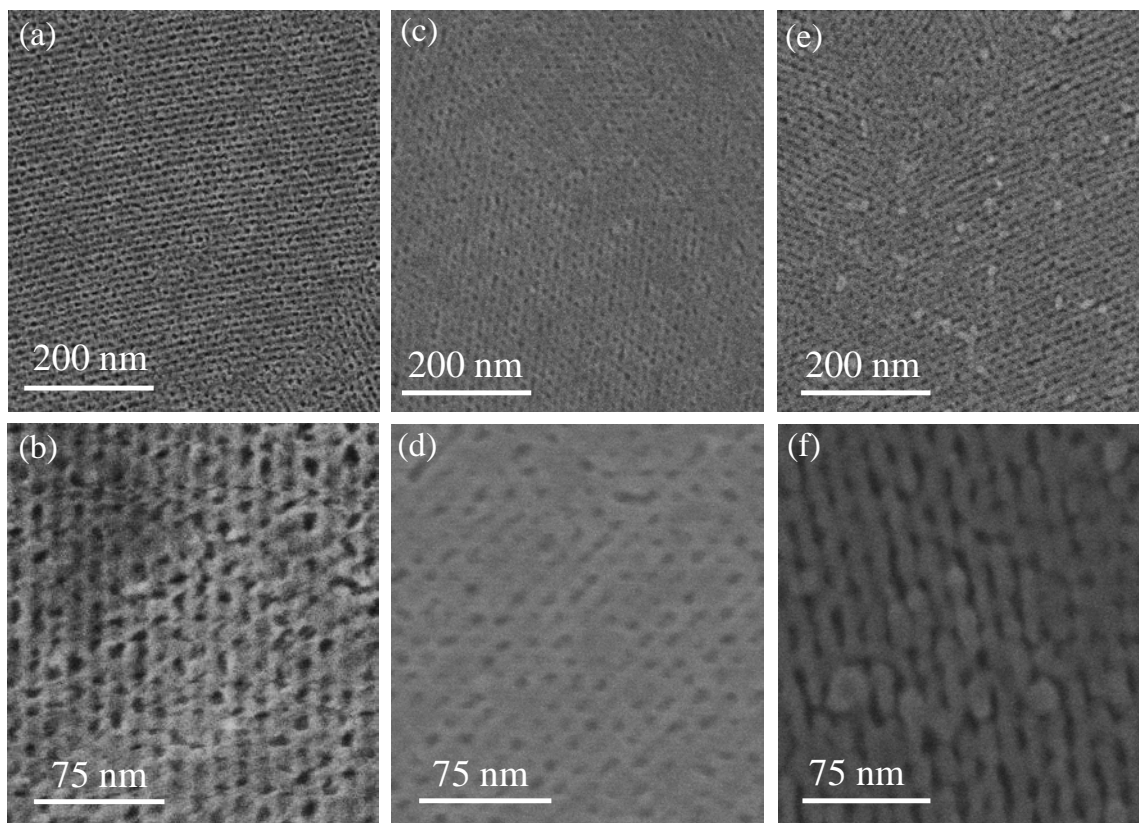


Figure 4.7. SEM images of (a,b) undoped TiO₂, (c, d) 30 min_N-TiO₂ and (e, f) 210 min_N-TiO₂ films.

Chapter 5. Remarkable Enhancement of Photocatalytic Water Oxidation in N₂/Ar Plasma Treated, Mesoporous TiO₂ Films

Reproduced with permission from Islam, S. Z., Reed, A. D., Wanninayake, N., Kim, D. Y., Rankin, S. E., *The Journal of Physical Chemistry C*, 2016, 120(26), 14069–14081.

4.1. Summary

Mesoporous TiO₂ films treated with N₂/argon plasma were studied for ultraviolet and visible light induced photocatalytic water oxidation activity. Compared to pristine TiO₂ films, plasma treated TiO₂ films showed remarkable enhancement of photocurrents (up to 80-240 times) in both ultraviolet light and visible light, greatly surpassing enhancements previously reported in the literature. The cubic ordered mesoporous TiO₂ thin films were prepared by a surfactant-templated sol-gel method and were treated with N₂/argon plasma, an approach hypothesized to capitalize on the high degree of disorder in the material and the high energy of the plasma species to achieve efficient nitrogen doping. The effects of reaction gas pressure and N₂ gas flow rate on photoelectrochemical (PEC) response were investigated. UV-vis absorbance spectra indicated that the incorporated N atoms significantly reduced the band gap of TiO₂ with the enhancement of visible light absorption, and XPS analysis showed primarily substitutional N atoms incorporation rather than interstitial. The photocatalytic activity of nitrogen-doped TiO₂ (N-TiO₂) films was evaluated by chronoamperometry and linear sweep voltammetry. The effect of light sources on PEC performance was explored using UV (365 nm), blue (455 nm) and green (530 nm) LEDs. N-TiO₂ films showed 242x and 240x enhancement of photocurrent, compared to undoped TiO₂ films under UV and blue LED irradiation, respectively. The N-doped films also showed overall enhancement of up to 70x and 92x with a broad spectrum Xe arc lamp and halogen bulb, respectively, and photocatalytic activity even with

green LED illumination, compared to no measurable activity without doping. The present study shows that plasma-induced doping of sol-gel materials enables the efficient incorporation of heteroatoms into disordered metal oxide nanostructures, thereby leading to remarkable enhancement in visible-light driven photoelectrochemical water oxidation.

5.2 Introduction

TiO₂ is one of the most extensively studied semiconductor photocatalysts for H₂ production from water splitting to address the worldwide energy shortage and concerns over climate change due to fossil fuel use.[70, 72] Since the first demonstration of hydrogen generation from the decomposition of water by Fujishima and Honda using a TiO₂ photocatalyst in 1972, titanium dioxide has attracted significant interest as a photocatalyst due to its favorable band edge positions (relative to the redox potential of water), opto-electronic properties which can be varied by changing lattice defects or oxygen stoichiometry, superior chemical stability, photocorrosion resistance, and low cost [13-16].

For the application of TiO₂ in photocatalysis, it is very important to control its morphology, nanostructure, and electronic properties to enhance the available surface area, light absorption, and effective charge carrier separation and transport [18, 30-32]. Surfactant-templated mesoporous TiO₂ thin films possess several advantageous properties that are beneficial for efficient photocatalysis [18, 33, 34]. First, surfactant-induced templating offers excellent control over pore size, pore orientation, interfacial structure and pore connectivity, which in turn allows rapid diffusion of reactants and products within the film. Second, the mesoporous structure of the TiO₂ films presents a high reactive surface area for photocatalysis. Third, the thin pore walls (< 10 nm thick) of mesoporous TiO₂

films provide a short distance for the transport of photogenerated charge carriers to the catalytic sites, which is expected to suppress charge recombination processes [5, 15, 33, 34].

Despite the aforementioned attractive features of TiO₂, due to its wide band gap it only absorbs ultraviolet light, which comprises 5% of the energy in the solar spectrum [72, 277]. To effectively utilize solar energy for water oxidation, its band gap must be tuned to allow visible light to be absorbed. Doping is one of the most feasible potential strategies to tune the band gap of TiO₂ [17, 40-42, 286]. Among various types of dopants (metallic and non-metallic) which have been investigated, nitrogen has been found to be the most effective [17, 18, 50]. Depending on the source and preparation method, nitrogen atoms are known to occupy either interstitial sites (possibly bonded to O) or substitutional sites (replacement of O atoms with N atoms) in titania [51]. Though interstitial nitrogen has been shown to increase visible light absorption, it does not reduce the band gap because it forms a discrete energy state between the valence band and conduction band [54]. Additionally, interstitial nitrogen has been found to be a charge recombination center, thereby reducing the photocatalytic performance of titania [54]. Most of prior theoretical and experimental studies have shown that the predominant active species in nitrogen doped TiO₂ is substitutional nitrogen, which reduces the band gap and increases visible light absorption [17, 51, 54-56]. The reduced band gap is attributed to an upward shift of the edge of valence band due to the hybridization of the N 2p with the O 2p orbitals [17].

Several N-doping methods have been used to date including: film sputtering [154], annealing under ammonia gas [20], ion implantation [155, 156], hydrazine treatment [157, 158], urea treatment [160, 161], treatment of sol-gel titania with nitrogen-containing

organics [162], electrochemical processing [163], and chemical vapor deposition [164]. Plasma treatment is another approach that stands out as a way to effectively incorporate substitutional nitrogen into the titania lattice [19, 21, 50, 165-172]. Moreover, while many of the methods listed above require high temperature or solvent-based treatments, plasma-assisted doping is conducted at relatively low temperature at which the nanostructure of TiO₂ can be maintained.

In our previous study, we demonstrated enhanced photocatalytic activity of mesoporous TiO₂ films by treating them with N₂/argon plasma [69]. The plasma treatment enabled the incorporation of a significant amount of substitutional nitrogen. In addition, the nanostructure of the TiO₂ films was found to be maintained over a significant dose of plasma exposure. Those films showed excellent performance in photocatalytic activity for the degradation of methylene blue under visible light illumination. In the present study, we report even more substantial effects for photocatalytic water oxidation under visible light using mesoporous TiO₂ films treated with N₂/argon plasma.

The hypothesis of the present work is that the efficient N₂/Ar plasma-induced doping approach applied to the ordered porous architecture of surfactant-templated TiO₂ thin films can be tuned to substantially enhance visible light driven water oxidation. While a significant body of literature exists on N-doped TiO₂, the morphology and method of preparation play a determining role in the activity of these materials. Nitrogen doped, ordered mesoporous TiO₂ thin films present a novel high surface area, readily doped platform for water oxidation under visible light that has not yet been investigated. Many prior studies of N-doping by plasma treatment have used anodized TiO₂ nanotube arrays [21, 166, 167]. As suggested in our previous paper,[69] surfactant templated mesoporous

TiO₂ films have several advantages over TiO₂ nanotubes. First, mesoporous titania films have smaller pores and thinner pore walls (both 10 nm or less) than titania nanotubes (22-110 nm pore diameters and 7-34 nm thick walls) which should result in higher surface areas and lower charge recombination.[21, 33, 166] Moreover, surfactant templating is a flexible, scalable approach adaptable to any substrate whereas anodized nanotubes can only be prepared on Ti foil or substrates amenable to thin film vapor deposition. Finally, the initially amorphous structure of surfactant-templated TiO₂ films is expected to enhance the incorporation of plasma-generated nitrogen species, especially substitutional nitrogen which is responsible for band gap reduction and photocatalytic activity. The disordered structure is expected to enhance surface defects, which have been suggested to enhance visible light absorption and charge carrier separation [31, 32].

To test the hypothesis, cubic ordered mesoporous TiO₂ thin films templated with Pluronic F127 were treated with microwave-generated N₂/Ar plasma. The effects of plasma treatment conditions such as gas pressure and nitrogen flow rate on the ultimate photocatalytic performance were studied. Finally, the effects of light sources with different wavelengths on the photocatalytic activity were explored. Photocatalytic activities of plasma-treated TiO₂ mesoporous films were studied by chronoamperometry, linear sweep voltammetry and electrochemical impedance spectroscopy. The results show exceptional improvements in photocatalytic water oxidation under both UV and visible light compared with prior reports due to the amorphous, high surface area nature of the surfactant templated mesoporous titania and suggest that these materials may be a promising platform for “disorder engineering” of photoelectrocatalysis.

5.3 Experimental Section

5.3.1 Materials

Anhydrous ethanol (99.99%, 200 proof, Absolute, Anhydrous, ACS/USP Grade, Pharmco Aaper), F127 (triblock copolymer with average structure HO-(CH₂CH₂O)₁₀₀(CH₂CHCH₃O)₆₅(CH₂CH₂O)₁₀₀H, Mn = 12,500 Da, Sigma-Aldrich), titanium tetrachloride (tech grade, 99.9%, Fisher Scientific), deionized ultrafiltered (DIUF) water (Fisher Scientific), colloidal graphite (Ted Pella, inc.), KOH (ACS reagent grade, 85%, Fisher Scientific), Nochromix powder (Fisher Scientific), concentrated sulfuric acid (Certified ACS Plus, Fisher Scientific), and epoxy adhesive (Loctite hysol 9462 brown two-part epoxy adhesive, R.S. Hughes) were all used as received.

5.3.2. Synthesis of mesoporous titania films

Nochromix solution, prepared according to manufacturer instructions, was used to clean borosilicate glass slides (Fisher Scientific). Sols for film deposition were prepared as described previously. [69] Briefly, 1.12 ml of TiCl₄ was added to a solution of 0.67 g of F127 in 18.43 g of ethanol in a nitrogen-filled glove bag. After stirring for 10 min to allow the chloride / ethoxy exchange to occur, 1.8 g of deionized water was slowly added, and the mixture was stirred for an additional 10 min. The cleaned glass slides were dip coated with this sol using a home built system at a rate of 6 cm/min, followed by aging in a refrigerator at high humidity (RH ~ 94%) and at 4 °C for 2 h. The high RH environment was provided by placing the slides in a sealed box with two beakers containing water. Immediately after aging, TiO₂ films were calcined in a muffle furnace (Vulcan 3-550) for 10 minutes at 350 °C. During heating, the ramp was 25 °C/min but the TiO₂ films were cooled rapidly after calcination back to room temperature. Rapid transfer directly from the

refrigerator to the furnace was carried out to avoid moisture condensation on the surface of the films [272].

5.3.3. *N₂/Ar plasma treatment of mesoporous TiO₂ film*

A microwave-assisted plasma CVD system (Seki Diamond Systems, AX5010) was used for the nitrogen doping of TiO₂ films. The schematic of the plasma system is shown in Figure 5.1. A TiO₂ sample was placed on the molybdenum (Mo) stage and the chamber was evacuated. After reaching a base pressure of 60 mtorr, the chamber was purged with Ar gas flowing at 100 sccm for 10 min. Then, the pressure was raised to 15 torr and Ar plasma was ignited using 300 W microwave power (2.45 GHz). Immediately upon plasma ignition, N₂ gas was introduced, the pressure was brought to a specified value, and the power to 300 watts where it remained through the rest of the treatment process. Pressure in the plasma reactor was varied from 30 torr to 70 torr under constant nitrogen flow of 40 sccm. To explore the effect of nitrogen flow rate, nitrogen flow in the plasma reactor was varied from 40 sccm to 100 sccm at the constant pressure of 70 torr. The microwave power and plasma treatment duration were kept constant at 300 watts and 30 min, respectively. After treatment, the films were cooled in a 250 torr N₂ atmosphere for 60 min prior to being removed from the chamber. The untreated TiO₂ sample and the TiO₂ samples treated for 40, 60, 80 and 100 sccm nitrogen flow in the plasma reactor are denoted as 0 sccm_N-TiO₂ and x sccm_N-TiO₂, respectively, where x is the nitrogen flow rate in sccm.

5.3.4. *Characterization*

Thermogravimetric analysis (TGA) was performed using a TA-SDT-Q600 simultaneous TGA/DSC instrument (TA Instruments). First, the TiO₂ films were dip coated and aged for 2 hours at 4 °C (RH ~ 94 %). Then the aged films were kept in an oven

at 100 °C overnight to remove solvents and water. Before the measurement, films were scratched from the substrate with a razor blade to generate a powder. TGA measurements were performed at various ramp rates in air. The morphology and structure of the TiO₂ films were characterized with a scanning electron microscope (SEM) attached to a dual-beam Helios Nanolab 660 (FEI). The samples for SEM characterizations were prepared by cutting the FTO substrate on which the TiO₂ thin film was coated using a glass cutter and then mounting the sample exactly at the center of a SEM stub coated with carbon tape. A scanning transmission electron microscopic (STEM) image was obtained from the same sample after focused ion beam (FIB) sectioning. High resolution images of powders scraped from the mesoporous TiO₂ films were obtained with a transmission electron microscope (TEM) (JEOL 2200FS). Low angle XRD analysis was carried out using a Bruker-AXS D8 DISCOVER diffractometer to determine the degree of mesostructural order. Films were scanned at 0.5 °/min in 2θ increments of 0.02° from 1° to 4°. The optical absorbance of the samples was measurement with an UV-vis absorption spectrometer (Ocean Optics, DT-MINI-2-GS). The measurement was carried out by placing the films at an angle of ~45° relative to the incident beam to avoid interference fringes in the spectra. X-ray photoelectron spectroscopic (XPS) analysis was conducted using a ThermoScientific K-Alpha photoelectron spectrometer using monochromatic Al K-α radiation with photon energy of 1486.6 eV. Prior to XPS characterization, samples were cleaned with ethanol to remove dust from their surface.

5.3.5. Photoelectrochemical measurements

For photoelectrochemical (PEC) experiments, the films of undoped TiO₂ and N-TiO₂ were prepared on fluorine-doped tin oxide (FTO) coated glass substrates. Prior to dip

coating, FTO slides were cleaned with DIUF water, acetone and isopropanol followed by UV-ozone treatment for 20 minutes to remove any organic contaminants. The photoelectrochemical measurement was carried out to evaluate the performance of N-TiO₂ films for water oxidation. These experiments were conducted in a photoelectrochemical system with an electrochemical cell (home-made glass cell) with three electrodes and a potentiostat (CHI 660D, CH Instruments, Inc.). A TiO₂ film mounted on FTO (either N-doped or undoped), a platinum wire, and a Ag/AgCl electrode were used for working, counter and reference electrodes, respectively. 1M KOH was used as an electrolyte. The area of the TiO₂ films exposed to the electrolyte solution was 2 cm² and the rest of the films was covered by epoxy paste. After adding the epoxy paste on the surface of the TiO₂ films, it was dried for 3 hours at 120 °C in air. Light sources were a Xe arc lamp with AM 1.5 G filter, halogen lamp (ELH Osram, 120 V, 300 W), a UV LED (365 nm, Thorlabs), a blue LED (455 nm, Thorlabs) and a green LED (530 nm, Thorlabs). Power density was recorded by a power energy meter (standard photodiode power sensor, Si, Thorlabs). The power densities of the Xe arc lamp with AM 1.5 G filter and halogen lamp were 100 mW/cm², and the power densities of the UV LED, blue LED (BLED) and green LED (GLED) were 6 mW/cm², 22.5 mW/cm² and 2.5 mW/cm², respectively. The emission spectra of light sources are shown in Appendix C Figure C.1.

Amperometric photocurrent-time (*i-t*) profiles were recorded with undoped TiO₂ and N-TiO₂ films by holding the potential at 0.4 V vs. Ag/AgCl. The light source was turned on and off every 300 seconds periodically to record photo- and dark currents. This experiment was performed for 1800 seconds. Oxygen produced from water oxidation with 100 sccm_N-TiO₂ film during an amperometric measurement under UVLED illumination

was measured using a Neulog oxygen sensor. The sensor measures oxygen in the electrolyte solution. Appendix C Figure C.6 shows the experimental set-up. All of the electrodes, nitrogen flow tubing and the oxygen sensor were dipped into the electrolyte solution in the photoelectrochemical cell. The cell was sealed with parafilm. First, the electrolyte solution was purged with nitrogen gas for 2 hours. Then, the nitrogen tubing was taken out of the electrolyte solution but kept inside the cell. The experiment was conducted with illumination for 2 hours. Then, the nitrogen purging was stopped completely and the nitrogen tubing was taken out the cell. The system with only the electrodes and oxygen sensor was sealed with parafilm, and the experiment was run with UVLED illumination for another 12.5 hours. Linear sweep voltammetric (LSV) measurements were performed from -0.8 V to 0.4 V vs. Ag/AgCl under Xe arc lamp and UVLED, and -0.5 V to 0.4 V vs. Ag/AgCl under BLED and GLED. The scan rate of LSV curves was 5 mV/s. The electrochemical impedance spectroscopy was carried out using the same potentiostat and electrolyte used for other photoelectrochemical measurements. A Mott-Schottky plot was recorded at the frequency of 1 Hz under dark condition in the potential between -1.5 V to -0.3 V vs. Ag/AgCl. Nyquist plots were obtained with and without halogen lamp illumination. The AC frequency was varied from 0.1 Hz to 100 kHz with the DC potential of -0.7 V vs. Ag/AgCl.

5.3.6. Zeta potential (ζ) measurements

The zeta potentials of TiO₂ and N-doped TiO₂ thin films were measured by the streaming potential technique using a SurPASS electrokinetic analyzer (Anton Parr). The undoped TiO₂ and N-doped TiO₂ films were prepared on Ti foils (each 2 cm x 1 cm) and mounted in the sample holder of an adjustable gap cell. 0.01 M KCl was used as electrolyte.

0.05 M HCl and 0.05 M NaOH were used in the automatic titrator to change the pH of the electrolyte solution from 2 to 10. Zeta potential was monitored as a function of pH.

5.3.7. Contact angle measurements

Surface wettability of undoped TiO₂ and N-doped TiO₂ were determined with contact angle goniometer (Ramé-hart Model 100). Prior to the measurement, samples were thoroughly washed with deionized water and vacuum dried for 24 hours. The contact angle was measured by gradually increasing the droplet volume and the maximum value reported as the advancing contact angle.

5.4. Results and Discussion

As a first characterization step, TGA was performed to confirm that calcination at 350 °C leads to complete template removal. The temperature program consisted of a ramp from 50 °C to 350 °C, isothermal heating for 10 min, and a second ramp from 350 °C to 450 °C. Two ramp rates (25 °C/min to mimic calcination conditions and a more typical TGA analysis rate of 5 °C/min) were used for separate samples. The TGA profiles (Appendix B Figure B.2) show that most of the weight loss occurred near 300 °C and is associated with decomposition of F127. A small amount of additional weight loss was observed during isothermal heating at 350 °C but was independent of the ramp rate, indicating no residual carbon due to rapid calcination at 350 °C. Upon heating to higher temperature (350 to 450 °C), mass was lost at a constant rate due to loss of water during coarsening of the TiO₂ films. This same rate of mass loss with heating was observed up to temperatures as high as 1000 °C.

Once the removal of template and formation of mesoporous titania films was confirmed, the effects of plasma treatment were investigated. In a previous study, relatively high plasma power (450 W) was used [69], but because of concerns about the stability of the FTO conducting layer in the current photoelectrochemical study, the effects of using a lower power (300 W) and treatment time (30 min) with varying pressure and gas flowrate were observed here. As can be seen in the inset of Figure 5.2, the transparent undoped TiO₂ films turned yellow after N₂/Ar plasma treatment at 70 torr and varying flowrate, indicating the impact of nitrogen doping on its visible light absorption. UV-visible absorbance showed that the treatment with N₂/Ar plasma is accompanied by the red shift in the spectral peak, as well as a significant increase of visible light absorption as shown in Figure 5.2. The change in absorption spectra is consistent with the color change of the film from colorless to yellow. This is attributed to new electronic energy states formed by nitrogen incorporation in the film. The visible light absorption increases with the nitrogen gas flow rate from 40 sccm to 60 sccm. However, the yellow color faded to some extent in 80 sccm_N-TiO₂ and 100 sccm_N-TiO₂ films resulting in slightly lower visible light absorption. On the other hand, the 100 sccm_N-TiO₂ film showed much higher absorption in the UV region. This may be because high nitrogen flow plasma treatment begins to induce changes in the atomic-scale ordering of the framework of the material, which may be associated with coarsening of the mesoporous structure and a decrease in the ability of the material to incorporate nitrogen (see below). A negative effect of excessive nitrogen plasma treatment on visible light absorption of TiO₂ was also reported by Jinlong et al [50].

The band gaps of undoped TiO₂ and N-TiO₂ films were estimated using Tauc plots (Appendix C Figure C.2). To do this, $(\alpha hv)^{1/2}$ vs. hv was plotted where α is the absorption coefficient and hv is the photon energy. The absorption coefficient was calculated from the absorbance divided by the film thickness. The band gap was estimated by extrapolating the linear portion of the Tauc plot to the x-axis where the value of $(\alpha hv)^{1/2}$ approaches zero [274]. The band gaps of 0 sccm_N-TiO₂, 40 sccm_N-TiO₂, 80 sccm_N-TiO₂ and 100 sccm_N-TiO₂ films are 3.5 eV, 2.95 eV, 2.95 eV and 2.88 eV, respectively. Since the Tauc plot for 60 sccm_N-TiO₂ film did not show a clear linear portion, the band gap could not be estimated. Generally, the band gap of crystalline anatase titania is 3.2 eV. However, amorphous TiO₂ films are known to have a band gap larger than that of anatase TiO₂, closer to 3.5 [30]. Overall, the N₂/Ar plasma treatment significantly reduced the bandgap from 3.5 eV to 2.88 eV, without a strong dependence on the N₂/Ar flow rate. In addition, the plasma treatment may introduce rich surface defects which are catalytically active, in contrast to bulk defect sites. Compared to other doping methods, our plasma treated N-TiO₂ showed considerably larger reduction of band gap. Previously reported band gap reductions in N-doped TiO₂ was 0.22 eV with hydrazine hydrate treatment,[269] and with various organic nitrogen sources were 0.4 eV (with triethylamine), 0.37 eV (with diethylenetriamine), 0.14 eV (with ethylenediamine) and 0.12 eV (with urea) [287].

XPS was carried out on undoped TiO₂, 40 sccm_N-TiO₂, 60 sccm_N-TiO₂, 80 sccm_N-TiO₂ and 100 sccm_N-TiO₂ films. Measurement was conducted at three points on each sample. Representative survey XPS spectra are presented in Appendix C Figure C.3a, and representative high-resolution spectra for N1s are presented in Figure 5.3a. All films showed a peak at about 395 eV due to substitutional nitrogen. The composition of nitrogen

was calculated based on XPS high resolution spectra of nitrogen, titanium and oxygen. The small peaks at about 402 eV and 407 eV for adsorbed N₂ were not considered in the composition analysis. Figure 5.3b shows the measured nitrogen content in N-TiO₂ films as a function of nitrogen flow rate in the plasma reactor. The average composition increases with nitrogen gas flow rate until 80 sccm. The maximum nitrogen content was about 5.5 at% for this sample. Further increasing the gas flow to 100 sccm, the nitrogen composition in the titania film decreased to about 3.5 at %. As noted above, the decrease might be due to atomic structure changes such as crystallization beginning with a more intense plasma treatment. Although none of the films exhibit x-ray diffraction (see below), nanocrystal formation during plasma treatment might expel some of the nitrogen in TiO₂ films leading to a lower nitrogen content in the 100 sccm_N-TiO₂ film. Compared to other doping methods, our plasma treated N-TiO₂ showed significantly higher nitrogen content. At most 1.31 at % interstitial (not substitutional) nitrogen was reported using hydrothermal ammonia treatment [183], and about 0.2 at % nitrogen species in hydrazine hydrate treated titania [188].

The depth profile of nitrogen in the 100 sccm_N-TiO₂ film was measured by XPS integrated with Argon ion etching (5 seconds per level in 20 levels using 1000 eV energy). As shown in Figure 5.3c, the content of nitrogen atoms was uniform throughout the film. This uniformity may result from the mesoporous nature of the sample, which allows rapid diffusion of reactive nitrogen species from the plasma. The XPS peaks for Ti 2p orbitals of undoped TiO₂ and N-TiO₂ films are presented in Figure 5.3d. The undoped TiO₂ exhibited Ti 2p binding energies of 457.98 eV and 463.78 eV, attributed to Ti 2p_{3/2} and Ti 2p_{1/2}, respectively. The peak positions shift to lower energies with increase in nitrogen flow

until reaching 457.48 eV for Ti 2p_{3/2} and 463.18 eV for Ti 2p_{1/2} in the 100 sccm_N-TiO₂ films. The lowering of binding energy by 0.5 - 0.6 eV after nitrogen plasma treatment is attributed to the different electronic interaction of Ti with nitrogen because of the lower electronegativity of nitrogen compared to oxygen, and is another indication of direct Ti-N interactions [267, 288, 289]. The doped films also showed a shoulder at about 456.5 eV binding energy which is associated with the Ti³⁺ state formed during plasma treatment [157]. The shoulder intensity is almost same for all the doped films. Appendix C Figure C.3b shows the XPS spectra in the Ti 2p range during 1000 eV Ar etching depth profiling of 100 sccm_N-TiO₂ films. It shows that the shoulder intensity at about 456.5 eV increases with the depth of the film, indicating that more Ti³⁺ is formed inside the film.

Along with the core-level study of N-TiO₂ films, valence band XPS provides insight into the doping mechanism [217, 277]. The valence band spectra of undoped TiO₂ and N-TiO₂ films are shown in Figure 5.4. The valence band edge for each film was estimated by linear extrapolation of the peaks to the baseline. Both undoped TiO₂ and N-TiO₂ films display typical VB density of state characteristics of TiO₂, with the edge of maximum energy at about 2.4 eV for undoped TiO₂ [217]. A red shift is observed in the valence band edges with N-doping. The valence band edge of all the N-TiO₂ film exhibited about the same red shift of ~0.8 eV. This shift is consistent with previous reports on nitrogen-doped TiO₂ [277] as well as the band gap results from Tauc analysis (Appendix C Figure C.2). Though the band gap was reduced significantly in the 40 sccm_N-TiO₂ film, it did not change with increasing nitrogen gas flow. Localized mid-gap states might be formed in the doped films treated with higher nitrogen gas flow rates, and specific surface

sites could be generated representing catalytically active arrangements of Ti, N and O. These would explain changes in absorbance not reflected in the band gap itself.

The morphology and nanostructure of undoped TiO₂ film were characterized by SEM, TEM, STEM and XRD as shown in Appendix C Figure 4.2. Accessible interconnected cubic ordered pores were obtained in the film. The film thickness is about 80 nm as determined from STEM images. The average pore diameter and wall thickness of the TiO₂ films are around 7 nm and 5.5 nm, respectively. The details of the nanostructure characterizations were described in the previous report by Islam et al [69]. Wide angle XRD was performed to investigate the phase of the mesoporous TiO₂ film, but no clear reflections were observed before or after plasma treatment. This indicates that the mesoporous TiO₂ films are x-ray amorphous (but most likely nanocrystalline[150]).

The effect of N₂/Ar plasma treatment on the nanostructure of the N-TiO₂ films was investigated by SEM as shown in Figure 5.5. No significant structural change was found in 40 sccm_N-TiO₂ films (Figure 5.5b). However, the pore structure was observed to deteriorate slightly in the films which were treated with 60 sccm nitrogen flow (Figure 5.5c). The structural deterioration increased with nitrogen flow (Figure 5.5d and Figure 5.5e). In addition, the surface of the doped films became rougher compared to undoped TiO₂ films. The pores were fused with each other by sintering, either because of the effects of excessive nitrogen doping or because of the temperature reached during plasma exposure. Huang et al. also reported surface area reduction of titania by plasma treatment due to sintering.[170] On the other hand, Ishihara et al. reported that excessive nitrogen plasma treatment causes surface defects in titania nanotubes.[21] Despite the coarsening of

the structure, accessible pores are still present in all samples, so they are likely to still be able to participate in photoelectrochemical reactions (see below).

Zeta-potential measurements were conducted to investigate the change in surface charge after N₂/Ar plasma treatment. Figure 5.6 illustrates the surface zeta potential measurements for undoped TiO₂ and 100 sccm_N-TiO₂ thin films. N-doped TiO₂ showed an increased negative zeta potential compared to undoped TiO₂. The surface charge of undoped TiO₂ is mainly governed by bridging and terminal hydroxyl (OH) groups. It has been reported that the bridging Ti-OH-Ti groups are acidic (pK_a 2.9) and the terminal Ti-OH groups are basic (pK_a 12.7) [290, 291]. Therefore, the isoelectric point (IEP) of undoped TiO₂ mainly depends on the relative density of bridging and terminal OH groups. The synthesis method influences the relative amounts of these OH groups, so IEP values have been reported in the literature for anatase TiO₂ ranging from 5.1 to 6.7 [291]. In this study, undoped TiO₂ showed an IEP of 4.9; this value is close to the literature reported IEP range [292][291]. In N-doped TiO₂, the IEP was shifted to 2.5, indicating that the surface became more negative than for undoped TiO₂. These results suggest higher acidity of N-doped TiO₂. Based on our XPS data, substitutional N-atoms predominate in N-doped TiO₂. Therefore, the predicted surface structures for undoped and N-doped TiO₂ can be illustrated as in Appendix C Figure C.4 [291]. The higher N-TiO₂ surface acidity originates from the imbalance in electronegativity of oxygen compared to substitutional nitrogen. Since oxygen (3.5) is more electronegative than nitrogen (3.0), the oxygens in terminal OH groups would be expected to draw electrons away from neighboring NH groups, thus weakening the N-H bond and generating higher surface acidity [293]. This not only explains the observed zeta potential results, but also suggests that water molecules should

have a stronger dipole interaction with N-doped TiO₂ than undoped TiO₂. This was investigated by surface wettability measurements.

The surface wettability is expected to play an important role in photocatalytic water oxidation activity. Therefore, it was probed by the water contact angle measurements. The contact angles measured for undoped and N-doped TiO₂ are 60° and 11°, confirming the higher hydrophilicity of N-doped TiO₂ (Appendix Table C.1). This hydrophilicity helps to keep the water molecules closer to the catalytic surface and facilitates efficient electron transfer at the electrode-electrolyte interface [19].

Amperometric i-t curves were recorded to evaluate the water oxidation performance of the undoped and plasma-treated films. A halogen lamp was used as the light source which was chosen to approximate the solar spectrum. The effect of plasma treatment parameters such as gas pressure (in torr) and N₂ flow rate (in sccm) on the water oxidation performance was explored. As shown in Figure 5.7, all films treated with N₂/Ar plasma showed a significant enhancement of photocurrent compared to the undoped TiO₂ film. In Figure 5.7a, the photocurrent was progressively enhanced with the increase of gas pressure from 30 to 70 torr, indicating more efficient N incorporation at high gas pressure. At pressures higher than 70 torr, the plasma was unstable and therefore could not be used for doping. The N-TiO₂ films prepared at 70 torr showed the maximum photocurrent. The enhancement of photocurrent prepared at 70 torr is about 20 times compared to the undoped TiO₂ film, and this pressure was used for the preparation of the rest of the samples.

Subsequently, the effect of nitrogen source gas flow rate on the photocatalytic activity was investigated. The nitrogen flow rate was varied from 0 sccm to 100 sccm. The flow rate of >100 sccm wasn't able to be assessed due to the limitation of the reactor

system. The gas pressure was kept at 70 torr. As seen in Figure 5.7b, the photocatalytic activity was gradually enhanced with the increasing flow rate. The 100 sccm_N-TiO₂ film showed the maximum photocurrent density, 1.84 $\mu\text{A}/\text{cm}^2$. This is equivalent to 0.08035 A/g based upon the estimated mass per area of the film, $2.29 \times 10^{-5} \text{ g}/\text{cm}^2$, calculated using the film thickness of 80 nm, pore diameter, and wall thickness from SEM images. The photocurrent enhancement for 100 sccm_N-TiO₂ film is about 92 times compared to undoped TiO₂ films.

In order to achieve the aim of efficiently utilizing the whole solar spectrum, it is important to evaluate photocatalytic activity under visible light as well as UV light. In an effort to evaluate photoactivity throughout the spectrum, amperometric i-t measurements were carried out using four different light sources (Xe arc lamp with AM 1.5 G filter, UVLED, BLED, and GLED). Figure 5.8a-d shows the amperometric i-t curves of undoped TiO₂ and 100 sccm_N-TiO₂ films under illumination with these four sources. The photocurrent densities under Xe arc lamp with AM 1.5 G filter, UVLED, BLED and GLED for 100 sccm_N-TiO₂ were 29.6 $\mu\text{A}/\text{cm}^2$, 230.45 $\mu\text{A}/\text{cm}^2$, 3.8 $\mu\text{A}/\text{cm}^2$, and 0.15 $\mu\text{A}/\text{cm}^2$, respectively. This is equivalent to 1.29 A/g, 10.06 A/g, 0.165 A/g and 0.007 A/g for Xe arc lamp, UVLED, BLED and GLED, respectively. The photocurrent enhancement of 100 sccm_TiO₂ compared to undoped TiO₂ was 70 times under Xe arc lamp and 242 times under UVLED while it was *240 times* for BLED. Also notable is that under GLED, no apparent photocurrent was observed for the undoped TiO₂ film, while significant photocurrent density was observed after plasma treatment and doping. The photocurrent obtained under Xe arc lamp is much higher than the photocurrent obtained with a halogen

bulb because of spectral difference between the two light sources in the 350 to 500 nm wavelength range, as shown in Appendix C Figure C.1a.

The long-term stability of the 100 sccm_N-TiO₂ thin film in photoelectrochemical water oxidation was evaluated by amperometric measurement under UVLED illumination for 5 hours. The amperometric current-time profile is presented in Appendix C Figure C.5. The film showed stable photocurrent throughout the measurement without any significant photocurrent reduction. The charge produced by the film over the course of the experiment is several orders of magnitude larger than would be associated with oxidation of the nitrogen in the film.

The photocurrent comes from water oxidation to produce oxygen gas. When light is absorbed by the titania films, electrons are excited from the valence band to the conduction band and simultaneously holes are formed in the valence band. Those holes oxidize water to produce oxygen gas. The evolution of oxygen was confirmed using an oxygen sensor to follow the concentration of oxygen in the electrolyte solution. Appendix C Figure C.7 shows the oxygen gas bubbles formed during photoelectrochemical water oxidation on the surface of the 100 sccm_N-TiO₂ film under UVLED illumination. Appendix C Figure C.8 shows the concentration profile of the dissolved oxygen gas produced from photoelectrochemical water oxidation. After purging the electrolyte solution for 2 hours with flowing nitrogen, the initial concentration of oxygen was 0.13 mg/l. After this initial solution purge, the nitrogen tube was removed from the solution and pulled into the headspace of the cell to blanket the solution with nitrogen during the photoelectrochemical reaction. After 2 hours of water oxidation, the oxygen concentration increased steadily to 0.28 mg/l. Then, the nitrogen tube was removed and the cell was

sealed with parafilm completely. During the nitrogen tube withdrawal, the oxygen concentration decreased to 0.23 mg/l, but the oxygen concentration then increased again with time until reaching 0.42 mg/l after 12 hours of reaction. The concentration remained at this plateau value until 14.5 hours of reaction. This indicates that the electrolyte solution became saturated with oxygen gas after 12 hours of the water oxidation. Hence, Appendix C Figure C. confirms that the photocurrent obtained from amperometric and linear sweep voltammetry with the 100 sccm_N-TiO₂ film results from photoelectrochemical water oxidation to produce oxygen.

In addition to chronoamperometric curves recorded at fixed potential (0.4 V vs. Ag/AgCl), linear sweep voltammetric (LSV) curves were recorded with undoped TiO₂ and 100 sccm_N-TiO₂. The LSV curves were recorded with chopping the light from a Xe arc lamp, UVLED, BLED and GLED as presented in Figure 5.9a-5.9d, respectively. Photocurrents increase with applied potential. The photocurrent enhancement determined at 0.35 V vs. Ag/AgCl under Xe arc lamp, UVLED and BLED are 55, 276 and 220 times, respectively. Since undoped TiO₂ film did not show any photoresponse under GLED, the enhancement could not be determined. The photoresponse in the LSV curves is consistent with the results of the chronoamperometric measurements (Figure 5.8). This photoelectrochemical enhancement significantly exceeds the values reported in prior literature. Sharma et al. and Ishihara et al. prepared plasma-treated nitrogen doped TiO₂ nanotubes and found 2 times enhancement of water oxidation photocurrent compared to undoped TiO₂ nanotubes under a solar simulator [21, 166]. Liu et al. also showed less than 2 times photocurrent enhancement in water oxidation under a 350 W Xe lamp for plasma treated N-TiO₂ nanotubes compared to undoped TiO₂ nanotubes [167]. Compared to other

doping methods, our plasma treated N-TiO₂ also shows significantly higher enhancement in photoactivity. For instance, Babu et al. prepared N-TiO₂ using urea as nitrogen precursor and found 7× photocurrent enhancement in photoelectrochemical water oxidation using a solar simulator [294]. Xu et al. prepared hydrazine treated titania nanotubes and found 2× enhancement in photoelectrochemical performance compared to undoped titania nanotubes in water oxidation under a halogen lamp [189].

It is difficult to make absolute comparison of the photocurrents obtained from photoelectrochemical water oxidation across different measurement systems in literature because of differences in several factors including light source, wavelength and intensity; catalyst amount; addition of various reagents (e. g. hole scavengers); addition of co-catalysts (e.g. metal nanoparticles); electrolyte pH; and applied potential. The specific photocurrent per gram of our nitrogen doped mesoporous titania was estimated to be on the scale of amperes, which is quite significant considering the low intensity of some of the LED sources (1.29 A/g for Xe arc lamp, 10.1 A/g for UVLED, 0.165 A/g for BLED and 0.007 A/g for GLED).

Further, to make a semi-quantitative comparison, the incident photon to current conversion efficiency (IPCE) and the absorbed photon to current conversion efficiency (APCE) of the plasma doped titania thin films were calculated using the photocurrent observed under UVLED and BLED illumination. The details of the calculations are provided in the Appendix C. The IPCE was calculated using $IPCE = 1240I/(\lambda J)$, where I indicates photocurrent density, J illuminated light intensity and λ light wavelength. The IPCE of the undoped TiO₂ and 100 sccm_N-TiO₂ films under UVLED were calculated to be 0.05% and 13.0%, respectively. The IPCE of the undoped TiO₂ and 100 sccm_N-TiO₂

films under BLED were 0.0002% and 0.05%, respectively. Since the thickness of our titania thin films is only 80 nm, APCE was calculated by dividing IPCE by the fraction of light absorbed at 365 nm and 455 nm (from Figure 5.2) under UVLED and BLED, respectively. The APCEs of the undoped TiO₂ and 100 sccm_N-TiO₂ films under UVLED were 0.5% and 33.6%, respectively. The APCEs of the undoped TiO₂ and 100 sccm_N-TiO₂ films under BLED were 0.004% and 0.3%, respectively. The IPCE of nitrogen doped titania has been rarely reported in literature. Hoang et al. prepared N-doped titania nanowire arrays of 2.6 μm thickness [295], and reported IPCEs of about 20% and 1% at 365 nm and 450 nm wavelength, respectively. The IPCE of our mesoporous titania films under UVLED and BLED are relatively smaller than these values, but this is mainly due to the thin films used in the present study. The APCE (33.6%) value measured under UVLED here is significantly improved relative to the IPCE value of Hoang et al. at 365 nm wavelength. It is expected that the IPCE of our mesoporous titania thin films can be further improved by preparing thicker films using a layer by layer deposition technique to be reported in a future contribution.

According to many previous studies, nitrogen doping does not improve photocatalytic activity under UV light irradiation [261, 274, 277]. In some cases, nitrogen doping has been found to deteriorate UV photoactivity [261, 274, 277]. In our study, N₂/Ar plasma treated mesoporous N-TiO₂ films showed significant enhancement of photocatalytic activity not only under visible light but also under UV light. This extraordinary behavior of the N-TiO₂ films is due to efficient plasma doping method which induces a high nitrogen content with preferentially substitutional nitrogen incorporation. The efficient doping method combined with advantageous mesoporous TiO₂ structure

seems to enable efficient charge separation and transport. Moreover, the amorphous nature of mesoporous TiO₂ film may assist the efficient incorporation of nitrogen in its lattice.

The defects present in bulk titania are thought to deteriorate photocatalytic performance since the defects work as charge recombination centers. However, the rich surface defects of mesoporous TiO₂ film might help create catalytic sites which enable the adsorption of water molecules. Those surface defects work as charge carrier traps and induce charge transfer to adsorbed molecules resulting in high photoelectrochemical performance. Li et al. showed that surface defects in TiO₂ enhance its photocatalytic activity [31]. Salari et al. also showed enhanced photocatalytic activity of titania due to the effects of surface disorder formed by heating at high temperature in the absence of oxygen [32]. Under the N₂/Ar plasma treatment of high-surface-area, mesoporous TiO₂ films, a high density of surface disorder might be created along with nitrogen doping. Therefore, both nitrogen doping and surface defects formed by plasma treatment may be responsible for the outstanding photocurrent enhancement observed in the present study under both UV and visible light irradiation.

Another interesting feature of the LSV and chronoamperometric curves is the time-dependent decay of photocurrents during the illumination periods. As can be seen in Figure 5.9a, 9c, and 9d, the photocurrents decay with a time scale of seconds before they reached constant values. The photocurrent decay is possibly due to charge accumulation at trap sites, leading to charge recombination. The photocurrent becomes stable when the rate of charge generation is equal to the rate of charge recombination. While photocurrents induced by a halogen lamp, BLED, and GLED showed photocurrent decays, the UVLED did not induce photocurrent decay, as shown in Figure 5.9b. Although the origin is not

clear, the difference between UV and visible light sources clearly reflect the different paths of charge carriers generated by UV and visible lights.

To gain more insight into the optoelectronic properties of the films, further photoelectrochemical characterization was performed. Open circuit potential (OCP) was measured with undoped TiO₂ and 100 sccm_N-TiO₂ films with and without illumination using a halogen lamp. The OCP values measured during the illumination with a halogen bulb were -0.19V and -0.34V for undoped TiO₂ and 100 sccm_N-TiO₂, respectively. The OCP values of undoped TiO₂ and 100 sccm_N-TiO₂ in the dark were -0.05 V and -0.09 V, respectively. A more negative value of OCP (found for N-TiO₂ in both light and dark conditions) indicates favorable energetics for water oxidation since it determines the difference between the Fermi level of a semiconductor and the redox potential of the electrolyte [166].

The electronic properties of TiO₂ films and the interface between TiO₂ film and electrolyte were investigated by electrochemical impedance spectroscopy (EIS). Mott-Schottky plots were obtained with 0 sccm_N-TiO₂ and 100 sccm_N-TiO₂ films as shown in Figure 5.10a. The positive slope in the Mott-Schottky plot indicates that TiO₂ is an n-type semiconductor with and without N-doping [158, 279]. The flat band potential (E_{fb}) was estimated by extrapolating the linear portion of the Mott-Schottky plot to the x-axis as shown in Appendix C Figure C.9. The E_{fb} values for undoped TiO₂ and 100 sccm_N-TiO₂ films are -0.93 and -0.813 V, respectively. E_{fb} represents the edge of the conduction band of TiO₂ since it is an n-type semiconductor [280-282, 284], so the reduction of flat band potential suggests that a new energy band for the Ti³⁺ state or oxygen vacancy might be formed just below the conduction band of TiO₂ due to the plasma treatment. Though it is

well known that nitrogen doping causes a negative shift of the valence band of titania[17], several studies suggested that nitrogen doping reduces E_{fb} by the positive shift of conduction band [281, 282, 285]. For instance, Bloth et al. showed that nitrogen doping caused a significant positive shift of the conduction band of titania [281]. They hypothesized two possibilities for this shift due to N-doping: (i) oxygen vacancies (which cause Ti^{3+} state formation below the conduction band), and (ii) interstitially doped nitrogen altering the polarization or geometry of the titanium ions, causing a change in the Ti 3d orbitals. In contrast to the above observations, Spadavecchia et al. demonstrated both experimentally and theoretically that nitrogen doping alone does not change E_{fb} [280]. Since in this case interstitial N is not indicated by XPS, the shift in E_{fb} is most likely due to generation of Ti^{3+} .

In n-type semiconductor, electrons are charge carriers. The density of charge carriers (N_D) was calculated from the slope of the linear portion of the Mott-Schottky plots. Equation 5.1 is the Mott-Schottky equation:

$$\frac{1}{C^2} = \left(\frac{2}{q\epsilon\epsilon_0 N_D} \right) \left(E - E_{fb} - \frac{\kappa T}{q} \right) \quad (5.1)$$

where C is the areal capacitance of the space charge layer, q is the elementary charge (1.6×10^{-19} C), ϵ_0 the vacuum permittivity (8.85×10^{-14} F cm⁻¹), ϵ the dielectric constant of the studied semiconductor, E_{fb} the flat band potential, E the applied external bias, κ Boltzmann's constant, and T the absolute temperature. The dielectric constant is assumed to be 41 for TiO₂ [281]. The calculated N_D values in undoped TiO₂ and 100 sccm_N-TiO₂ films are 8.67×10^{19} cm⁻³ and 3.06×10^{20} cm⁻³, respectively. So, there is a significant (3.5 times) increase in charge carrier density upon plasma treatment. When introduced by N-

plasma treatment, nitrogen atoms work as electron acceptors (tending to decrease N_D) [280, 285] and Ti^{3+} as electron donors (tending to increase N_D) [158]. The balance of the two determines the net change in N_D , and excessive nitrogen doping has been suggested to convert Ti^{3+} to Ti^{4+} species [280]. Cao et al. reported that charge carrier density increased from $3.5 \times 10^{19} \text{ cm}^{-3}$ in undoped TiO_2 to $5.7 \times 10^{20} \text{ cm}^{-3}$ upon nitrogen doping [296]. Recently, Wang et al. also reported the increased donor density upon nitrogen doping [56]. This increased donor density was attributed to the Ti^{3+} formation during the nitrogen implantation process. On the other hand, Hanzu et al. reported a reduction in N_D from $6.7 \times 10^{20} \text{ cm}^{-3}$ in undoped TiO_2 nanotubes to $3.9 \times 10^{20} \text{ cm}^{-3}$ upon nitrogen doping [285]. The significant change observed here suggests formation of a combination of substitutional N and Ti^{3+} , although more studies are necessary to elucidate the mechanism of the positive shift of conduction band edge and change in charge carrier density due to nitrogen doping of titania.

Nyquist plots were recorded for undoped TiO_2 and 100 sccm_N- TiO_2 films with and without illumination by a halogen lamp as shown in Figure 5.10b. A much smaller area under the semicircular portion of the curves is observed for the N-doped TiO_2 film compared to undoped TiO_2 , indicating more efficient charge transfer at the electrolyte-electrode interface due to doping [19]. Hence, more efficient photogenerated electron-hole pair separation and faster interfacial charge transfer occurred in N- TiO_2 compared to undoped TiO_2 film. The facilitated charge transfer kinetics of the 100 sccm_N- TiO_2 films is consistent with the photocurrent enhancement in the amperometric and LSV measurements.

5.5. Conclusion

This study reported the rapid and efficient nitrogen doping of ordered, mesoporous TiO₂ thin films using nitrogen/argon (N₂/Ar) plasma for water oxidation under both visible and ultraviolet illumination. Cubic ordered mesoporous TiO₂ thin films were prepared by a surfactant templated sol-gel method and were treated with N₂/Ar plasma. Optical spectroscopic analysis suggested a significant reduction in band gap of the TiO₂ films from 3.5 eV to 2.88 eV after plasma treatment. Photoelectrochemical (PEC) measurements demonstrated a dramatic enhancement in photocurrents for N-TiO₂ films under both UV and visible-light illumination. The effect of plasma parameters such as gas pressure and nitrogen gas flow rate on the photocurrent were explored. The greatest photocurrent enhancements observed under UVLED and BLED illumination were 242 times and 240 times, respectively, for films treated for 30 min under a 300 W plasma at 70 torr and 100 sccm flow rate. These results show that, consistent with the hypothesized advantages, plasma treated sol-gel derived N-TiO₂ films showed remarkable enhancement in water oxidation not only with visible light of both short and long wavelength, but also under UV light. This enhancement in water oxidation is much greater than in previous reports (where a maximum of 7 times enhancement was reported [294]). The extraordinary enhancement observed in this study suggests that there is room to explore greater levels of doping and the effect of disorder by using plasma-induced doping combined with a mesoporous TiO₂ architecture. We also suspect that the effect is enhanced by the generation of catalytically active surface sites, which will be a subject for future investigation.

Figures of Chapter 5

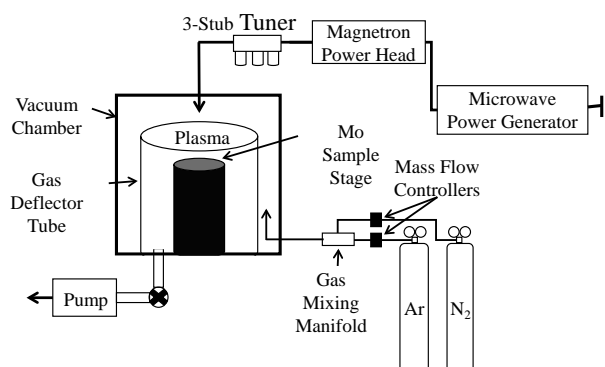


Figure 5.1. Schematic of the plasma reactor used for N₂/Ar plasma treatment of TiO₂ films.

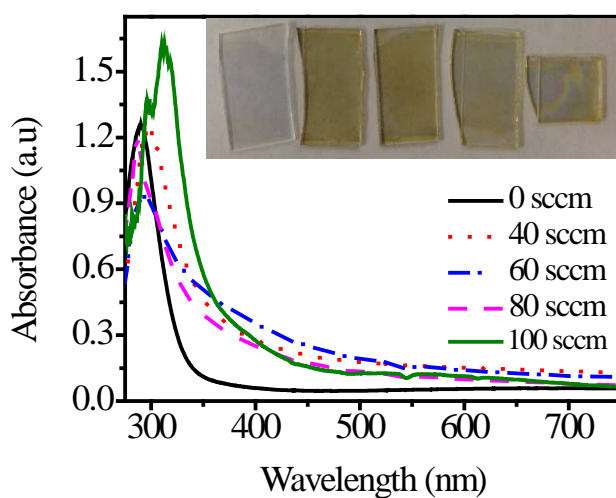


Figure 5.2. UV-vis absorption spectra of undoped and N-doped TiO₂ films prepared with different nitrogen gas flow rate (0-100 sccm) in the plasma reactor at 70 torr. The inset shows photographs of the corresponding 0 sccm_N-TiO₂, 40 sccm_N-TiO₂, 60 sccm_N-TiO₂, 80 sccm_N-TiO₂ and 100 sccm_N-TiO₂ films (from left to right).

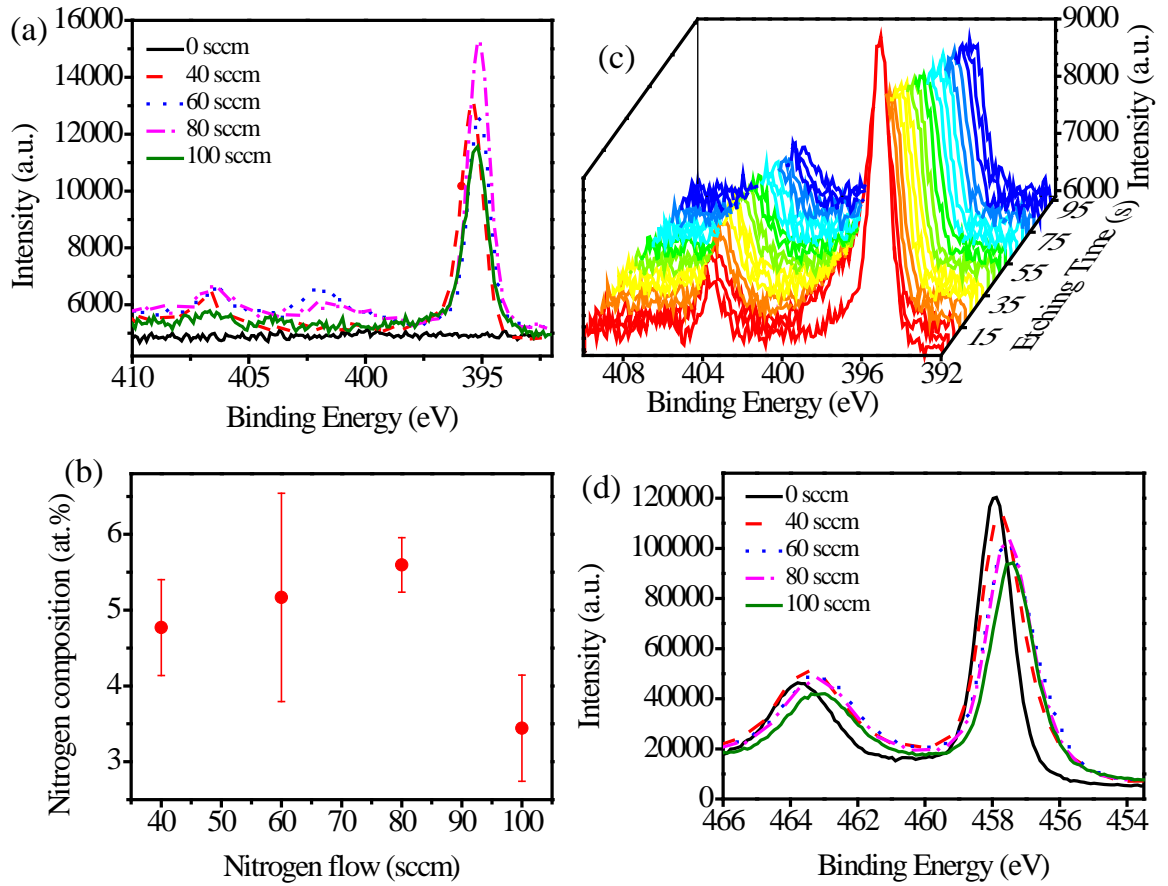


Figure 5.3. (a) High resolution N 1s XPS spectra, (b) plot of surface N content from XPS vs. nitrogen flow rate in the plasma reactor, (c) XPS N 1s depth profile for the 100 sccm_N-TiO₂ sample and (d) high resolution Ti 2p XPS spectra.

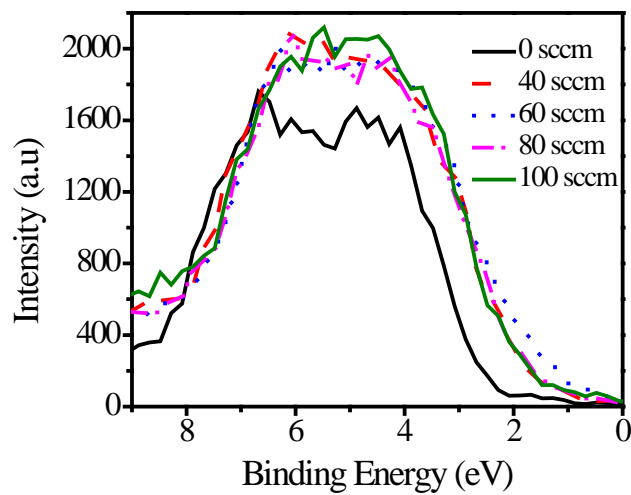


Figure 5.4. Valence band XPS spectra of undoped TiO₂ and N-TiO₂ films.

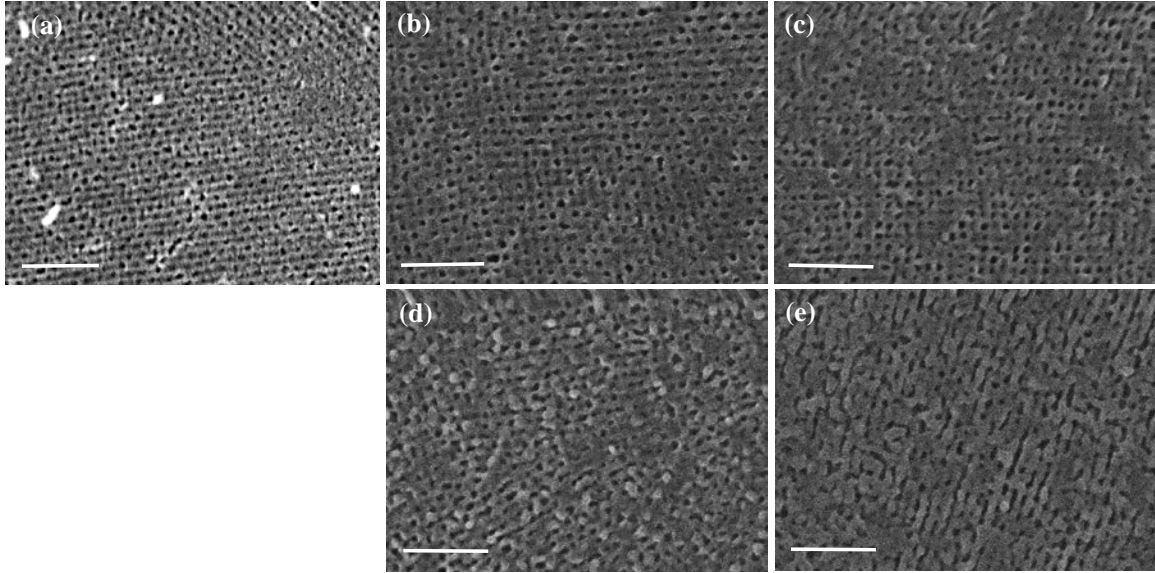


Figure 5.5. SEM images of (a) 0 sccm_N-TiO₂, (b) 40 sccm_N-TiO₂, (c) 60 sccm_N-TiO₂, (d) 80 sccm_N-TiO₂ and (e) 100 sccm_N-TiO₂ films (Scale bar = 100 nm).

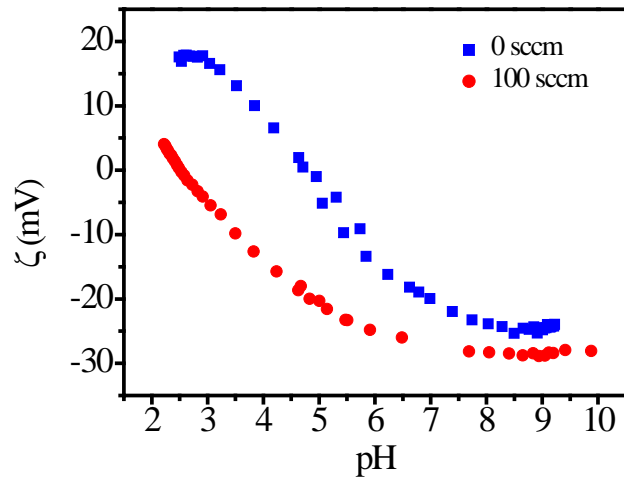


Figure 5.6. Zeta potential (ζ) of the undoped TiO₂ and 100 sccm_N-TiO₂ thin films as a function of pH.

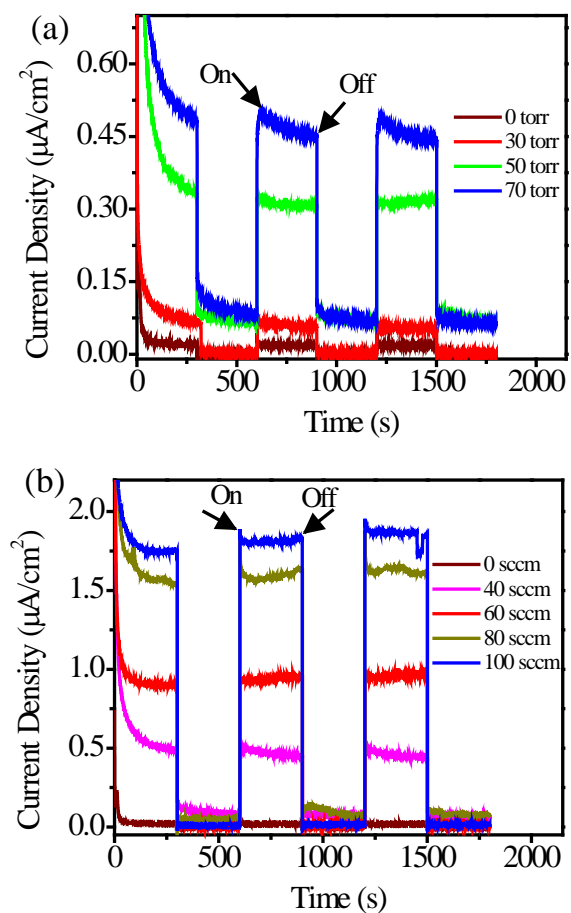


Figure 5.7. The effect of plasma treatment conditions on photocatalytic current-time ($i-t$) profiles under halogen lamp illumination representing water oxidation reaction (a) with a gas pressure variation and (b) with a different N_2 gas flow rate in the plasma reactor.

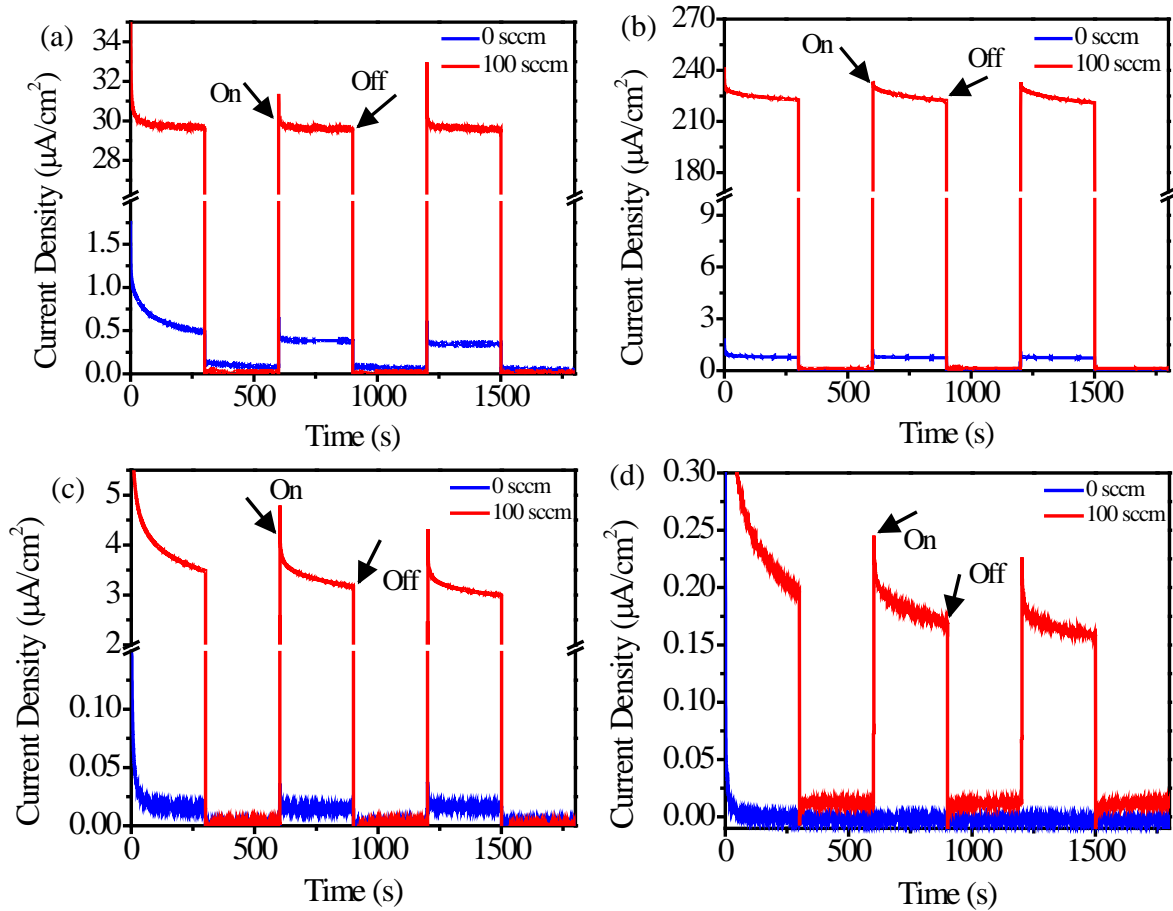


Figure 5.8. Amperometric current-time profiles with 0 sccm_N-TiO₂ (undoped) and 100 sccm_N-TiO₂ films under the illumination of (a) Xe arc lamp with AM 1.5 G filter (b) UVLED, (c) BLED and (d) GLED.

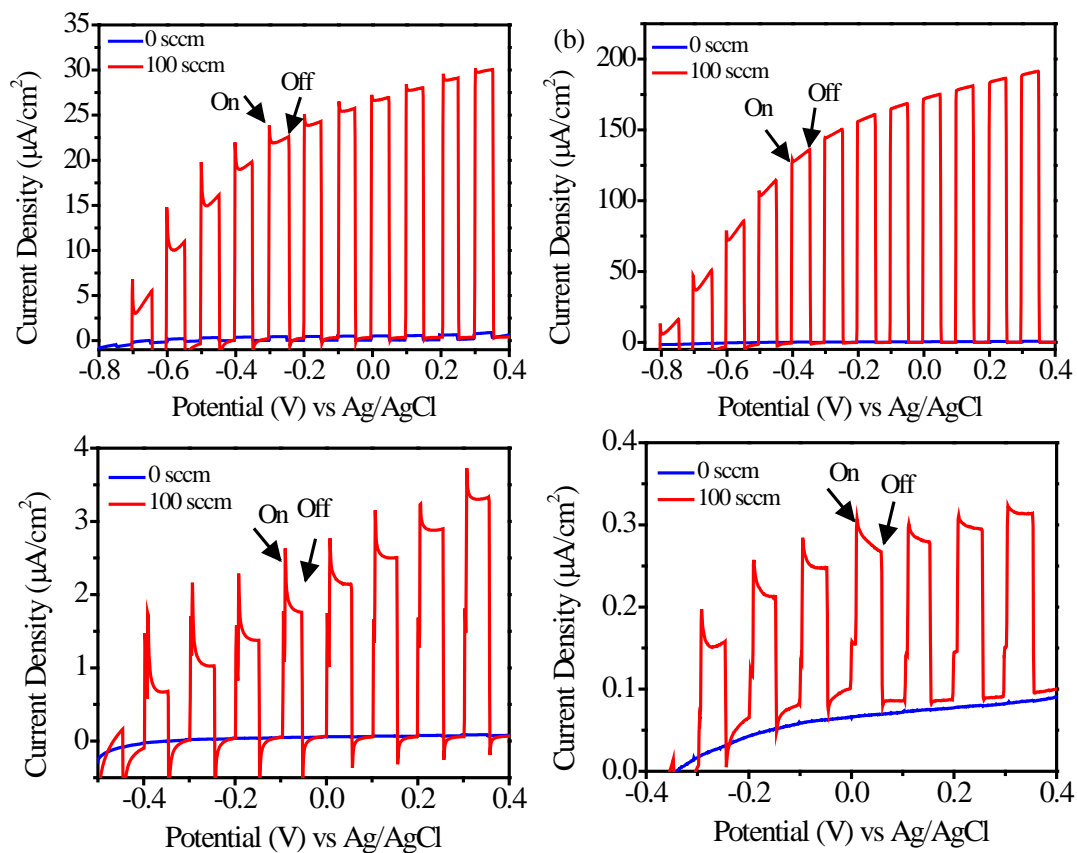


Figure 5.9. Linear sweep voltammetric (LSV) curves recorded with 0 sccm_N-TiO₂ (undoped) and 100 sccm_N-TiO₂ films under the illumination of (a) Xe arc lamp with AM 1.5 G filter, (b) UVLED, (c) BLED and (d) GLED.

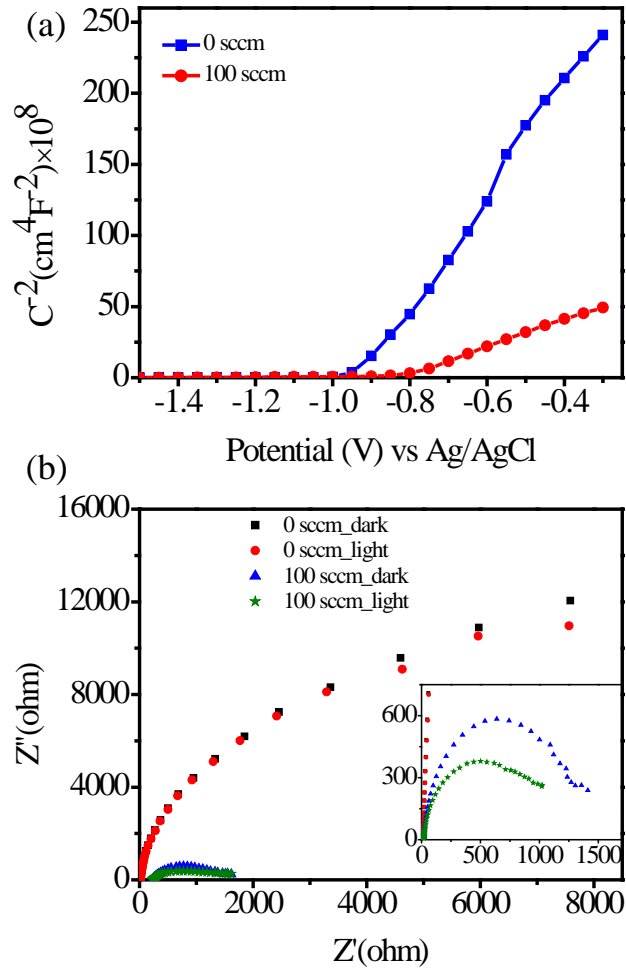


Figure 5.10. (a) Mott-Schottky plot and (b) Nyquist plot recorded for 0 sccm_N-TiO₂ and 100 sccm_N-TiO₂ films.

Chapter 6. Synergistic Effects of Graphene Quantum Dot Sensitization and Nitrogen Doping of Mesoporous TiO₂ Films for Water Oxidation Photocatalysis

6.1. Summary

In this study, we report the synthesis and photoelectrochemical (PEC) behavior of surfactant templated mesoporous TiO₂ films simultaneously doped with nitrogen by plasma treatment and sensitized with graphene quantum dots (GQD/N-TiO₂). These novel nanocomposite structures have been applied successfully as photoanodes for PEC water oxidation under visible light irradiation. First, cubic ordered mesoporous TiO₂ films were prepared by a surfactant templated sol-gel method. Then, TiO₂ films were treated with N₂/Ar plasma to incorporate substitutional N atoms into the lattice of TiO₂. GQDs with an average size of ~5 nm were prepared by chemically oxidizing carbon nano-onions. The immobilization of GQDs onto the titania surface was accomplished by hydrothermal deposition. Successful immobilization of GQDs onto N-TiO₂ was probed by UV-Vis, XPS, zeta potential and contact angle measurements. The nitrogen-doped TiO₂ (N-TiO₂) showed a significant reduction of band-gap (3.5 eV to 2.88 eV) and high enhancement (191 times) of photocatalytic water oxidation under visible light, while GQD/TiO₂ gave a modest (4 times) enhancement. However, when combined, GQD/N-TiO₂ films showed a remarkable 275 times enhancement compared to TiO₂ films due to synergistic effects of nitrogen doping and GQD sensitization resulting in enhanced visible light absorption and efficient charge separation, transport, and transfer. The results demonstrate the importance of designing and manipulating the energy band alignment in composite nanomaterials for fundamentally improving visible light absorption, charge separation and transport, and thereby PEC properties.

6.2. Introduction

TiO₂ has been a well-known semiconductor material for applications in photocatalysis directed at addressing the worldwide energy shortage and concerns over climate change due to fossil fuel use. TiO₂ is especially relevant because of its favorable opto-electronic properties, superior chemical stability, photocorrosion resistance, and low cost [13-16]. In addition, means are available to control its morphology, nanostructure, and electronic properties to enhance the available surface area, light absorption, and charge carrier separation and transport, making titania attractive for photocatalysis, especially photocatalytic hydrogen production by water splitting [18, 30-32].

Mesoporous TiO₂ thin films synthesized by surfactant-templated sol-gel methods have high surface area and controlled pore size, pore orientation, interfacial structure, and pore connectivity. These features allow rapid diffusion of reactants and products within the film, and their thin pore walls reduce photogenerated charge recombination [5, 15, 18, 33, 34, 103, 105, 150, 297]. In order to overcome their innate inability to absorb the abundant visible light from the solar spectrum, the band gap of mesoporous titania thin films was reduced in our previous studies by substitutional nitrogen doping using a plasma-based doping approach [69, 195]. The plasma treatment enabled the incorporation of a large amount of substitutional nitrogen which is responsible for band gap reduction and photocatalytic activities. In addition, the nanostructure of the TiO₂ films was found to be maintained over significant doses of plasma exposure. We demonstrated enhanced photocatalytic activity of plasma-assisted doped mesoporous TiO₂ films [69]. Under visible light, N₂/Ar plasma treated TiO₂ films showed excellent photocatalytic activity for the degradation of methylene blue, and even more substantial effects for photocatalytic

water oxidation [195]. Compared to other methods of doping with molecular precursors (ammonia, hydrazine, etc.), plasma-based doping in mesoporous titania shows superior photocatalytic enhancements [297]. Reasons for the high photocatalytic activity of plasma-treated titania include the initial amorphous structure of the surfactant templated TiO₂ films and the reactive nitrogen species generated at low temperatures by plasma systems. Plasma-generated nitrogen species are readily incorporated into the amorphous structure of surfactant-templated TiO₂ films to give a large amount of substitutional nitrogen. The disordered structure also has many surface defects, which have been suggested to enhance visible light absorption and charge carrier separation [31, 32].

Recently, utilization of tunable narrow band gap semiconductor quantum dots has drawn interest to sensitize wide band gap semiconductors (such as the metal oxides) as a strategy to increase their photoresponse [59]. Several semiconductor quantum dots (QDs) with large extinction coefficients including CdS, CdSe, CdTe, and PbS have been shown to be able to strongly absorb visible light and inject electrons into the conduction band of metal oxides such as TiO₂, and thereby contribute to increased solar energy utilization [59, 60]. However, the heterojunctions formed between these semiconductor quantum dots and wide band gap semiconductor photocatalysts are inefficient because of rich surface traps on bare QDs which increase charge recombination [61]. In addition, quantum dots are often passivated with long chain organic molecules, which block efficient charge transfer between the quantum dot and metal oxide [61]. Furthermore, these semiconductor quantum dots contain toxic heavy metals, and can be susceptible to photooxidation degrading their performance. For example, Pan et al. reported that CdS and CdSe QD sensitized TiO₂

nanotube arrays show significant cycling instability due to significant photooxidization in a liquid medium under light irradiation [61].

As an emerging class of QDs, graphene quantum dots (GQDs) are metal free and green sensitizers, which can be synthesized from a wide variety of carbon precursors. They are of growing interest for their novel properties including size-dependent band gap due to strong quantum confinement and edge effects, excellent thermal and chemical stability, and environmentally friendly nature [62, 63]. Pan et al. showed that GQD heterojunctions are superior to conventional semiconductor QDs in terms of visible-light catalytic activity, durability, and environmental friendliness [61]. It has also been reported that composites of GQDs and TiO₂ exhibit enhanced visible light absorption due to charge transfer from GQDs to the conduction band of TiO₂ [62, 64-66]. Williams et al. demonstrated the feasibility of hot electron harvesting from GQDs to titania using time-resolved second harmonic generation, and found evidence for ultrafast electron injection from photoexcited GQDs to the conduction band of titania. Titania with various morphologies including nanotubes, fibers and nanoparticles have been sensitized with GQDs [62, 64-68]. To further improve the performance of GQDs/TiO₂, surfactant templated mesoporous titania films can be employed. As suggested in our previous paper [69], surfactant templated mesoporous TiO₂ films have several advantages over nanotubes for photoelectrochemical (PEC) applications including smaller pore size and thinner pore walls which result in higher surface area and lower charge recombination, and a flexible and scalable synthesis approach.

To date, doping and sensitization of titania have been explored as separate phenomena, and no work has been done in which the two approaches are combined for

solar energy conversion applications. Here, we report the first example of GQDs sensitized and N-doped titania for PEC water oxidation. We hypothesize that synergistic effects of GQD sensitization and nitrogen doping in titania can be obtained. Photoexcited electrons are expected to be available from GQDs, and the N-states formed at the top of the valence band of titania are expected to facilitate charge carrier transfer. Further, GQDs will help achieve better charge separation in GQD/N-TiO₂ due to their hole extraction affinity. It is believed the π -conjugated basal plane of GQDs will effectively transport holes and facilitate the water oxidation on the catalytic sites of GQDs [298]. To confirm this hypothesis, first we prepare cubic ordered mesoporous titania thin films by evaporation induced self-assembly using surfactant templating. Then, the films are treated with nitrogen/argon plasma for substitutional nitrogen doping. Green emitting graphene quantum dots (GQDs) are synthesized by chemical oxidation of carbon nano-onions. Finally, GQDs are attached to the nitrogen doped titania films by hydrothermal deposition method. These films are used for water oxidation under visible light. Photocatalytic activities of plasma-treated TiO₂ mesoporous films are studied by chronoamperometry, linear sweep voltammetry and electrochemical impedance spectroscopy. The results from indicate that synergistic interaction between GQDs and N-TiO₂ can significantly improve water oxidation under visible light.

6.3. Experimental Section

6.3.1. Materials

Anhydrous ethanol (99.99%, Absolute, Anhydrous, ACS/USP Grade, Pharmco Aaper), F127 (triblock copolymer with average structure HO-(CH₂CH₂O)₁₀₀(CH₂CHCH₃O)₆₅(CH₂CH₂O)₁₀₀H, Mn = 12,500 Da, Sigma-Aldrich),

titanium tetrachloride (tech grade, 99.9%, Fisher Scientific), deionized ultrafiltered (DIUF) water (Fisher Scientific), colloidal graphite (Ted Pella, inc.), KOH (ACS reagent grade, 85%, Fisher Scientific), Nochromix powder (Fisher Scientific), concentrated sulfuric acid (Certified ACS Plus, Fisher Scientific), and epoxy adhesive (Loctite hysol 9462 brown two-part epoxy adhesive, R.S. Hughes) were all used as received. Carbon nano-onions (CNOs) were prepared by thermal annealing of commercially available nanodiamond powders (Dynalene NB50) at 1650 °C for 1h under the flow of helium in a graphitization furnace. HNO₃ and KOH were purchased from SigmaAldrich. All chemicals were used as received without further purification. Dialysis bags were purchased from Spectrum Labs.

6.3.2. Synthesis of mesoporous titania films

Nochromix solution, prepared according to manufacturer instructions, was used to clean borosilicate glass slides (Fisher Scientific). Sols for film deposition were prepared as described previously [69]. Briefly, 1.12 ml of TiCl₄ was added to a solution of 0.67 g of F127 in 18.43 g of ethanol in a nitrogen-filled glove bag. After stirring for 10 min to allow the chloride / ethoxy exchange to occur, 1.8 g of deionized water was slowly added, and the mixture was stirred for an additional 10 min. The cleaned glass slides were dip coated with this sol at a rate of 6 cm/min, followed by aging in a refrigerator at high humidity (RH ~ 94%) and at 4 °C for 2 h. The high RH environment was provided by placing the slides in a sealed box with two beakers containing water. Immediately after aging, TiO₂ films were calcined in a muffle furnace (Vulcan 3-550) for 10 minutes at 350 °C at 25 °C/min ramp but cooled rapidly after calcination back to room temperature. Previous report showed that calcination at 350 °C for 10 min is sufficient for the complete removal of the surfactant from the films [69].

6.3.3. *N₂/Ar plasma treatment of mesoporous TiO₂ film*

A microwave-assisted plasma CVD system (Seki Diamond Systems, AX5010) was used for the nitrogen doping of TiO₂ films. The plasma conditions used for nitrogen doping was microwave power 300 watts, microwave pressure 70 torr, nitrogen flow rate 100 sccm and plasma treatment duration 30 min. The details of the plasma treatment procedure is provided in Chapter 4 and 5.

6.3.4. *Synthesis of GQDs*

Graphene quantum dots (GQDs) were prepared using carbon nano-onion (CNO) precursor. First, 200 mg of CNOs were placed in a three-neck round bottom flask followed by 67 ml of conc. H₂SO₄ (Sigma-Aldrich, ACS reagent 95-98%) and 33 ml of HNO₃ (Fisher Scientific, Assay-69.5%) solutions. A thermometer was used to monitor the temperature of the solution. After attaching a reflux condenser, the round bottom flask was heated using a silicone oil bath at 105 °C for 5 hours to produce GQDs. Next, the GQDs solution was cooled down to room temperature, and 300 ml of deionized (DI) water was added. Then, the solution was placed in an ice bath and neutralized using KOH (VWR analytical) pellets. The precipitated salts during the neutralization process were removed by vacuum filtration. The remaining salts in the filtrate containing GQDs were removed by dialyzing (using a 1 kD molecular weight cutoff dialysis bag (Spectrum Labs)) for one week in DI water. Finally, solid GQDs were obtained by drying the solution at low humid environment at 50 °C under vacuum.

6.3.5. Attachment of GQDs to TiO₂ and nitrogen doped TiO₂

GQDs were attached to TiO₂ and N-TiO₂ using a hydrothermal deposition method. First, 1 mg/ml GQD solution was prepared using DI water. Then, 10 ml of the GQD solution was poured into a Teflon container and a TiO₂ film was immersed in it. The Teflon container was tightly capped and placed in a stainless-steel autoclave reactor. The autoclave reactor was heated to 110°C for 5 hours to attach GQDs to TiO₂. After cooling down the autoclave reactor to room temperature, the sample was taken out and further dried under vacuum for 24 hours. Finally, the GQD functionalized TiO₂ (GQD/TiO₂) film was rinsed with DI water to remove excess GQDs and dried for another 24 hours under vacuum. A similar procedure was followed to obtain GQD functionalized nitrogen doped films (GQD/N-TiO₂). The synthesis steps of graphene quantum dot from carbon nano onions and GQD sensitized, nitrogen doped mesoporous titania thin films are summarized in Figure 6.1.

6.3.6. Characterization

The morphology and structure of the TiO₂ films were characterized with a scanning electron microscope (SEM) attached to a dual-beam Helios Nanolab 660 (FEI). The samples for SEM characterizations were prepared by cutting the FTO substrate on which the TiO₂ thin film was coated using a glass cutter and then mounting the sample exactly at the center of a SEM stub coated with carbon tape. The optical absorbance of the samples was measurement with an UV-vis absorption spectrometer (Ocean Optics, DT-MINI-2-GS). The measurement was carried out by placing the films at an angle of ~45° relative to the incident beam to avoid interference fringes in the spectra. X-ray photoelectron spectroscopic (XPS) analysis was conducted using a ThermoScientific K-Alpha

photoelectron spectrometer using monochromatic Al K- α radiation with photon energy of 1486.6 eV. In the XPS spectra, the binding energy shifts were corrected using the C 1s level at 284.6 eV as an internal standard.

The grazing incidence small angle x-ray scattering (GISAXS) pattern of titania films was collected in order to confirm the orientation of the pores before and after nitrogen plasma treatment. GISAXS experiments were done at the Advanced Photon Source at Argonne National Laboratory at beamline 8-ID-E using a wave length of 1.148 Å and a sample-detector distance of 1040 mm [299]. Calcined undoped TiO₂ and hydrogen plasma treated TiO₂ films on glass substrates were placed on a sample holder. GISAXS patterns were collected at 0.14° incidence angle at room temperature. The beam size was 100 μm \times 50 μm (H \times V) and data were collected with a Pilatus 1M pixel array detector using a 10 s exposure time. Images were corrected for detector nonuniformity and converted to q-space using the GIXSGUI package for Matlab [150].

The zeta potentials (ζ) of TiO₂ thin films and modified films were measured with a SurPASS electrokinetic analyzer (Anton Parr). TiO₂ films were prepared on thin Ti foils (each 2 cm \times 1 cm). The samples were mounted in a cell with an adjustable gap. In the main electrolyte containing 0.01 M KCl, the pH of the solution was changed from 2 to 10 by adding either 0.05 M HCl or 0.05 M NaOH in an automatic titrator. The results provided zeta potential measurements as a function of pH.

Surface wettability of TiO₂, GQD/TiO₂, N-TiO₂ and GQD/N-TiO₂ were determined with contact angle goniometer (Ramé-hart Model 100). Prior to the measurement, samples were thoroughly washed with deionized water and vacuum dried

for 24 hours. The contact angle was measured by gradually increasing the droplet volume and the maximum value reported as the advancing contact angle.

6.3.7. Photoelectrochemical measurements

For photoelectrochemical (PEC) experiments, films of TiO₂, GQD/TiO₂, N-TiO₂ and GQD/N-TiO₂ were prepared on fluorine-doped tin oxide (FTO) coated glass substrates. Prior to dip coating, FTO slides were cleaned with DIUF water, acetone and isopropanol followed by UV-ozone treatment for 20 minutes to remove any organic contaminants. The performance of TiO₂, GQD/TiO₂, N-TiO₂ and GQD/N-TiO₂ films for water oxidation was measured using an electrochemical cell (home-made glass cell) with three electrodes and a potentiostat (CHI 660D, CH Instruments, Inc.). A TiO₂ film (modified or unmodified) deposited on FTO, a platinum wire, and a Ag/AgCl electrode were used for working, counter and reference electrodes, respectively. 1M KOH was used as the electrolyte. The area of the TiO₂ films exposed to the electrolyte solution was 2 cm² and the rest of the films was covered by epoxy paste. After adding the epoxy paste on the surface of the TiO₂ films, it was dried for 3 hours at 120 °C in air. Light sources were a halogen lamp (ELH Osram, 120 V, 300 W) and a blue LED (455 nm, Thorlabs). Power density was recorded by a power energy meter (standard photodiode power sensor, Si, Thorlabs). The power densities of the halogen lamp and blue LED (BLED) were 100 mW/cm² and 22.5 mW/cm², respectively. The emission spectra of light sources are available from the manufacturers.

Amperometric photocurrent-time (*i-t*) profiles were recorded with TiO₂, GQD/TiO₂, N-TiO₂ and GQD/N-TiO₂ films by holding the potential at 0.4 V vs. Ag/AgCl. The light source was turned on and off every 300 seconds periodically to record photo- and dark currents. This experiment was performed for 1800 seconds. Linear sweep

voltammetry (LSV) was performed from -0.45 V to 0.4 V vs. Ag/AgCl under halogen bulb, and -0.4 V to 0.4 V vs. Ag/AgCl under BLED. The scan rate of LSV curves was 5 mV/s. Electrochemical impedance spectroscopy was carried out using the same potentiostat and electrolyte used for other photoelectrochemical measurements. A Mott-Schottky plot was recorded at the frequency of 1 Hz under dark condition for potential varying from -1.5 V to -0.3 V vs. Ag/AgCl. Nyquist plots were obtained with a DC potential of -0.7 V vs. Ag/AgCl under BLED illumination for frequencies between 0.1 Hz to 100 kHz at 0.005 V amplitude.

6.4. Results and Discussion

Figure 6.2a shows the UV-Visible absorption spectrum of a GQD suspension. The highest energy absorbance of GQDs can be assigned to the $\pi \rightarrow \pi^*$ transition in the sp^2 domains. The nonbonding electrons present in the GQDs correspond to oxygen functional groups such as C=O or C-O, and yield $n \rightarrow \pi^*$ transitions at lower energies [300]. Figure 6.2b shows the fluorescence emission spectra obtained with varying excitation wavelength (250 nm - 600 nm). The emission maximum is constant for excitation from 250 nm to 420 nm. At higher excitation wavelengths emission maxima is further red shifted, indicating the presence of GQDs with slightly different sizes and functionalities [300]. The TEM image of GQDs is shown in Figure 6.2c. As illustrated by the size distribution histogram of GQDs shown in the right hand inset, the mean diameter of a GQD is 4.82 nm. The left hand inset shows a high resolution TEM image of a GQD, which consists of layers with the 0.23 nm lattice spacing of graphene [300]. The surface functional groups of GQDs were probed by FT-IR. The spectrum in Figure 6.2d shows the characteristic bands of C=O/O-C=O stretching near 1700 cm^{-1} , benzene C=C ring skeletal vibration around 1582

cm^{-1} , and the broad peak for O-H vibrations from alcohols and carboxylic acid groups around 2500 cm^{-1} to 3500 cm^{-1} . The results of UV-Vis, TEM and FT-IR characterizations indicate that GQDs are spherical particles composed of sp^2 basal planes and various oxygenated functional groups.

UV-visible spectroscopy (Figure 6.3) was used as a first characterization of combined N-doping and GQD incorporation into TiO_2 films. As observed previously, the transparent undoped TiO_2 films turned yellow after N_2/Ar plasma treatment (inset of Figure 6.3), and UV-vis spectroscopy indicates a red shift of the primary peak, as well as a significant increase of visible light absorption consistent with nitrogen incorporation [195]. The primary change compared to undoped TiO_2 in the UV-visible spectrum in GQD- TiO_2 films (Figure 6.3) is a red shift in the primary absorption feature due to the sensitization of TiO_2 film by the GQDs. In addition to the red shift, the GQD/ TiO_2 showed higher absorbance in the range of 350-500 nm. Enlarged spectra of the films in the visible light region are shown in the lower inset of Figure 6.3. The inset reveals that the absorbance tail extends towards longer wavelengths upon incorporation of both GQD and nitrogen in TiO_2 films. The lower inset of Figure 6.3 also shows that the absorbance at long wavelengths of the GQD/ TiO_2 is higher than that of TiO_2 and similarly, the absorbance of GQD/N- TiO_2 is higher than that of N- TiO_2 films, due to the sensitization effect of GQD on the TiO_2 and N- TiO_2 films.

The band gaps of undoped TiO_2 , GQD/ TiO_2 , N- TiO_2 and GQD/N- TiO_2 films were estimated using Tauc plots (Appendix D Figure D.1). To do this, $(\alpha h\nu)^{1/2}$ vs. $h\nu$ was plotted where α is the absorption coefficient and $h\nu$ is the photon energy. The absorption coefficient was calculated from the absorbance divided by the film thickness. The band

gap was estimated by extrapolating the linear portion of the Tauc plot to the x-axis where the value of $(\alpha h\nu)^{1/2}$ approaches zero [274]. The band gaps of TiO₂, GQD/TiO₂, N-TiO₂ and GQD/N-TiO₂ films are 3.5 eV, 3.25 eV, 2.88 eV and 3.0 eV, respectively. Generally, the band gap of crystalline anatase titania is 3.2 eV. However, amorphous TiO₂ films are known to have a band gap larger than that of anatase TiO₂, closer to 3.5 eV [30]. The reason for a lower band gap of GQD/TiO₂ compared to TiO₂ might be due to the combination of amorphous titania with high band gap and GQD with low band gap, and/or hydrothermal treatment of the TiO₂ for GQD attachment. Even though the band gap has not been changed upon GQD functionalization in N-TiO₂ films, the light absorption in the long wavelength visible region has been increased resulting in the maximum visible light absorption in the GQD/N-TiO₂ films among all the films as shown in inset of Figure 6.3.

The undoped TiO₂ films were shown to be 80 nm thick, with interconnected cubic ordered pores approximately 7 nm in diameter and walls 5.5 nm thick [69]. XRD analysis indicated a peak at low angle consistent with the ordered pore structure and no distinct reflections at high angle, suggesting a disordered or fine nanocrystalline structure [69]. The effect of N₂/Ar plasma treatment on the nanostructure of the N-TiO₂ films was investigated by SEM as shown in Figure 6.4. Accessible pores are clearly seen in the SEM image of the N-TiO₂ films as shown in Figure 4c. However, the pore structure was observed to deteriorate slightly in the films. The pores fused with each other due to the effects of sintering, either because of exposure to a large dose of high-energy nitrogen species or because of the temperature reached during plasma exposure. After and before nitrogen doping, GQDs were attached to the titania surface by hydrothermal treatment. Figure 6.4b and 6.4d are the SEM images of GQD/TiO₂ and GQD/N-TiO₂ films, respectively. Pores

are clearly seen in the GQD/TiO₂ and GQD/N-TiO₂ films. However, fewer accessible pores are found after GQD attachment. Still, most of the pores in the GQD/TiO₂ and GQD/N-TiO₂ films are accessible and the hydrothermal treatment did not induce excessive coarsening relative to each starting film.

The GISAXS patterns of the undoped TiO₂ and N-TiO₂ films are shown in Figure 6.5. Three bright diffraction spots in the GISAXS pattern were observed for the undoped TiO₂ films (Figure 6.5a) indexed to the (110), (101) and (1 $\bar{1}$ 0) plane of a distorted cubic (Im3m) mesostructure [18]. As shown in Figure 6.5b, the GISAXS pattern after nitrogen plasma treatment shows two vertical rod on either side of the beam stop indicating the presence of an orthogonally oriented hexagonal close packed (o- HCP) cylindrical mesophase. These rods can be indexed to primary (100) spacing of the close-packed pores, and their rod shape can be attributed to the finite cylindrical shape of the pores [103, 105, 150]. The patterns were found at q of ca. 0.045 Å⁻¹ corresponding to d-spacing 14 nm, which is consistent with the pore spacing in the SEM image (Figure 6.4c). Although characterization of the N-TiO₂ films was reported previously [69], these new GISAXS results show a new result: the pores in N-TiO₂ films become vertically oriented channels due to contraction normal to the film and fusing of some of the pores due to the transformation during the plasma treatment. It has also been reported in literature that heat treatment can transform cubic ordered pores into vertically oriented pores which is consistent with our study [144].

The elemental compositions and chemical nature of unmodified TiO₂, GQD/TiO₂, N-TiO₂ and GQD/N-TiO₂ films were probed by XPS analyses. High resolution C 1s XPS spectra of the unmodified TiO₂, GQD/TiO₂, N-TiO₂ and GQD/N-TiO₂ films are presented

in Figure 6.6a. All films showed peaks for carbon at about 284.6 eV and 288.3 eV which correspond to C=C and COOH groups, respectively [301]. The source of the carbon in TiO₂ and N-TiO₂ films might be the solvent added during the synthesis of TiO₂ films and adventitious carbon from the environment. The carbon peak for GQD/TiO₂ films is noticeably broader than that of unmodified TiO₂ films, which indicates a wider distribution of carbon-containing species than in unsensitized TiO₂. Similarly, the C1s peak intensity for GQD/N-TiO₂ film is much wider and stronger than that for N-TiO₂ films, consistent with the formation of a GQD/N-TiO₂ hybrid. Further, the absence of a peak at 281.0 eV for Ti-C confirmed that TiO₂ was not doped with carbon. Yu et al. suggested that a GQD/TiO₂ composite is formed by conjugation via Ti-O-C bonds due to the hydrothermal treatment of TiO₂ in GQD solution [301].

High resolution XPS was carried out to investigate the presence of nitrogen in TiO₂, GQD/TiO₂, N-TiO₂ and GQD/N-TiO₂ films. High-resolution spectra for N1s are presented in Figure 6.6b. The TiO₂ film did not show any peak for nitrogen but GQD/TiO₂ film showed a very wide peak at about 400 eV for nitrogen. This nitrogen might come from the functional groups of attached GQD, which is another indication that GQD is attached to the TiO₂ film. On the other hand, N-TiO₂ and GQD/N-TiO₂ films showed a sharp peak at about 395 eV due to substitutional nitrogen. The composition of nitrogen calculated based on XPS high resolution spectra of nitrogen, titanium, oxygen and carbon is 5.82 at. % and 6.07 at. % in N-TiO₂ and GQD/N-TiO₂ films, respectively. The small peaks at about 399.5 eV for nitrogen in both GQD/TiO₂ and GQD/N-TiO₂ films might come from the nitrogen-containing functional group of GQD.

Zeta potential measurements (ζ) were used to examine the surface charge after GQD functionalization. Figure 6.7 illustrates the zeta potential measurements obtained for undoped TiO₂, GQD/TiO₂, N/TiO₂, and GQD/N-TiO₂. GQDs contain functional groups such as -COOH and -OH. These functional groups adopt a negative surface charge at high pH values due to deprotonation. Therefore, both GQD/TiO₂ and GQD/N-TiO₂ samples showed relatively large negative surface charges. The isoelectric points (IEPs) for undoped TiO₂, N-TiO₂, GQD/TiO₂ and GQD/N-TiO₂ are 4.9, 2.5, 2.7 and 2.0, respectively. Compared with the N-TiO₂ surface, GQD immobilized surfaces showed higher acidity due to the functional groups associated with GQDs [302, 303]. These functional groups are expected to play a significant role in adsorbing polar species and catalyzing surface reactions.[304] Interestingly, the GQD/N-TiO₂ sample exhibits two inflections in the ζ curve corresponding to titration of acid groups, near pH 3.5 and 6.5, rather than just the single inflection observed for GQD-TiO₂ at pH 6.5. The more acidic groups are not observed in either N-TiO₂ or GQD-TiO₂ alone and form in the composite.

The surface wettability of the films was investigated by contact angle measurements. The contact angles measured for TiO₂, N-TiO₂, GQD/TiO₂ and GQD/N-TiO₂ are 50.9±0.3°, 12.8±0.3°, 32.2±0.2°, and 25.7±0.7°, respectively (Appendix D Table D.1). N-TiO₂ showed the smallest contact angle, indicating the highest hydrophilicity. The hydrophilicity of GQD/TiO₂ is higher than that of TiO₂. GQD/N-TiO₂ showed an intermediate hydrophilicity between N-TiO₂ and GQD/TiO₂. GQDs contain a hydrophobic aromatic domain as well as hydrophilic surface functionality [305]. Therefore, the balance between these two factors and the surface roughness may govern the overall behavior of the surface hydrophilicity of the GQD immobilized surface[306]. This surface

hydrophilicity will affect the interaction between electrode and electrolyte and thereby influence the charge transfer kinetics at the catalyst surface.

The photocatalytic activity of TiO₂, N-TiO₂, GQD/TiO₂ and GQD/N-TiO₂ films in water oxidation were evaluated by recording amperometric *i-t* curves under visible light using a blue LED (455 nm wavelength) light source (Figure 6.8a). A summary of the photoelectrochemical performance of the titania films in amperometric *i-t* measurements is provided in Table 6.1. The photocurrent densities of TiO₂, N-TiO₂, GQD/TiO₂ and GQD/N-TiO₂ films were 0.0175 μA/cm², 3.352 μA/cm², 0.0807 μA/cm², and 4.815 μA/cm², respectively. This is equivalent to 0.764 mA/g, 146.4 mA/g, 3.52 mA/g and 210.26 mA/g, respectively, based upon the estimated mass per area of the film, 2.29 × 10⁻⁵ g/cm², calculated using the film thickness of 80 nm, pore diameter, and wall thickness from SEM images. The photocurrent enhancement of the N-TiO₂, GQD/TiO₂ and GQD/N-TiO₂ films over unmodified films are 191, 4.6 and 275 times, respectively (Table 6.1). Further, *i-t* curves were recorded to evaluate the water oxidation performance of the unmodified and modified titania films under a halogen bulb with a wide spectrum of emission as shown in Figure 6.8b. The photocurrent enhancement of N-TiO₂, GQD/TiO₂ and GQD/N-TiO₂ films compared to TiO₂ was ca. 101 times, 4.6 times and 128 times. This clearly indicates that GQD sensitization of TiO₂ and N-TiO₂ films significantly improved their photocatalytic activity in water oxidation under visible light irradiation. When the performance is compared between GQD sensitization and nitrogen doping alone, nitrogen doping is more effective than GQD sensitization. However, combining GQD sensitization and nitrogen doping gives performance of the hybrid material much higher than a linear combination of enhancements due to sensitization and doping alone. That indicates a

synergistic effect on photocatalysis of GQD and N-doping under both narrow spectrum visible light (BLED) and broad spectrum light (halogen bulb). These superior results hint at effects from charge separation by GQDs beyond their strong visible light absorption.

In addition to chronoamperometric curves recorded at fixed potential (0.4 V vs. Ag/AgCl), linear sweep voltammetry (LSV) curves were recorded with chopping of the light from a BLED and halogen bulb, as shown in Figure 6.9. Photocurrents increase with applied potential. The current of the unmodified and modified titania films, and the enhancement of current upon modification of the films in LSV measurements at 0.35 V vs. Ag/AgCl are presented in Table 6.2. The photocurrent enhancement for N-TiO₂, GQD/TiO₂ and GQD/N-TiO₂ films over TiO₂ film are 222, 8.5 and **346 times**, respectively under BLED illumination. The results as shown in Table 6.2 from the linear sweep voltammetry measurement indicate that the photocatalytic activities of the TiO₂ and N-TiO₂ films were improved significantly by GQD sensitization, and GQD and N-doping exhibit excellent synergistic effect in photocatalysis, which is consistent with the chronoamperometric results (Table 6.1). Reasons for the superior performance of our hybrid materials is attributed to several factors, mainly: enhanced visible light absorption, good charge separation, high surface area of the mesoporous titania films, efficient interface formation between the GQD and mesoporous titania, small pore wall thickness of the titania film, ease of nitrogen doping by efficient plasma treatment into sol-gel derived amorphous titania, and finally synergistic electronic effects of GQD and N-doping together.

The observed photoelectrochemical enhancements with N-doping and GQD/N-doping significantly exceed values reported in prior literature for other relevant systems.

Sharma et al. and Ishihara et al. prepared plasma-treated nitrogen doped TiO₂ nanotubes and found 2 times enhancement of water oxidation photocurrent compared to undoped TiO₂ nanotubes under a solar simulator [21, 166]. Liu et al. also showed less than 2 times photocurrent enhancement in water oxidation under a 350 W Xe lamp for plasma treated N-TiO₂ nanotubes compared to undoped TiO₂ nanotubes [167]. Compared to other doping methods, our plasma treated N-TiO₂ also shows significantly higher enhancement in photoactivity. For instance, Babu et al. prepared N-TiO₂ using urea as nitrogen precursor and found 7× photocurrent enhancement in photoelectrochemical water oxidation using a solar simulator [294]. Xu et al. prepared hydrazine treated titania nanotubes and found 2× enhancement in photoelectrochemical performance compared to undoped titania nanotubes in water oxidation under a halogen lamp [189]. The only comparison to a GQD-containing system is from Yu et al., who prepared GQD sensitized TiO₂ using the hydrothermal treatment [301]. This GQD/TiO₂ showed about 2 times enhancement in photocurrent compared to unmodified TiO₂. Thus, when compared to other N-doped and GQD-conjugated photocatalytic systems, the results in Tables 6.1 and 6.2 show enormous enhancements for the water oxidation reaction.

The incident photon to current conversion efficiency (IPCE) and the absorbed photon to current conversion efficiency (APCE) of all films were calculated using the photocurrent observed from linear sweep voltammetry measurements under BLED illumination as presented in Figure 6.8a. The details of the calculations are provided in the Appendix D. The IPCE was calculated using $IPCE = 1240I/(\lambda J)$, where I indicates photocurrent density, J illuminated light intensity and λ light wavelength. The IPCE of the TiO₂, GQD/TiO₂, N-TiO₂ and GQD/N-TiO₂ films were calculated to be 0.00018%,

0.0015%, 0.04% and 0.06%, respectively. Since the thickness of our titania thin films is only 80 nm, APCE was calculated by dividing IPCE by the fraction of light absorbed at 455 nm (from Figure 6.3). The APCE of the TiO₂, GQD/TiO₂, N-TiO₂ and GQD/N-TiO₂ films were calculated to be 0.0039%, 0.024%, 0.25% and 0.37%, respectively. Since, either IPCE or photocurrents obtained from photoelectrochemical water oxidation depends on many factors including light source, electrolyte, additives in electrolyte, catalyst and co-catalyst and so on, it is difficult to make absolute comparison across different measurement systems in literature. Further, the IPCE of nitrogen doped or GQD sensitized titania has been rarely reported in the literature. Hoang et al. prepared N-doped titania nanowire arrays of 2.6 μm thickness,[295] and reported IPCE of about 1% at 450 nm wavelength. The IPCE of our mesoporous titania films under BLED are smaller than this value, but this is mainly due to the thin films (1/10 the thickness of Hoang et al.) used in the present study. It is expected that the IPCE of our mesoporous titania thin films can be further improved by preparing thicker films using a layer-by-layer deposition technique to be reported in a future contribution.

Another interesting feature of the LSV and chronoamperometric curves is the time-dependent decay of photocurrents during the illumination periods. As can be seen in Figure 6.8 and Figure 6.9, the photocurrents decay with a time scale of seconds before they reached constant values. The photocurrent decay is possibly due to charge accumulation at trap sites, leading to charge recombination. The photocurrent becomes stable when the rate of charge generation is equal to the rate of charge recombination. It is noticed that the transient photocurrent decreased gradually for all of the films but at different rates which indicates that these charge recombination processes follow different kinetics based on

doping and sensitization of titania films. To further understand this phenomenon, transient kinetic analysis was performed on the chronoamperometric curves. It is assumed that the charge recombination follows first order kinetics [307, 308]. The decay kinetics of the transient photocurrent is calculated by an exponential approach using equation 6.1.

$$C_t = C_{ss} + (C_i - C_{ss}) \times e^{-kt} \quad (6.1)$$

where C_t is the current density with time, C_i is the initial current density, C_{ss} is the steady-state value (at long times from the start of a transient), k is the recombination rate constant and t is the time. If equation 6.1 is rearranged, it can be written as:

$$\ln\left(\frac{C_t - C_{ss}}{C_i - C_{ss}}\right) = -kt \quad (6.2)$$

In other words, $\ln(R) = -kt$ where $R = \left(\frac{C_t - C_{ss}}{C_i - C_{ss}}\right)$.

Since the recombination process is very rapid, the first 12 seconds after light exposure at the 600 second overall time point was used for analysis of the data. Figure 6.10 plots of $\ln(R)$ vs. t all four films. From these plots, it becomes clear that charge recombination happens in two stages – one fast process that reaches completion within the first 2 seconds followed by a slower decay towards steady state. To account for these processes, two lines were fit to the initial and later segments of the data in Figure 6.10. The rapid (k_1) and slower (k_2) rate coefficients are presented in Table 6.3. The first rate coefficient (k_1) is increased by nitrogen doping, showing that while N-TiO₂ absorbs and utilizes photons effectively, charge recombination is worsened. For the GQD/N-TiO₂ and GQD/TiO₂ films, k_1 decreases significantly over N-TiO₂ and TiO₂ films, indicating that recombination of photoinduced electron-hole pairs is slowed due to the presence of GQDs. Along with the enhancement of light absorption due to sensitization and doping, these

results further confirm that separation of photogenerated electrons and holes by GQDs contributes to the synergistic enhancement of photocatalytic activity of sensitized and doped titania films. The second rate constants (k_2) for the GQD/N-TiO₂ and N-TiO₂ film are similar which indicates the GQDs do not have a significant contribution over this time scale, and a similar observation was made for TiO₂ and GQD/TiO₂ films. In the second part of the curve, in each case there is only a small fraction of charges left after the rapid recombination step, so this is expected to have little influence on the observed photocatalysis. Overall, Table 6.3 shows the slowest charge recombination in the GQD/N-TiO₂ sample.

As a final measurement of the electrochemical characteristics of the films, Nyquist plots were recorded for all films under BLED illumination as shown in Figure 6.11. When GQD was attached onto the TiO₂ surface, the area under the semicircle for the GQD/TiO₂ decreased, indicating that the charge transfer kinetics at the interface were improved, which is in agreement with the literature [301]. A much smaller area under the semicircular portion of the curves is observed for the N-TiO₂ film compared to undoped TiO₂, indicating that doping also improves charge transport at the interface [19]. Hence, more efficient photogenerated electron-hole pair separation and faster interfacial charge transfer occurred in N-TiO₂ compared to undoped TiO₂ film. On the other hand, the radius of the GQD/N-TiO₂ is greater than that of N-TiO₂ film but similar to that of the GQD/TiO₂ film. This indicates that GQDs dominate charge transfer at the surface of the electrodes regardless of nitrogen doping.

To further understand the synergistic enhancement of nitrogen doping and GQD immobilization, band alignments of TiO₂, N-TiO₂ and GQDs were investigated. Based on

the Tauc plot analysis above, TiO₂, N-TiO₂ and GQDs have band gaps of 3.5 eV, 2.88 eV, and 2.42 eV, respectively. Ultraviolet photoelectron spectroscopy (UPS) was conducted to elucidate the position of the valance band edge of TiO₂ and N-TiO₂ with respect to vacuum. Cyclic voltammetry experiment was conducted to determine the lowest unoccupied molecular orbital (LUMO) position of GQDs (experimental details are available in Appendix D). The highest occupied molecular orbital (HOMO) level of GQDs and the conduction band positions of TiO₂ and N-TiO₂ were deduced from the band gap of each material. The obtained energy band diagram is illustrated in Figure 6.12. For optimal catalytic performance, the positions of the valence band and conduction band are important. Upon nitrogen doping of TiO₂, the position of the valence band shifts towards the conduction band and simultaneously brings it closer to the HOMO level of GQDs. It has been reported that the high valence band offset at the junction can yield to increased hole transport barriers due to strong charge carrier scattering [309], thus reducing the device efficiency [310]. Based on the energy band diagram, after nitrogen doping, the valance band offset reduces. Therefore, GQD/N-TiO₂ has more favorable band alignments than GQD/TiO₂ to generate higher charge separation efficiency [311].

6.5. Conclusion

This study reported the synthesis of novel nanocomposite materials based on visible-light-absorbing GQDs and N-doped mesoporous TiO₂ films with properties tailored for photoelectrochemical (PEC) water oxidation. Synergistic effects of sensitization and nitrogen doping in mesoporous titania films were observed in photoelectrochemical water oxidation, with remarkable photocurrent enhancements as a result. Cubic ordered mesoporous TiO₂ thin films were prepared by a surfactant templated sol-gel method and

were treated with N₂/Ar plasma for the incorporation of substitutional N atoms into the lattice of TiO₂. Optical spectroscopic analysis suggested a significant reduction in band gap of the TiO₂ films from 3.5 eV to 2.88 eV after plasma treatment. GQDs with an average size of ~5 nm were prepared by chemically oxidizing carbon nano-onions. The immobilization of GQDs onto the titania surface was accomplished by a hydrothermal deposition method.

As reported previously, N-TiO₂ showed orders of magnitude enhancement (191 times) in photocatalytic water oxidation rate under blue LED (455 nm wavelength) illumination. When TiO₂ and N-TiO₂ films were sensitized by GQDs, the GQD/TiO₂ and GQD/N-TiO₂ films showed about 4 times and 275 times enhancement compared to the TiO₂ film, respectively. When halogen bulb with a broad spectrum was used as a light source, the photocurrent enhancement of GQD/TiO₂, N-TiO₂, and GQD/N-TiO₂ films compared to TiO₂ was ca. 4.6 times, 101 times and 128 times, respectively. This enhancement in water oxidation is much greater than in previous reports for either N-doping of TiO₂ (where a maximum of 7 times enhancement was reported [294]) or GQD sensitization of TiO₂ (where a maximum of 2 times enhancement was reported [301]) alone. The high level of enhancement by N-doping observed in this study is due to the effect of using plasma-induced doping combined with a disordered, thin-walled mesoporous TiO₂ architecture. Adding sensitization by GQDs to the plasma-induced doping approach in sol-gel derived mesoporous titania yields large synergistic effects for photocatalytic water oxidation due to differences in charge carrier creation and separation. The absorbance found by UV-vis spectroscopy is not vastly increased by GQD addition to N-TiO₂, but direct evidence is found for improved valence band alignment, and for reduced

rates of charge carrier recombination in GQD/N-TiO₂, presumably due to easy charge carrier transport. The study provides a new pathway for developing nanostructured composite materials based on energy band alignment for fundamentally improving visible light absorption, charge separation and transport, and thereby energy and environmental applications.

Figures of Chapter 6

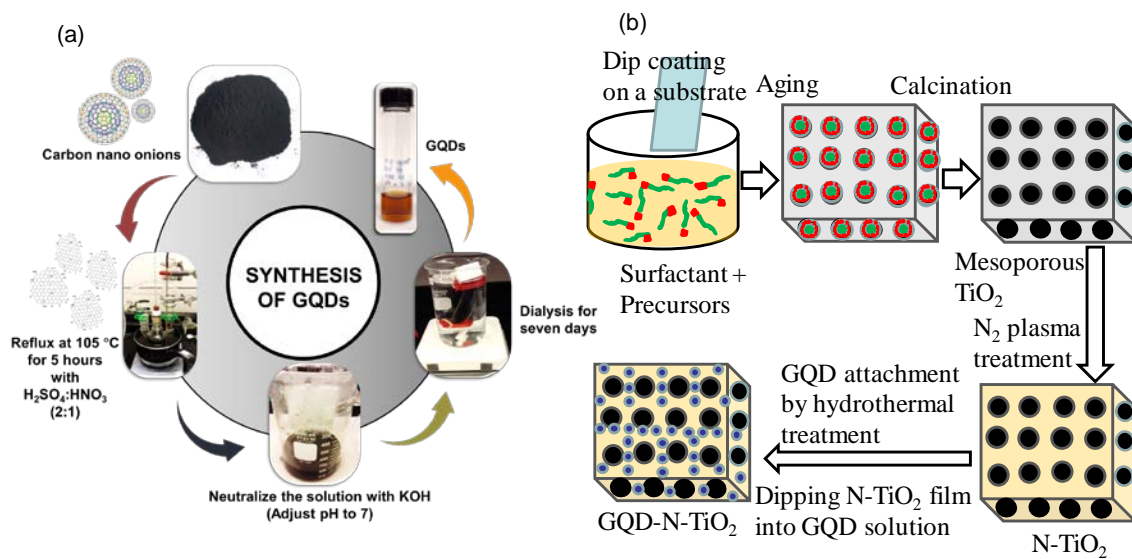


Figure 6.1. Synthesis steps of (a) graphene quantum dots, and (b) graphene quantum dot sensitized nitrogen doped mesoporous titania thin films

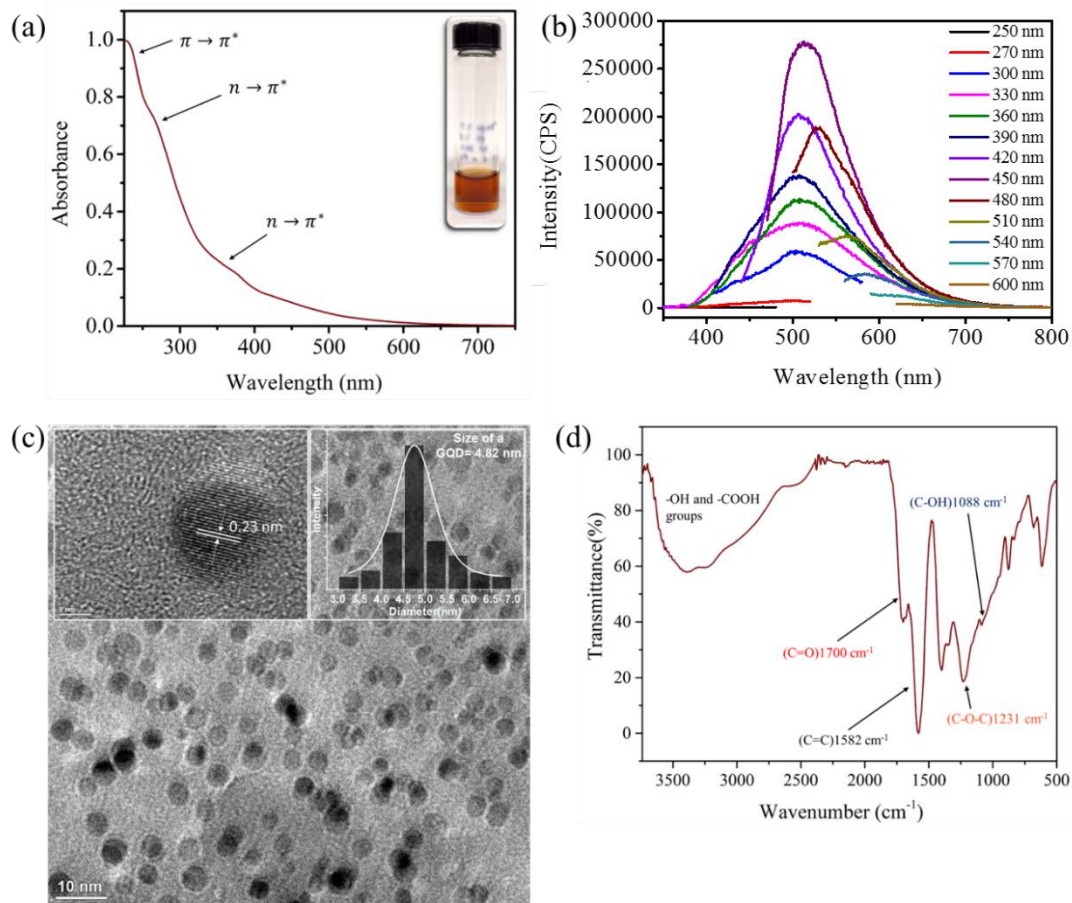


Figure 6.2. (a). UV-VIS absorbance, (b). Fluorescence, (c) low resolution and high-resolution TEM images and (d) FTIR spectrum of graphene quantum dots

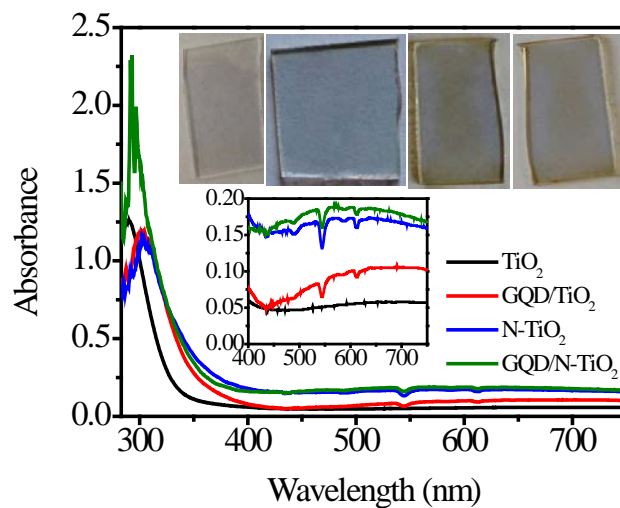


Figure 6.3. UV-vis spectra of pure TiO₂, GQD/TiO₂, N-TiO₂ and GQD/N-TiO₂ films. The inset shows photographs of the corresponding TiO₂, GQD/TiO₂, N-TiO₂ and GQD/N-TiO₂ films (from left to right). The inset also shows an enlarged region in the visible wavelength range.

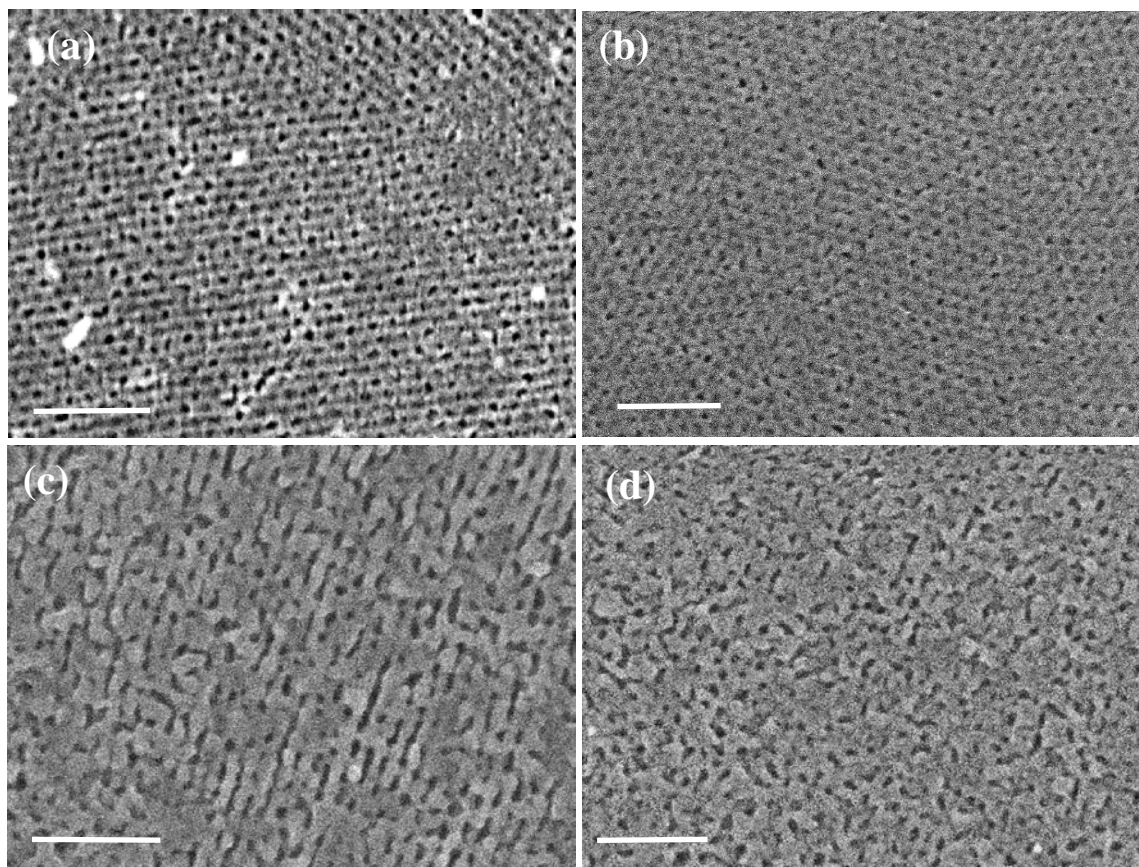


Figure 6.4. SEM images of (a) undoped TiO₂, (b) GQD/TiO₂, (c) N-TiO₂ films and (d) GQD/N-TiO₂ films (Scale bar = 100 nm).

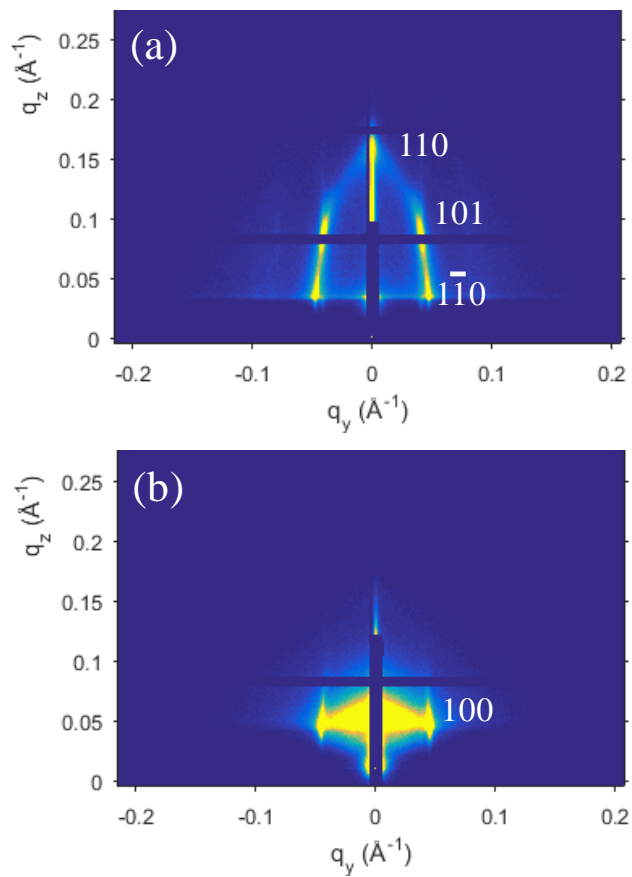


Figure 6.5. GISAXS patterns of (a) undoped TiO_2 and (b) N- TiO_2 films

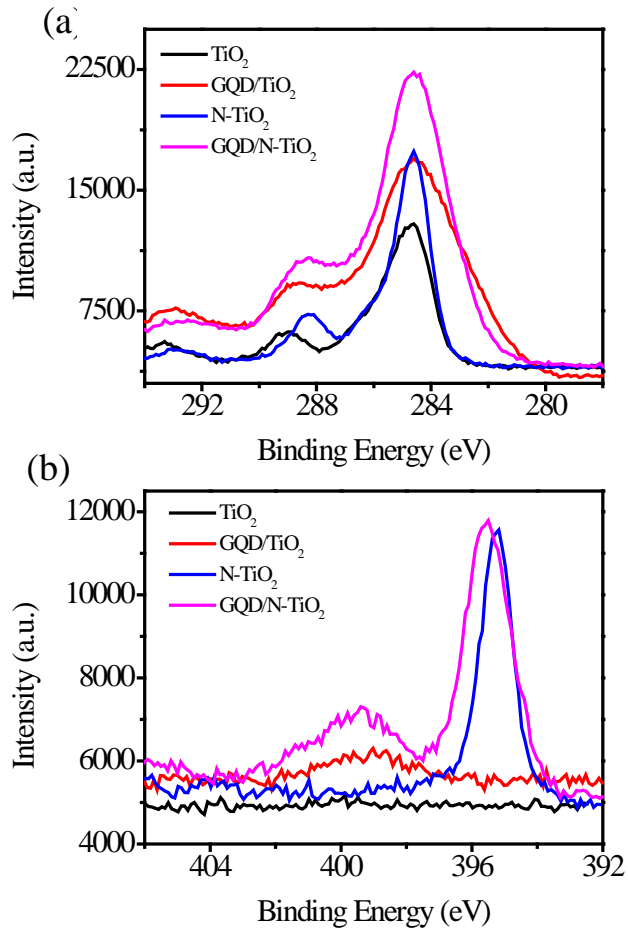


Figure 6.6. (a) High resolution (a) C 1s and (b) N 1s XPS spectra of TiO₂, GQD/TiO₂, N-TiO₂ and GQD/N-TiO₂ films

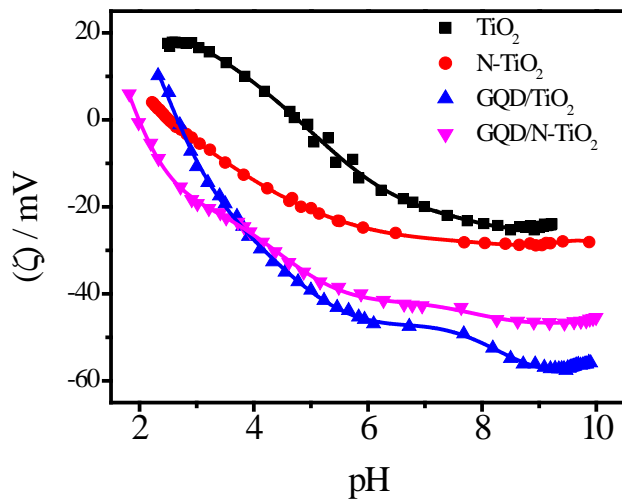


Figure 6.7. Zeta potential (ζ) of the undoped TiO_2 and GQD/TiO_2 , N-TiO_2 and $\text{GQD}/\text{N-TiO}_2$ films as a function of pH.

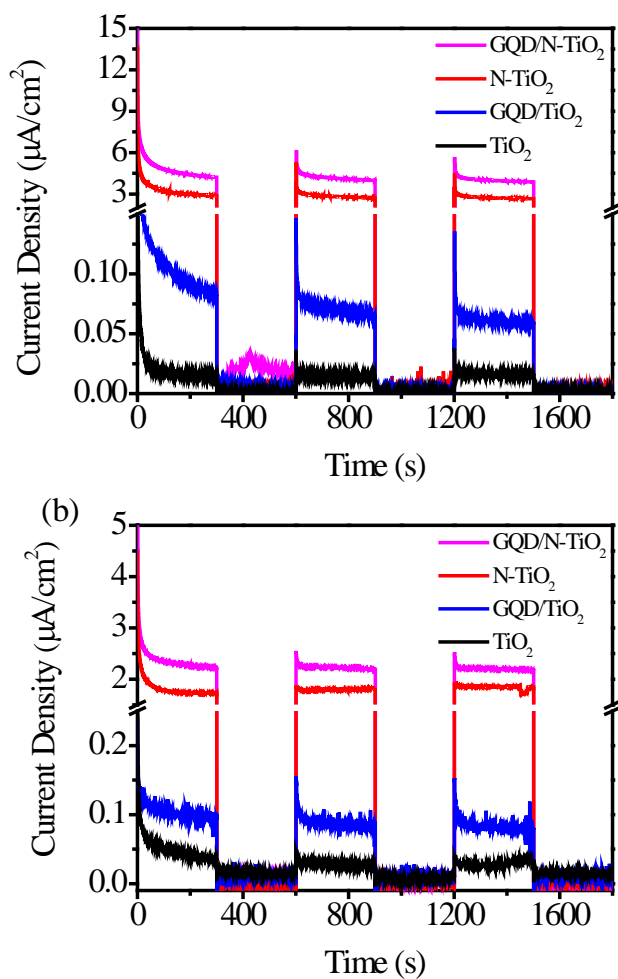


Figure 6.8. Amperometric current-time profiles with undoped TiO_2 , GQD/TiO_2 , N-TiO_2 and $\text{GQD}/\text{N-TiO}_2$ films under the illumination of (a) BLED and (b) halogen bulb.

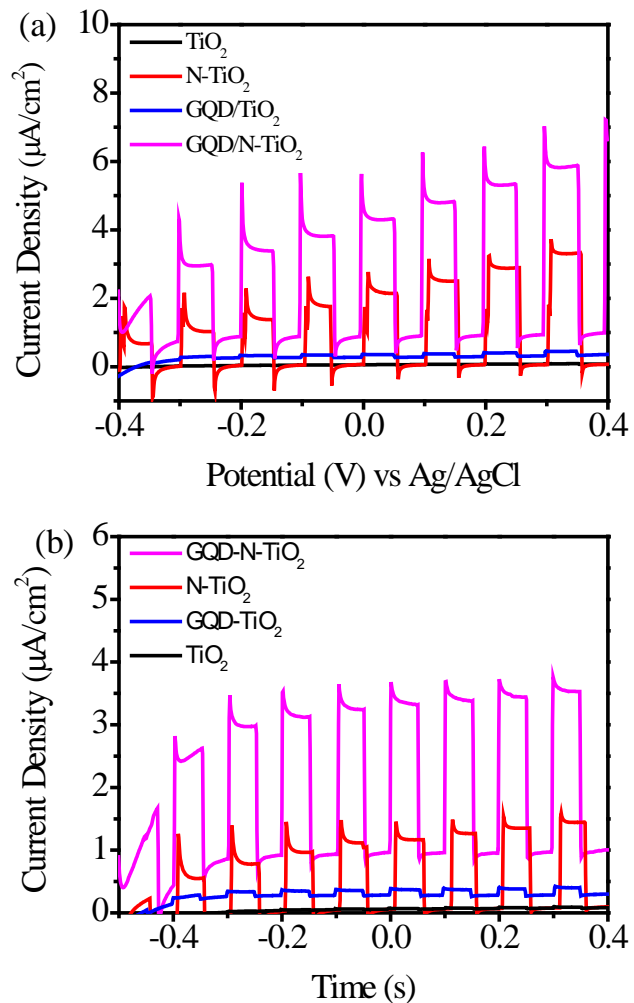


Figure 6.9. Linear sweep voltammetric (LSV) curves recorded with undoped TiO_2 and GQD/TiO_2 , N-TiO_2 and GQD/N-TiO_2 films under the illumination of (a) BLED and (b) Halogen bulb.

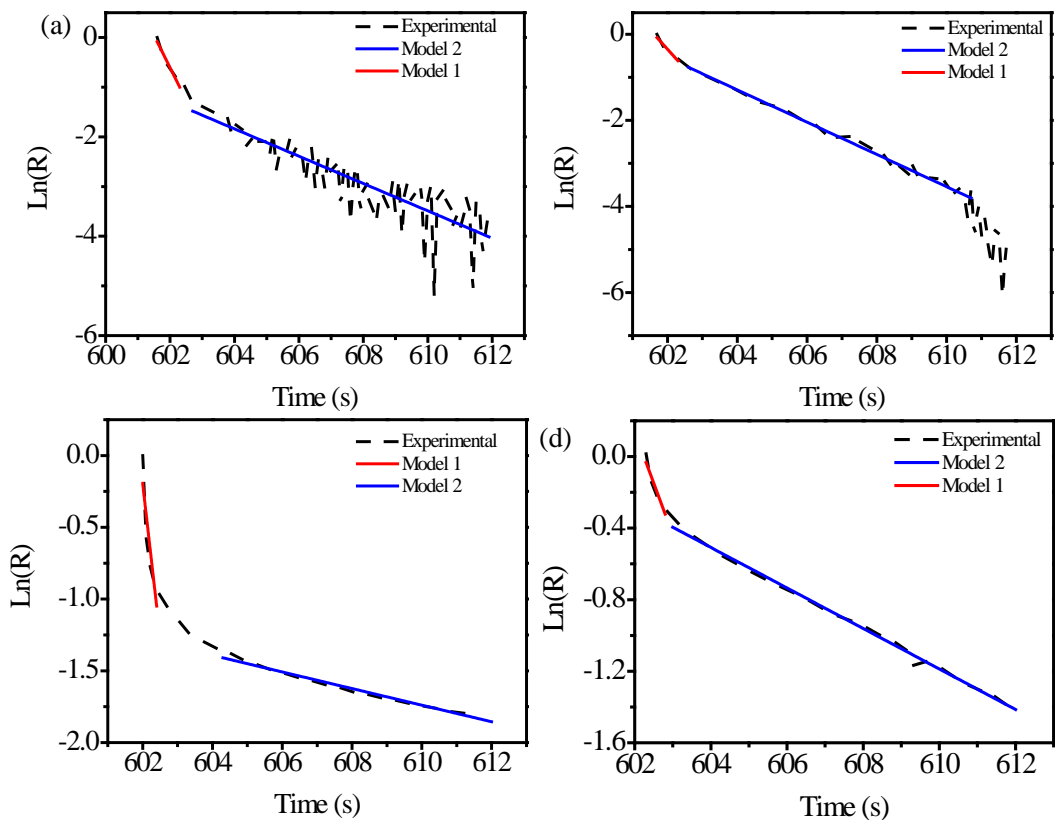


Figure 6.10. Linear fit for the $\ln(R)$ vs time curve considering only the linear portion with (a) TiO_2 , (b) GQD/TiO_2 , (c) N-TiO_2 and (d) $\text{GQD}/\text{N-TiO}_2$ film

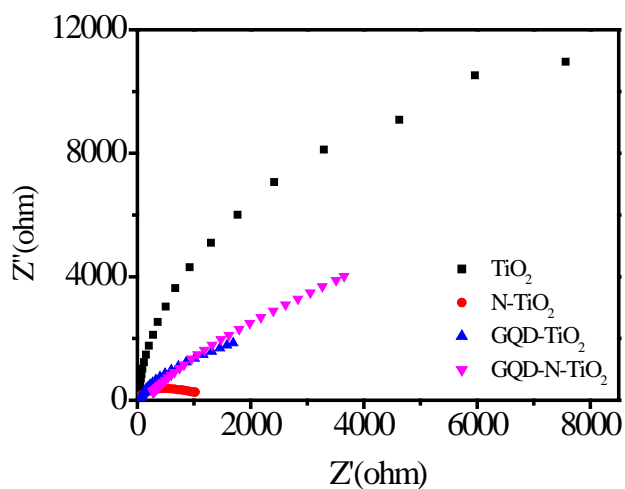


Figure 6.11. Nyquist plot recorded for TiO_2 , N-TiO_2 , GQD/TiO_2 and $\text{GQD}/\text{N-TiO}_2$ films

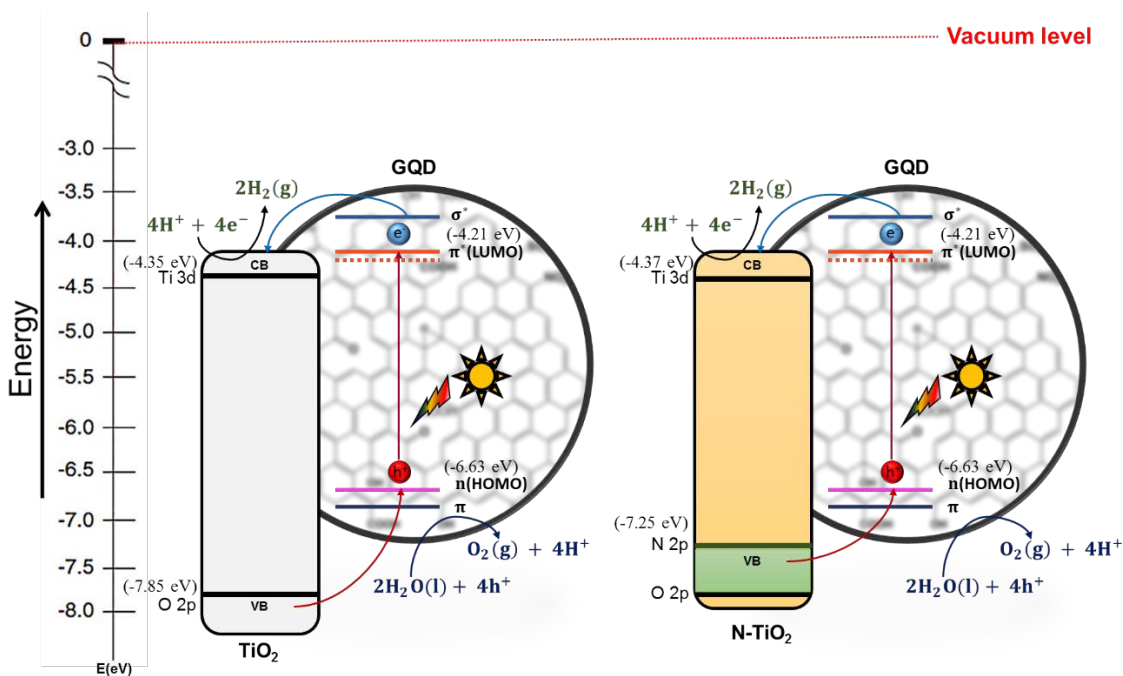


Figure 6.12. Energy band diagram for GQD/TiO₂ and GQD/N-TiO₂

Table 6.1. Photoelectrochemical water oxidation performance of titania films in amperometric *i-t* measurements

Film	Current ($\mu\text{A}/\text{cm}^2$) under BLED	Current ($\mu\text{A}/\text{cm}^2$) under halogen bulb	Enhancement under BLED	Enhancement under halogen bulb
TiO ₂	0.0175	0.018	-	-
N-TiO ₂	3.352	1.817	191	101
GQD/TiO ₂	0.0807	0.0825	4.6	4.6
GQD/N-TiO ₂	4.815	2.31	275	128

Table 6.2. Photoelectrochemical water oxidation performance of titania films in linear sweep voltammetry measurements (currents are taken at 0.35 V vs. Ag/AgCl)

Film	Current ($\mu\text{A}/\text{cm}^2$) under BLED	Current ($\mu\text{A}/\text{cm}^2$) under halogen bulb	Enhancement under BLED	Enhancement under halogen bulb
TiO ₂	0.0148	0.018	-	-
N-TiO ₂	3.289	1.4	222	78
GQD/TiO ₂	0.126	0.12	8.5	6.6
GQD/N-TiO ₂	5.1345	3.178	346	177

Table 6.3. Charge recombination rate constants for TiO₂, GQD/TiO₂, N-TiO₂ and GQD/N-TiO₂ films in the transient photocurrent decay kinetics

Film	k₁(s⁻¹)	k₂(s⁻¹)
TiO ₂	1.3	0.275
GQD/TiO ₂	0.9	0.375
N-TiO ₂	2.14	0.058
GQD/N-TiO ₂	0.58	0.113

Chapter 7. Plasma Treated Hydrogen Doped Mesoporous Black TiO₂ Thin Films for Water Oxidation Photocatalysis

7.1. Summary

In this work, we use neutron reflectometry (NR) to investigate the roles of hydrogen in plasma treated hydrogen doped mesoporous black titania thin films in their visible light absorption and enhanced photoactivity for water oxidation. The cubic ordered mesoporous TiO₂ thin films are prepared by a surfactant-templated sol-gel method and are treated with hydrogen plasma, an approach hypothesized to capitalize on the high degree of disorder in the material and the high energy of the plasma species to achieve efficient hydrogen doping. UV-vis absorbance spectra indicate that H₂ plasma treatment makes TiO₂ films black, with broad-spectrum enhancement of visible light absorption, and XPS analysis shows peak for Ti³⁺ state in treated films. The presence of hydrogen in black mesoporous titania (H-TiO₂) films is confirmed by the scattering length density (SLD) profiles obtained from neutron reflectometry measurements. The H-TiO₂ shows ca. 28 times and 8 times higher photocurrent for photoelectrochemical water oxidation compared to undoped TiO₂ films under UV (365 nm) and blue (455 nm) LED irradiation, respectively. These findings provide the first direct evidence that the dramatic change in visible light absorbance of H-treated black TiO₂ is accompanied by significant hydrogen uptake and not just Ti³⁺ generation or surface disordering.

7.2. Introduction

Sunlight driven hydrogen production by water splitting using semiconductor photocatalysts is a promising approach for the large scale production of carbon-free fuels to address worldwide energy demand and concerns over climate change due to fossil fuel use [11, 70, 72, 312-314]. Since the first demonstration of H₂ generation from the decomposition of water by Fujishima and Honda in 1972, titania has attracted significant interest as a photocatalyst due to its favorable band edge positions (which are well-matched with the redox potential of water), opto-electronic properties which can be varied by changing lattice defects or oxygen stoichiometry, superior chemical stability, photocorrosion resistance, and low cost [13-16, 195].

Despite its attractive features, the utilization of sunlight by TiO₂ has been limited, due to its large band gap. Undoped TiO₂ only absorbs ultraviolet light, which comprises 5% of the energy in the solar spectrum [72, 277]. To effectively utilize solar energy for water splitting, its band gap must be tuned to allow visible light to be absorbed. Doping is one of the most feasible potential strategies to tune the band gap of TiO₂ [17, 40-42, 286]. Various types of metallic and non-metallic dopants have been investigated [17, 18, 50]. However, satisfactory performance of metal and nonmetal doped titania has not been achieved yet. Recently, hydrogenated titania (H-TiO₂) has drawn tremendous interest because it is black and thus can absorb light over a wide range of the solar spectrum [15, 74, 214-217, 315]. The photocatalytic activity of H-TiO₂ improved significantly at UV wavelengths. However, black TiO₂ has so far exhibited minimal photocatalytic reactivity in visible light. This raises intriguing fundamental questions about the reasons for

hydrogenation turning TiO₂ black and the translation of light absorption to photochemical activity.

Some reports have shown that H-doping reduces the band gap of TiO₂ by modifying the conduction band and enhancing its photocatalytic activity [74]. It has been claimed that hydrogenation of TiO₂ leads to Ti³⁺ (or oxygen vacancy) formation which is responsible for the black color, although this is not a settled hypothesis [316]. On the other hand, many research groups have proposed that surface disorder in H-TiO₂ is primarily responsible for its black color [74, 214, 317]. Chen et al. showed that hydrogen induces disordered material at the surface of crystalline anatase nanoparticles. The hydrogen causes changes in the electronic structure and formation of mid-gap states. These mid-gap states allow electromagnetic radiation of a wide range of wavelengths to be absorbed, giving rise to the black color of TiO₂. The energy distribution of these mid-gap states obtained from large amounts of lattice disorder differs from that of a single defect in a crystal. A continuum extending to and overlapping with the conduction band edge can be formed from these mid-gap states instead of forming discrete donor states near the conduction band edge. In extreme cases, these states can also merge with the valence band. The dominant centers for optical excitation and relaxation can come from these extended energy states in combination with the energy levels produced by dopants [74].

Meanwhile, other research groups also prepared surface disordered TiO₂ (d-TiO₂) which is not black. Recent reports showed that surface defects enhance visible light absorption and charge carrier separation [31, 32]. However, the surface defects are introduced to the TiO₂ surface by heat treatment and without the introduction of hydrogen, and this d-TiO₂ is not black. Li et al. prepared sub-10 nm rutile titanium dioxide

nanoparticles from TiCl_4 by rapid hydrolysis and found efficient visible-light-driven photocatalytic hydrogen production. They argued that surface defects happen due to bridging hydroxyl group and oxygen vacancy formation. These defects bring an upward shift of the valence top of TiO_2 due to band bending associated with charge imbalance induced by the defect energy levels. In another study, Salari et al. performed surface disorder engineering in TiO_2 nanotube arrays by heat treatment in an oxygen free atmosphere and found highly efficient solar-driven oxygen evolution [32]. Heat treatment in an oxygen-free atmosphere promotes the formation of high energy facets that help to form lattice disorder on the TiO_2 and electron traps associated with undercoordinated Ti atoms. This lattice disorder forms mid-gap states instead of discrete donor states that can merge either with the valence or conduction band. This consequently leads to improved visible light absorption. Interestingly, those disordered TiO_2 nanotubes are not black but are active in visible light, which contrasts with disordered H- TiO_2 which is black in color and mostly active under UV light illumination. These studies suggest that surface disorder in H- TiO_2 is not the sole reason for its black color or for its photocatalytic activity at mostly UV wavelengths.

The above results inspired further detailed studies of H- TiO_2 to understand the origin of broad spectrum light absorption and enhanced photocatalytic activities. The presence of hydrogen may play a critical role in allowing TiO_2 to absorb both visible and infrared light. However, no studies performed to date have yielded direct evidence of hydrogen in black titania. X-ray photoelectron spectroscopy (XPS) has showed the presence of Ti^{3+} in H- TiO_2 . However, XPS cannot detect hydrogen directly due to its small atomic number. Other approaches commonly used to investigate the composition and

bonding in materials, such as energy dispersive x-ray spectroscopy and infrared spectroscopy, are also insensitive to hydrogen. To directly investigate the presence of hydrogen in H-TiO₂, we employ neutron reflectometry (NR). Generally, neutrons are powerful probes for determining structural information about light elements such as hydrogen, as neutrons interact directly with nuclei rather than electrons (as do x-rays). Furthermore, information about chemical composition of a material can be obtained from NR measurements since neutron-nucleus interactions are sensitive to differences in both atomic number and isotope [318]. Hydrogen has been successfully detected in different materials using NR [319-321]. The non-destructive nature and ability to see hydrogen and buried interfaces are other rare qualities that make NR an invaluable technique. However, no studies have been reported of hydrogen in titania using NR. Here, we use NR to investigate the presence of hydrogen in black H-TiO₂ and relate the composition and structure of the material to light absorption and enhanced photocatalytic performance of H-TiO₂.

For the application of TiO₂ in photocatalysis, it is very important to control its morphology, nanostructure, and electronic properties to enhance the available surface area, light absorption, and effective charge carrier separation and transport [18, 30-32]. Surfactant-templated mesoporous TiO₂ thin films possess several advantageous properties that are beneficial for efficient photocatalysis [18, 33, 34]. First, surfactant templating offers excellent control over structural features including nanopore size, pore orientation, interfacial structure and pore connectivity. Second, the mesoporous structure of the TiO₂ films presents a high reactive surface area for photocatalysis. Third, the thin pore walls (< 10 nm thick) of mesoporous TiO₂ films provide a short distance for the transport of

photogenerated charge carriers to catalytic sites, thereby having the potential to suppress charge recombination processes [5, 15, 33, 34]. Fourth, these nanostructured films can improve light distribution via light scattering, and provide surface area-enhanced charge transfer to lower the required interfacial overpotential [322]. Finally, neutron reflectometry measurement requires an ultra-smooth surface, which is provided by surfactant templated mesoporous TiO₂ thin films but not in other materials such as particle arrays.

For TiO₂ hydrogenation, most studies have used high temperature annealing in a hydrogen atmosphere [213, 315, 323, 324]. Plasma treatment may be a superior approach for mesoporous films because plasma-assisted doping is conducted at relatively low temperature at which the nanostructure of TiO₂ can be maintained [216, 315, 325-327]. In addition, the ionic, the high energy and active nature of the hydrogen species in the plasma makes this method more effective to incorporate hydrogen into the TiO₂ host. Finally, hydrogen plasma treatment does not cause phase transformation of titania, so the phase of titania can also be maintained [315].

In the present study, we report the first direct evidence for the incorporation of hydrogen into mesoporous TiO₂ films by H₂ plasma treatment. While some literature exists on H- TiO₂, the morphology and method of preparation play decisive roles in the activity of these materials. Hydrogen doped, ordered mesoporous TiO₂ thin films present a novel high surface area, readily doped platform for water oxidation under visible light that has not yet been investigated. Many prior studies of hydrogen doping by plasma treatment have used anodized TiO₂ nanotubes or nanoparticles [216, 326, 327]. We hypothesize that surfactant templated mesoporous TiO₂ films have several advantages over TiO₂ nanotubes. First, mesoporous titania films have smaller pores and thinner pore walls (both on the order

of 10 nm or less) than titania nanotubes (22-110 nm pore diameters and 7-34 nm thick walls) which result in higher surface areas and lower expected charge recombination in mesoporous titania films [21, 33, 166]. Moreover, surfactant templated mesoporous titania films can be prepared on any substrate whereas anodized nanotubes can only be prepared on Ti foil or substrates amenable to thin film vapor deposition. Finally, the initially amorphous structure of surfactant-templated TiO₂ films is expected to enhance the incorporation of plasma-generated high energy hydrogen species and to achieve efficient hydrogen doping and may have photocatalytic advantages based on recent reports that surface defects enhance visible light absorption and charge carrier separation [31, 32].

Further, we use NR to investigate hydrogen in hydrogen plasma treated black mesoporous TiO₂ thin films, and the films are used for photoelectrochemical water oxidation. First, cubic ordered mesoporous TiO₂ thin films are synthesized by templating films derived from TiCl₄ with Pluronic F127. Then, the films are treated with H₂ plasma generated by a microwave-assisted chemical vapor deposition (CVD) system. The structure of the films is investigated with a number of techniques including grazing incidence small angle x-ray scattering (GISAXS). For direct investigation of hydrogen, results are reported of NR performed at the Spallation Neutron Source (SNS) at Oak Ridge National Laboratory. Photocatalytic activities of hydrogen plasma-treated mesoporous TiO₂ films are studied by photoelectrochemical water oxidation under both UV and visible light irradiation.

7.3. Experimental Section

7.3.1. *Materials*

Anhydrous ethanol (200 proof, Pharmco Aaper), F127 (triblock copolymer with average structure $\text{HO}-(\text{CH}_2\text{CH}_2\text{O})_{100}(\text{CH}_2\text{CH}(\text{CH}_3)\text{O})_{65}(\text{CH}_2\text{CH}_2\text{O})_{100}\text{H}$, $M_n = 12,500$ Da, Sigma-Aldrich), TiCl_4 (tech grade, Sigma-Aldrich), deionized ultrafiltered (DIUF) water (Fisher Scientific), colloidal graphite (Ted Pella, inc.), KOH (ACS reagent grade, 85%, Fisher Scientific), Nochromix powder (Fisher Scientific), and concentrated sulfuric acid (Fisher Scientific) were all used as received.

7.3.2. *Synthesis of mesoporous titania films*

Nochromix solution, prepared by following the instructions of the supplier, was used to clean borosilicate glass slides (Fisher Scientific). Sol preparation was begun by preparing a solution of 0.67 g of surfactant F127 in ethanol (18.43g). TiCl_4 (1.12 ml) was added to the previously prepared F127 solution in a nitrogen-filled glove bag. The solution was stirred for 10 min to allow for chloride / ethoxy exchange to take place. 1.8 g of deionized water was then added to the solution slowly. The solution was stirred again for 10 minutes. The cleaned glass slides were dip coated using a home built system at a rate of 6 cm/min from this solution to prepare the TiO_2 films, followed by aging in a highly humid environment (RH ~ 94%) in a refrigerator at a temperature of 4 °C for 2 h. The high RH environment was provided by placing the slides in a sealed box with two beakers containing water. Immediately after aging, TiO_2 films were calcined in a muffle furnace (Vulcan 3-550) for 10 minutes at 350 °C. The temperature of the furnace was increased to 350 °C at a ramp of 25 °C/min but the calcined TiO_2 films were cooled rapidly after 10

minutes at the final temperature. Rapid transfer directly from the refrigerator to the furnace was carried out to avoid moisture condensation on the surface of the films [272].

7.3.3. *H₂ Plasma Treatment*

Hydrogen plasma treatment was carried out using a microwave-assisted plasma CVD system (AX5010, Seki Diamond). The schematic diagram of the plasma system is shown in Figure 7.1. The TiO₂ film was placed on a Molybdenum (Mo) stage and the chamber was evacuated. Once a base pressure of 60 mTorr was established, the chamber was purged with H₂ gas at a flow rate of 100 sccm for 10 min. Then, the pressure was brought to 5 Torr H₂ and the plasma was ignited using 300 W microwave power (2.45 GHz). With the plasma on, the pressure and power were slowly increased to 40 Torr and 400 W, respectively, where they remained for 30 minutes. For samples prepared to investigate photoelectrochemical water oxidation, the FTO slides are not stable at the harsh plasma conditions described above. Therefore, the plasma conditions were changed to a mild level at which the FTO slides are stable. At mild conditions, the plasma treatment time, pressure, power and hydrogen gas flow were 5 min, 5 Torr, 300 watts and 100 sccm, respectively.

7.3.4. *Characterization*

The morphology and structure of TiO₂ films were characterized with a scanning electron microscope (SEM) attached to a dual-beam Helios Nanolab 660 (FEI). The samples for SEM characterizations were prepared by cutting the FTO substrate on which the TiO₂ thin film was mounted using a glass cutter and then mounting the sample exactly at the center of a SEM stub coated with carbon tape. A scanning transmission electron microscopic (STEM) image was obtained from the same sample using a Helios Nanolab

660 (FEI). High resolution images of powders scraped from the mesoporous TiO₂ films were obtained by a transmission electron microscope (TEM) (JEOL 2200FS). Low angle XRD analysis was carried out using a Bruker-AXS D8 DISCOVER diffractometer to determine the degree of mesostructural order. Films were scanned at 0.5 °/min in 2θ increments of 0.02° from 1° to 4°. The optical absorbance of the samples was measurement with an UV-vis absorption spectrometer (Ocean Optics, DT-MINI-2-GS). The measurement was carried out by placing the films at an angle of ~45° relative to the incident beam to avoid interference fringes in the spectra. X-ray photoelectron spectroscopic (XPS) analysis was conducted using a ThermoScientific K-Alpha photoelectron spectrometer using monochromatic Al K-α radiation with photon energy of 1486.6 eV. Prior to XPS characterization, samples were cleaned with ethanol to remove dust from their surface.

In order to probe the presence of hydrogen in H-TiO₂ film, neutron reflectometry experiments were performed at the Liquids Reflectometer (beamline 4B) at the Spallation Neutron Source (SNS) at Oak Ridge National Laboratory (ORNL). The LR is a horizontal geometry instrument using the time-of-flight technique with an effective single bandwidth of 3.5 Å at an accelerator pulse frequency of 60 Hz. The reflectivity $R(Q)$, was measured as a function of perpendicular wave vector transfer, $Q = (4\pi/\lambda)\sin \theta$, where λ is the neutron wavelength and θ the angle between neutron beam and sample surface [328]. For these measurements, neutrons of wavelength 2.5-17.5 Å together with three incidence angles $\theta = 0.30^\circ$, 0.8° , and 1.8° , provided a wave vector transfer (Q). An incidence beam slit was adjusted for each incident angle in order to maintain a constant beam profile on the sample. The films were prepared on 5 mm thick circular silicon wafers with a diameter of 50 mm by the same modification and dip coating procedures described above. Neutron

reflectometry measurements were performed in air at room temperature and atmospheric pressure. To study the pore accessibility of the cubic ordered mesoporous titania films, neutron reflectometry experiments were performed in D₂O medium. Computer modeling and fitting program Motofit developed by A. Nelson was used to analyze the specularly reflected neutron data [318, 329]. For comparison to the experimentally acquired NR data, the Motofit program uses the Abeles formalism to calculate reflectivity from a model scattering length density (SLD) profile [330]. The average neutron scattering length density (SLD) is determined as a function of depth of the sample with a given measured reflectivity of that sample. However, the SLD profile cannot be directly determined from the measured reflectivity profile of a sample. To determine the SLD profile, Modeling of the SLD profile is performed based on the initial guess of the sample parameters on which a least squares fit is performed to the reflectivity profile. In this process, generally the known values of some parameters are kept fixed but the value of unknown parameters are varied within a given range [318]. For instance, the SLD of the backing layer (silicon wafer substrate) and the fronting layer (air or D₂O) are known and were fixed during the modeling procedure. In this work, the SLD and thickness of the TiO₂, H-TiO₂ and SiO₂ (on top of the Si substrate) were varied within a physically allowable range to obtain a best fit of the model data with the experimentally acquired reflectivity data.

The GISAXS patterns of titania films were measured in order to confirm the orientation of the pores before and after hydrogen plasma treatment. GISAXS experiments were done at the Advanced Photon Source at Argonne National Laboratory at beamline 8-ID-E using a wave length of 1.148 Å (10.86 keV) and a sample-detector distance of 2185 mm [299]. Prepared undoped TiO₂ and hydrogen plasma treated TiO₂ films were placed

on a sample holder. GISAXS patterns were collected at 0.14° incident angle at room temperature with both the sample and flight path in vacuum. The beam size was $100\ \mu\text{m} \times 50\ \mu\text{m}$ (H \times V). Data were collected with a Pilatus 1M pixel array detector using a 10 sec exposure time. Images were corrected for detector nonuniformity and converted to q-space using the GIXSGUI package for Matlab [331].

For the investigation of the crystallinity of the sol-gel templated titania thin films, GIWAXS was performed on the films before and after hydrogen plasma treatment at Advanced Photon Source at Argonne National Laboratory at beamline 8-ID-E. The plane of the thin film surface was oriented horizontally, and the sample was mounted inside a vacuum chamber. For GIWAXS, the same Pilatus detector was brought to a sample-to-detector distance of 228 mm. These measurements were performed at an X-ray wavelength of $1.148\ \text{\AA}$, with the sample under vacuum. The incident angle of the beam was fixed to 0.14° . At a beam size was $200\ \mu\text{m} \times 20\ \mu\text{m}$ (H \times V). In-plane diffraction patterns were collected as a function of the scattering vector q . The x-ray beam was allowed to enter the chamber through a mica window and was incident on the samples. Scattered x-rays exited the chamber through a Kapton window and data were collected with a Pilatus 1M pixel array detector with 10 sec exposure time. Images were corrected for detector nonuniformity and converted to q-space using the GIXSGUI package for Matlab [299, 331]. Integrated line-cut profiles of x-ray intensity vs. q_y were computed from the 2D GIWAXS patterns along angular direction ($90^\circ < \phi < 180^\circ$) using the GIXSGUI package.

The zeta potentials (ζ) of TiO_2 and hydrogenated TiO_2 thin films were measured by the streaming potential technique using a SurPASS electrokinetic analyzer (Anton Parr). The undoped TiO_2 and hydrogenated TiO_2 films were prepared on thin Ti foils (each 2 cm

× 1 cm) as flexible substrates, which are necessary for zeta potential measurement. Due to Ti foil susceptibility to hydrogen embrittlement, instead of performing hydrogenation at harsh plasma condition, hydrogenation was performed under the plasma conditions of 400 W power, 10 Torr pressure, 100 sccm flow rate and 30 minute exposure time for this measurement. Prepared samples were mounted on the sample holder of an adjustable gap cell. 0.01 M KCl was used as the electrolyte. The pH value of the electrolyte was changed from 2 to 10 using 0.05 M HCl and 0.05 M NaOH in an automatic titrator. Finally, the zeta potential measurements were recorded as a function of pH.

Contact angle measurements were performed by using a contact angle goniometer (Ramé-Hart model 100). Before the measurement, samples were thoroughly washed with deionized water and dried under vacuum for 24 hours. Advancing contact angle was recorded as the maximum angle noted upon the gradual increase of the water droplet volume.

7.3.5. Photoelectrochemical characterization

For photoelectrochemical (PEC) experiments, the films of undoped TiO₂ and H-TiO₂ were prepared on fluorine-doped tin oxide (FTO) coated glass substrates. Prior to dip coating, FTO slides were cleaned with DIUF water, acetone and isopropanol followed by UV-ozone treatment for 20 minutes to remove any organic contaminants. The photoelectrochemical measurement was carried out to evaluate the performance of H-TiO₂ films for water oxidation. These experiments were conducted in a system with a home-made glass electrochemical cell with three electrodes and a potentiostat (CHI 660D, CH Instruments, Inc.). A TiO₂ film mounted on FTO (either N-doped or undoped), a platinum wire, and a Ag/AgCl electrode were used as working, counter and reference electrodes,

respectively. 1M KOH was used as an electrolyte. Light sources were a UV LED (365 nm, Thorlabs), and a blue LED (455 nm, Thorlabs). The power densities of the UV LED and blue LED (BLED) were 6 mW/cm^2 and 22.5 mW/cm^2 , respectively. The emission spectra of light sources are shown in Appendix C Figure C.1).

Amperometric photocurrent-time (*i-t*) profiles were recorded with undoped TiO₂ and H-TiO₂ films by holding the potential at 0.4 V vs. Ag/AgCl. The light source was turned on and off every 300 seconds periodically to record photo- and dark currents. This experiment was performed for 1800 seconds. For electrochemical impedance spectroscopy (EIS), mesoporous titania thin films were deposited on boron doped Si wafers. EIS was carried out using the same potentiostat and 0.5M Na₂SO₄ as an electrolyte solution. Nyquist plots were obtained with and without halogen lamp illumination. The AC frequency was varied from 0.1 Hz to 100 kHz with the DC potential of -0.005 V vs. Ag/AgCl.

7.4. Results and Discussion

Figure 7.2 presents the UV-vis absorption spectra of pristine TiO₂ and H-TiO₂ films prepared using harsh plasma conditions. As shown in the inset of Figure 7.2, the transparent TiO₂ film becomes black after treatment with hydrogen plasma, indicating a profound effect on its optical response in the visible range. UV-vis absorbance spectra reveal that H-TiO₂ film absorbs almost the whole range of visible light (350-800 nm) whereas the absorbance of the TiO₂ film is limited only to UV light. The broad spectrum light absorption in these black films is consistent with literature [74].

The morphology and nanostructure of undoped TiO₂ film were characterized by SEM, TEM, STEM and XRD as shown in Figure 4.2 in Chapter 4. Accessible interconnected cubic ordered pores were obtained in the film. The film thickness is ca. 80

nm as determined from STEM images. The average pore diameter and wall thickness of the TiO₂ films are around 7 nm and 5.5 nm, respectively. The details of the nanostructure characterizations were described in the previous report by Islam et al.[195] The effect of H₂ plasma treatment on the nanostructure of the H-TiO₂ films prepared by harsh plasma treatment was investigated. Figure 7.3a and Figure 7.3b show SEM images of undoped TiO₂ and H-TiO₂ films, respectively. As shown in Figure 7.3b, while significant roughening of the H-TiO₂ film is observed, the majority of the pores are still accessible.

GISAXS was used to determine whether the disordered mesostructure at the top surface extended into the films after harsh plasma treatment. The GISAXS patterns of the undoped TiO₂ and H-TiO₂ films are shown in Figure 7.4a and Figure 7.4b. Three diffraction spots were observed for the undoped TiO₂ films as shown in Figure 7.4a. Those spots can be indexed to the (110), (101) and ($\bar{1}\bar{1}0$) planes of a distorted cubic ($Im\bar{3}m$) mesostructure [18]. This distortion, or contraction of the cubic structure normal to the film surface, is consistent with the STEM image as shown in Figure 4.2c. As shown in Figure 7.4b, the GISAXS pattern of a hydrogen plasma treated film indicates that the films maintain an ordered mesostructure. However, the GISAXS pattern for the H-TiO₂ film differs from the undoped TiO₂ film in that it contains only two mostly vertical rods on either side of the beam stop (Figure 7.4b). Generally, the presence of the orthogonally oriented hexagonal close packed (o- HCP) cylindrical mesophase is indicated by a single intense rod extending in the out-of-plane direction, on either side of the beam stop. These rods can be indexed to the (100) plane of the HCP structure, and their rod shape can be attributed to the finite cylindrical shape of the pores (Kiessig fringes are most likely not observed because of a distribution of rod lengths and orientations) [103, 105, 150]. The

Bragg rods were found at q_y of $\pm 0.045 \text{ \AA}^{-1}$, corresponding to a d-spacing of 14 nm which is consistent with the d-spacing (8 nm pore size and 6 nm wall thickness) indicated in the SEM images (Figure 7.3). This GISAXS study indicates that the pores in the hydrogen plasma treated titania films become vertically oriented cylindrical channels, whereas globular pores are arranged in 3-dimensional cubic order in the undoped titania films. The most likely explanation is that the plasma treatment caused the body centered cubic pores to merge into a system of vertical pores due to contraction normal to the film and fusing of pore walls. It has been proposed previously that heat treatment can transform cubic ordered pores into vertically oriented channels by this mechanism [144].

Grazing incidence wide angle x-ray scattering (GIWAXS) was performed to investigate the effect of hydrogen plasma treatment on crystallization of H-TiO₂ films. Appendix E Figure E.1a, E.1b and E.1c show the GIWAXS patterns of glass substrate, undoped TiO₂ and H-TiO₂ prepared by harsh plasma treatment, respectively. Neither sample exhibited any sharp GIWAXS features, indicating that they are amorphous. For a comparison between amorphous and anatase films, more fully crystallized titania films were prepared by calcining at 600 °C for 60 min. This film gave a GIWAXS pattern with several bright rings consistent with the powder pattern of anatase titania, as shown in Appendix E Figure E.1d. To further analyze the results, the GIWAXS data integrating along the angular direction ($90^\circ < \phi < 180^\circ$) using the GIXSGUI package to generate the 1D patterns in Figure 7.5 for glass substrate, undoped TiO₂, H-TiO₂ and anatase TiO₂ (heated at 600 °C for 60 min). As discussed above, the undoped TiO₂ and H-TiO₂ films did not show any sharp peaks in the x-ray scattering pattern which means that undoped titania is mostly of an amorphous phase. On the other hand, TiO₂ film calcined at 600 °C showed

peaks at 1.76 \AA^{-1} , 2.61 \AA^{-1} , 3.27 \AA^{-1} and 3.71 \AA^{-1} corresponding to d-spacing values of 3.57 \AA , 2.41 \AA , 1.92 \AA and 1.7 \AA , respectively. These are indexed to the (101), (103), (200) and (211) planes of anatase [332]. All 1D GIWAXS patterns in Figure 7.5 also have a broad hump over the range of $0.5 \text{ \AA}^{-1} < q < 2.5 \text{ \AA}^{-1}$, which is attributed to the presence of amorphous TiO_2 and glass substrate in the system. Thus, hydrogen plasma treatment of TiO_2 films does not induce any crystallization, even under relatively harsh conditions that induce surface roughening and a transformation of the mesophase to vertically aligned channels. This is consistent with the UV-vis measurement that hydrogen plasma does not reduce the band gap of titania films, and with prior literature that showed no phase transformation due to hydrogenation of titania [315].

X-ray photoelectron spectroscopy (XPS) was performed to investigate the effect of hydrogen plasma treatment on the chemical states of the elements in TiO_2 films. Figure 7.6a show the Ti 2p XPS spectrum of the undoped TiO_2 and H- TiO_2 films. In the undoped TiO_2 films, two peaks observed at 457.88 eV and 463.78 eV are assigned to Ti $2p_{1/2}$ and Ti $2p_{3/2}$ of Ti^{4+} , respectively [213]. The H- TiO_2 film also showed two peaks shifted to 458.38 eV and 463.98 eV for Ti $2p_{1/2}$ and Ti $2p_{3/2}$ of Ti^{4+} , respectively. Adjacent to the Ti $2p_{1/2}$ peak, a shoulder at ca. 456.0 eV was observed upon hydrogen plasma treatment. The appearance of the new shoulder at 456.0 eV in H- TiO_2 film is attributed to formation of reduced Ti^{3+} sites [333]. These Ti^{3+} states are generally attributed to oxygen vacancies in TiO_2 (assuming Schottky defects where reduction in cation charge is compensated by loss of anions), but it is also possible that in hydrogenated TiO_2 , Ti^{3+} can form by substitution of O^{2-} with H. Density functional theory calculations by Lu et al. suggest that a combination of Ti-H and Ti-OH bonds are readily formed on some facets of anatase titania,

and are responsible for the introduction of midgap states that give H-TiO₂ its black color [334]. Peak fitting was performed to deconvolute the contributions of Ti 2p_{1/2}, Ti 2p_{2/3} and Ti³⁺ in the Ti 2p spectrum of the H-TiO₂ film as shown in Appendix E Figure E.2. The content of Ti³⁺ in the H-TiO₂ film determined by deconvolution is 14.0%.

XPS O 1s spectra of pristine TiO₂ and H-TiO₂ films are shown in Figure 7.6b. Peaks were observed at 529.7 eV and 530.0 eV for pristine TiO₂ and H-TiO₂ films, respectively. Both spectra showed a small peak at about 532 eV indicating the presence of hydroxyl groups on the surface of the films. However, the peak intensity at 532 eV for the H-TiO₂ film is much higher compared to the undoped TiO₂ film, suggests that H₂ plasma treatment introduces more hydroxyl group on the films in addition to the possibility of Ti-H bond formation [335].

In order to more directly investigate the presence of hydrogen in H-TiO₂ films, neutron reflectometry was performed. Reflectivity (*R*) data were obtained as a function of the scattering vector *Q* and the data were analyzed using Motofit [329] software as implemented in Igor Pro. The model was fitted to the raw *R* vs. *Q* data resulting in a multilayer neutron scattering length density (SLD) profile as a function of normalized film depth. A materials' SLD relates its chemical composition and density according to Equation 7.1:

$$SLD = \frac{N_a \rho_m}{M} \sum_{i=1}^n b_i \quad (7.1)$$

where *M* is molecular weight of the compound, *N_a* is Avogadro's number, *ρ_m* mass density and *b_i* the bound coherent scattering length of *i*th atom comprising the material [328]. These are calculated using the SLD calculator in Motofit. The theoretical value of SLD for nonporous titania is 2.34×10⁻⁶ Å⁻² based on a mass density of 3.78 g/cm³ for anatase titania.

From the top view SEM image, the porosity calculated for titania films with cubic ordered pores is 29% (based on pore diameter of 7 nm and pore wall thickness 5.5 nm, calculated using Image J [195]), which would give a SLD of $1.65 \times 10^{-6} \text{ \AA}^{-2}$ due to the reduction in density of the film.

Appendix E Figure E.3 shows the NR data and model fit for a mesoporous TiO_2 film in air. No fringes in the NR data were observed in this sample, which did not permit SLD modelling with a great deal of confidence in the parameters. Figure 7.7 shows the neutron reflectometry data and model fit for a H- TiO_2 film measured in air. The SLD profile obtained from model fitting is presented in the inset of Figure 7.7. This profile consists of air (front layer), porous TiO_2 , SiO_2 and Si substrate (backing layer). A layer of SiO_2 a few Ångstroms thick was observed due to oxide formation on top of the Si substrate. The SLD for the porous H- TiO_2 film layer was estimated to be $0.74 \times 10^{-6} \text{ \AA}^{-2}$ which is much lower than the theoretical SLD of an undoped mesoporous TiO_2 film ($1.65 \times 10^{-6} \text{ \AA}^{-2}$). Since hydrogen has a negative SLD, it reduced the SLD of TiO_2 when incorporated in a H- TiO_2 film, so the observed reduction suggests that hydrogen has been incorporated into the lattice of the TiO_2 films. For instance, if the oxygen content of the films does not change, a material of composition $\text{TiO}_2\text{H}_{1.2}$ and 29% porosity would have a SLD of $0.75 \times 10^{-6} \text{ \AA}^{-2}$, which is similar to the experimental value. Moreover, hydrogen is uniformly distributed across the film thickness, since model containing a single layer of uniform SLD for the H- TiO_2 film was found to fit the NR data in Figure 7.7. Thus, for the first time, neutron reflectometry showed that the dramatic change in visible light absorbance of hydrogenated black TiO_2 [3] is accompanied by significant hydrogen uptake and not just Ti^{3+} generation or disordered surface formation.

Further, NR was carried out to investigate the pore accessibility of mesoporous titania films in a D₂O medium. Modeling was performed with the NR data of undoped mesoporous titania films in D₂O media as shown in Figure 7.8. The SLD profile is presented in the inset of the Figure 7.8. This profile consists of D₂O (front layer), porous TiO₂, SiO₂ and Si substrate (backing layer). A layer of D₂O of few Angstrom thickness was observed at the top of the TiO₂ film. The SLD for the mesoporous titania film was $3.24 \times 10^{-6} \text{ \AA}^{-2}$. The theoretical value of SLD for D₂O is $5.91 \times 10^{-6} \text{ \AA}^{-2}$ calculated based on the mass density of 1.1 g/cm^3 . Considering the porosity of the mesoporous films and SLD of each material, the SLD of D₂O infiltrated mesopores of titania film is expected to be a volume-weight average value. As above, assuming 29% porous titania, the calculated SLD of 71% titania and 29% D₂O is $3.38 \times 10^{-6} \text{ \AA}^{-2}$. This agrees well with the measured SLD of the D₂O-infiltrated mesoporous TiO₂ film. The calculated SLD ($3.38 \times 10^{-6} \text{ \AA}^{-2}$) of a mesoporous TiO₂ film in D₂O is much higher than the SLD ($1.65 \times 10^{-6} \text{ \AA}^{-2}$) of a film in air due to the high positive SLD value of D₂O. This indicates that the pores of the mesoporous TiO₂ films are accessible to and wetted by D₂O. Further, the thickness of the mesoporous TiO₂ film obtained from the SLD profile fit to the NR data (inset of Figure 7.8) is 95 nm, which is consistent with the thickness (98 nm) measured by profilometry previously [195].

Zeta potential measurements were carried out to probe the change in surface charge after hydrogenation. Figure 7.9 illustrates the zeta potential measurements for H-TiO₂ and undoped TiO₂ films. Apparently, the H-TiO₂ sample showed an increased negative surface charge. The surface charge of undoped TiO₂ is mainly determined by the relative density of bridging (Acidic, pKa~2.9) and terminal hydroxyl (Basic, pKa~12.7) groups [195]. Usually, these two types of hydroxyl groups have similar densities on the surface of

undoped TiO₂ [336]. Therefore, the isoelectric point (IEP) of undoped TiO₂ typically around a neutral value. However, the experimental IEP values for undoped TiO₂ available in the literature varies from 3 to 7 [337]. Measured IEP values vary mainly due to the synthesis method and the electrolyte used for the experiment [337]. Here, undoped TiO₂ showed an IEP of 4.1 which is in the range of reported literature values. After treatment with hydrogen, the IEP value was shifted to 2.63 indicating a higher relative surface acidity. This observation suggests the hydrogenation influences the surface density of bridging and terminal hydroxyl groups. Wang et al. reported that hydrogenation increases the bridging hydroxide density of TiO₂. Also, they showed proton nuclear magnetic resonance evidence for bridging hydroxyl groups present in the H-TiO₂ sample [216]. Therefore, in this study the hydrogen plasma treatment is expected to increase the relative density of bridging hydroxyl groups, although this may be due to reduction of terminal hydroxyl groups and substitution with Ti-H bonds. As a result, IEP was shifted from 4.1 to 2.63 increasing the surface acidity. Consequently, the increased negative surface charge improves the surface hydrophilicity.

The increase in surface hydrophilicity was confirmed using contact angle measurements. H-TiO₂ showed hydrophilic nature with a contact angle of 31° whereas undoped TiO₂ was more hydrophobic (contact angle of 61° - see Appendix E Table E.1). This observation is consistent with the previous reports [338]. A more negatively charged surface near pH 7 has a strong water dipole moment. Thus, H-TiO₂ possess a higher hydrophilicity. This hydrophilicity of hydrogenated TiO₂ plays a significant role in the photocatalytic water oxidation by promoting the interaction of water molecules with the catalytic surface for efficient electron transfer at the interface.

For hydrogen production from photoelectrochemical water oxidation, mesoporous titania thin films were prepared on conductive fluorine doped tin oxide (FTO) substrate. However, at harsh hydrogen plasma conditions used for NR measurement, FTO slides were unstable and photoelectrochemical water oxidation could not be performed. To get stable FTO slides, much milder plasma conditions were used to prepare H-TiO₂ films. Appendix E Figure E.4 show the UV-vis spectra of H-TiO₂ films prepared under mild conditions. At mild condition, the visible light absorption of H-TiO₂ film is a little higher than undoped TiO₂ films. SEM images of H-TiO₂ films after plasma treatment with mild conditions are presented in Appendix E Figure E.5, where accessible pores are clearly visible. This indicates mild plasma condition does not change the mesostructure of the titania films.

Amperometric i-t curves were recorded to evaluate the performance of the undoped TiO₂ and H-TiO₂ films in photoelectrochemical water oxidation as shown in Appendix E Figure E.6a and E.6b. A UV-LED and Blue-LED were used as the UV and visible light sources. Hydrogen plasma treatment of the film increased the dark current. For the sake of a direct comparison of photocurrents of the undoped and doped films, the dark current is subtracted from the total current observed for the H-TiO₂ film in Figure 7.10a and 7.10b. The photocurrent densities under UVLED and BLED for undoped TiO₂ were 0.81 $\mu\text{A}/\text{cm}^2$ and 0.018 $\mu\text{A}/\text{cm}^2$, respectively whereas the photocurrent densities under UVLED and BLED for H-TiO₂ were 22.9 $\mu\text{A}/\text{cm}^2$ and 0.16 $\mu\text{A}/\text{cm}^2$, respectively. The photocurrents of the H-TiO₂ film under UVLED and BLED are equivalent to 1.0 A/g and 0.007 A/g, respectively based upon the estimated mass per area of the film, $2.29 \times 10^{-5} \text{ g}/\text{cm}^2$, calculated using the film thickness of 80 nm, pore diameter, and wall thickness from SEM images. The photocurrents of the H-TiO₂ films in water oxidation are ca. 28 times and 8

times compared to undoped TiO₂ films under UV and visible light irradiation, respectively. This enhancement is due to the effect of hydrogen doping coupled with the mesostructure of the titania films. The reason for higher performance in UV light illumination is due to the increased charge transport and separation upon hydrogen doping. The greater enhancement found here may be a result of the ease with which the initially amorphous sol-gel titania film is doped by hydrogen plasma treatment. This photoelectrochemical enhancement significantly exceeds the values reported in prior literature. Huo et al. showed 2.6 times enhanced photocurrent in water splitting using hydrogenated Ti³⁺ self-doped TiO₂ under visible light illumination [317]. Pesci et al. prepared hydrogen-treated TiO₂ nanowires and found 2 times enhancement of water oxidation photocurrent compared to undoped TiO₂ nanotubes under a 75 W Xe lamp [323]. Zheng et al. showed 3.2 times photocurrent enhancement in water splitting by hydrogen treating TiO₂ nanowire-microspheres [339]. However, the hydrogen production from water splitting of these studies decreased drastically when only visible light was used.

While most of the literature shows that hydrogenation of titania only improves under UV light illumination, our hydrogen plasma treated mesoporous titania thin films showed not only under UV light but also visible light illumination. The absolute current density of our titania film is relatively small compared to the current density of some other titania reported in literature. The reason for lower photocurrent of our mesoporous titania thin films are very low thickness (80 nm) and low light intensity of our LEDs with low energy (365 nm and 455 nm). However, it is difficult to make absolute comparison of the photocurrents obtained from photoelectrochemical water oxidation across different measurement systems in literature because of differences in several factors including light

source, wavelength and intensity; catalyst amount; addition of various reagents (e. g. hole scavengers); addition of co-catalysts (e.g. metal nanoparticles); electrolyte pH; and applied potential. The specific photocurrent per gram of our doped mesoporous titania was estimated to be on the scale of amperes, which is quite significant considering the low intensity of the LEDs sources. The performance of our mesoporous titania thin films can be improved by depositing this hydrogen doped mesoporous titania on a substrate which is stable under harsh plasma conditions. Moreover, the absolute photocurrent of our mesoporous titania thin films can be further improved by preparing thicker films using a layer by layer deposition technique to be reported in a future contribution.

Another interesting feature of the chronoamperometric curves is the time-dependent decay of photocurrents during the illumination periods. As can be seen in Figure 7.10b, the photocurrents decay with a very rapid step (on the order of seconds) followed by slower decay before they reached constant values. The photocurrent decay is possibly due to charge accumulation at trap sites, leading to charge recombination. The photocurrent becomes stable when the rate of charge generation is equal to the rate of charge recombination. While photocurrents induced by a BLED showed prominent photocurrent decays, the UVLED did not induce noticeable photocurrent decay, as shown in Figure 7.10a. Although the origin is not clear, the difference between UV and visible light sources clearly reflect the different paths of charge carriers generated by UV and visible wavelengths. Another possibility is that this current decay might be due to lower energy of the BLED. The excited electrons and holes can easily recombine when generated by blue light, while excited electrons and holes generated by the higher energy UV- LED have less

chance to recombine. Excited electrons reach the top of the conduction band with the high energy of UV-LED and are not available to recombine with the holes in the valence band.

As a final measurement of the electrochemical characteristics of the films, Nyquist plots were recorded for undoped TiO₂ and H-TiO₂ films in 0.5M Na₂SO₄ in the dark, as shown in Figure 7.11. A much smaller area under the semicircular portion of the curves is observed for the H-doped TiO₂ film compared to undoped TiO₂, indicating more efficient charge transfer at the electrolyte-electrode interface due to hydrogen doping. Hence, more efficient photogenerated electron-hole pair separation and faster interfacial charge transfer are able to occur in H-TiO₂ compared to undoped TiO₂ film. The accelerated charge transfer kinetics of the H-TiO₂ films is consistent with the photocurrent enhancement in the amperometric measurements. To gain more insight into the optoelectronic properties of the films, further photoelectrochemical characterization was performed. Open circuit potentials (OCP) were measured for undoped TiO₂ and H-TiO₂ films in dark condition in 0.5M Na₂SO₄. The OCP values of undoped TiO₂ and H-TiO₂ film in the dark were 0.228 V and -0.07 V, respectively. A more negative value of OCP found for H-TiO₂ indicates favorable energetics for water oxidation since it determines the difference between the Fermi level of a semiconductor and the redox potential of the electrolyte [166].

7.5. Conclusion

In this study, neutron reflectometry was used to detect the hydrogen in plasma hydrogen doped mesoporous titania thin films, and the films were used for hydrogen gas production via photoelectrochemical water oxidation. The mesoporous titania films prepared by a surfactant templated sol-gel process became black and showed significantly enhanced absorption of visible light after hydrogen plasma treatment. Direct evidence of

the effects of hydrogen plasma treatment in surfactant templated TiO₂ thin films could only be determined using neutron reflectometry and showed that the SLD for hydrogen doped films is smaller than that of undoped mesoporous TiO₂ films, which is consistent with hydrogen incorporation into the lattice of the titania films. Thus, for the first time, neutron reflectometry showed that the dramatic change in visible light absorbance of H-treated black TiO₂ is accompanied by significant hydrogen uptake and not just Ti³⁺ generation or surface disorder. GISAXS measurements also showed that the film remained mesoporous after hydrogen plasma treatment whereas GIWAXS measurements confirm that the film maintains its atomically disordered phase. The hydrogen doping effect was demonstrated by hydrogen production by photoelectrochemical water oxidation, which showed an increase in photocurrent of ca. 28 times and 8 times compared to undoped TiO₂ films under UV and visible light irradiation, respectively. Further, impedance spectroscopy measurement showed that hydrogenation in mesoporous titania films improves the charge transfer kinetics. This study demonstrated that hydrogen plays a critical role in the black color of plasma treated hydrogen doped mesoporous titania thin films and in more complete utilization of UV and visible light for water oxidation photocatalysis. The new insights into hydrogenated titania introduced here will be useful for the design of efficient nanostructured photocatalysts for energy applications.

Figures of Chapter 7

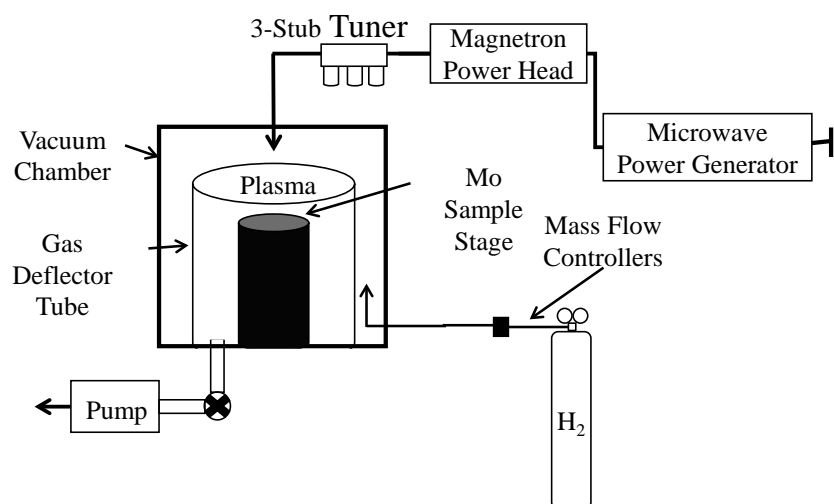


Figure 7.1. Schematic of the plasma reactor used for H₂ plasma treatment of TiO₂ films.

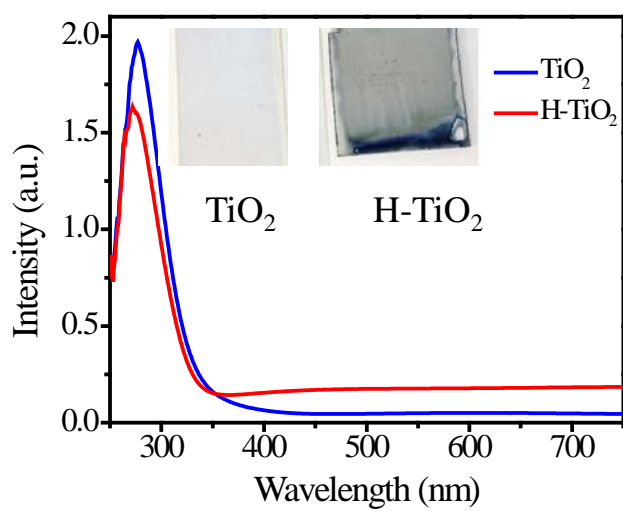


Figure 7.2. UV-vis spectra of mesoporous undoped TiO₂ and H-TiO₂ films

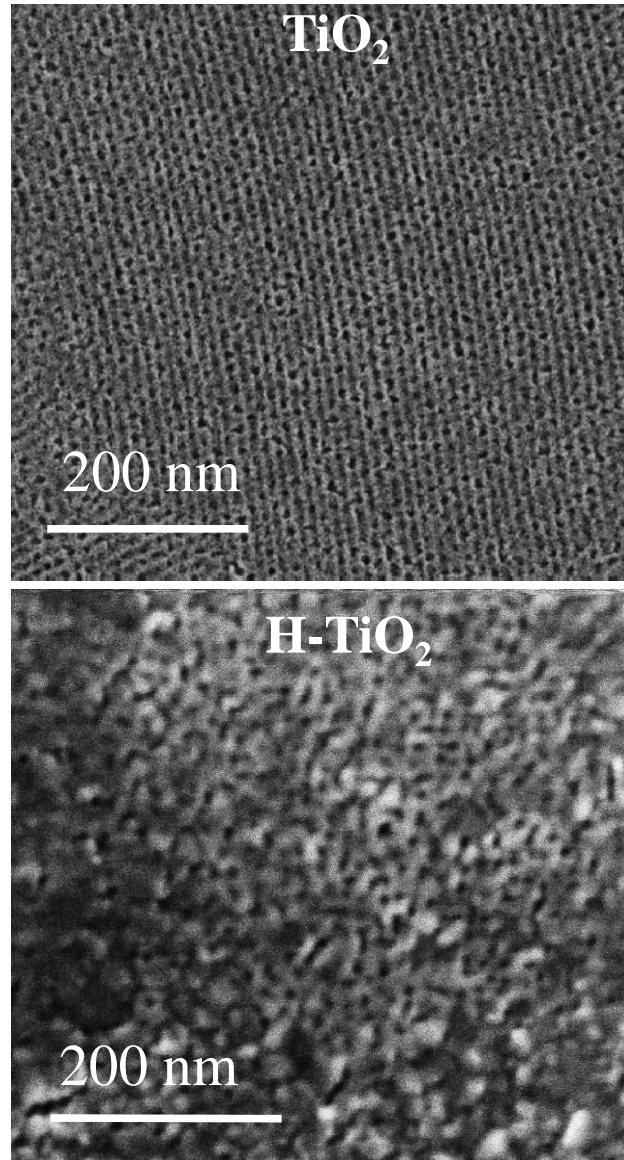


Figure 7.3. SEM images of (a) undoped TiO_2 and (b) H-TiO_2 films

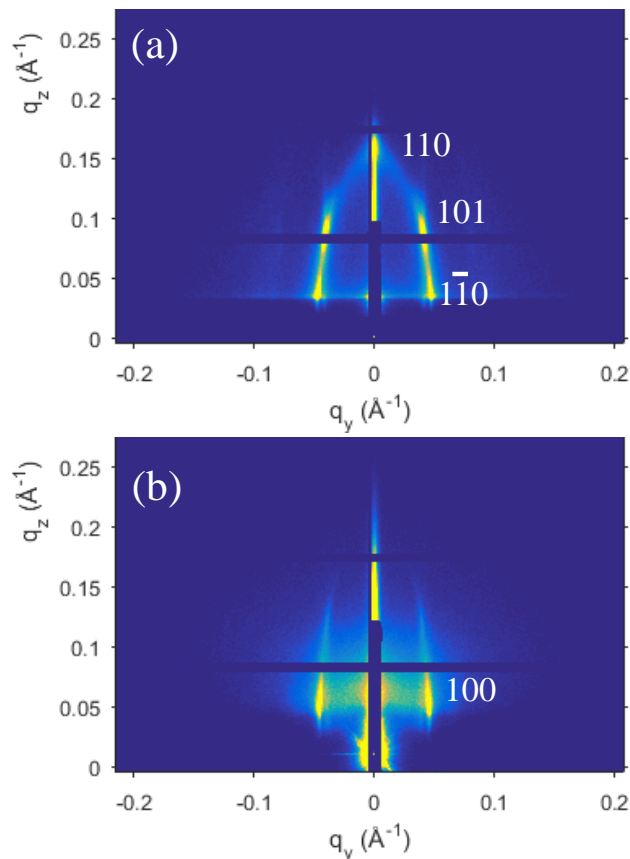


Figure 7.4. GISAXS patterns of (a) undoped TiO₂ and (b) H-TiO₂ films

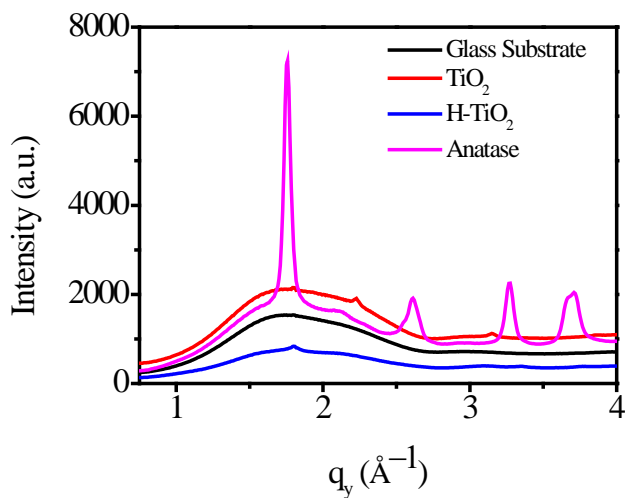


Figure 7.5. GIWAXS line cut patterns of undoped TiO₂, H-TiO₂ and anatase TiO₂ (calcined at 600 °C for 60 min) films. Integrated line-cut profiles of x-ray intensity vs. q_y were computed from the 2D GIWAXS patterns along angular direction ($90^\circ < \phi < 180^\circ$) at a fixed range of q_y values using GIXSGUI package.

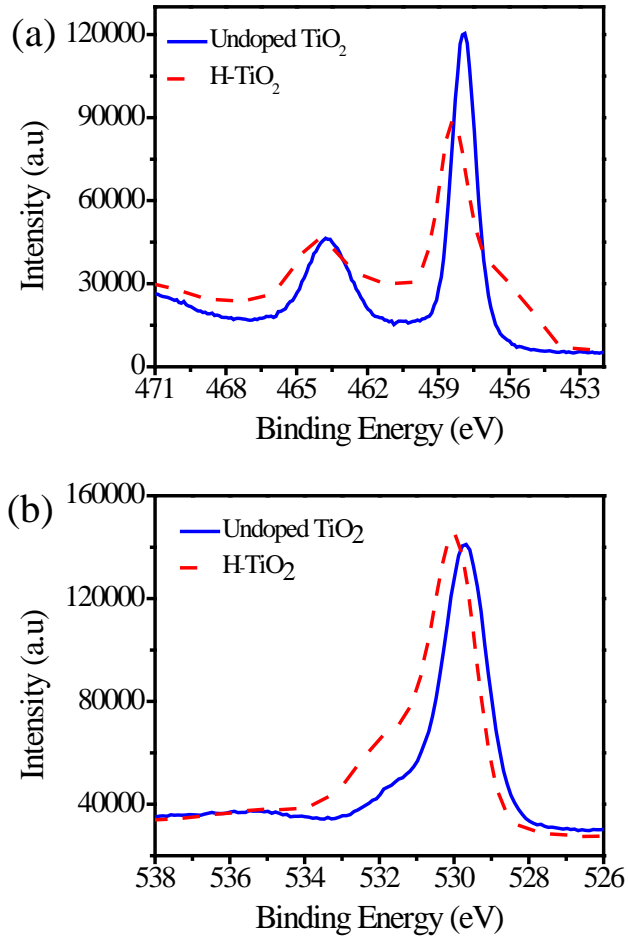


Figure 7.6. (a) Ti 2p and (b) O 1s high resolution XPS spectra of undoped TiO₂ and H-TiO₂ films.

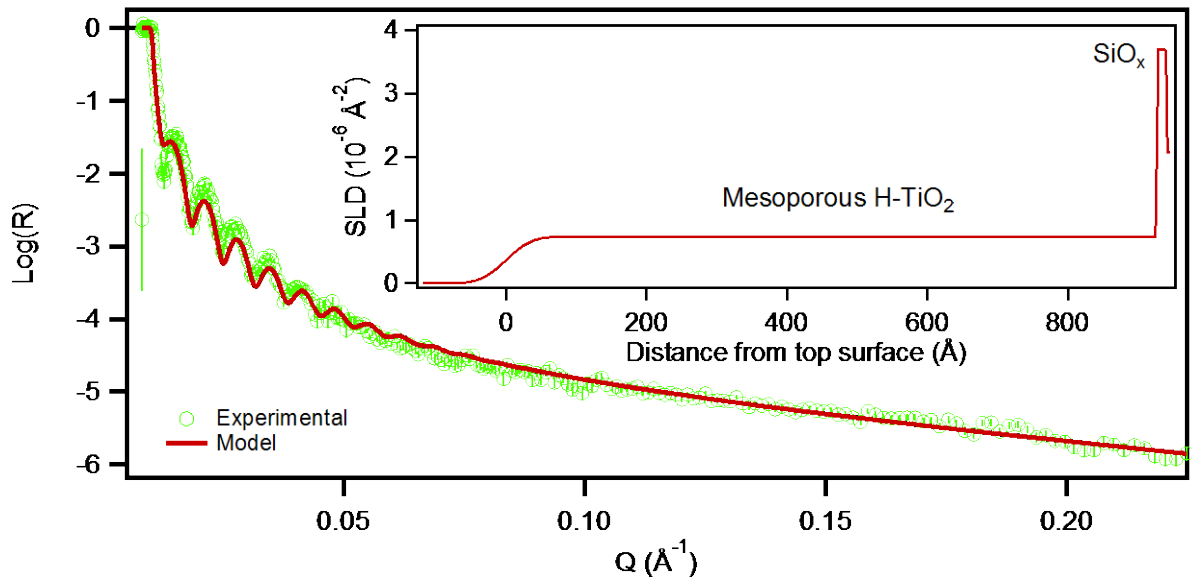


Figure 7.7. NR profile of H-doped mesoporous TiO₂ film in air. The inset shows the scattering length density (SLD) profile of the fitted model.

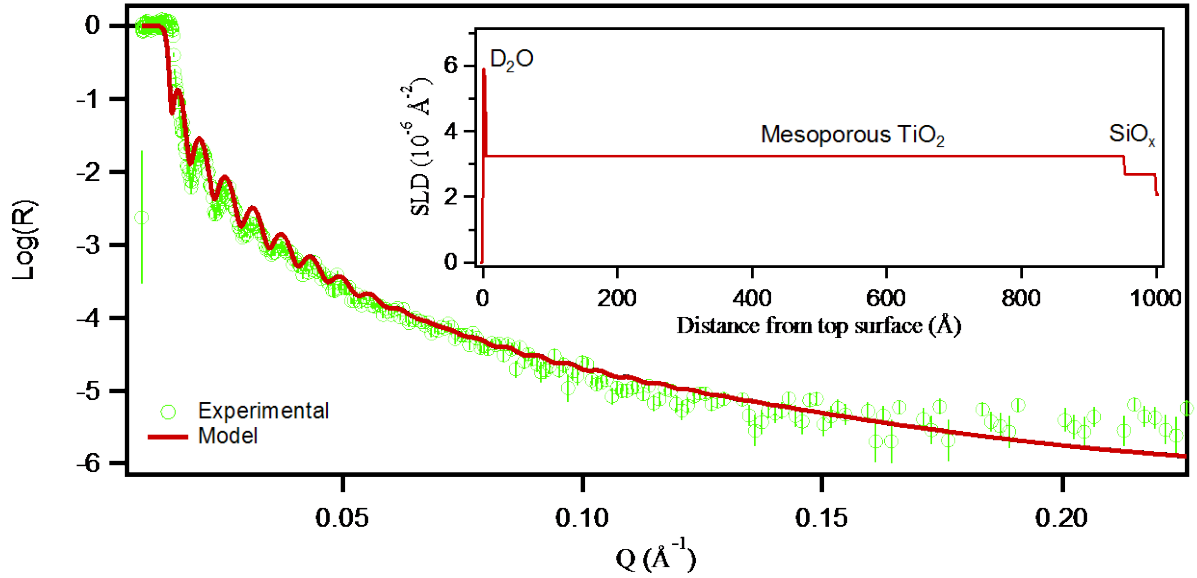


Figure 7.8. NR profile of undoped mesoporous TiO₂ film in D₂O. The inset shows the scattering length density (SLD) profile of the fitted model.

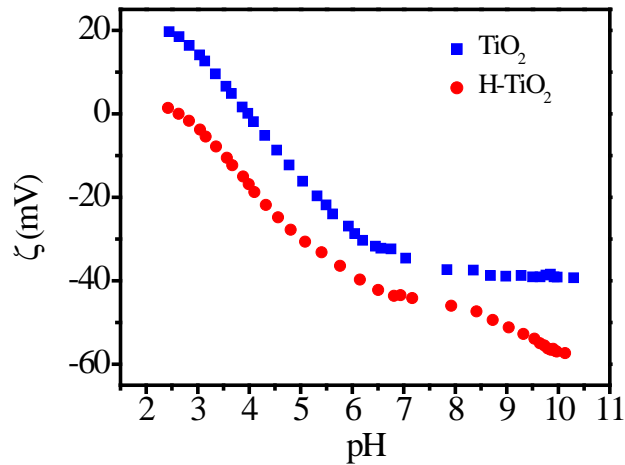


Figure 7.9. Zeta potential measurements of undoped TiO₂ and H-TiO₂ films

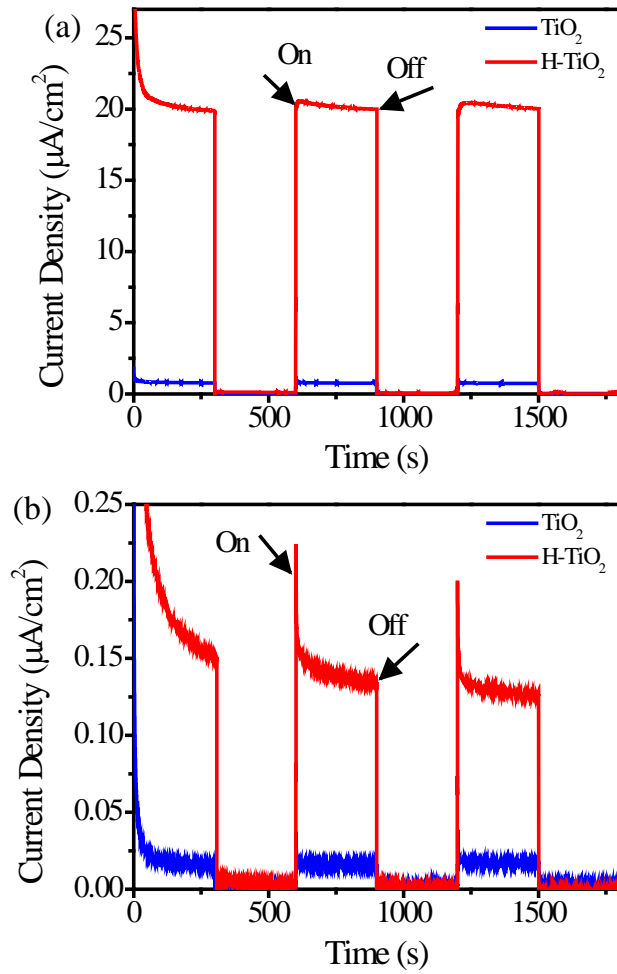


Figure 7.10. Photocurrent-time measurement with undoped TiO_2 film and H-TiO_2 films under (a) UVLED and (b) BLED light irradiation.

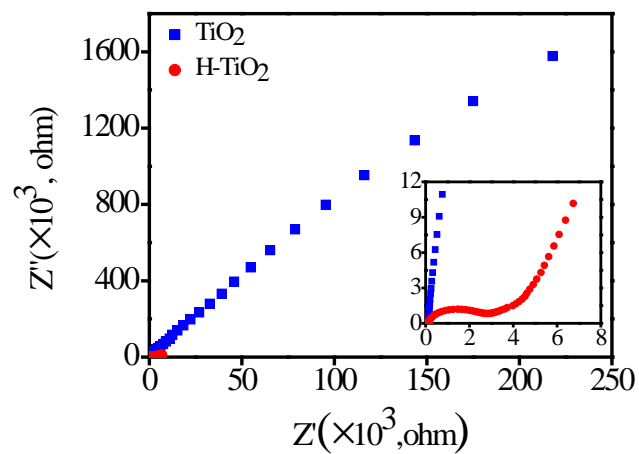


Figure 7.11. Nyquist plot of TiO_2 and H-TiO_2 films (Inset shows enlarged plot).

Chapter 8. Conclusions and Future Work

8.1. Conclusions

This dissertation addressed the synthesis of mesoporous titania thin films by the surfactant templated sol-gel process, and the application of these films in energy conversion, with special emphasis on hydrogen production by photocatalytic water splitting under visible light illumination. Mesoporous TiO_2 presents opportunities for use in a number of applications due to combining a favorable morphology (accessible pores, high surface area, well-defined mesostructure, tunable pore size and shape, and thin pore walls) with innate optoelectronic activity. It is of particular interest for high-volume applications because of its low cost and environmentally benign nature. These unique properties make it highly promising in environmental, energy conversion and storage applications. To address the challenge of using titania as a photocatalyst, whose band gap is larger than the energy of abundant visible light in the solar spectrum, doping a foreign element into titania lattice is one of the potential strategies to tune the band gap of titania to enhance the visible light driven photocatalytic activity. However, incorporation of a foreign element into the mesoporous TiO_2 lattice while controlling its phase and mesostructure remains a challenge because successfully producing doped titania for photocatalytic applications involves a tradeoff between maintaining the favorable morphology of the material (high specific surface area, controlled pore morphology, crystalline phase, etc.) while selecting doping source and method that effectively introduces dopants at a high enough level and in the appropriate chemical state for band gap reduction, visible light absorption, control of charge carrier recombination, and ultimately, enhancement in photocatalytic activity.

In this dissertation, the band gap of mesoporous titania thin films was engineered by modification of the conduction and valence band using nitrogen and hydrogen doping by two different doping methods. For nitrogen doping in these mesoporous titania thin films, molecular precursor (hydrazine) based and plasma based methods have been developed. Results showed that plasma-based doping (which made the films yellow in color while pristine titania is colorless) is superior to molecular precursor-based doping for incorporation of substitutional nitrogen in titania. The substitutional form is primarily responsible for band gap reduction, visible light absorption and photocatalytic activity. Furthermore, the nanostructure of the films was better maintained in the plasma-based treatment than in molecular precursor-based doping. To modify the conduction band of the mesoporous titania films, hydrogenation was performed using a plasma system and found to turn the mesoporous titania films black. This study addressed the fundamental reason for this black color of hydrogenated titania films by probing for the presence of hydrogen in the films using neutron reflectivity. Along with band gap engineering for visible light absorption, sensitization using environmental friendly graphene quantum dots was also performed in mesoporous titania thin films. For the first time, graphene quantum dot sensitization and nitrogen doping of titania were combined for enhancement visible absorption, charge separation, and photocatalytic activity. For applications, all modified films were tested for activity in hydrogen production by photoelectrochemical water splitting under visible light illumination.

Before all the modifications by band gap engineering and sensitization, and subsequent photocatalytic tests, first, cubic ordered mesoporous titania thin films were synthesized by surfactant templating sol-gel method using a Pluronic surfactant F127. For

molecular precursor-based doping, hydrazine was used to prepare titanium (Ti^{3+}) and nitrogen co-doped mesoporous TiO_2 thin films as presented in Chapter 3. The cubic ordered mesoporous TiO_2 thin films were treated with hydrazine in a closed vessel to allow long-term exposure to hydrazine from the vapor phase. XPS characterization showed that both interstitial and substitutional nitrogen are present inside of the doped films. The doped films were tested by photocatalytic degradation of methylene blue under visible-light illumination (blue-LED) and found a significant enhancement in photocatalytic activity over undoped TiO_2 films. The Ti^{3+} -N- TiO_2 film prepared by 10 hours of hydrazine treatment showed the optimal photocatalytic performance with the determined rate coefficient of 0.12 h^{-1} ($85 \text{ min}^{-1}/(\text{g catalyst})$), roughly 3 times greater than that of undoped TiO_2 films. The Ti^{3+} -N- TiO_2 films prepared with 10 hours of hydrazine treatment also showed optimal performance in the photoelectrochemical water oxidation, roughly four times the photocurrent of undoped TiO_2 films. This study thus demonstrates the effectiveness of hydrazine treatment as a single source of Ti^{3+} and N dopant for mesoporous TiO_2 thin films prepared by surfactant templating, which leads to improved photocatalytic and photoelectrochemical performance.

For plasma-based doping, mesoporous TiO_2 films were treated with N_2/Ar plasma. XPS showed about 2-3 at% substitutional nitrogen in the doped films. The band gap of the films was reduced from 3.5 eV (in undoped TiO_2 films) to 3.0 eV (in N- TiO_2 films) by plasma treatment as confirmed by UV-vis spectroscopy characterization. The photocatalytic evaluation of the plasma treated N- TiO_2 films was conducted by methylene blue degradation under visible light illumination (blue-LED). The N- TiO_2 films showed roughly 6 times greater (rate coefficient of 0.24 h^{-1}) degradation than that of undoped TiO_2

films. This enhancement in photocatalytic activity is significantly greater than the enhancement reported on plasma treated titania with other morphologies and phases.

Further, the visible light active plasma treated N-TiO₂ films developed in Chapter 4 was applied for hydrogen production from photoelectrochemical water splitting. In Chapter 5, the nitrogen plasma condition was reassessed to obtain nitrogen doped mesoporous titania films onto a stable conductive fluorine doped tin oxide substrate. Moreover, plasma pressure and nitrogen flow rate in the plasma chamber were varied to find out an optimum condition for the best performance of the doped films in photoelectrochemical water oxidation. The greatest photocurrent enhancements observed under UV (UVLED with 365 nm wavelength) and visible (Blue-LED) light illumination were 242 times and 240 times, respectively. Interestingly, these results show that plasma treated sol-gel derived N-TiO₂ films showed remarkable enhancement in water oxidation not only with visible light, but also under UV light which is rarely observed in literature. This enhancement in water oxidation is much greater than the values of previous reports (where a maximum of 7 times enhancement was reported [294]). The combination of a sol-gel approach to forming disordered mesoporous TiO₂, and using N₂/Ar plasmas to introduce a high level of substitutional nitrogen under mild conditions contributed to these two order of magnitude increases in photocatalytic activity. Preventing rapid crystallization into anatase TiO₂ seems to be important to accomplishing this high level of enhancement. We also suspect that the effect is enhanced by the generation of catalytically active surface sites. These remarkable enhancements of the plasma treated nitrogen doped mesoporous titania in photocatalytic and photoelectrochemical activities demonstrate that plasma-based

approach is an efficient way to modify sol-gel derived metal oxides for their optoelectronic properties and catalytic activities.

The visible light driven photocatalytic activity of nitrogen doped titania films developed in Chapter 4 and 5 was further enhanced by sensitization. In Chapter 6, nitrogen doping by plasma-based approach and sensitization using graphene quantum dots (GQDs) are combined in mesoporous titania films for better visible light absorption and efficient photogenerated charge separation. First, GQDs were prepared by chemically oxidizing carbon nano-onions and were immobilized onto the mesoporous titania surface using a hydrothermal method. In photoelectrochemical water oxidation under blue LED illumination, the GQD/TiO₂ and GQD/N-TiO₂ films showed about 4 times and 275 times enhancement, respectively while N-TiO₂ showed about 191 times enhancement compared to unmodified TiO₂ film. This indicates that when sensitization with graphene quantum dots is combined with plasma-induced nitrogen doping in sol-gel derived mesoporous titania, synergistic effect emerges for photocatalytic water oxidation. This synergistic effect is attributed to enhanced visible light absorption, efficient charge separation, transport and transfer. This study provides new pathways for developing nanostructured composite materials based on engineering the energy band alignments of doped materials and quantum dots for fundamentally improving visible light absorption, charge separation and transport, and thereby energy and environmental applications.

While substitutional nitrogen doping modifies the valence band of titania, hydrogen doping affects the conduction band, thus impacting both electronic properties and photocatalytic activity. Hydrogenated titania is black but there are several hypotheses about the cause of this, as reviewed in Chapter 7. Neutron reflectometry was used to detect

hydrogen in hydrogen plasma-doped mesoporous titania thin films, and the films were used for photoelectrochemical water oxidation in Chapter 7. Direct evidence of the effects of hydrogen plasma treatment in TiO₂ was found using neutron reflectometry by observing changes in scattering length density (SLD). A decrease in SLD for hydrogen doped films indicated hydrogen incorporation into the lattice of the titania films. Thus, for the first time, neutron reflectometry showed that the dramatic change in visible light absorbance of H-treated black TiO₂ is accompanied by significant hydrogen uptake and not just Ti³⁺ generation or surface disorder. The hydrogen doping effect was demonstrated by measurements of photoelectrochemical water oxidation, where increases in photocurrent were measured of ca. 28 times and 8 times compared to undoped TiO₂ films under UV and visible light irradiation, respectively. This study demonstrated that hydrogen incorporation plays a critical role for the development of black color in plasma-treated hydrogen doped mesoporous titania thin films, and helps to utilize the absorbed UV and visible light for water oxidation photocatalysis. The new insights into hydrogenated titania found here will be useful for the design of efficient nanostructured photocatalysts for energy and environmental applications.

8.2. Future Work

Although significant progress in visible-light photoactivity of titania has been made already, further improvements in visible light absorption, separation of photogenerated charge carriers, and charge transfer to reactants are necessary for the use of titania in practical photocatalytic applications. In Chapter 4, 5 and 7, plasma based nitrogen and hydrogen doping were carried out in mesoporous titania films separately and found remarkable photocatalytic enhancement. Since nitrogen and hydrogen co-doping enhances

the visible light absorption and photocatalytic activities of titania more than doping with either nitrogen or hydrogen alone, co-doping using hydrogen and nitrogen plasma treatments provide a promising direction for future research. A new direction that may provide opportunities for better charge separation would be to develop heterojunctions of hydrogen-doped titania and nitrogen-doped titania. When electrons and holes are excited in either hydrogen doped region or the nitrogen doped region of the films, those charge carriers will propagate to physically separated regions resulting in better charge separation. For instance, when electrons are excited in hydrogen-doped domains, before combining with the holes in the same domain, those electrons can move to the empty conduction band of nitrogen-doped domains. On the other hand, when electrons are excited in nitrogen doped domain, holes are formed in the valence band and those excited holes can easily move the hydrogen doped domain which results in better charge separation. Since the hole and electron diffusion lengths of TiO_2 are on the order of 10 nm and 10 μm , respectively, and the pore walls of mesoporous TiO_2 are thinner than 10 nm, the photogenerated holes can easily move to the TiO_2 surface for reaction before recombination.

An intimate junction between nitrogen and hydrogen doped region can be achieved using single-mask plasma lithography, which takes advantage of the directionality of plasma exposure. Patterning of the H-doped and N-doped regions can be accomplished by masking regions not to be exposed to plasma. A preliminary demonstration of this possibility is shown in Figure 8.1 where H-doped and N-doped films patterned were formed by masking mesoporous titania films with fractured Si wafers. Plasma treated N- TiO_2 films prepared by masking some portion of the film created macroscopically well-defined undoped (colorless) and doped (yellow) regions as shown in Figure 8.1. A XPS

line scan was performed across the film as shown in Figure 8.2. A distinct N1s peak was found in the doped portion of the film whereas undoped portion of the films did not show significant signal. The line scan across the N-doped interface shows that a gradient of substitutional nitrogen has been achieved over a length scale on the order of 100 μm . To form heterojunctions with domain size in the order of a micron or less, a novel single-mask plasma lithography process is envisioned in which the effects of H_2 plasma treatment are first reversed with O_2 plasma or N_2 plasma so that only one mask is needed. This will address potential concerns about double-doping of some areas and also help to form an intimate contact between two doped regions. After successful preparation of the heterojunction, the methods developed as part of this dissertation can be used to understand the effects of the heterojunction on light absorption, electrochemical properties of the materials, and photocatalytic water oxidation.

In Chapter 6, sensitization of N-doped titania with graphene quantum dots was found to cause significant enhancement in visible light absorption and photocatalytic activity of titania films. A new direction to enhance visible light absorption of titania would be sensitization with bioinspired compounds such as dopamine. Dopamine is an enediol ligand and is expected to have large affinity for under-coordinated surface metal sites due to its ability to chelate with transition metals to satisfy their desired coordination [340]. An enhanced interfacial charge transfer rate was found due to the formation of charge-transfer complexes with enediols on TiO_2 [341]. Further, dopamine derivatives sensitize TiO_2 to improve its visible light absorption [342, 343]. Moreover, dopamine contains an amine group which would change the surface charge in the positive direction, and would be expected to promote the absorption of anionic and hydrogen bonding solutes for

photocatalysis. Hence, it is hypothesized that dopamine functionalized mesoporous titania films will be very active in visible light driven photocatalysis by taking advantage of electronic and surface chemistry tuning on the surface of mesoporous titania films.

Preliminary experiments on dopamine sensitized mesoporous titania films were conducted. Cubic ordered mesoporous TiO₂ films were submersed in an aqueous solution of 1.0 mM dopamine to allow dopamine to be adsorbed onto the film. The films were then removed and allowed to air-dry. Figure 8.3 shows photographs of an unmodified (colorless) TiO₂ film and a dopamine functionalized TiO₂ (DA-TiO₂) film. The treated film has a yellow/orange color, which arises only because of the interaction between dopamine and titania (since each component alone is colorless). The modified films were tested for activity in photoelectrochemical water splitting with illumination using a blue LED (455 nm wavelength). The initial photocurrent measured for DA-TiO₂ films was found to improve significantly over unmodified TiO₂ films (data not shown). However, the photocurrent of DA-TiO₂ films decays significantly over time, suggesting that the modification is not stable either due to desorption or degradation of dopamine. This is most likely due to the high pH (13.5) of the KOH solution used by default in this dissertation for water splitting. To gain the benefits of dopamine modification in a stable photoelectrochemical system, future directions to pursue include developing a stable functionalization strategy using either heat treatments, pH or chemical modification of the surfaces; and using different conditions for photoelectrochemical measurements to avoid destabilization of the films during photocatalysis measurements.

Future directions to improve the efficiency of doped and sensitized mesoporous TiO₂ films will be aimed at better understanding the bottlenecks in environmental

remediation, energy conversion, and energy storage systems that limit the commercialization of these materials. It is essential to understand the charge transfer dynamics among dopants, sensitizer, mesoporous TiO₂ and reactants molecule to further improve the photocatalytic performance of mesoporous TiO₂ films. The effects of doping, sensitization and heterojunction formation on the charge carrier lifetime can be investigated using ultrafast pump-probe spectroscopy. This technique was attempted using doped titania films and sensitized titania films in collaboration with the Ultrafast Spectroscopy Facility at the University of Louisville. However, the experiments were not successful because the low quantity of material present in the thin films developed in this dissertation. To be able to use this technique, the quantity of material need to be increased by depositing multilayer films using layer-by-layer deposition technique, which is an approach under development in the Rankin laboratory. The photoactivity can also be improved by making this thick multilayer films to optimize light absorption vs. reactant and charge carrier diffusion in the materials.

In addition to non-metal dopants themselves, there is room to better understand metal co-catalysts. Noble metals act as passive sinks for electrons to promote the interfacial charge transfer process and enhance the quantum efficiency of photocatalytic system [44, 255-257]. In addition, metal nanoparticles show plasmonic effects and provide hot electrons into the conduction band of titania. Incorporation of noble metal nanoparticles (such as Pt, Au, Ag) and transition metals such as Cu onto non-metal doped mesoporous TiO₂ film would benefit from further exploration. Furthermore, the fabrication of non-metal doped mesoporous TiO₂ composites with other metal oxides such as hematite and

perovskite such as strontium titanate will open the door to enhanced visible light absorption and charge separation for further improving photocatalytic activity.

Although great progress has been made in the development of the materials in terms of functionality and visible light absorption for applications in degradation of organic pollutants such as methylene blue (which may be considered as model pollutant), and hydrogen production from water splitting, all the modified titania films developed in this dissertation are very promising materials for applications in other environmental organic pollutants (such as, chlorinated aromatic hydrocarbons, surfactant, dyes, herbicides, etc.) and inorganic pollutants (such as, CN^- , CrO_4^{2-} , etc.); in other energy conversions such as CO_2 reduction; and in energy storage such as in lithium ion batteries and supercapacitors. Future work in all of these directions is expected to yield significant insights into the nature and generality of the electronic modifications induced by plasma doping in mesoporous titania materials.

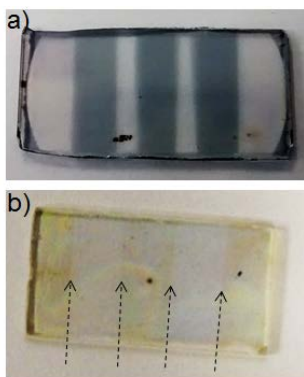


Figure 8.1. Preliminary test of masking with a fractured Si wafer for (a) H-doping and (b) N-doping. A line scan by XPS of the N-doped interface.

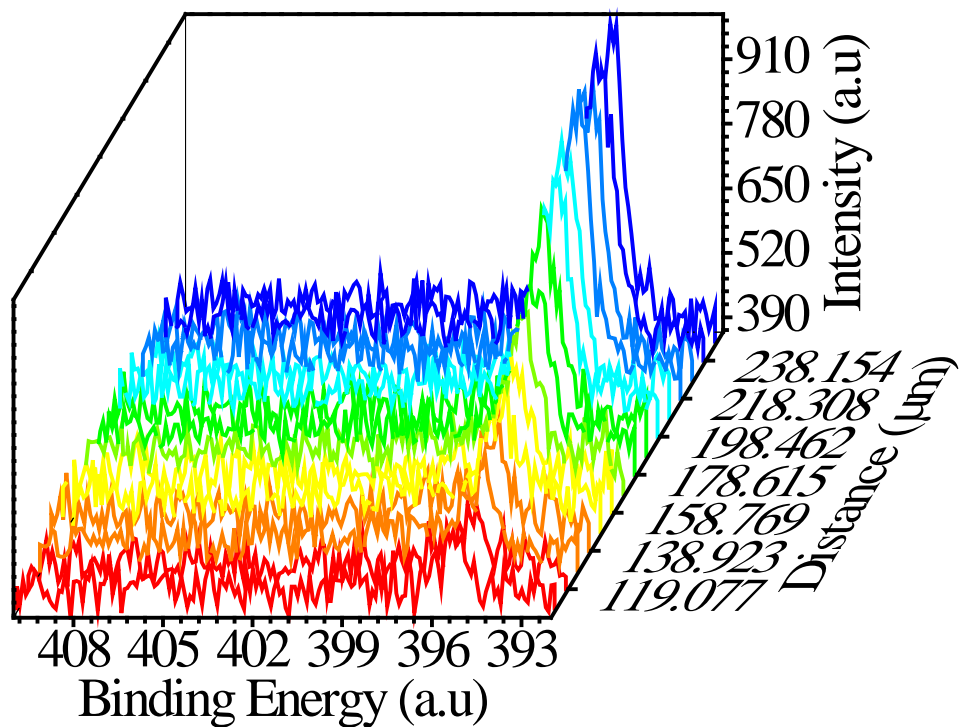


Figure 8.2. XPS N1s spectra of N-TiO₂ film prepared by masking some portions of the film (line scan was performed) (small scale).



Figure 8.3. An untreated TiO₂ film (left) compared to a dopamine treated TiO₂ film (right).

APPENDIX

APPENDIX A Supporting Information of Chapter 3

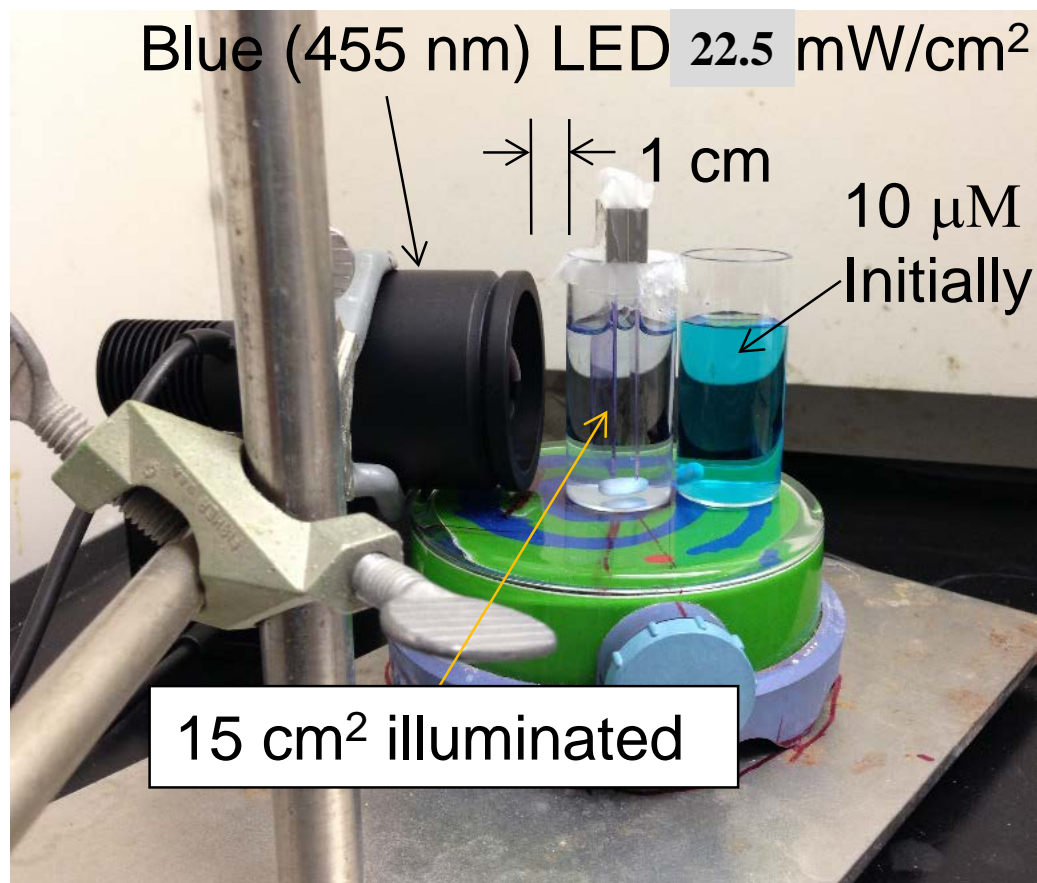


Figure A.1. Photograph of the experimental set-up for methylene blue degradation reaction measurements.

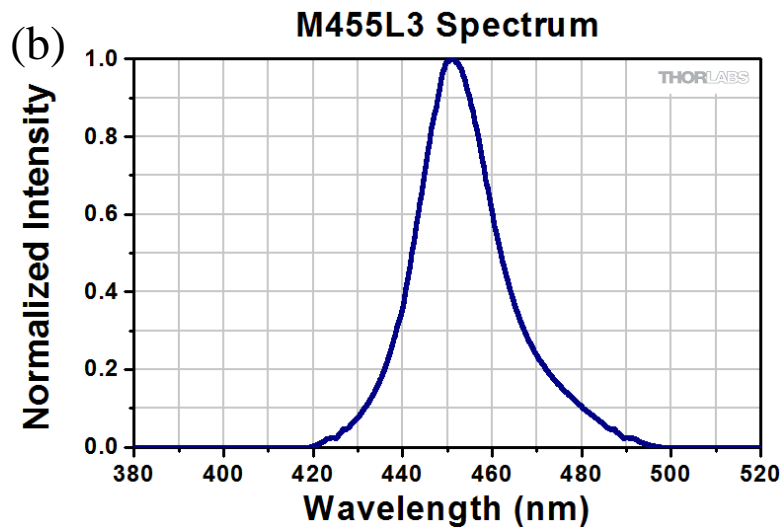
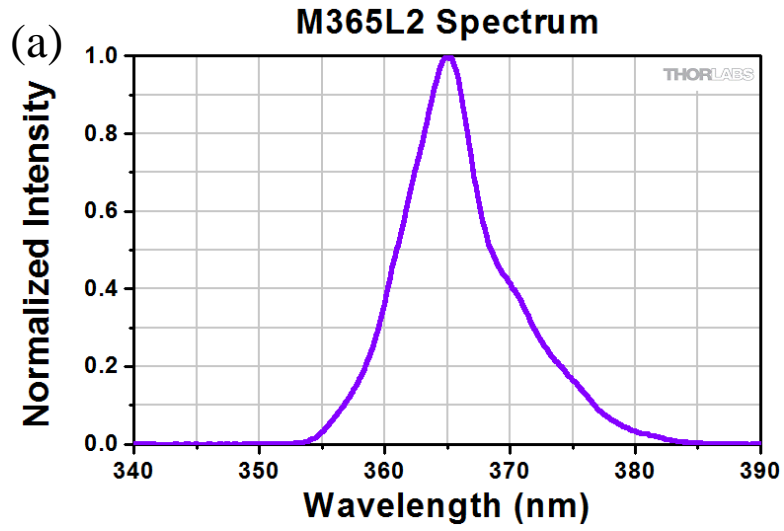


Figure A.2. Spectra of (a) UVLED and (b) BLED reproduced from Thorlabs.

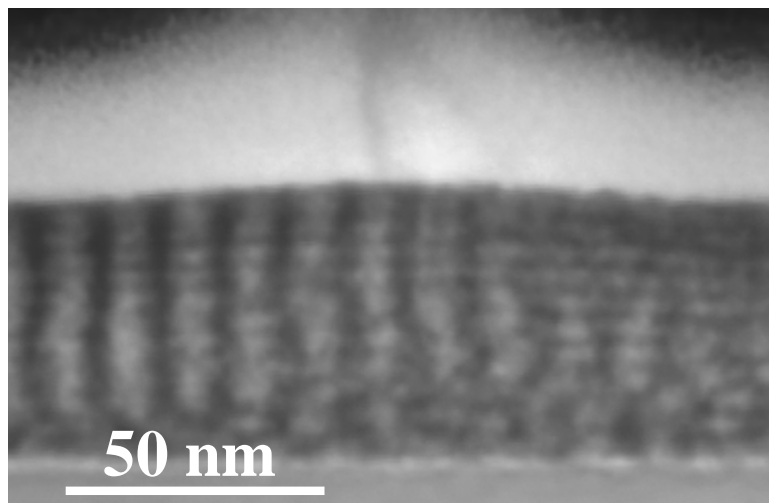


Figure A.3. Cross sectional bright-field STEM image of the F127-templated TiO₂ film after calcination and without hydrazine treatment.

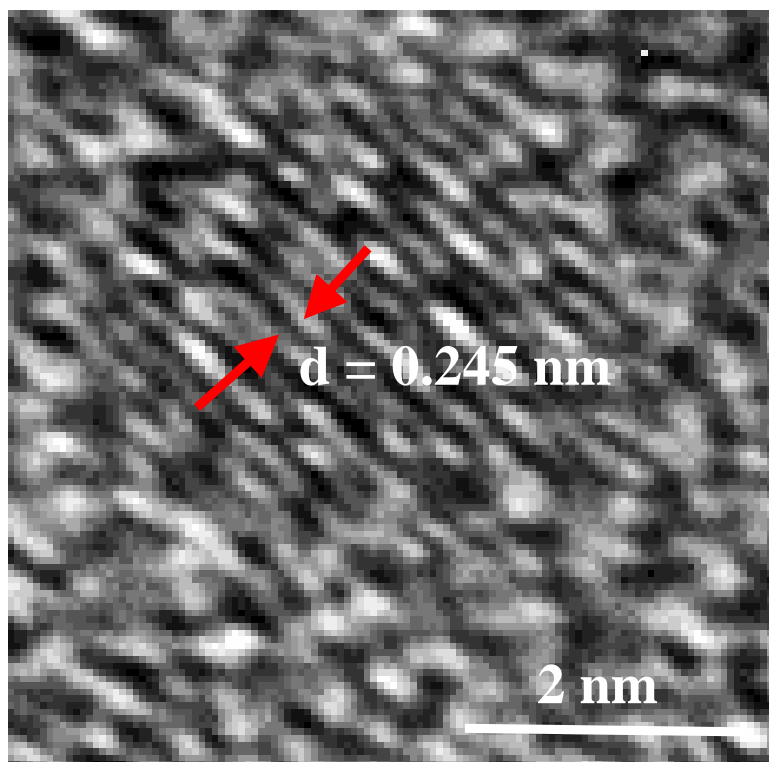


Figure A.4. HRTEM image of undoped TiO₂ film.

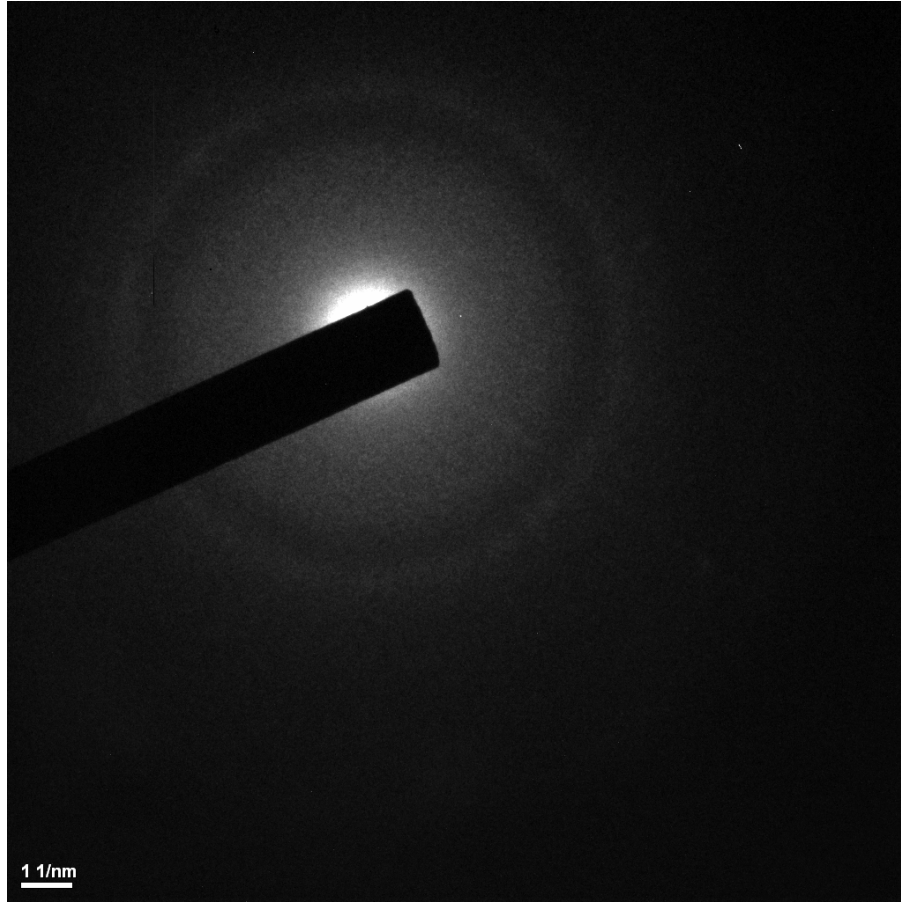


Figure A.5. SAED pattern of undoped TiO₂ film.

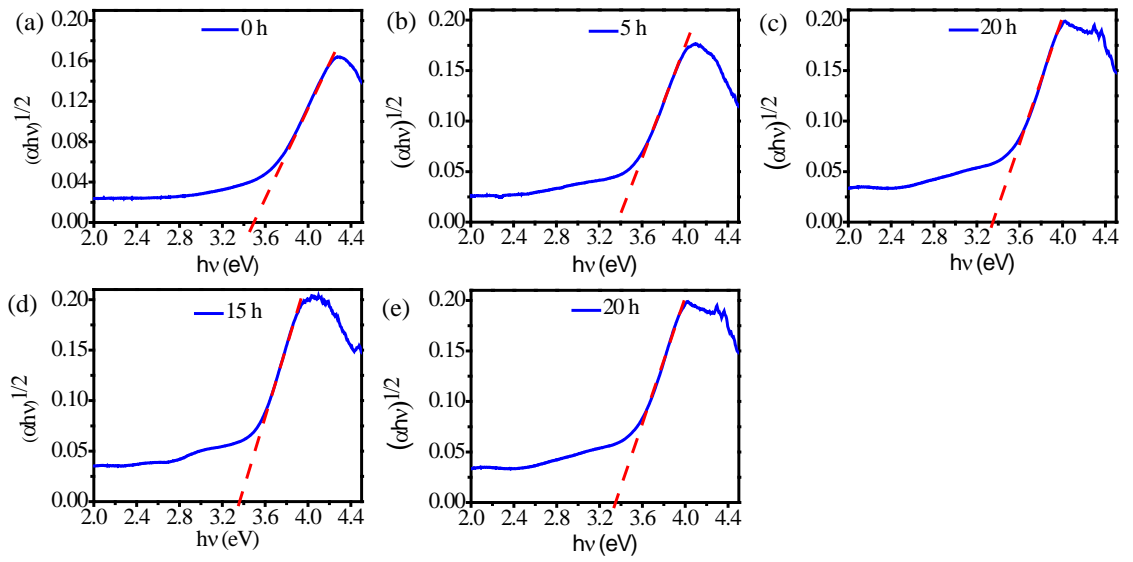


Figure A.6. Tauc plots of (a) undoped TiO_2 (0 h) (b) Ti^{3+} -N- TiO_2 _5 h (c) Ti^{3+} -N- TiO_2 _10 h (d) Ti^{3+} -N- TiO_2 _15 h and (e) Ti^{3+} -N- TiO_2 _20 h. Extrapolation of the linear portion of each curve to the horizontal axis gives the band gap.

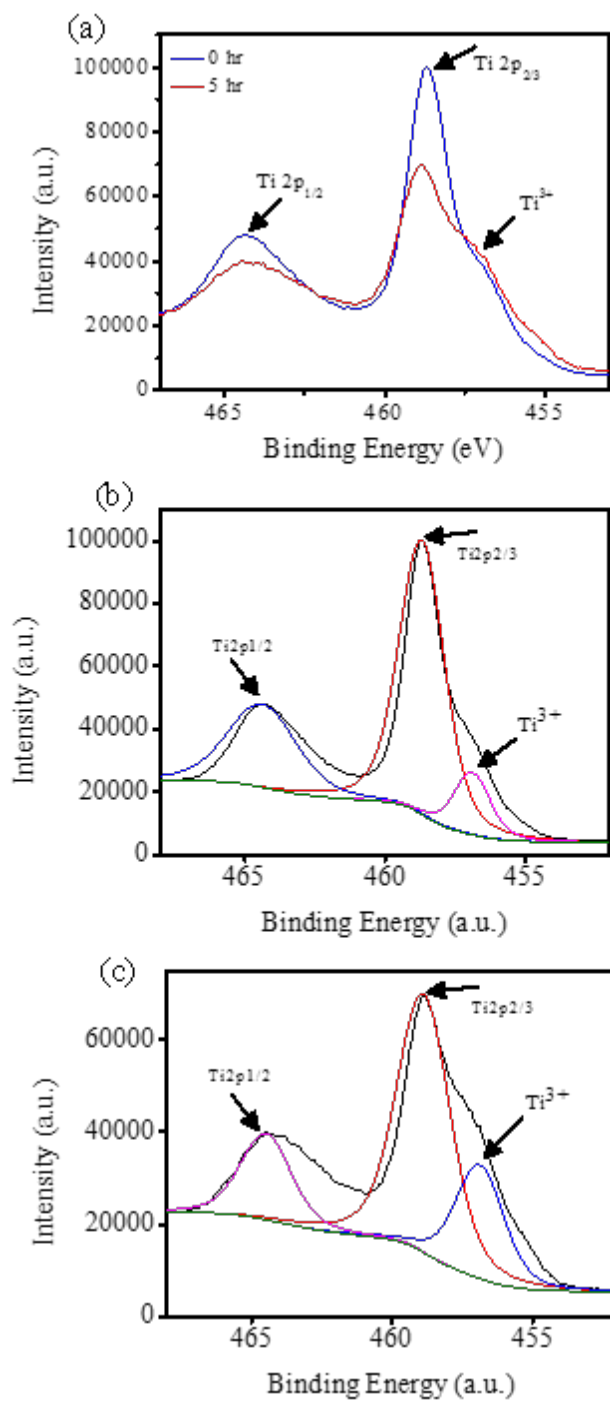


Figure A.7. (a) XPS Ti 2p spectra (after 45 second etching) of undoped TiO₂ and 5 h-Ti³⁺-N-TiO₂ films with peak fitting of (b) undoped TiO₂ and (c) 5 h-Ti³⁺-N-TiO₂ films.

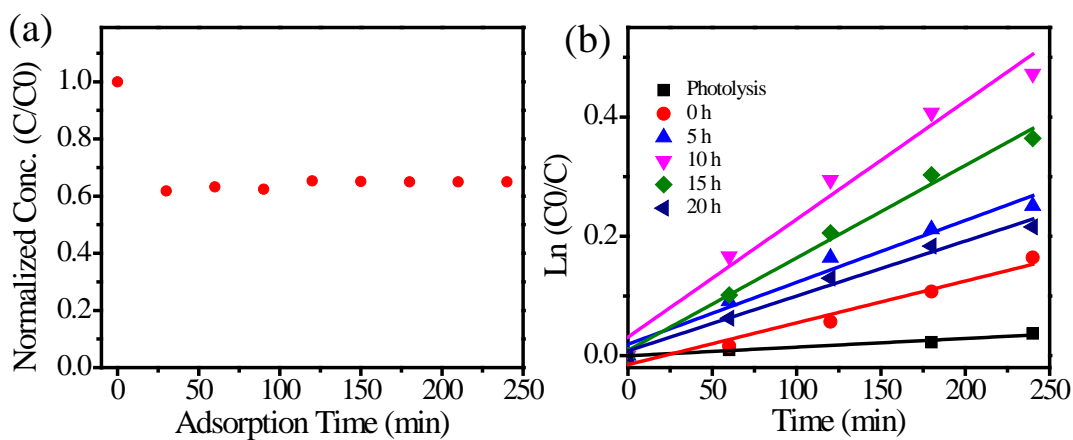


Figure A.8. (a) Measurement of methylene blue adsorption on undoped TiO_2 films in the dark confirming that steady state adsorption is reached within 30 min, and (b) fitting of first order kinetics for the MB decomposition reaction with undoped TiO_2 , Ti^{3+} -N- TiO_2 films and without films (photolysis).

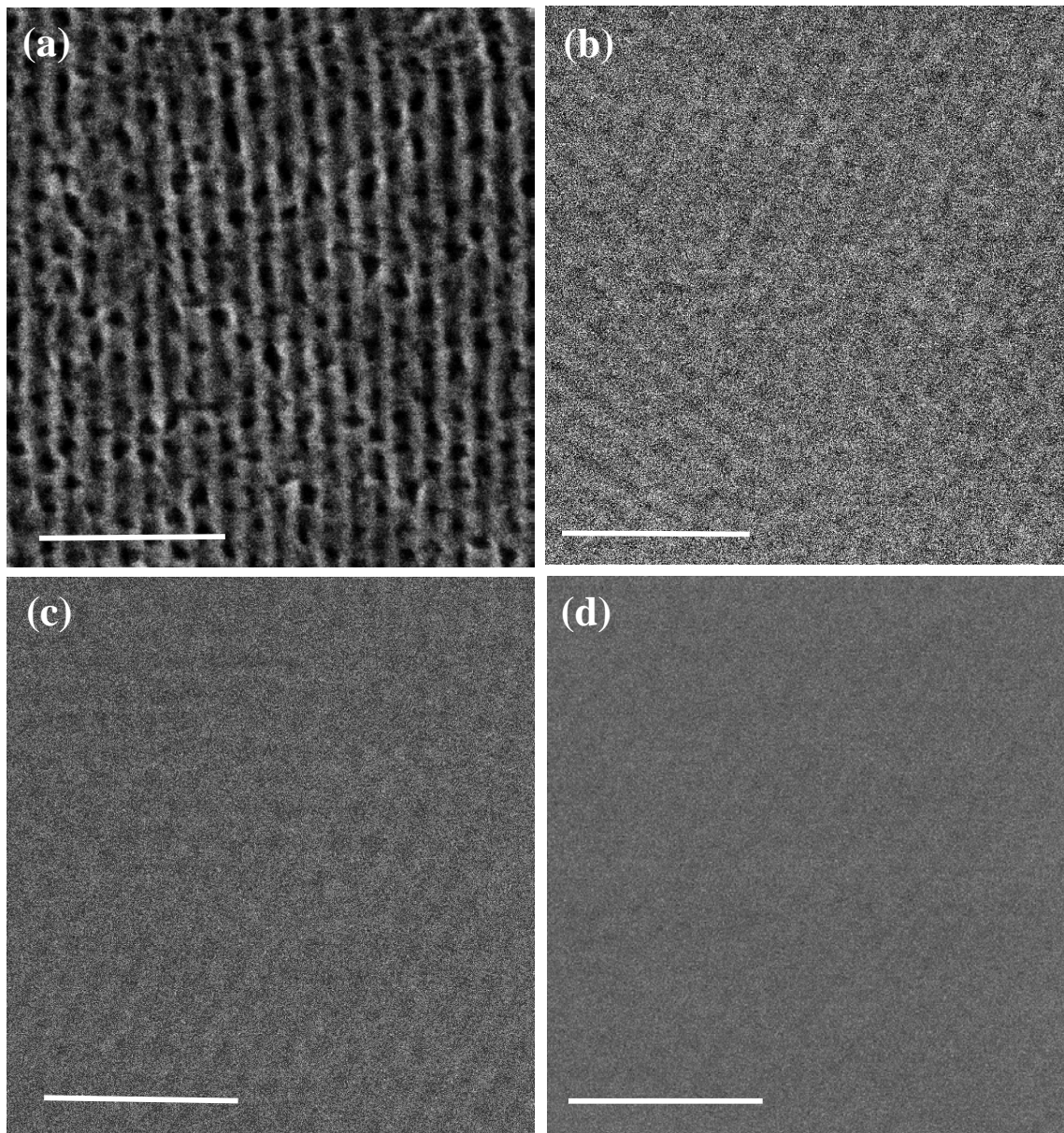


Figure A.9. Plan view SEM images of (a) undoped TiO₂, (b) 5 h Ti³⁺-N-TiO₂, (c) 10 h Ti³⁺-N-TiO₂, and (d) 20 h Ti³⁺-N-TiO₂ films (Scale bar width = 86 nm).

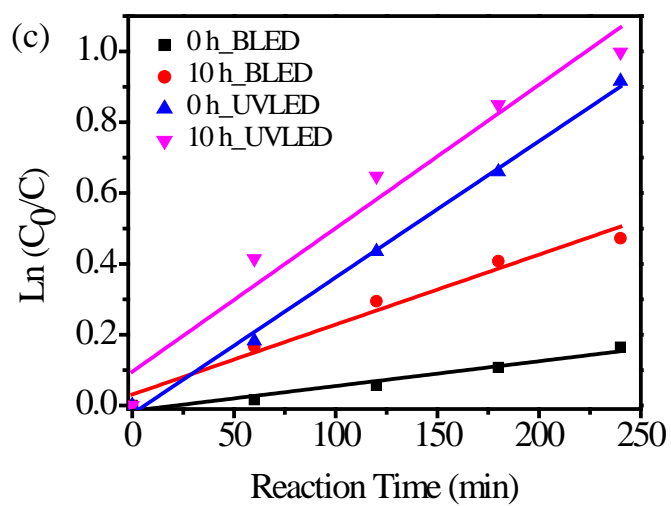
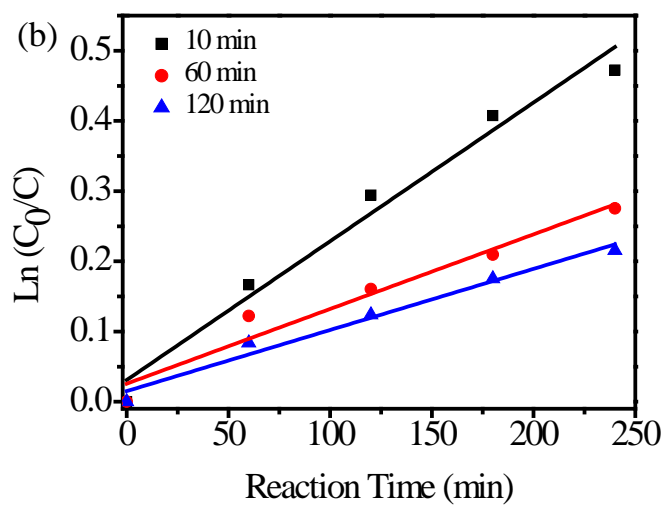
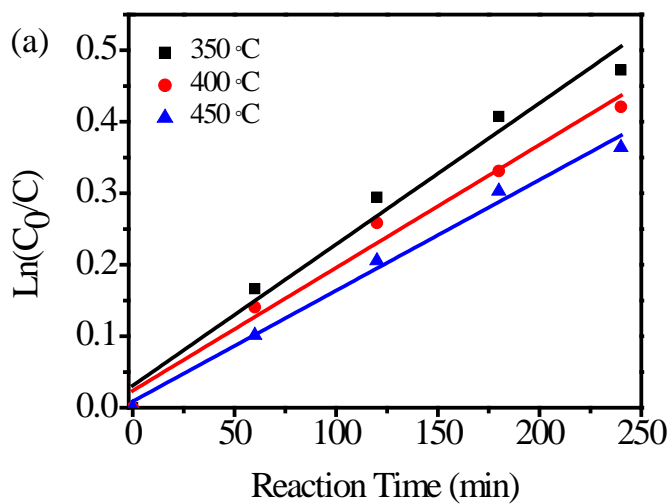


Figure A.10. Fitting of first order kinetics for the MB decomposition reaction with 10 h Ti^{3+} -N-TiO₂ films (a) calcined at varying temperature for 10 min, (b) calcined at 350 °C for varying time; and (c) calcined for 10 min at 350 °C but with two light sources (BLED and UVLED).

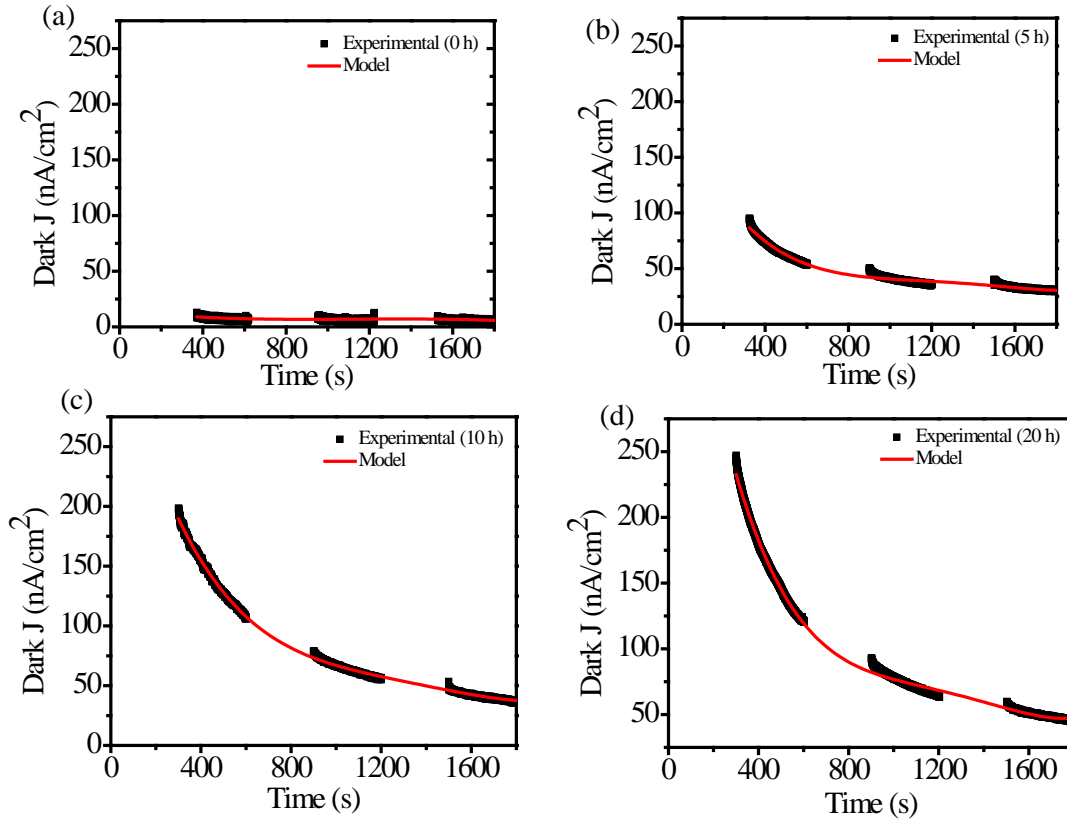


Figure A.11. Dark current density vs. time for undoped TiO₂ and Ti^{3+} -N-TiO₂ films and fitting of 4th order polynomials to each data set.

The following are the equations found from fitting the dark current in Figure A.11.

$$\text{For 0 h:} \quad y=15.27-0.025x+2.43E^{-5}x^2-8.4E^{-9}x^3+5.429E^{-13}x^4 \quad (\text{A.1})$$

$$\text{For 5 h:} \quad y=180.44-0.42x+4.79E^{-4}x^2-2.44E^{-7}x^3+4.56E^{-11}x^4 \quad (\text{A.2})$$

$$\text{For 10 h:} \quad y=361.355-0.779x+8.016E^{-5}x^2-3.87E^{-7}x^3+7.054E^{-11}x^4 \quad (\text{A.3})$$

$$\text{For 20 h:} \quad y=505.29-1.288x+0.0015x^2-7.815E^{-7}x^3+1.518E^{-10}x^4 \quad (\text{A.4})$$

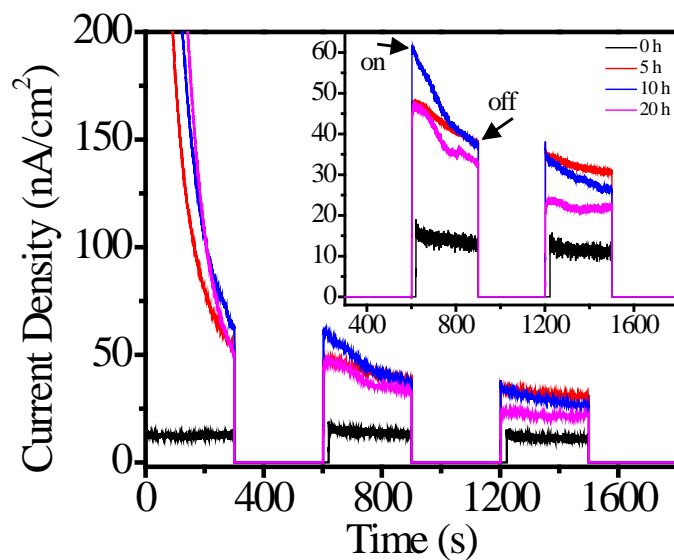


Figure A.12. Photocurrent density vs. time during the water splitting reaction with undoped TiO_2 and Ti^{3+} -N- TiO_2 films after subtracting the best-fit dark current functions from Figure A.11. The inset shows the enlarged region from 400 s to 1800 s.

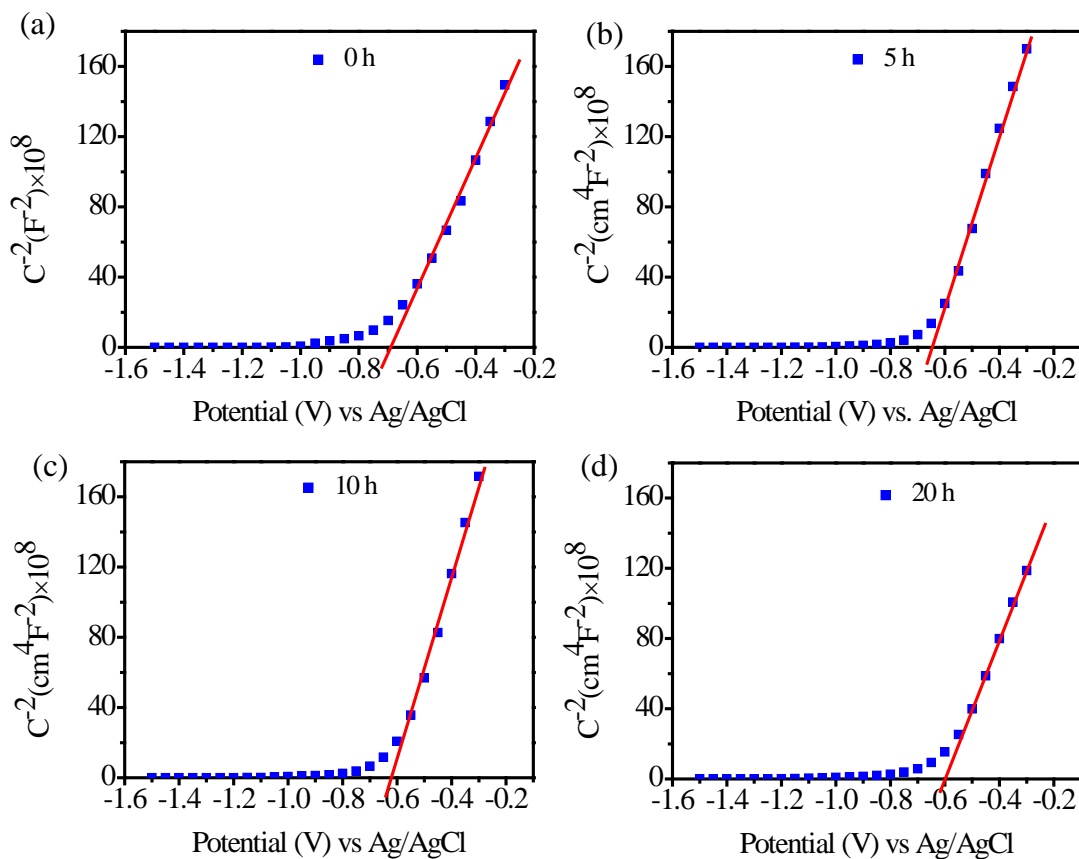


Figure A.13. Flat band potential estimation using Mott-Schottky plots for each mesoporous thin film sample by extrapolating the linear part of the curves to the horizontal axis.

APPENDIX B Supporting Information of Chapter 4

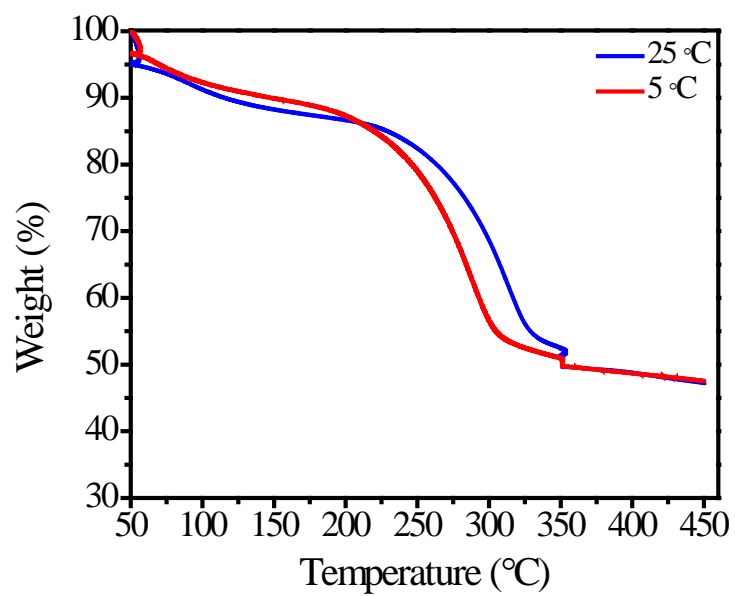


Figure B.1. TGA of uncalcined TiO₂ films heated from 50 °C to 450 °C at 5 °C/min and 25 °C/min ramp with intermediate isothermal heating at 350 °C for 10 min.

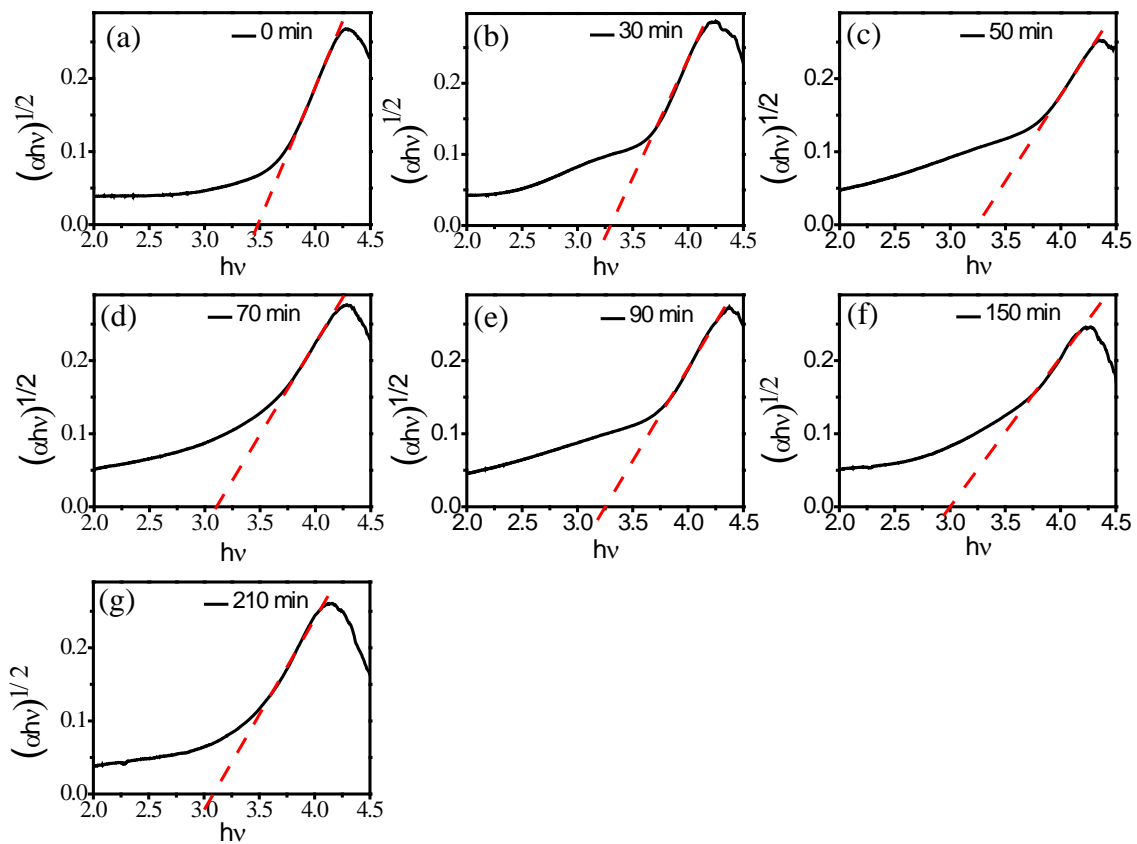


Figure B.2. Tauc plot of (a) undoped TiO_2 (0 min), (b) 30 min_N- TiO_2 , (c) 50 min_N- TiO_2 , (d) 70 min_N- TiO_2 , (e) 90 min_N- TiO_2 , (f) 150 min_N- TiO_2 , and (g) 210 min_N- TiO_2 films.

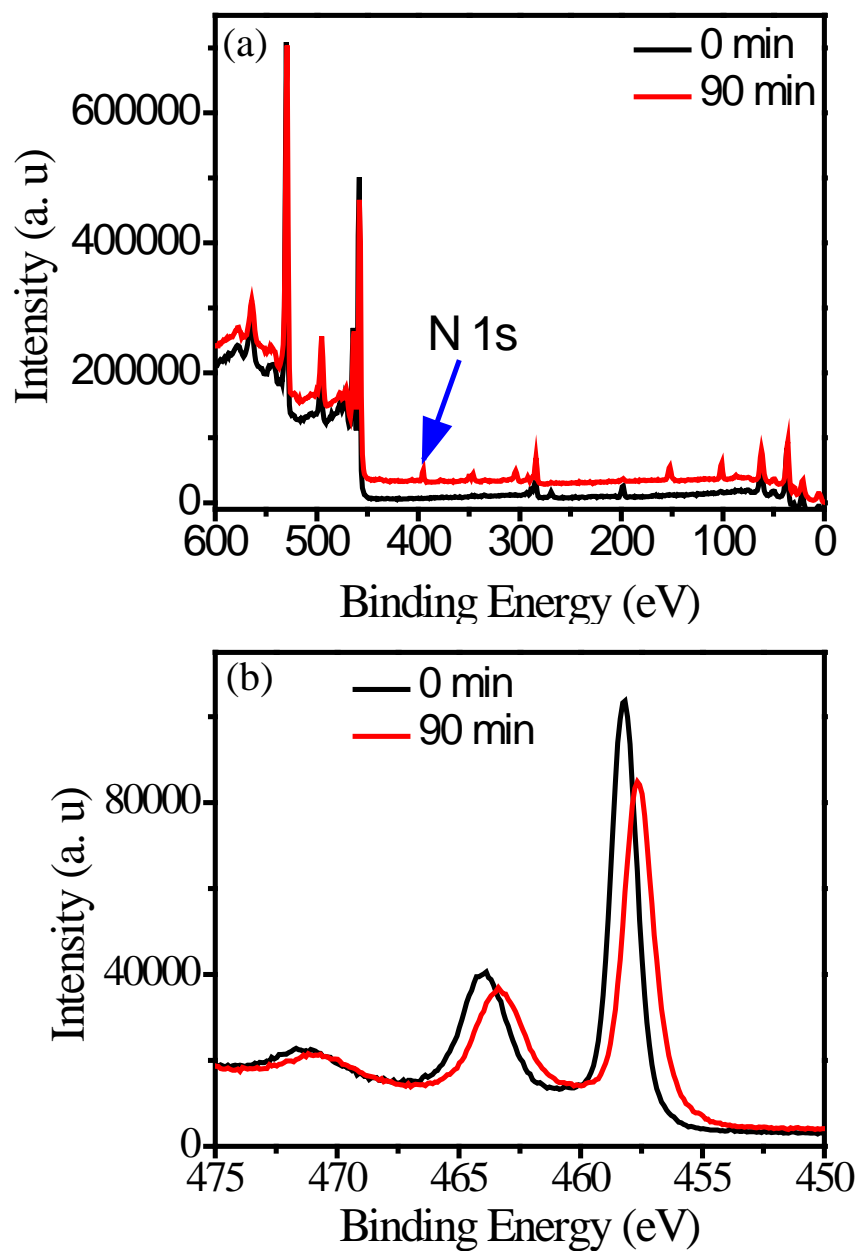


Figure B.3. (a) XPS survey spectra of undoped TiO₂ (0 min) and N-TiO₂ (90 min) (the spectrum of undoped TiO₂ was offset by 20000 value) and (b) XPS Ti 2p spectra of undoped TiO₂ and 90 min_N-TiO₂ films.

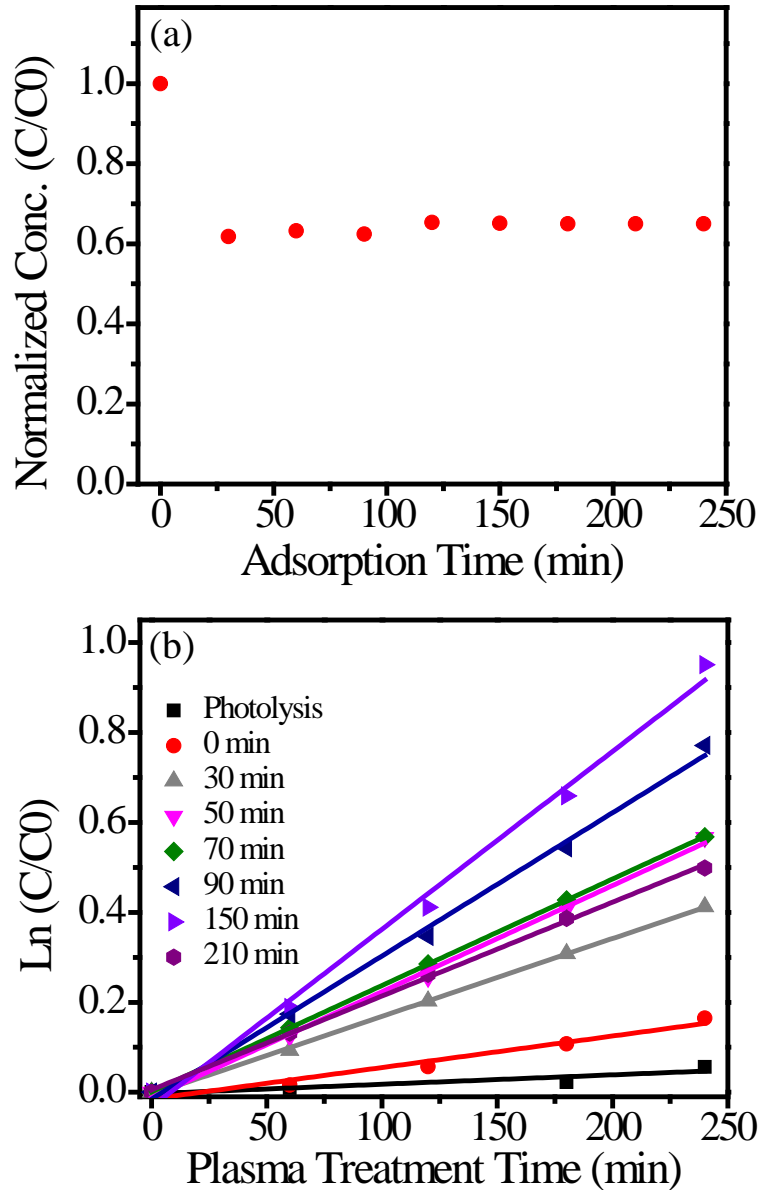


Figure B.4. (a) Methylene blue adsorption on undoped TiO_2 films in dark and (b) Fitting first order kinetics of MB reaction.

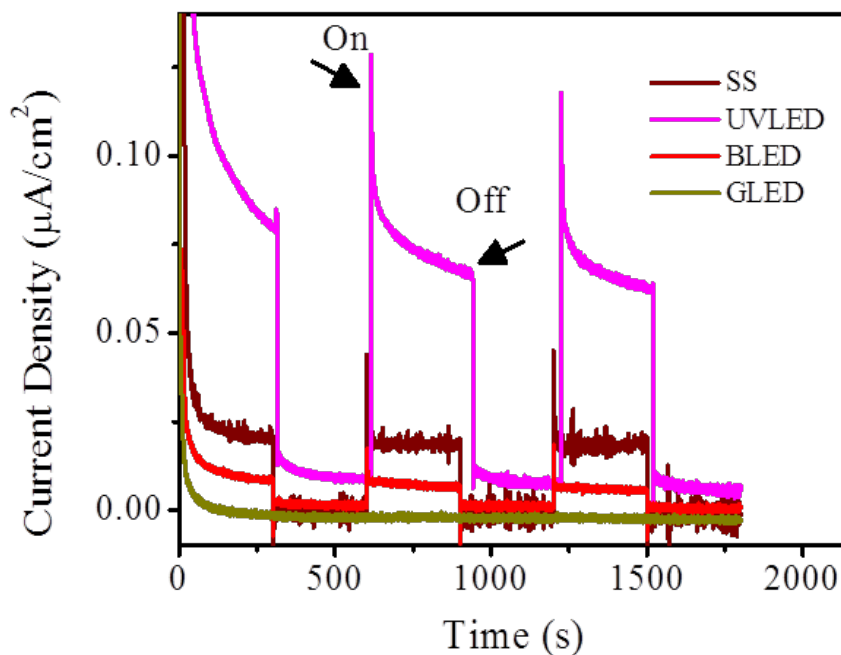


Figure B.5. Photocurrent-time measurement for undoped cubic mesoporous TiO_2 film on FTO-coated borosilicate glass slide using various light sources. The electrolyte for these experiments was 1 M KOH, and the light sources were a solar simulator (halogen bulb with intensity of $100 \text{ mW}/\text{cm}^2$), ultraviolet LED (UVLED) with $\lambda = 365 \text{ nm}$ and intensity $6 \text{ mW}/\text{cm}^2$, blue LED (BLED) with $\lambda = 455 \text{ nm}$ and intensity $= 22.5 \text{ mW}/\text{cm}^2$, and green LED (GLED) with $\lambda = 530 \text{ nm}$ and intensity $= 2.5 \text{ mW}/\text{cm}^2$. All LED sources were from Thor labs and the current measurements were done using a Ag/AgCl reference electrode, Pt counterelectrode, and 0.4 V applied potential.

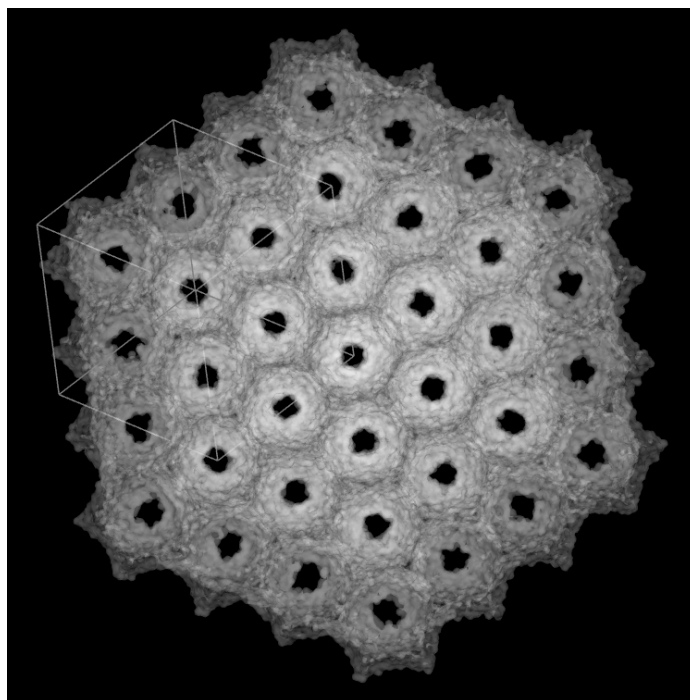


Figure B.6. (111) projection of an $Im\bar{3}m$ cubic mesoporous material illustrating the geometry used to estimate the mass of catalyst film. The box contains 2 unit cells x 2 unit cells x 2 unit cells. The pore-pore distance in this projection (12.5 nm from SEM) indicates a unit cell parameter of 15.3 nm. Assuming a pore diameter of 7 nm, this gives a volume fraction of solid material of 90%.

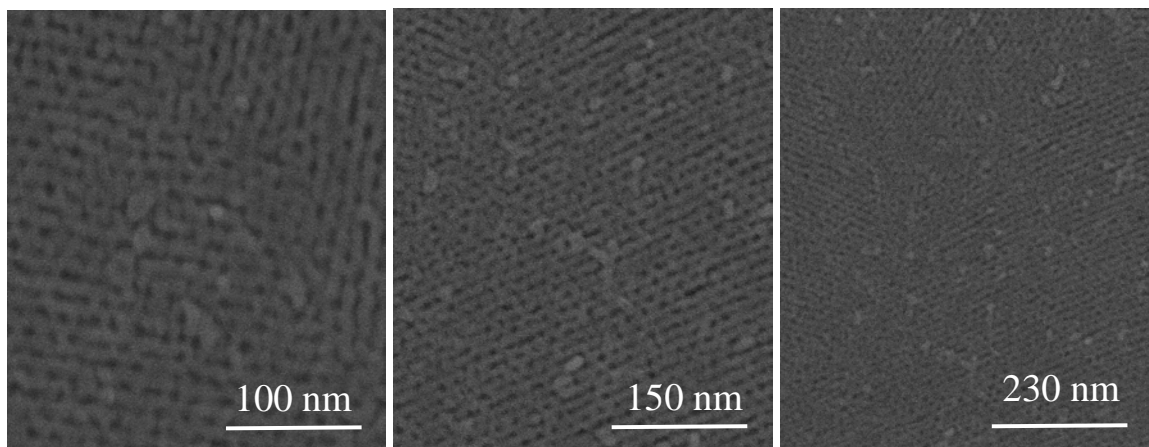


Figure B.7. SEM images of 210 min_N-TiO₂ films of different magnifications taken from different spots of the films.

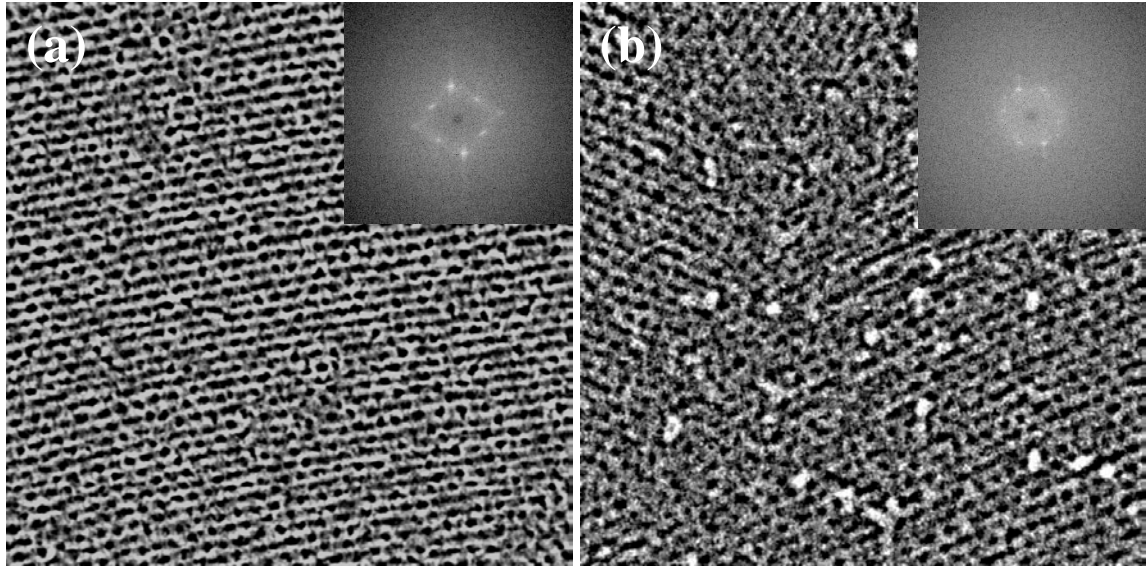


Figure B.8. ImageJ contrast-enhanced SEM images of (a) 0 min_N-TiO₂ and (b) 210 min_N-TiO₂ films (image size – 500 nm×500 nm). Insets are fast Fourier transforms (FFTs) of the images.

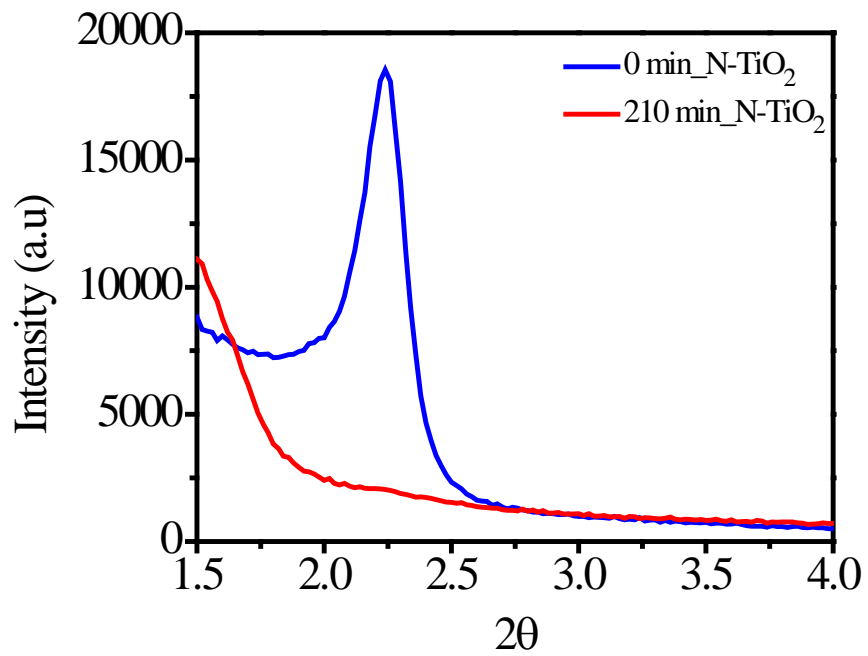


Figure B.9. XRD pattern of 0 min_N-TiO₂ (undoped) and 210 min_N-TiO₂ films.

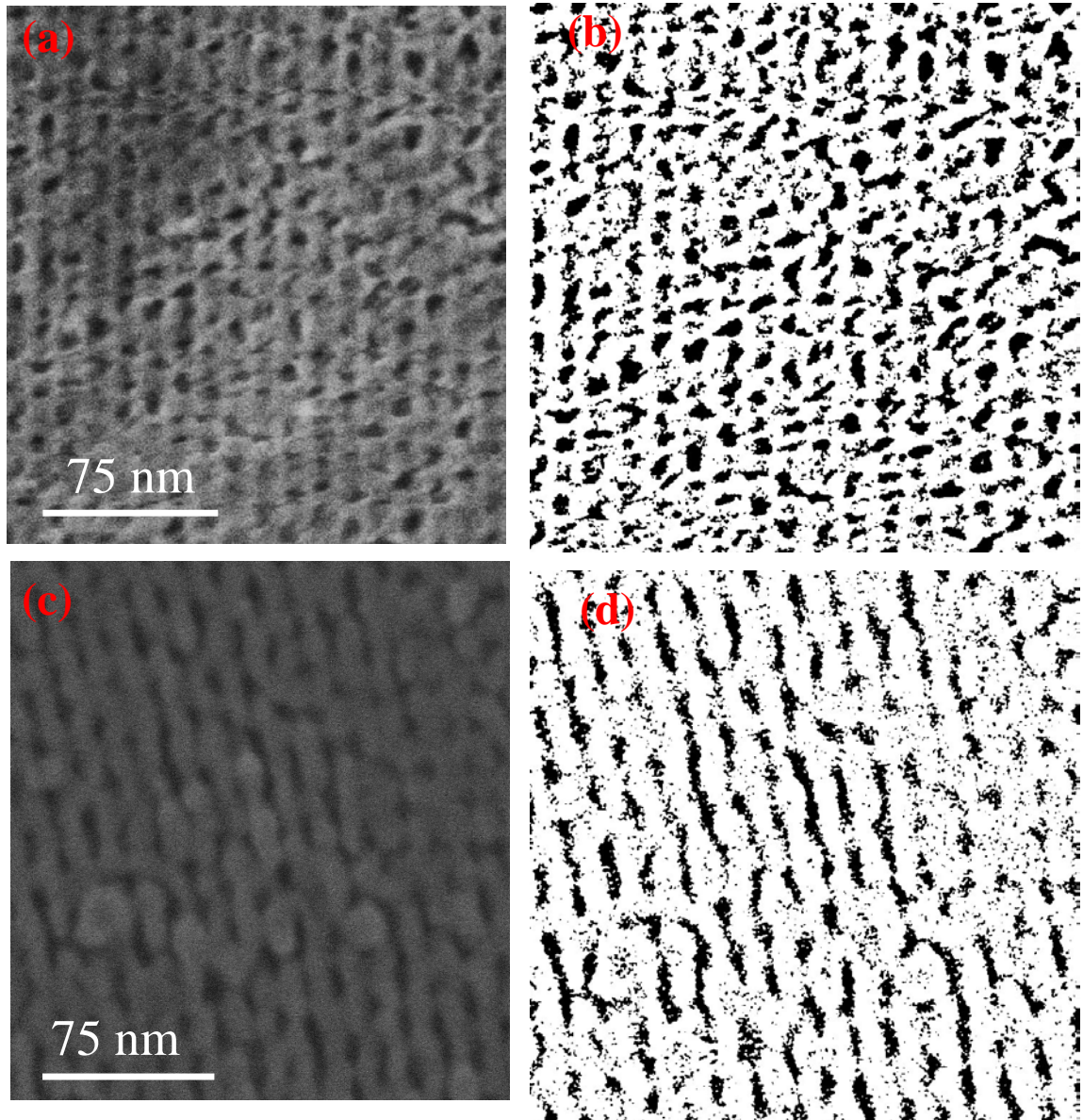


Figure B.10. SEM images of (a) 0 min_N-TiO₂ (undoped) and (b) 0 min_N-TiO₂ (undoped) after brightness / contrast adjustment by ImageJ; and (c) 210 min_N-TiO₂ and (d) 210 min_N-TiO₂ films after processing by ImageJ for the particle analysis tool.

Particle analysis in ImageJ was performed on the SEM images shown in Figure

B.10.

Parameters value found using particle analysis from Image J:

For undoped TiO₂ film,

No. of counts: 1494

Total area of pores: 11700 nm²

Percentage of area covered by pores in the image: 29.4%

Average pore perimeter: 10.3 nm

For 210 min_TiO₂ film,

No of counts: 2299

Total area of pores: 8260 nm²

Percentage of area covered by pores in the image: 20.6%

Average pore perimeter: 6.12 nm

Calculation of specific surface area

Assuming that the density of titania = 3.8 g/cm³, specific surface area is calculated assuming that perimeter is proportional to area and that pore area is proportional to pore volume. In this case,

$$SSA = \frac{\text{Total perimeter of pores}}{(1 - \% \text{ pore area}) * (\text{image area}) * \text{density}}$$

For undoped films,

$$\begin{aligned} SSA &= 1494 \times (10.3 \times 10^{-9}) / (1 - 0.294) / (200 \times 10^{-9} \times 200 \times 10^{-9}) / (3.8 \times 10^6) \\ &= 143 \text{ m}^2/\text{g} \end{aligned}$$

For 210 min_N-TiO₂ films,

$$\begin{aligned} SSA &= 2299 \times (6.12 \times 10^{-9}) / (1 - 0.206) / (200 \times 10^{-9} \times 200 \times 10^{-9}) / (3.8 \times 10^6) \\ &= 117 \text{ m}^2/\text{g} \end{aligned}$$

APPENDIX C Supporting Information of Chapter 5.

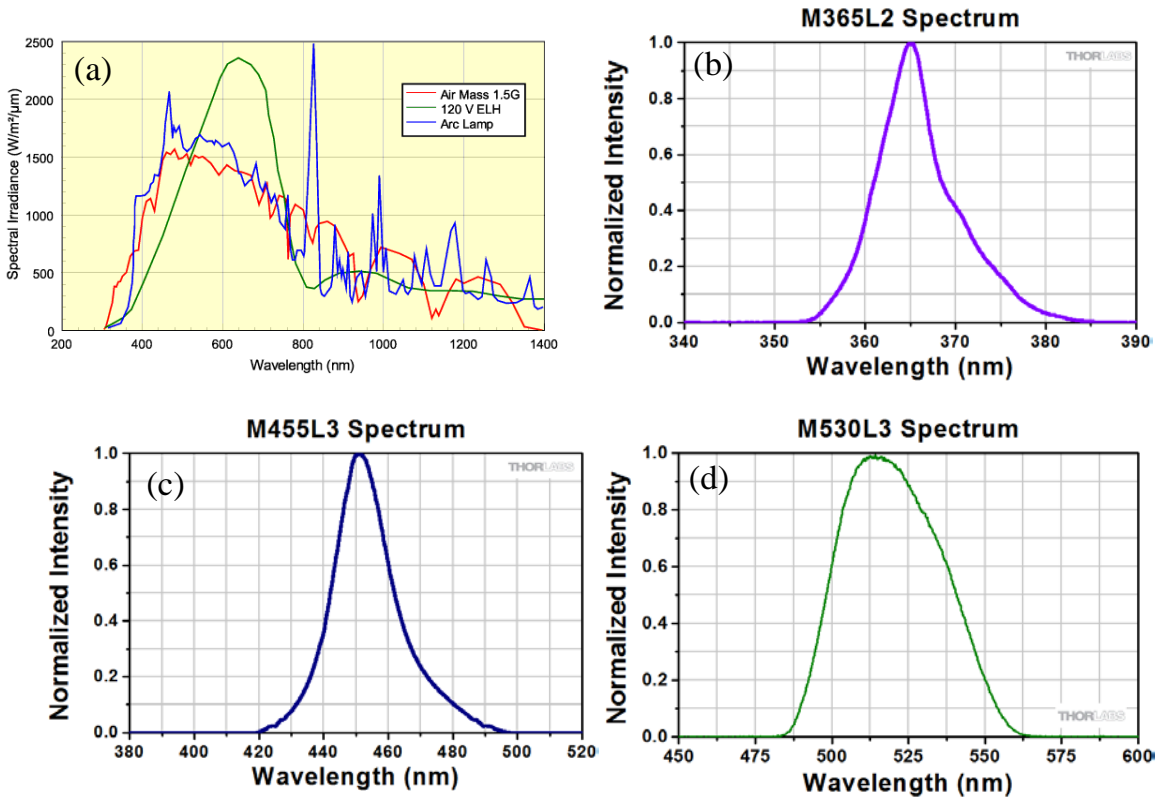


Figure C.1. Spectra of (a) Halogen bulb (120 V ELH) and Xe arc lamp reproduced from <http://www.pveducation.org/pvcdrom/characterisation/illumination-sources>, (b) UVLED, (c) BLED and (d) GLED reproduced from Thorlabs.

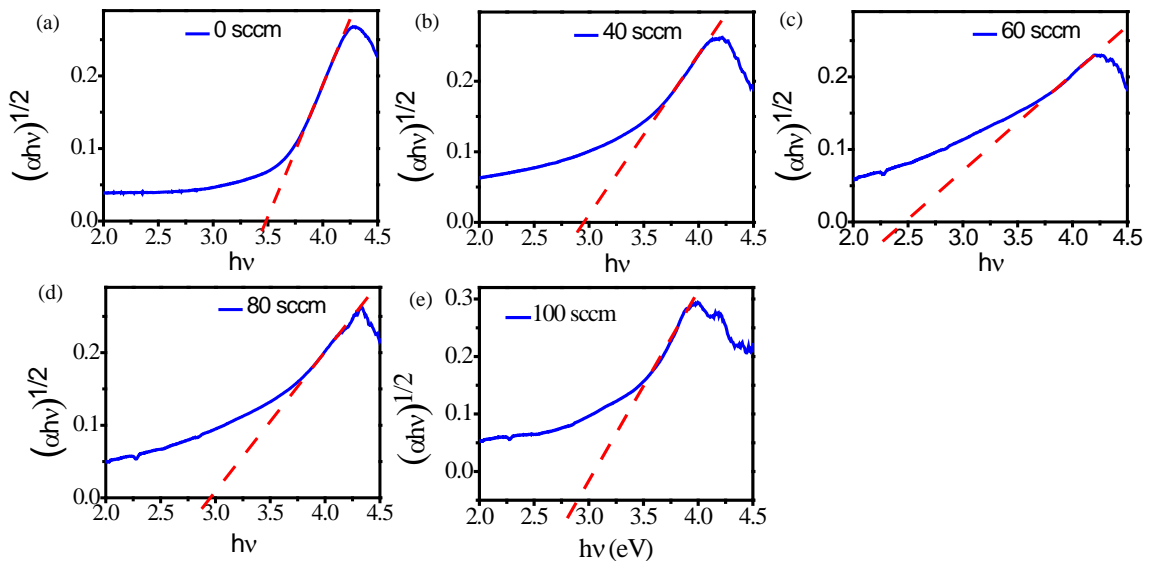


Figure C.2. The determination of band gaps by Tauc plot for (a) 0 sccm_N-TiO₂ (undoped), (b) 40 sccm_N-TiO₂, (c) 60 sccm_N-TiO₂, (d) 80 sccm_N-TiO₂ and (e) 100 sccm_N-TiO₂ films

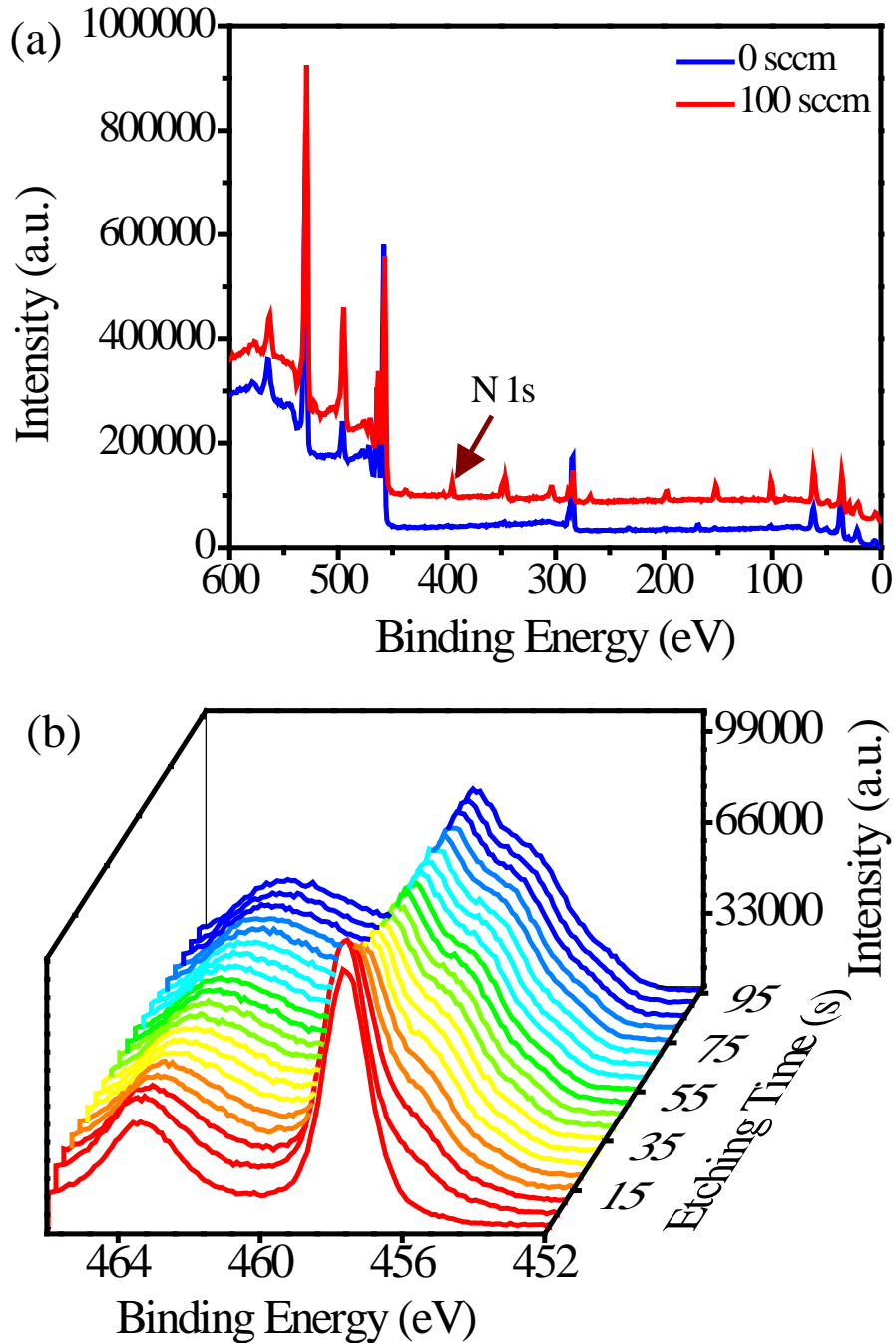


Figure C.3. (a) XPS survey spectra of undoped TiO₂ (0 sccm) and 100 sccm_N-TiO₂ (100 sccm) (the spectrum of N-TiO₂ was offset by 50000 intensity units) and (b) XPS Ti 2p depth profile for the 100 sccm_N-TiO₂ sample.

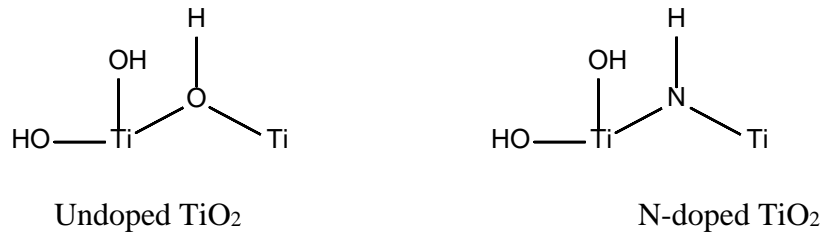


Figure C.4. Predicted surface structures for undoped TiO₂ and N-doped TiO₂ films.

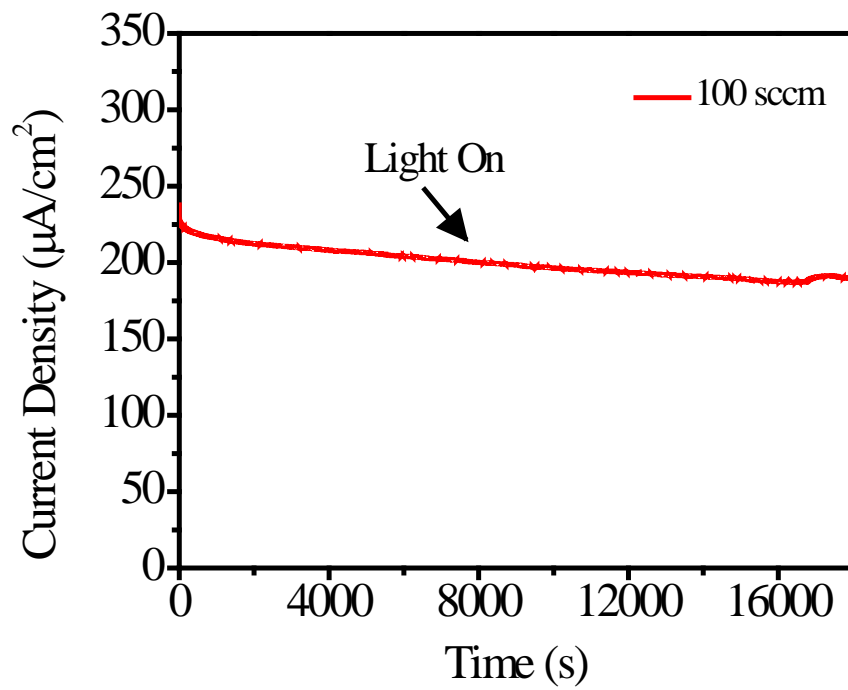


Figure C.5. Amperometric current-time profile of water oxidation for long term stability test for 100 sccm_N-TiO₂ film under UVLED illumination.

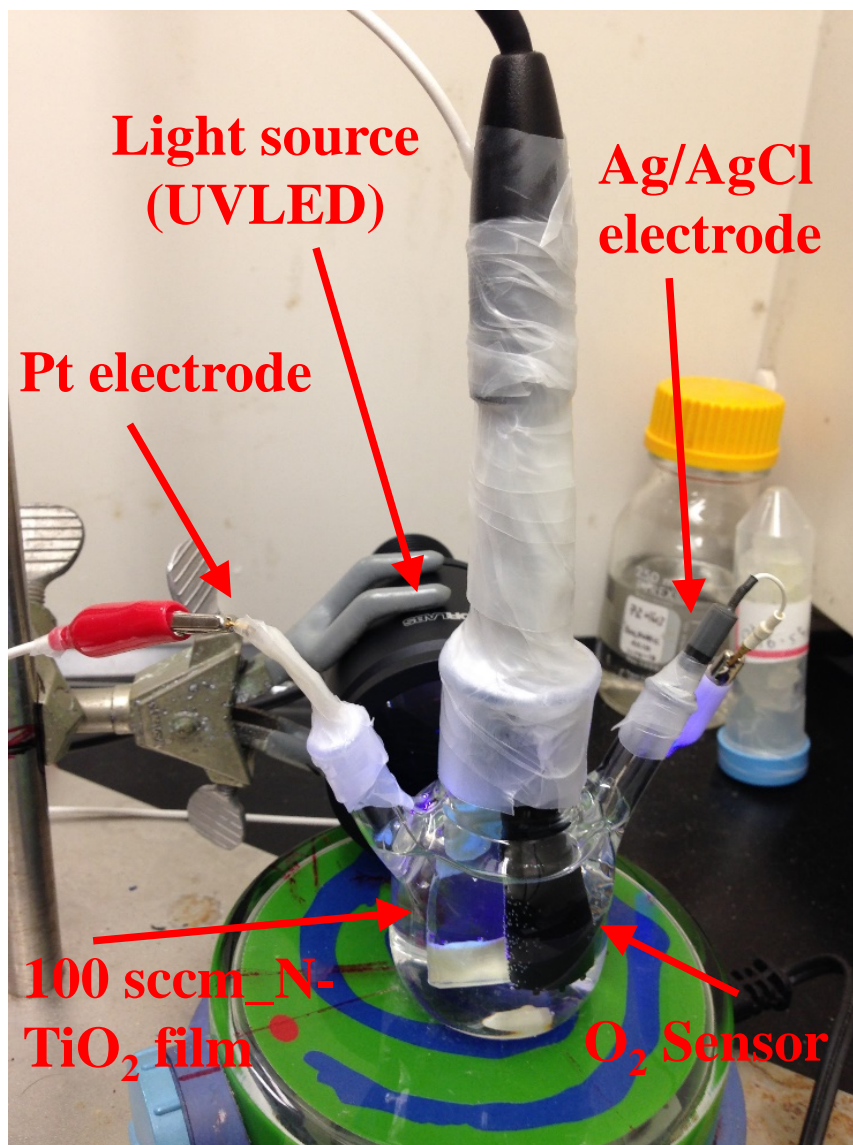


Figure C.6. Experimental set-up for oxygen measurement using oxygen sensor from water oxidation with 100 sccm_N-TiO₂ film under UVLED illumination.

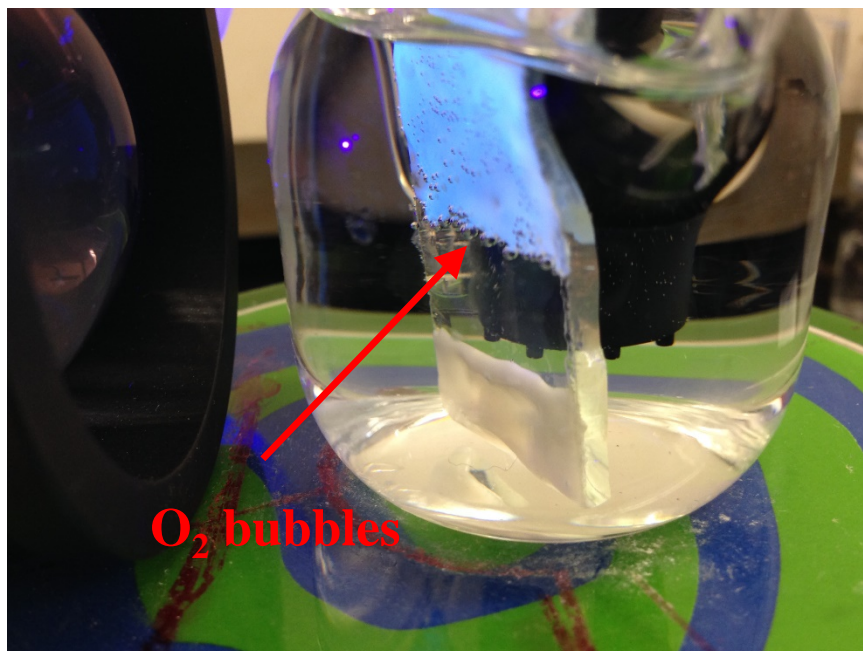


Figure C.7. Oxygen gas bubbles on the surface of the 100 sccm_N-TiO₂ film formed by water oxidation under UVLED illumination.

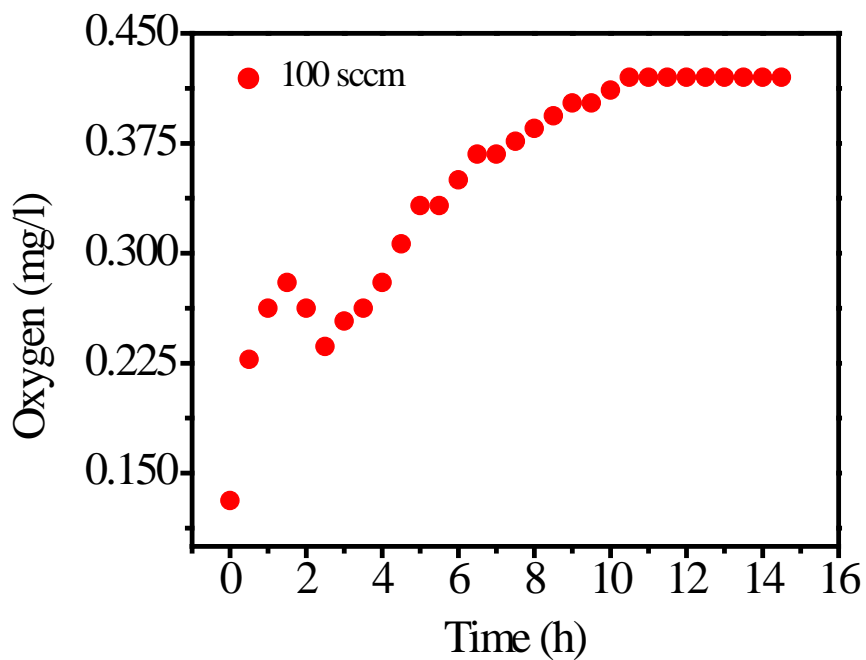


Figure C.8. Concentration profile of dissolved oxygen produced by water oxidation with 100 sccm_N-TiO₂ film under UVLED illumination.

IPCE Calculations

Calculation for 100 sccm_N-TiO₂ film under UVLED illumination

$$\begin{aligned} \text{IPCE} &= 1240I/(\lambda J), I = 230.45 \times 10^{-6} \text{ A/cm}^2, J = 6 \times 10^{-3} \text{ W/cm}^2, \lambda = 365 \text{ nm} \\ &= 1240 \times 230.45 \times 10^{-6} / (365 \times 6 \times 10^{-3}) = 0.13023 = 13.023\% \end{aligned}$$

$$\text{APCE} = \text{IPCE}/\text{Absorbance}$$

The absorbance of the double sided titania films on glass slide at 365 nm taken from Figure 5.2 = 0.427

The absorbance of the single sided titania films on glass slide at 365 nm taken from Figure 5.2 = 0.427/2 = 0.2135

$$A = \log(1/T), \text{ so } 0.2135 = \log(1/T), T = 0.6116$$

$$A = 1 - T = 1 - 0.6116 = 0.388$$

$$\text{So, APCE} = 13.023\% / 0.388 = 33.56\%$$

Calculation for undoped TiO₂ film under UVLED illumination

$$\begin{aligned} \text{IPCE} &= 1240I/(\lambda J), I = 0.81 \times 10^{-6} \text{ A/cm}^2, J = 6 \times 10^{-3} \text{ W/cm}^2, \lambda = 365 \text{ nm} \\ &= 1240 \times 0.81 \times 10^{-6} / (365 \times 6 \times 10^{-3}) = 0.00046 = 0.046\% \end{aligned}$$

$$\text{APCE} = \text{IPCE}/\text{Absorbance}$$

The absorbance of the double sided titania films on glass slide at 365 nm taken from Figure 5.2 = 0.085

The absorbance of the single sided titania films on glass slide at 365 nm taken from Figure 5.2 = 0.085/2 = 0.0425

$$A = \log(1/T), \text{ so } 0.0425 = \log(1/T), T = 0.907$$

$$A = 1 - T = 1 - 0.907 = 0.093$$

$$\text{So, APCE} = 0.046\% / 0.093 = 0.49\%$$

Calculation for 100 sccm_N-TiO₂ film under Blue-LED illumination

$$\begin{aligned} \text{IPCE} &= 1240I/(\lambda J), I = 3.7 \times 10^{-6} \text{ A/cm}^2, J = 22.5 \times 10^{-3} \text{ W/cm}^2, \lambda = 455 \text{ nm} \\ &= 1240 \times 3.7 \times 10^{-6} / (455 \times 22.5 \times 10^{-3}) = 0.000448 = 0.0448\% \end{aligned}$$

$$\text{APCE} = \text{IPCE}/\text{Absorbance}$$

The absorbance of the double sided titania films on glass slide at 365 nm taken from Figure 5.2 = 0.15

The absorbance of the single sided titania films on glass slide at 365 nm taken from Figure 5.2 = $0.15/2 = 0.075$

$$A = \log(1/T), \text{ so } 0.075 = \log(1/T), T = 0.84$$

$$A = 1 - T = 1 - 0.84 = 0.16$$

$$\text{So, APCE} = 0.0448\% / 0.16 = 0.28\%$$

Calculation for undoped TiO₂ film under Blue-LED illumination

$$\begin{aligned} \text{IPCE} &= 1240I/(\lambda J), I = 0.017 \times 10^{-6} \text{ A/cm}^2, J = 22.5 \times 10^{-3} \text{ W/cm}^2, \lambda = 455 \text{ nm} \\ &= 1240 \times 0.017 \times 10^{-6} / (455 \times 22.5 \times 10^{-3}) = 2.06 \times 10^{-6} = 2.06 \times 10^{-4}\% \end{aligned}$$

$$\text{APCE} = \text{IPCE} / \text{Absorbance}$$

The absorbance of the double sided titania films on glass slide at 365 nm taken from Figure 5.2 = 0.047

The absorbance of the single sided titania films on glass slide at 365 nm taken from Figure 5.2 = $0.047/2 = 0.0235$

$$A = \log(1/T), \text{ so } 0.0235 = \log(1/T), T = 0.947$$

$$A = 1 - T = 1 - 0.947 = 0.053$$

$$\text{So, APCE} = 2.06 \times 10^{-4}\% / 0.053 = 0.0039\%$$

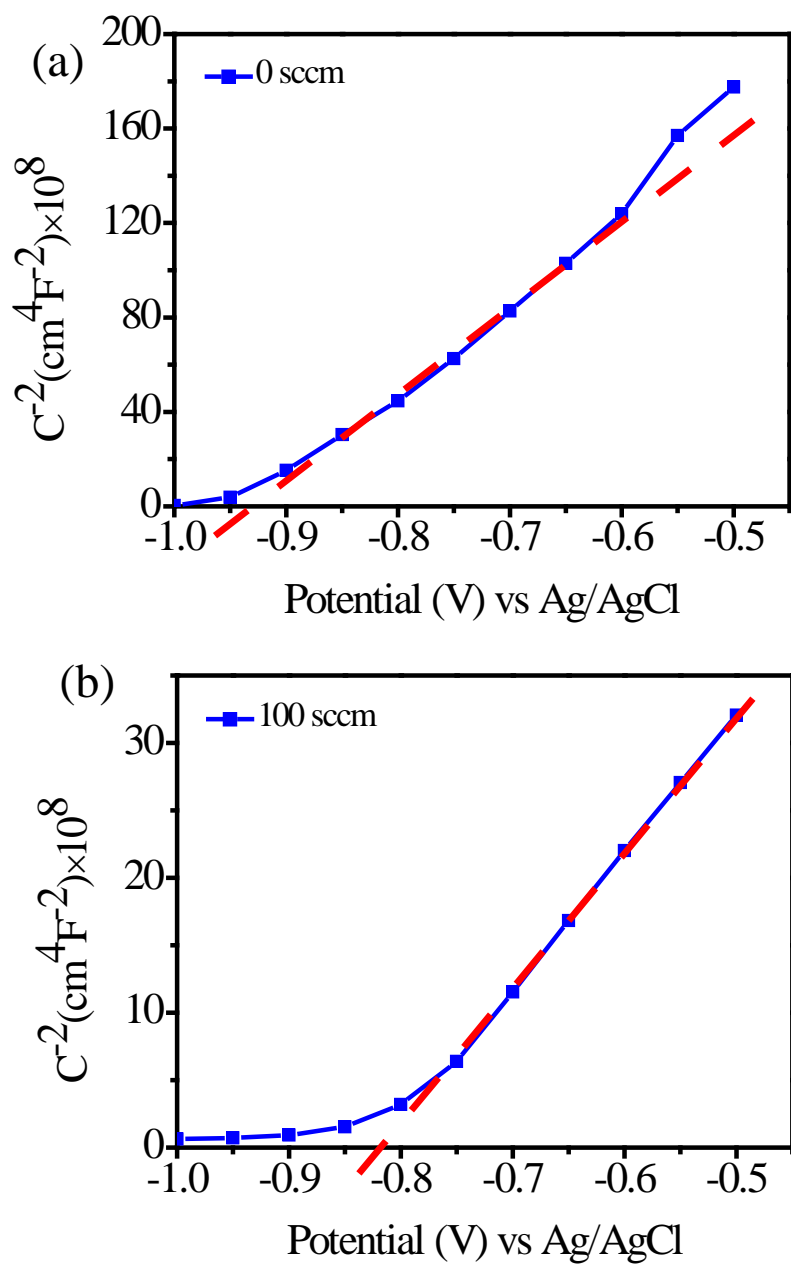


Figure C.9. Estimation of flat band potential for (a) 0 sccm_N-TiO₂ and (b) 100 sccm_N-TiO₂ films using Mott-Schottky plots.

Table C.1. Contact angles of undoped TiO₂ and N-doped TiO₂ films.

Sample	Reading 1	Reading 2	Reading 3	Average contact angle (n=3)
Ti-TiO ₂	60°	61°	60°	60°±1°
N-Doped TiO ₂	10°	11°	12°	11°±1°

APPENDIX D Supporting Information of Chapter 6.

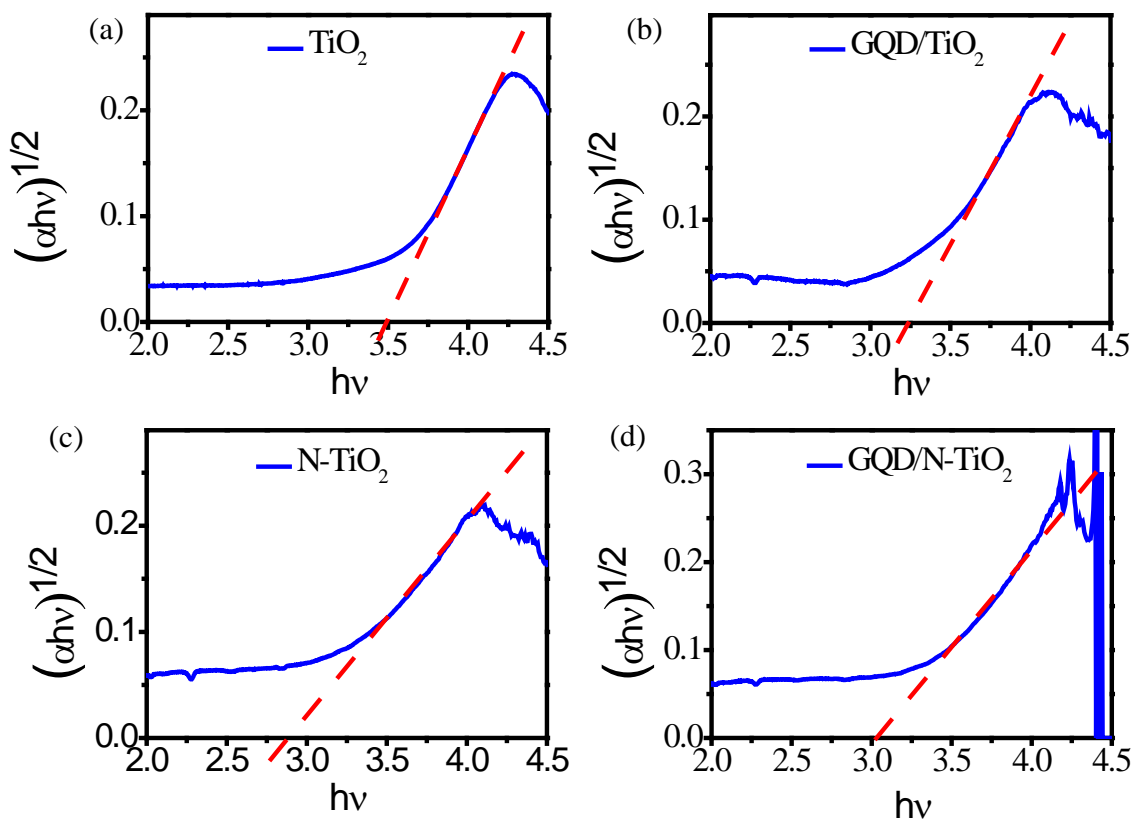


Figure D.1. The determination of band gaps by Tauc's method for (a) TiO₂, (b) GQD/TiO₂, (c) N-TiO₂, (d) GQD/N-TiO₂ films

IPCE Calculations

The photocurrents of TiO₂, N-TiO₂, GQD/TiO₂ and GQD/N-TiO₂ films at 0.35 V vs. Ag/AgCl in linear sweep voltammetry under BLED illumination are 0.0148 μA/cm², 3.29 μA/cm², 0.126 μA/cm², and 5.13 μA/cm², respectively. Absorbance at 455 nm taken from Figure 6.3 for TiO₂, GQD/TiO₂, N-TiO₂ and GQD/N-TiO₂ films are 0.047, 0.057, 0.154, 0.163, respectively. Based on these values, the incident photon conversion efficiency (IPCE) and absorbed photon conversion efficiency (APCE) values can be calculated

Calculation for TiO₂

Calculations for undoped TiO₂ film under blue LED illumination:

IPCE = $1240I/(\lambda J)$ where $I = 0.0148 \times 10^{-6}$ A/cm², $J = 22.5 \times 10^{-3}$ W/cm² and $\lambda = 455$ nm.

Thus, IPCE = $1240 \times 0.017 \times 10^{-6} / (455 \times 22.5 \times 10^{-3}) = 2.06 \times 10^{-6} = 2.06 \times 10^{-4}\%$

APCE = IPCE/(A) where A = fraction of light absorbed by film.

The absorbance of the double sided titania films on glass slide at 455 nm taken from Figure 6.3 = 0.047, so the absorbance of the single titania film = $0.047/2 = 0.0235$.

$A = \log(1/T)$, so $0.0235 = \log(1/T)$, $T = 0.947$

$A = 1 - T = 1 - 0.947 = 0.053$

So, APCE = $2.06 \times 10^{-4}\% / 0.053 = 0.0039\%$

Calculation for GQD/TiO₂

Calculations for GQD-modified TiO₂ film under blue LED illumination:

IPCE = $1240I/(\lambda J)$ where $I = 0.126 \times 10^{-6}$ A/cm², $J = 22.5 \times 10^{-3}$ W/cm², $\lambda = 455$ nm.

IPCE = $1240 \times 0.126 \times 10^{-6} / (455 \times 22.5 \times 10^{-3}) = 15.2 \times 10^{-6} = 15.2 \times 10^{-4}\%$

APCE = IPCE/A

The absorbance of the double sided GQD-TiO₂ films on glass slide at 455 nm taken from Figure 6.3 = 0.057, so for a single film, absorbance = $0.057/2 = 0.0285$.

$A = \log(1/T)$, so $0.0285 = \log(1/T)$, $T = 0.936$

$A = 1 - T = 1 - 0.936 = 0.0635$

So, APCE = $15.24 \times 10^{-4}\% / 0.0635 = 0.024\%$

Calculation for N-TiO₂

Calculation for N-doped TiO₂ film under blue LED illumination:

IPCE = $1240I/(\lambda J)$ where $I = 3.29 \times 10^{-6}$ A/cm², $J = 22.5 \times 10^{-3}$ W/cm², $\lambda = 455$ nm.

IPCE = $1240 \times 3.29 \times 10^{-6} / (455 \times 22.5 \times 10^{-3}) = 3.98 \times 10^{-4} = 3.98 \times 10^{-2}\%$.

APCE = IPCE/A

The absorbance of the double sided titania films on glass slide at 455 nm taken from Figure 6.3 = 0.154, so for a single film, absorbance = $0.154/2 = 0.077$.

$A = \log(1/T)$, so $0.077 = \log(1/T)$, $T = 0.84$

$A = 1 - T = 1 - 0.84 = 0.16$

So, APCE = $3.98 \times 10^{-2}\% / 0.16 = 0.25\%$

Calculation for GQD/N-TiO₂

Calculation for GQD/N-TiO₂ film under blue LED illumination:

$$\begin{aligned} \text{IPCE} &= 1240I/(\lambda J), I = 5.13 \times 10^{-6} \text{ A/cm}^2, J = 22.5 \times 10^{-3} \text{ W/cm}^2, \lambda = 455 \text{ nm} \\ &= 1240 \times 5.13 \times 10^{-6} / (455 \times 22.5 \times 10^{-3}) = 6.22 \times 10^{-4} = 6.22 \times 10^{-2}\% \end{aligned}$$

$$\text{APCE} = \text{IPCE}/\text{Absorbance}$$

The absorbance of the double sided titania films on glass slide at 455 nm taken from Figure 6.3 = 0.163, so for a single film, absorbance = 0.163/2 = 0.0815.

$$A = \log(1/T), \text{ so } 0.0285 = \log(1/T), T = 0.83$$

$$A = 1 - T = 1 - 0.936 = 0.17$$

So, APCE = $6.22 \times 10^{-2}\% / 0.17 = 0.37\%$

Table S1. Contact angles of TiO₂, N-TiO₂, GQD/TiO₂ and GQD/N-TiO₂ films.

Sample	Reading 1	Reading 2	Reading 3	Average contact angle
Ti-TiO ₂	50.9°	50.6°	51.2°	50.9° ± 0.3°
N-Doped TiO ₂	12.9°	13.1°	12.5°	12.8° ± 0.3°
GQD/TiO ₂	32.0°	32.1°	32.4°	32.2° ± 0.2°
GQD/N-TiO ₂	25.1°	26.2°	25.9°	25.7° ± 0.7°

Determination of HOMO-LUMO positions of GQDs using Cyclic voltammetry

Background

Cyclic voltammetry can be used to determine the HOMO-LUMO positions of a compound using Ferrocene as an internal standard. From CV, the oxidation onset of the substance represents the HOMO, and the reduction onset of the substance represents the LUMO.

E_{HOMO} of ferrocene (Fc) = 4.8 eV below the vacuum level will be used as the reference value.

Method

- 1.) Electrode preparation (glassy carbon (GC) electrode was polished and prepared for the procedure)
 - A. Carbon nano-onions (1mg) + 0.5% Nafion solution (5 μ l) + DI water(100 μ l) \rightarrow (Sonication for 30 mins) \rightarrow Drop cast 5 μ l onto GC electrode
 - B. Carbon nano-onions (1mg) + GQD (0.1mg) + 0.5% Nafion solution (5 μ l) + DI water (95 μ l) \rightarrow (Sonication for 30 mins) \rightarrow Drop cast 5 μ l onto GC electrode
- 2.) Both electrodes were dried at 50 °C under a vacuum for 5 hours to remove the water
- 3.) 0.1M tetrabutylammonium hexafluorophosphate (TBAH) in dry acetonitrile was used as the electrolyte solution.
- 4.) Reference electrode was prepared by filling Ag wire containing electrode with 10 mM AgNO₃ + 0.1 M TBAH in dry acetonitrile
- 5.) Prior to the electrochemical measurement, 6 ml of non-aqueous electrolyte was purged with N₂ for 15 minutes to remove dissolved oxygen.

Results

Cyclic voltammogram of Background – Electrode A

Cyclic voltammogram of GQD loaded electrode – Electrode B

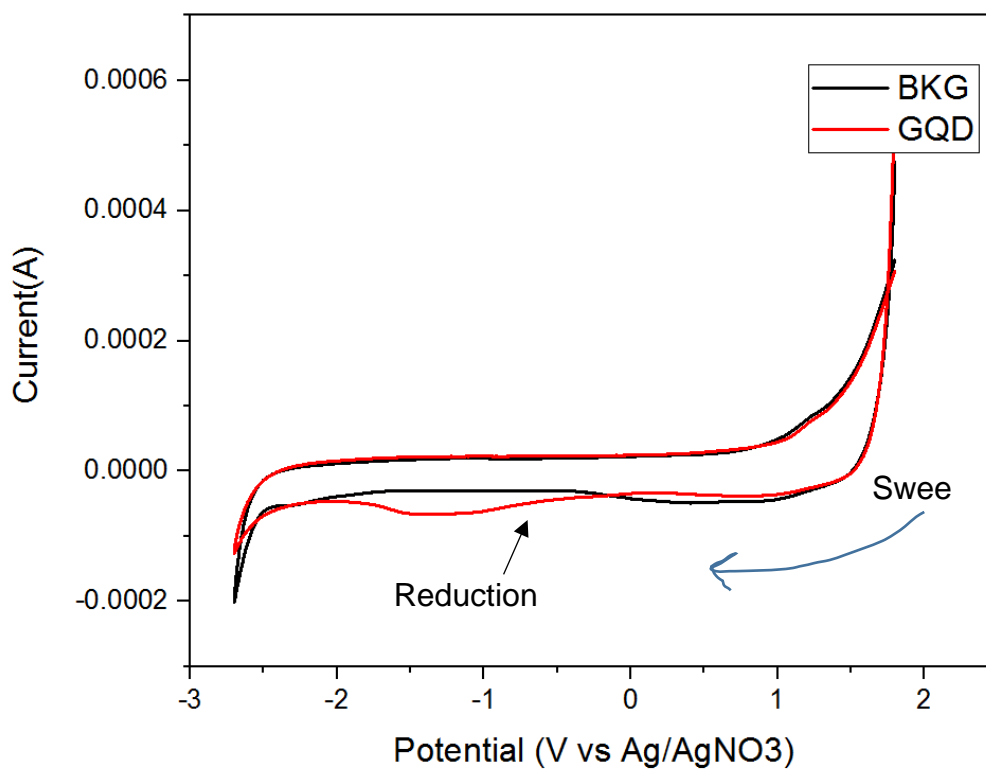


Figure D.2. Cyclic voltammogram of Background – Electrode A and Cyclic voltammogram of GQD loaded electrode – Electrode B

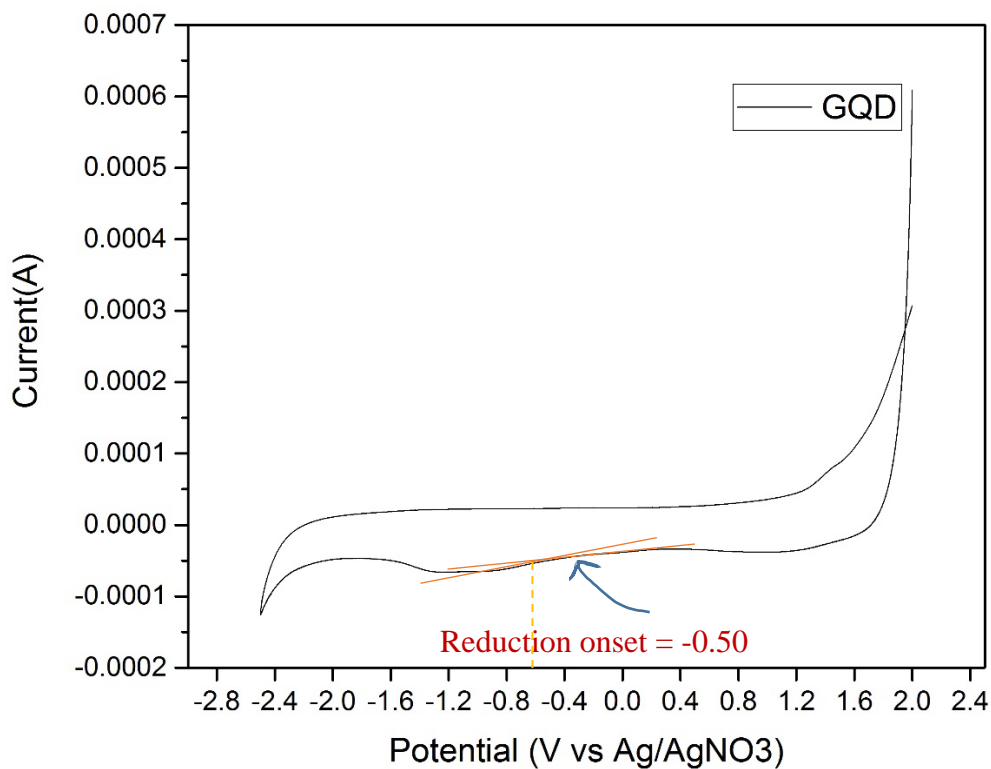


Figure D.3. Cyclic voltammogram with GQD

Ferrocene (E°) = 0.086 V vs Ag/AgNO₃

$$E_{LUMO} = -e[E_{red} - E_{1/2}(\text{Ferrocene}) + 4.8]$$

$$E_{LUMO} = -e[-0.50 - 0.09 + 4.8]$$

$$E_{LUMO} = -4.21 \text{ eV}$$

From previous data (UV VIS measurements) GQD band gap = 2.42 eV

HOMO level of GQD = -6.63 eV vs. vacuum

LUMO level of GQD = -4.21 eV vs. vacuum

Determination of valance band position of TiO₂ and N-TiO₂ using ultraviolet photoelectron spectroscopy (UPS)

Source - E-LUXTM121

Source energy = 10.2 eV (H Lyman- α photon source)

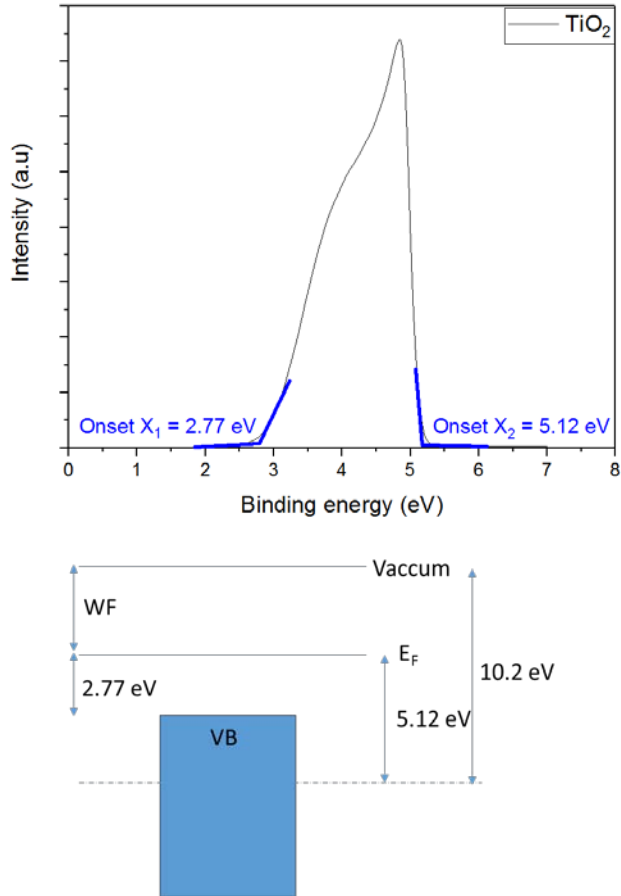


Figure D.4. Valance band spectra obtained by UPS(left side) and the coresponding energy level diagram(Right side)

Calculation

$$\text{Work function (WF)} = 10.2 \text{ eV} - X_2 \text{ eV}$$

$$\text{WF} = 10.2 \text{ eV} - 5.12 \text{ eV} = 5.08 \text{ eV}$$

$$\text{Valance Band (VB)} = \text{WF} + X_1$$

$$\text{VB} = 5.08 \text{ eV} + 2.77 \text{ eV} = 7.85 \text{ eV with respect to vacuum}$$

(Valance band position of N-TiO₂ was also determined by following the same procedure)

APPENDIX E Supporting Information of Chapter 7.

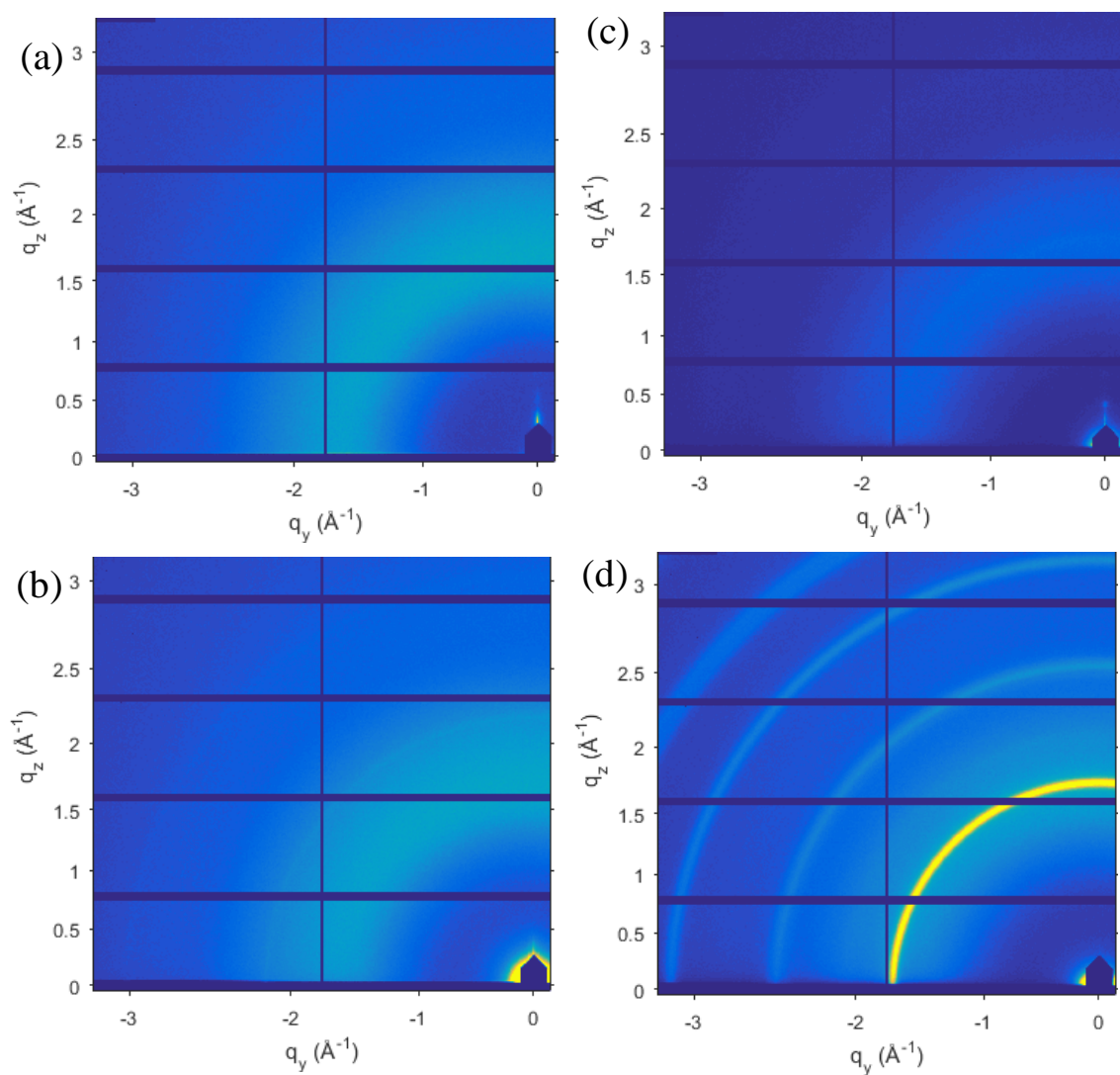


Figure E.1. GIWAXS patterns of (a) glass substrate, (b) undoped TiO_2 , (c) H- TiO_2 and (d) anatase films

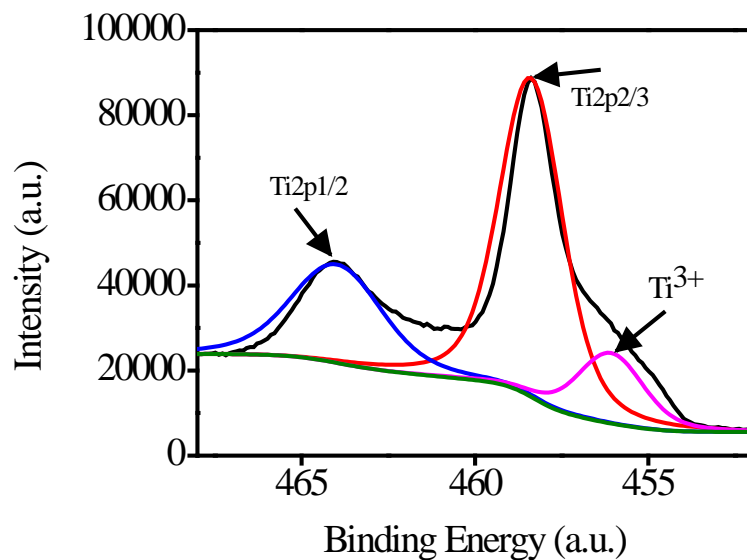


Figure E.2. XPS Ti 2p spectra H-TiO₂ films with peak fitting

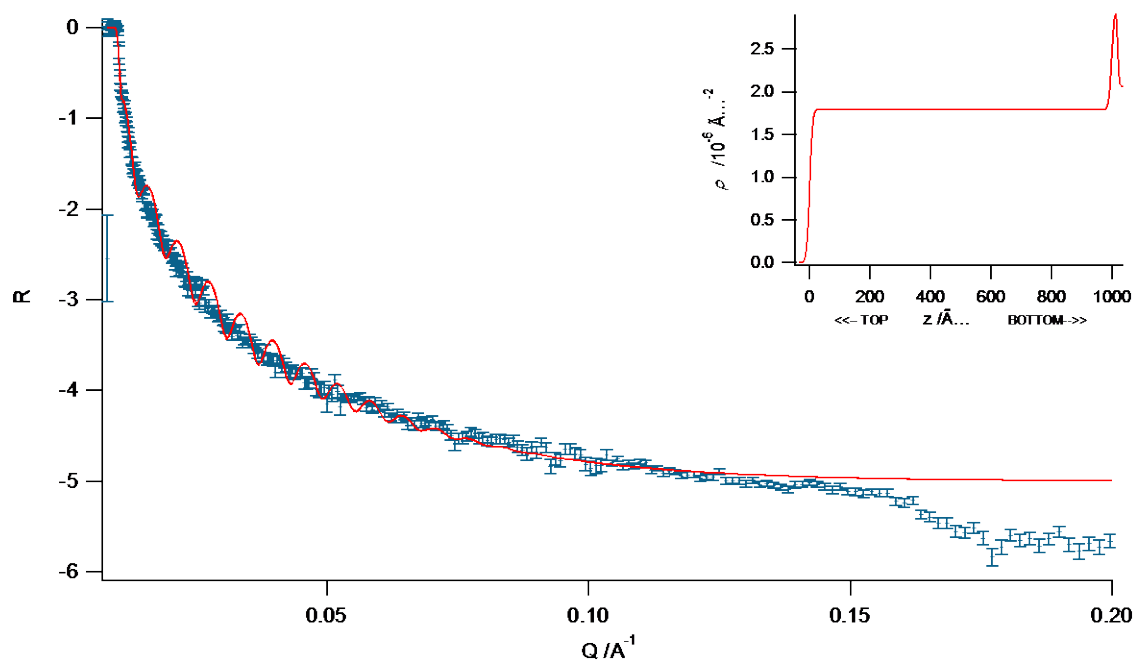


Figure E.3. Neutron Reflectivity profile of (model fit-line, experimental-bar) of undoped mesoporous TiO₂ film in air

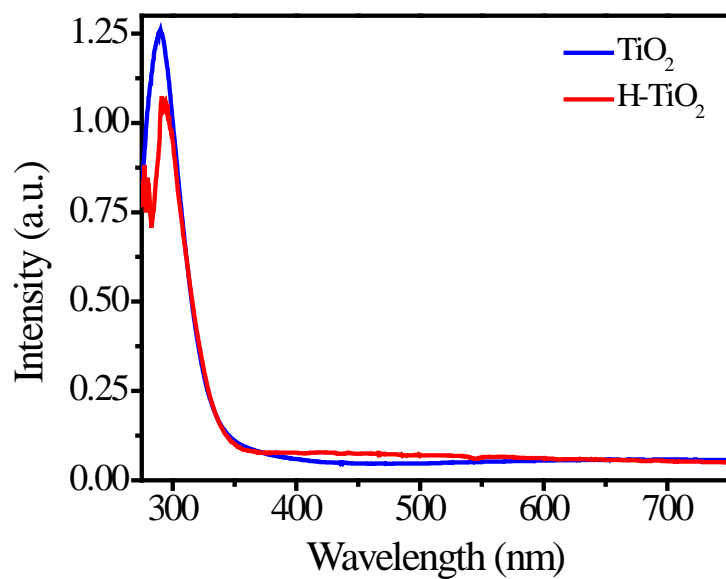


Figure E.4. UV-Vis spectra of pure and hydrogenated TiO₂ (mild condition)

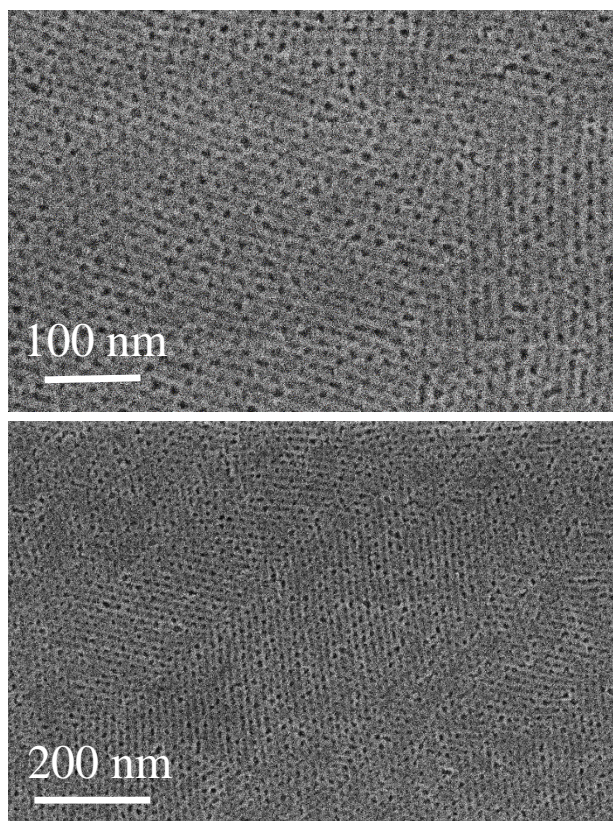


Figure E.5. SEM images of H-TiO₂ prepared using mild plasma conditions

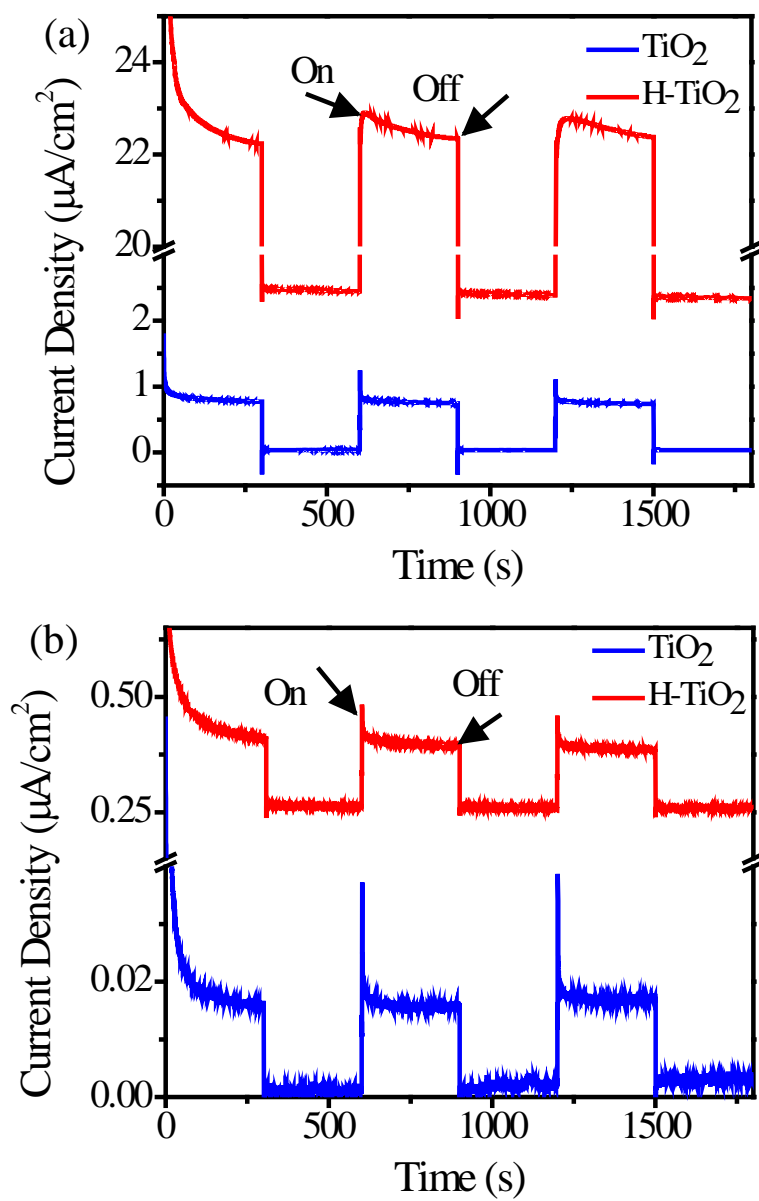


Figure E.6. Photocurrent-time measurement with undoped TiO₂ film and H-TiO₂ films under (a) UVLED and (b) BLED light irradiation

Table E.1. Contact angles of undoped TiO₂ and H-doped TiO₂ films

Sample	Reading 1	Reading 2	Reading 3	Average contact angle
TiO ₂	60°	61°	62°	~61°
H-TiO ₂	31°	31°	30°	~31°

References

1. Kondratenko, E.V., et al., *Status and perspectives of CO₂ conversion into fuels and chemicals by catalytic, photocatalytic and electrocatalytic processes*. Energy Environ. Sci., 2013. **6**(11): p. 3112.
2. *Solar hydrogen generation toward a renewable energy future*, ed. K. Rajeshwar, et al. 2008: Springer.
3. Grimes, C.A., O.K. Varghese, and S. Ranjan, *Light, water, hydrogen the solar generation of hydrogen by water photoelectrolysis*. 2008, NY USA: Springer Science.
4. Li, K., et al., *A critical review of CO₂ photoconversion: catalysts and reactors*. Catal. Today, 2014. **224**: p. 3-12.
5. Varghese, O.K., et al., *High-rate solar photocatalytic conversion of CO₂ and water vapor to hydrocarbon fuels*. Nano Lett., 2009. **9**(2): p. 731-737.
6. Roy, S.C., et al., *Toward solar fuels: photocatalytic conversion of carbon dioxide to hydrocarbons*. ACS Nano, 2010. **4**(3): p. 1259-1278.
7. Fan, J., et al., *Synergistic effect of N and Ni²⁺ on nanotitania in photocatalytic reduction of CO₂*. J. Environ. Eng., 2011. **137**(3): p. 171-176.
8. Zhao, Z., et al., *Effect of heating temperature on photocatalytic reduction of CO₂ by N-TiO₂ nanotube catalyst*. Catal. Commun., 2012. **21**: p. 32-37.
9. Oomman K. Varghese, M.P., Thomas J. LaTempa, and Craig A. Grimes, *High-Rate Solar Photocatalytic Conversion of CO₂ and Water Vapor to Hydrocarbon Fuels*. Nano Letters, 2009. **9**(2): p. 7.
10. *Climate Change 2007, An Assessment of the IPCC*. 2007.
11. Islam, S.Z., V.G. Deshmame, and S. Ilias, *Thermal stability study of Pd-composite membrane fabricated by surfactant induced electroless plating (SIEP)*. Separ. Sci. Technol., 2016. **51**(7): p. 1176-1188.
12. Katsuhiko Hirano, K.I., and Tomomi Yatsu, *Photocatalysed reduction of CO₂ in aqueous TiO₂ suspension mixed with copper powder*. Journal of Photochemistry and Photobiology A: Chemistry, 1992. **64**(4): p. 255.
13. Fujishima, A. and K. Honda, *Electrochemical photolysis of water at a semiconductor electrode*. Nature, 1972. **238**: p. 37-38.
14. Grätzel, M., *Photoelectrochemical cells*. Nature, 2001. **414**: p. 338-344.
15. Wang, G., et al., *Hydrogen-treated TiO₂ nanowire arrays for photoelectrochemical water splitting*. Nano Lett., 2011. **11**(7): p. 3026-33.
16. Dholam, R., et al., *Hydrogen production by photocatalytic water-splitting using Cr- or Fe-doped TiO₂ composite thin films photocatalyst*. Int. J. Hydrogen Energy, 2009. **34**(13): p. 5337-5346.
17. Asahi, R., et al., *Visible-light photocatalysis in nitrogen-doped titanium oxides*. Science, 2001. **293**(5528): p. 269-271.
18. Soni, S.S., et al., *Visible-light photocatalysis in titania-based mesoporous thin films*. Adv. Mater., 2008. **20**(8): p. 1493-1498.
19. Shaozheng, H., et al., *Improved photocatalytic hydrogen production property over Ni/NiO/N-TiO_{2-x} heterojunction nanocomposite prepared by NH₃ plasma treatment*. J. Power Sources, 2014. **250**: p. 30-39.

20. Lan, M., X. Peng, and W. Pei-Nan, *Experimental study on the band gap narrowings of TiO₂ films calcined under N₂ or NH₃ atmosphere*. Appl. Surf. Sci., 2008. **255**(5): p. 2574-2580.
21. Hidetaka, I., et al., *Electrochemical synthesis of titania nanostructural arrays and their surface modification for enhanced photoelectrochemical hydrogen production*. Chem. Phys. Lett., 2010. **489**(1-3): p. 81-85.
22. Lewis, N.S., *Toward cost-effective solar energy use*. Science, 2007. **315**(5813): p. 798-801.
23. Cao, X.P., et al., *Synthesis of visible-light responsive C, N and Ce co-doped TiO₂ mesoporous membranes via weak alkaline sol-gel process*. J. Mater. Chem., 2012. **22**(30): p. 15309-15315.
24. Zhang, H., G. Chen, and D.W. Bahnemann, *Photoelectrocatalytic materials for environmental applications*. J. Mater. Chem., 2009. **19**(29): p. 5089-5121.
25. Liu, G., et al., *Titania-based photocatalysts—crystal growth, doping and heterostructuring*. J. Mater. Chem., 2010. **20**(5): p. 831-843.
26. Zhang, L., et al., *Significantly enhanced photocatalytic activities and charge separation mechanism of Pd-decorated ZnO-graphene oxide Nanocomposites*. ACS Appl. Mater. Interfaces, 2014. **6**(5): p. 3623-3629.
27. Zhang, L., et al., *Role of graphene in great enhancement of photocatalytic activity of ZnO nanoparticle-graphene hybrids*. Physica E, 2013. **47**: p. 279-284.
28. Li, J. and N. Wu, *Semiconductor-based photocatalysts and photoelectrochemical cells for solar fuel generation: a review*. Catal. Sci. Technol., 2015. **5**(3): p. 1360-1384.
29. Banerjee, S., et al., *New insights into the mechanism of visible light photocatalysis*. J. Phy. Chem. Lett., 2014. **5**(15): p. 2543-2554.
30. Liao, Y.T., et al., *Synthesis of mesoporous titania thin films (MTTFs) with two different structures as photocatalysts for generating hydrogen from water splitting*. Appl. Energ., 2012. **100**: p. 75-80.
31. Li, L., et al., *Sub-10 nm rutile titanium dioxide nanoparticles for efficient visible-light-driven photocatalytic hydrogen production*. Nat. Commun., 2015. **6**(5881).
32. Salari, M., et al., *Disorder engineering of undoped TiO₂ nanotube arrays for highly efficient solar-driven oxygen evolution*. Phys. Chem. Chem. Phys., 2015. **17**: p. 5642-5649.
33. Crepaldi, E.L., et al., *Controlled formation of highly organized mesoporous titania thin films: From mesostructured hybrids to mesoporous nanoanatase TiO₂*. J. Am. Chem. Soc., 2003. **125**: p. 9770-9786.
34. Feng, D., et al., *Multi-layered mesoporous TiO₂ thin films with large pores and highly crystalline frameworks for efficient photoelectrochemical conversion*. J. Mater. Chem. A, 2013. **1**(5): p. 1591-1599.
35. Martinez-Ferrero, E., et al., *Nanostructured titanium oxynitride porous thin films as efficient visible-active photocatalysts*. Adv. Funct. Mater., 2007. **17**(16): p. 3348-3354.
36. Crepaldi, E.L., et al., *Controlled formation of highly organized mesoporous titania thin films: from mesostructured hybrids to mesoporous nanoanatase TiO₂*. J. Am. Chem. Soc., 2003. **125**(32): p. 9770-9786.

37. Shi, J.W., et al., *Facile one-pot synthesis of Eu, N-codoped mesoporous titania microspheres with yolk-shell structure and high visible-light induced photocatalytic performance*. Appl. Catal., A, 2012. **435**: p. 86-92.
38. Landmann, M., et al., *Fingerprints of order and disorder in the electronic and optical properties of crystalline and amorphous TiO₂*. Phys. Rev. B, 2012. **86**(6): p. 064201.
39. Pelaez, M., et al., *A review on the visible light active titanium dioxide photocatalysts for environmental applications*. Appl. Catal., B, 2012. **125**: p. 331-349.
40. Burda, C., et al., *Enhanced nitrogen doping in TiO₂ nanoparticles*. Nano Lett., 2003. **3**(8): p. 1049-1051.
41. Ismail, A.A. and D.W. Bahnemann, *Mesoporous titania photocatalysts: preparation, characterization and reaction mechanisms*. J. Mater. Chem., 2011. **21**(32): p. 11686-11707.
42. Bingham, S. and W.A. Daoud, *Recent advances in making nano-sized TiO₂ visible-light active through rare-earth metal doping*. J. Mater. Chem., 2011. **21**(7): p. 2041-2050.
43. Nagaveni, K., M.S. Hegde, and G. Madras, *Structure and photocatalytic activity of Ti_{1-x}MxO_{2±δ} (M = W, V, Ce, Zr, Fe, and Cu) synthesized by solution combustion method*. J. Phys. Chem. B, 2004. **108**(52): p. 20204-20212.
44. Devi, L.G. and R. Kavitha, *A review on non metal ion doped titania for the photocatalytic degradation of organic pollutants under UV/solar light: Role of photogenerated charge carrier dynamics in enhancing the activity*. Appl. Catal., B, 2013. **140**: p. 559-587.
45. Choi, W., A. Termin, and M.R. Hoffmann, *The role of metal ion dopants in quantum-sized TiO₂: correlation between photoreactivity and charge carrier recombination dynamics*. J. Phys. Chem., 1994. **98**(51): p. 13669-13679.
46. Choi, J., H. Park, and M.R. Hoffmann, *Effects of single metal-ion doping on the visible-light photoreactivity of TiO₂*. J. Phys. Chem. C, 2010. **114**(2): p. 783-792.
47. Zhang, Y., et al., *Ethanol supercritical route for fabricating bimodal carbon modified mesoporous TiO₂ with enhanced photocatalytic capability in degrading phenol*. Appl. Catal., B, 2012. **115**: p. 236-244.
48. Liu, S.-H. and H.-R. Syu, *High visible-light photocatalytic hydrogen evolution of C,N-codoped mesoporous TiO₂ nanoparticles prepared via an ionic-liquid-template approach*. Int. J. Hydrogen Energy, 2013. **38**(32): p. 13856-13865.
49. Cong, Y., et al., *Synthesis and characterization of nitrogen-doped TiO₂ nanophotocatalyst with high visible light activity*. J. Phys. Chem. C 2007. **111**: p. 6976-6982.
50. Jinlong, L., et al., *Fabrication of nitrogen-doped mesoporous TiO₂ layer with higher visible photocatalytic activity by plasma-based ion implantation*. Thin Solid Films, 2010. **519**(1): p. 101-105.
51. Varley, J.B., A. Janotti, and C.G. Van de Walle, *Mechanism of visible-light photocatalysis in nitrogen-doped TiO₂*. Adv. Mater., 2011. **23**(20): p. 2343-2347.
52. Asahi, R., et al., *Nitrogen-doped titanium dioxide as visible-light-sensitive photocatalyst: designs, developments, and prospects*. Chem. Rev., 2014. **114**(19): p. 9824-9852.

53. Serpone, N., *Is the band gap of pristine TiO₂ narrowed by anion- and cation-doping of titanium dioxide in second-generation photocatalysts*. J. Phys. Chem. B, 2006. **110**(48): p. 24287-24293.
54. Pan, H., et al., *Effects of H-, N-, and (H, N)-doping on the photocatalytic activity of TiO₂*. J. Phys. Chem. C, 2011. **115**(24): p. 12224-12231.
55. Lynch, J., et al., *Substitutional or interstitial site-selective nitrogen doping in TiO₂ nanostructures*. J. Phys. Chem. C, 2015. **119**(13): p. 7443-7452.
56. Wang, G., et al., *Significantly enhanced visible light photoelectrochemical activity in TiO₂ nanowire arrays by nitrogen implantation*. Nano Lett., 2015. **15**(7): p. 4692-4698.
57. Chen, X.B., et al., *Formation of oxynitride as the photocatalytic enhancing site in nitrogen-doped titania nanocatalysts: Comparison to a commercial nanopowder*. Adv. Funct. Mater., 2005. **15**(1): p. 41-49.
58. Wang, J., et al., *Visible-light-driven reversible and switchable hydrophobic to hydrophilic nitrogen-doped titania surfaces: correlation with photocatalysis*. Nanoscale, 2010. **2**(10): p. 2257-2261.
59. López-Luke, T., et al., *Nitrogen-doped and CdSe quantum-Dot-sensitized nanocrystalline TiO₂ films for solar energy conversion applications*. J. Phys. Chem. C 2008. **112**: p. 1282-1292.
60. Hensel, J., et al., *Synergistic effect of CdSe quantum dot sensitization and nitrogen doping of TiO₂ nanostructures for photoelectrochemical solar hydrogen generation*. Nano Lett. , 2010. **10**: p. 478-483.
61. Pan, D., et al., *Electrophoretic fabrication of highly robust, efficient, and benign heterojunction photoelectrocatalysts based on graphene-quantum-dot sensitized TiO₂ nanotube arrays*. J. Mater. Chem. A, 2013. **1**: p. 3551-3555.
62. Shujuan Zhuo, M.S., and Shuit-Tong Lee, *Upconversion and downconversion fluorescent graphene quantum dots: ultrasonic preparation and photocatalysis*. ACS nano, 2012. **6**(2): p. 1059-1064.
63. Liu, Y. and D.Y. Kim, *Ultraviolet and blue emitting graphene quantum dots synthesized from carbon nano-onions and their comparison for metal ion sensing*. Chem. Commun., 2015. **51**(20): p. 4176-9.
64. Kenrick J. Williams, C.A.N., Xin Yan, Liang-Shi Li, and Xiaoyang Zhu, *Hot electron injection from graphene quantum dots to TiO₂*. ACS Nano, 2013. **7**(2): p. 1388-1394.
65. Qu, D., et al., *Highly luminescent S, N co-doped graphene quantum dots with broad visible absorption bands for visible light photocatalysts*. Nanoscale, 2013. **5**(24): p. 12272-7.
66. Li, H., et al., *Preparation of coaxial heterogeneous graphene quantum dot-sensitized TiO₂ nanotube arrays via linker molecule binding and electrophoretic deposition*. Carbon, 2015. **81**: p. 474-487.
67. Chan, D.K., P.L. Cheung, and J.C. Yu, *A visible-light-driven composite photocatalyst of TiO₂ nanotube arrays and graphene quantum dots*. Beilstein J Nanotechnol, 2014. **5**: p. 689-95.
68. Yifu Yu, J.R., and Ming Meng, *Photocatalytic hydrogen evolution on graphene quantum dots anchored TiO₂ nanotubes-array*. Int. J. Hydrogen Energy, 2013. **38**: p. 12266-12272.

69. Islam, S.Z., et al., *N₂/Ar plasma induced doping of ordered mesoporous TiO₂ thin films for visible light active photocatalysis*. *Microporous Mesoporous Mater.*, 2016. **220**: p. 120-128.
70. Leung, D.Y.C., et al., *Hydrogen production over titania-based photocatalysts*. *Chemosuschem*, 2010. **3**(6): p. 681-694.
71. Xiang, Q., J. Yu, and M. Jaroniec, *Synergetic effect of MoS₂ and graphene as cocatalysts for enhanced photocatalytic H₂ production activity of TiO₂ nanoparticles*. *J. Am. Chem. Soc.*, 2012. **134**: p. 6575–6578.
72. Tong, H., et al., *Nano-photocatalytic materials: possibilities and challenges*. *Adv. Mater.*, 2012. **24**: p. 229–251.
73. Di Valentin, C. and G. Pacchioni, *Trends in non-metal doping of anatase TiO₂: B, C, N and F*. *Catal. Today*, 2013. **206**: p. 12-18.
74. Chen, X., et al., *Increasing solar absorption for photocatalysis with black hydrogenated titanium dioxide nanocrystals*. *Science*, 2011. **331**(6018): p. 746-750.
75. El-Sheikh, S.M., et al., *High performance sulfur, nitrogen and carbon doped mesoporous anatase-brookite TiO₂ photocatalyst for the removal of microcystin-LR under visible light irradiation*. *J. Hazard. Mater.*, 2014. **280**: p. 723-733.
76. Liu, G., et al., *Synergistic effects of B/N doping on the visible-light photocatalytic activity of mesoporous TiO₂*. *Angew. Chem. Int. Ed.*, 2008. **47**(29): p. 5277-5277.
77. Xu, J.-H., et al., *Simple fabrication of twist-like helix N,S-codoped titania photocatalyst with visible-light response*. *Appl. Catal., B*, 2008. **79**(1): p. 72-80.
78. Liu, G., et al., *Enhanced visible light photocatalytic activity of CN-codoped TiO₂ films for the degradation of microcystin-LR*. *J. Mol. Catal. A: Chem.*, 2013. **372**: p. 58-65.
79. Katsanaki, A.V., et al., *Photocatalytic oxidation of nitrogen oxides on N-F-doped titania thin films*. *Appl. Catal., B*, 2013. **140-141**: p. 619-625.
80. Periyat, P., et al., *One-pot synthesis of anionic (nitrogen) and cationic (sulfur) codoped high-temperature stable, visible light active, anatase photocatalysts*. *J. Phys. Chem. C*, 2009. **113**(8): p. 3246-3253.
81. Pelaez, M., et al., *A comparative study on the removal of cylindrospermopsin and microcystins from water with NF-TiO₂-P25 composite films with visible and UV-vis light photocatalytic activity*. *Appl. Catal., B*, 2012. **121-122**: p. 30-39.
82. Kontos, A.G., et al., *Visible light induced wetting of nanostructured N-F co-doped titania films*. *Photochem. Photobiol. Sci.*, 2011. **10**(3): p. 350-354.
83. Pelaez, M., et al., *Visible light-activated N-F-codoped TiO₂ nanoparticles for the photocatalytic degradation of microcystin-LR in water*. *Catal. Today*, 2009. **144**(1-2): p. 19-25.
84. Zhao, C., et al., *UV and visible light activated TiO₂ photocatalysis of 6-hydroxymethyl uracil, a model compound for the potent cyanotoxin cylindrospermopsin*. *Catal. Today*, 2014. **224**: p. 70-76.
85. Shao, G.S., et al., *Hierarchical mesoporous phosphorus and nitrogen doped titania materials: Synthesis, characterization and visible-light photocatalytic activity*. *Appl. Catal., B*, 2009. **92**(1-2): p. 61-67.
86. Cavalcante, R.P., et al., *Synthesis and characterization of B-doped TiO₂ and their performance for the degradation of metoprolol*. *Catal. Today*, 2015. **252**: p. 27-34.

87. Bagheri, S., et al., *Progress on mesoporous titanium dioxide: synthesis, modification and applications*. Microporous Mesoporous Mater., 2015. **218**: p. 206-222.
88. Mahoney, L. and R. Koodali, *Versatility of evaporation-induced self-assembly (EISA) method for preparation of mesoporous TiO₂ for energy and environmental applications*. Materials, 2014. **7**(4): p. 2697.
89. Zhang, R., et al., *Mesoporous titania: From synthesis to application*. Nano Today, 2012. **7**(4): p. 344-366.
90. Li, W., et al., *A perspective on mesoporous TiO₂ materials*. Chem. Mater., 2014. **26**(1): p. 287-298.
91. Zhou, W. and H. Fu, *Mesoporous TiO₂: preparation, doping, and as a composite for photocatalysis*. Chemcatchem, 2013. **5**(4): p. 885-894.
92. Antonelli, D.M. and J.Y. Ying, *Synthesis of hexagonally packed mesoporous TiO₂ by a modified sol-gel method*. Angew. Chem. Int. Ed., 1995. **34**(18): p. 2014-2017.
93. Yu, J., et al., *Hydrothermal preparation and photocatalytic activity of hierarchically sponge-like macro-/mesoporous titania*. J. Phys. Chem. C, 2007. **111**(28): p. 10582-10589.
94. Wang, H., et al., *Mesoporous spherical aggregates of anatase nanocrystals with wormhole-like framework structures: their chemical fabrication, characterization, and photocatalytic performance*. Langmuir, 2004. **20**(26): p. 11738-11747.
95. Liu, X., et al., *Highly crystalline spindle-shaped mesoporous anatase titania particles: solution-phase synthesis, characterization, and photocatalytic properties*. Langmuir, 2010. **26**(11): p. 7671-7674.
96. Joo, J.B., et al., *Mesoporous anatase titania hollow nanostructures through silica-protected calcination*. Adv. Funct. Mater., 2012. **22**(1): p. 166-174.
97. Da Silva, R.O., et al., *Synthesis of recrystallized anatase TiO₂ mesocrystals with Wulff shape assisted by oriented attachment*. Nanoscale, 2011. **3**(4): p. 1910-1916.
98. Bleta, R., P. Alphonse, and L. Lorenzato, *Nanoparticle route for the preparation in aqueous medium of mesoporous TiO₂ with controlled porosity and crystalline framework*. J. Phys. Chem. C, 2010. **114**(5): p. 2039-2048.
99. Moonosawmy, K.R., et al., *Mesoporous and macroporous brookite thin films having a large thermal stability range*. Langmuir, 2012. **28**(16): p. 6706-6713.
100. Wang, J., et al., *Thermal stability and optimal photoinduced hydrophilicity of mesoporous TiO₂ thin films*. J. Phys. Chem. C, 2012. **116**(17): p. 9517-9525.
101. Yin, J.B. and X.P. Zhao, *Enhanced electrorheological activity of mesoporous Cr-doped TiO₂ from activated pore wall and high surface area*. J. Phys. Chem. B, 2006. **110**(26): p. 12916-12925.
102. Guo, C., et al., *Hierarchical mesoporous TiO₂ microspheres for the enhanced photocatalytic oxidation of sulfonamides and their mechanism*. RSC Adv. , 2012. **2**(11): p. 4720-4727.
103. Nagpure, S., et al., *In situ GISAXS investigation of low-temperature aging in oriented surfactant-mesostructured titania thin films*. J. Phys. Chem. C, 2015. **119**(40): p. 22970-22984.
104. Das, S., et al., *In-situ GISAXS investigation of pore orientation effects on the thermal transformation mechanism in mesoporous titania thin films*. J. Phys. Chem. C, 2013. **118**(2): p. 968-976.

105. Das, S., et al., *Pore orientation effects on the kinetics of mesostructure loss in surfactant templated titania thin films*. Phys. Chem. Chem. Phys., 2016. **18**: p. 2896--2905.
106. Han, O.H., et al., *Selective synthesis of lamellar titania with carboxylate precursor and characterization by solid-state NMR*. Chem. Mater., 2007. **19**(15): p. 3615-3623.
107. Livage, J., M. Henry, and C. Sanchez, *Sol-gel chemistry of transition metal oxides*. Prog. Solid State Chem., 1988. **18**(4): p. 259-341.
108. Schubert, U., *Chemical modification of titanium alkoxides for sol-gel processing*. J. Mater. Chem., 2005. **15**(35-36): p. 3701-3715.
109. Kallala, M., C. Sanchez, and B. Cabane, *Structures of inorganic polymers in sol-gel processes based on titanium oxide*. Phys. Rev. E, 1993. **48**(5): p. 3692-3704.
110. Park, J.K., et al., *Reaction mechanism for the hydrolysis of titanium alkoxides*. Bull. Korean Chem. Soc., 2003. **24**(5): p. 671-673.
111. Weymann-Schildknecht, S. and M. Henry, *Mechanistic aspects of the hydrolysis and condensation of titanium alkoxides complexed by tripodal ligands*. J. Chem. Soc., Dalton Trans. , 2001. **0**(16): p. 2425-2428.
112. Soler-Illia, G.J.D.A.A. and C. Sanchez, *Interactions between poly(ethylene oxide)-based surfactants and transition metal alkoxides: their role in the templated construction of mesostructured hybrid organic-inorganic composites*. New J. Chem., 2000. **24**(7): p. 493-499.
113. Schlipf, D.M., et al., *Effects of pore size and tethering on the diffusivity of lipids confined in mesoporous silica*. Adv. Mater. Interfaces, 2017.
114. Antonelli, D.M., *Synthesis of phosphorus-free mesoporous titania via templating with amine surfactants*. Microporous Mesoporous Mater., 1999. **30**(2-3): p. 315-319.
115. Brinker, C.J., et al., *Evaporation-induced self-assembly: nanostructures made easy*. Adv. Mater., 1999. **11**(7): p. 579-585.
116. Alberius, P.C.A., et al., *General predictive syntheses of cubic, hexagonal, and lamellar silica and titania mesostructured thin films*. Chem. Mater., 2002. **14**(8): p. 3284-3294.
117. Kirsch, B.L., et al., *In-situ X-ray diffraction study of the crystallization kinetics of mesoporous titania films*. J. Phys. Chem. B, 2004. **108**(34): p. 12698-12706.
118. Choi, S.Y., et al., *Thermally stable two-dimensional hexagonal mesoporous nanocrystalline anatase, meso-nc-TiO₂: bulk and crack-free thin film morphologies*. Adv. Funct. Mater., 2004. **14**(4): p. 335-344.
119. Haseloh, S., et al., *Towards flexible inorganic "mesomaterials": one-pot low temperature synthesis of mesostructured nanocrystalline titania*. Chem. Comm., 2004. **13**: p. 1460-1461.
120. Sanchez, C., et al., *Design, synthesis, and properties of inorganic and hybrid thin films having periodically organized nanoporosity*. Chem. Mater., 2008. **20**(3): p. 682-737.
121. Huo, Q., D.I. Margolese, and G.D. Stucky, *Surfactant control of phases in the synthesis of mesoporous silica-based materials*. Chem. Mater., 1996. **8**(5): p. 1147-1160.

122. Bosc, F., et al., *Mesostructure of anatase thin films prepared by mesophase templating*. Chem. Mater., 2004. **16**(11): p. 2208-2214.
123. Israelachvili, J.N., *Intermolecular and Surface Forces*. 2nd ed. 1992, New York: Academic Press. 366-394.
124. Wu, Q. and S.E. Rankin, *Tuning the wall thickness and pore orientation in mesoporous titania films prepared with low-temperature aging*. J. Sol-Gel Sci. Technol., 2011. **60**(1): p. 81-90.
125. Jang, K.S., et al., *Using the effects of pH and moisture to synthesize highly organized mesoporous titania thin films*. Chem. Comm., 2004. **13**: p. 1514-1515.
126. Kellogg, G., et al., *Observed surface energy effects in confined diblock copolymers*. Phys. Rev. Lett., 1996. **76**(14): p. 2503.
127. Huang, E., et al., *Neutrality conditions for block copolymer systems on random copolymer brush surfaces*. Macromolecules, 1999. **32**(16): p. 5299-5303.
128. Huang, E., et al., *Using surface active random copolymers to control the domain orientation in diblock copolymer thin films*. Macromolecules, 1998. **31**(22): p. 7641-7650.
129. Thurn-Albrecht, T., et al., *Nanosopic templates from oriented block copolymer films*. Adv. Mater., 2000. **12**(11): p. 787-791.
130. Huinink, H., et al., *Asymmetric block copolymers confined in a thin film*. J. Chem. Phys., 2000. **112**(5): p. 2452-2462.
131. Pickett, G.T. and A.C. Balazs, *Equilibrium orientation of confined diblock copolymer films*. Macromolecules, 1997. **30**(10): p. 3097-3103.
132. Koganti, V.R., et al., *Generalized coating route to silica and titania films with orthogonally tilted cylindrical nanopore arrays*. Nano Lett., 2006. **6**(11): p. 2567-2570.
133. Tasinkevych, M. and A. Ciach, *Structural transformations in confined lamellar phases in oil-water-surfactant mixtures*. J. Chem. Phys., 2001. **115**(18): p. 8705-8713.
134. Rankin, S.E., A.P. Malanoski, and F. Van Swol. *Monte Carlo simulation of amphiphile self-assembly during dip coating*. in *Nonlithographic and Lithographic Methods of Nanofabrication -From Ultralarge-Scale Integration to Photonics to Molecular Electronics, November 26, 2000 - December 1, 2000*. 2001. Boston, MA, United states: Materials Research Society.
135. Richman, E.K., T. Brezesinski, and S.H. Tolbert, *Vertically oriented hexagonal mesoporous films formed through nanometre-scale epitaxy*. Nat. Mater., 2008. **7**(9): p. 712-717.
136. Grosso, D., et al., *A first insight in the mechanisms involved in the self-assembly of 2D-hexagonal templated SiO₂ and TiO₂ mesostructured films during dip-coating*. J. Sol-Gel Sci. Technol., 2003. **26**(1-3): p. 561-565.
137. Grosso, D., et al., *An in situ study of mesostructured CTAB-silica film formation during dip coating using time-resolved SAXS and interferometry measurements*. Chem. Mater., 2002. **14**(2): p. 931-939.
138. Grosso, D., et al., *Two-dimensional hexagonal mesoporous silica thin films prepared from block copolymers: detailed characterization and formation mechanism*. Chem. Mater., 2001. **13**(5): p. 1848-1856.

139. Grosso, D., et al., *Phase transformation during cubic mesostructured silica film formation*. Chem. Comm., 2002(7): p. 748-749.
140. Grosso, D., et al., *Fundamentals of mesostructuring through evaporation-induced self-assembly*. Adv. Funct. Mater., 2004. **14**(4): p. 309-322.
141. Faustini, M., et al., *From chemical solutions to inorganic nanostructured materials: a journey into evaporation-driven processes*. Chem. Mater., 2013. **26**(1): p. 709-723.
142. Koganti, V.R., S. Das, and S.E. Rankin, *In situ FTIR investigation of the kinetics of silica polycondensation in surfactant templated, mesostructured thin films*. J. Phys. Chem. C, 2014. **118**(33): p. 19450-19461.
143. Ko, Y.-S., et al., *Synthesis of mesoporous titania thin films with vertical pore channels and thick and crystalline walls*. Microporous Mesoporous Mater., 2011. **145**(1): p. 141-145.
144. Koh, C.-W., et al., *Mesoporous titania thin film with highly ordered and fully accessible vertical pores and crystalline walls*. Chem. Asian J. , 2008. **3**: p. 862 – 867.
145. Grosso, D., et al., *Highly porous TiO₂ anatase optical thin films with cubic mesostructure stabilized at 700 °C*. Chem. Mater., 2003. **15**(24): p. 4562-4570.
146. Wanka, G., H. Hoffmann, and W. Ulbricht, *Phase diagrams and aggregation behavior of poly(oxyethylene)-poly(oxypropylene)-poly(oxyethylene) triblock copolymers in aqueous solutions*. Macromolecules, 1994. **27**(15): p. 4145-4159.
147. Lee, U.H., et al., *Mesoporous titania thin films with pseudo-cubic structure: synthetic studies and applications to nanomembranes and nanotemplates*. Microporous Mesoporous Mater., 2006. **88**(1-3): p. 48-55.
148. Liu, K., et al., *Preparation of large-pore mesoporous nanocrystalline TiO₂ thin films with tailored pore diameters*. J. Phys. Chem. B, 2005. **109**(40): p. 18719-18722.
149. Li, X.S., et al., *Effects of template and precursor chemistry on structure and properties of mesoporous TiO₂ thin films*. Langmuir, 2004. **20**(21): p. 9095-9102.
150. Das, S., et al., *In-situ GISAXS investigation of pore orientation effects on the thermal transformation mechanism in mesoporous titania thin films*. J. Phys. Chem. C 2014. **118**(2): p. 968–976.
151. Lee, D.W., et al., *Synthesis of bimodal mesoporous titania with high thermal stability via replication of citric acid-templated mesoporous silica*. Chem. Mater., 2007. **19**(4): p. 937-941.
152. Yue, W., et al., *Mesoporous monocrystalline TiO₂ and its solid-state electrochemical properties*. Chem. Mater., 2009. **21**(12): p. 2540-2546.
153. Zhang, Z., F. Zuo, and P. Feng, *Hard template synthesis of crystalline mesoporous anatase TiO₂ for photocatalytic hydrogen evolution*. J. Mater. Chem., 2010. **20**(11): p. 2206-2212.
154. McDonnell, K.A., et al., *Influence of doping on the photoactive properties of magnetron-sputtered titania coatings: experimental and theoretical study*. Phys. Rev. B: Condens. Matter, 2012. **86**(11): p. 115306.
155. Ghicov, A., et al., *TiO₂ nanotube layers: dose effects during nitrogen doping by ion implantation*. Chem. Phys. Lett., 2006. **419**(4-6): p. 426-429.

156. Ghicov, A., et al., *Ion implantation and annealing for an efficient N-doping of TiO₂ nanotubes*. Nano Lett., 2006. **6**(5): p. 1080-1082.
157. Aman, N., et al., *Facile synthesis of mesoporous N doped zirconium titanium mixed oxide nanomaterial with enhanced photocatalytic activity under visible light*. J. Mater. Chem., 2010. **20**(48): p. 10876-10882.
158. Mao, C., et al., *In situ preparation of a Ti³⁺ self-doped TiO₂ film with enhanced activity as photoanode by N₂H₄ reduction*. Angew. Chem. Int. Ed., 2014. **53**(39): p. 10485-10489.
159. Liu, Z., et al., *Characteristics of doped TiO₂ photocatalysts for the degradation of methylene blue waste water under visible light*. J. Alloys Compd., 2010. **501**(1): p. 54-59.
160. Gohin, M., et al., *Photocatalytic activity of mesoporous films based on N-doped TiO₂ nanoparticles*. J. Mater. Chem., 2010. **20**(37): p. 8070-8077.
161. Sivaranjani, K. and C.S. Gopinath, *Porosity driven photocatalytic activity of wormhole mesoporous TiO_{2-x}N_x in direct sunlight*. J. Mater. Chem., 2011. **21**(8): p. 2639-2647.
162. Ananpattarachai, J., P. Kajitvichyanukul, and S. Seraphin, *Visible light absorption ability and photocatalytic oxidation activity of various interstitial N-doped TiO₂ prepared from different nitrogen dopants*. J. Hazard. Mater., 2009. **168**(1): p. 253-61.
163. Liu, H., G. Liu, and X. Shi, *N/Zr-codoped TiO₂ nanotube arrays: fabrication, characterization, and enhanced photocatalytic activity*. Colloids Surf., A, 2010. **363**(1-3): p. 35-40.
164. Kafizas, A. and I.P. Parkin, *The combinatorial atmospheric pressure chemical vapour deposition (cAPCVD) of a grading N-doped mixed phase titania thin film*. J. Mater. Chem., 2010. **20**(11): p. 2157-2169.
165. Miao, L., et al., *Structural and compositional characterization of N₂-H₂ plasma surface-treated TiO₂ thin films*. Appl. Surf. Sci., 2005. **244**(1-4): p. 412-417.
166. Sharma, R., et al., *Enhancement of the photoelectrochemical conversion efficiency of nanotubular TiO₂ photoanodes using nitrogen plasma assisted surface modification*. Nanotechnology, 2009. **20**(7): p. 075704.
167. Liu, X., et al., *Characteristics of N-doped TiO₂ nanotube arrays by N₂-plasma for visible light-driven photocatalysis*. J. Alloys Compd., 2011. **509**(41): p. 9970-9976.
168. Lee, H.U., et al., *Visible-light-responsive bicrystalline (anatase/brookite) nanoporous nitrogen-doped TiO₂ photocatalysts by plasma treatment*. Chem. Eng. J., 2014. **254**: p. 268-275.
169. Pulsipher, D.J., I.T. Martin, and E.R. Fisher, *Controlled nitrogen doping and film colorimetrics in porous TiO₂ materials using plasma processing*. ACS Appl. Mater. Interfaces, 2010. **2**(6): p. 1743-1753.
170. Huang, C.M., et al., *Effect of nitrogen-plasma surface treatment to the enhancement of TiO₂ photocatalytic activity under visible light irradiation*. J. Mol. Catal. A: Chem., 2007. **261**(2): p. 218-224.
171. Chen, C., H. Bai, and C. Chang, *Effect of plasma processing gas composition on the nitrogen-doping status and visible light photocatalysis of TiO₂*. J. Phys. Chem. C 2007. **111**(42): p. 15228-15235.

172. Napoli, F., et al., *The Nitrogen photoactive centre in N-doped titanium dioxide formed via interaction of N atoms with the solid. nature and energy level of the species.* Chem. Phys. Lett., 2009. **477**(1-3): p. 135-138.
173. Li, G.S., et al., *A mesoporous TiO₂-xNx photocatalyst prepared by sonication pretreatment and in situ pyrolysis.* Sep. Purif. Technol., 2009. **67**(2): p. 152-157.
174. Liu, G., et al., *Drastically enhanced photocatalytic activity in nitrogen doped mesoporous TiO₂ with abundant surface states.* J. Colloid Interface Sci., 2009. **334**(2): p. 171-5.
175. Nassoko, D., et al., *Nitrogen-doped TiO₂ nanoparticles by using EDTA as nitrogen source and soft template: Simple preparation, mesoporous structure, and photocatalytic activity under visible light.* J. Alloys Compd., 2012. **540**: p. 228-235.
176. Cheng, Y.H., et al., *Nitrogen-sensitized dual phase titanate/titania for visible-light driven phenol degradation.* J. Solid State Chem., 2012. **196**: p. 518-527.
177. Qiao, M., et al., *Novel sol-gel synthesis of N-doped TiO₂ hollow spheres with high photocatalytic activity under visible light.* J. Sol-Gel Sci. Technol., 2010. **55**(3): p. 377-384.
178. Fu, J., et al., *Soft-chemical synthesis of mesoporous nitrogen-modified titania with superior photocatalytic performance under visible light irradiation.* Chem. Eng. J., 2013. **219**: p. 155-161.
179. Elghniji, K., M. Ksibi, and E. Elaloui, *Sol-gel reverse micelle preparation and characterization of N-doped TiO₂: Efficient photocatalytic degradation of methylene blue in water under visible light.* J. Ind. Eng. Chem., 2012. **18**(1): p. 178-182.
180. Zhou, W., et al., *Ultrasonic fabrication of N-doped TiO₂ nanocrystals with mesoporous structure and enhanced visible light photocatalytic activity.* Chin. J. Catal., 2013. **34**(6): p. 1250-1255.
181. Nolan, N.T., et al., *Effect of N-doping on the photocatalytic activity of sol-gel TiO₂.* J. Hazard. Mater., 2012. **211-212**: p. 88-94.
182. Hu, Z., L. Xu, and J. Chen, *Ordered arrays of N-doped mesoporous titania spheres with high visible light photocatalytic activity.* Mater. Lett., 2013. **106**: p. 421-424.
183. Li, X., et al., *Preparation of homogeneous nitrogen-doped mesoporous TiO₂ spheres with enhanced visible-Light photocatalysis.* Appl. Catal., B, 2015. **164**: p. 352-359.
184. Hou, Y.D., et al., *N-doped SiO₂/TiO₂ mesoporous nanoparticles with enhanced photocatalytic activity under visible-light irradiation.* Chemosphere, 2008. **72**(3): p. 414-421.
185. Joshi, M.M., et al., *Visible light induced photoreduction of methyl orange by N-doped mesoporous titania.* Appl. Catal., A, 2009. **357**(1): p. 26-33.
186. Zuo, F., et al., *Self-doped Ti³⁺ enhanced photocatalyst for hydrogen production under visible light.* J. Am. Chem. Soc. , 2010. **132**: p. 11856-11857.
187. Zuo, F., et al., *Active facets on titanium(III)-doped TiO₂: an effective strategy to improve the visible-light photocatalytic activity.* Angew. Chem. Int. Ed., 2012. **51**(25): p. 6223-6226.
188. Sun, H., et al., *Visible-light-driven TiO₂ catalysts doped with low-concentration nitrogen species.* Sol. Energy Mater. Sol. Cells 2008. **92**(1): p. 76-83.

189. Xu, J., et al., *Photoelectrochemical property and photocatalytic activity of N-doped TiO₂ nanotube arrays*. Appl. Surf. Sci., 2010. **256**(13): p. 4397-4401.
190. Ao, Y., et al., *Visible-light responsive C,N-codoped titania hollow spheres for X-3B dye photodegradation*. Microporous Mesoporous Mater., 2009. **118**(1-3): p. 382-386.
191. Yang, G., et al., *Preparation of highly visible-light active N-doped TiO₂ photocatalyst*. J. Mater. Chem., 2010. **20**(25): p. 5301-5309.
192. Su, J., X. Zou, and J.S. Chen, *Self-modification of titanium dioxide materials by Ti³⁺ and/or oxygen vacancies: new insights into defect chemistry of metal oxides*. RSC Adv., 2014. **4**(27): p. 13979-13988.
193. Wang, J., et al., *Synchronical pollutant degradation and H₂ production on a Ti³⁺-doped TiO₂ visible photocatalyst with dominant (001) facets*. Appl. Catal., B, 2013. **134-135**: p. 198-204.
194. Selvam, K., et al., *Mesoporous nitrogen doped nano titania—a green photocatalyst for the effective reductive cleavage of azoxybenzenes to amines or 2-phenyl indazoles in methanol*. Appl. Catal., A, 2012. **413-414**: p. 213-222.
195. Islam, S.Z., et al., *Remarkable enhancement of photocatalytic water oxidation in N₂/Ar plasma treated, mesoporous TiO₂ films*. J. Phys. Chem. C, 2016. **120**(26): p. 14069-14081.
196. Mei, P., et al., *EPR study of nitrogen-doped mesoporous TiO₂ powders*. J. Phys. Chem. Solids, 2010. **71**(1): p. 1-6.
197. Soni, S.S., et al., *Visible light induced cell damage of Gram positive bacteria by N-doped TiO₂ mesoporous thin films*. Thin Solid Films, 2013. **531**: p. 559-565.
198. Yao, N., et al., *Simple synthesis and characterization of mesoporous (N, S)-codoped TiO₂ with enhanced visible-light photocatalytic activity*. Ceram. Int., 2012. **38**(2): p. 1671-1675.
199. Xiao, Q., et al., *Preparation and visible light photocatalytic activity of mesoporous N, S-codoped TiO₂(B) nanobelts*. Appl. Surf. Sci., 2011. **257**(8): p. 3652-3656.
200. Ao, Y., et al., *Synthesis of C,N,S-tridoped mesoporous titania with enhanced visible light-induced photocatalytic activity*. Microporous Mesoporous Mater., 2009. **122**(1-3): p. 1-6.
201. Wang, J., et al., *Mesoporous TiO₂-xAy (A = N, S) as a visible-light-response photocatalyst*. Solid State Sci., 2010. **12**(4): p. 490-497.
202. Zalas, M., *Synthesis of N-doped template-free mesoporous titania for visible light photocatalytic applications*. Catal. Today, 2014. **230**: p. 91-96.
203. Liu, S.H. and H.R. Syu, *One-step fabrication of N-doped mesoporous TiO₂ nanoparticles by self-assembly for photocatalytic water splitting under visible light*. Appl. Energ., 2012. **100**: p. 148-154.
204. Gandhe, A.R., S.P. Naik, and J.B. Fernandes, *Selective synthesis of N-doped mesoporous TiO₂ phases having enhanced photocatalytic activity*. Microporous Mesoporous Mater., 2005. **87**(2): p. 103-109.
205. Chi, B., L. Zhao, and T. Jin, *One-step template-free route for synthesis of mesoporous N-doped titania spheres*. J. Phys. Chem. C, 2007. **111**(17): p. 6189-6193.

206. Horikawa, T., M. Katoh, and T. Tomida, *Preparation and characterization of nitrogen-doped mesoporous titania with high specific surface area*. *Microporous Mesoporous Mater.*, 2008. **110**(2-3): p. 397-404.
207. Shao, G.S., X.J. Zhang, and Z.Y. Yuan, *Preparation and photocatalytic activity of hierarchically mesoporous-macroporous TiO₂-xNx*. *Appl. Catal., B*, 2008. **82**(3-4): p. 208-218.
208. Parida, K.M. and B. Naik, *Synthesis of mesoporous TiO₂-xNx spheres by template free homogeneous co-precipitation method and their photo-catalytic activity under visible light illumination*. *J. Colloid Interface Sci.*, 2009. **333**(1): p. 269-276.
209. Wu, Y.M., et al., *Preparation of nitrogen and fluorine co-doped mesoporous TiO₂ microsphere and photodegradation of acid orange 7 under visible light*. *Chem. Eng. J.*, 2010. **162**(2): p. 710-717.
210. Liu, E., et al., *Fabrication and photocatalytic activity of highly crystalline nitrogen doped mesoporous TiO₂*. *Chin. J. Catal.*, 2012. **33**(9-10): p. 1665-1671.
211. Jia, T., et al., *Sonochemical synthesis, characterization, and photocatalytic activity of N-doped TiO₂ nanocrystals with mesoporous structure*. *Int. J. Photoenergy*, 2014. **2014**: p. 1-7.
212. Sreethawong, T., S. Laehsatee, and S. Chavadej, *Comparative investigation of mesoporous- and non-mesoporous-assembled TiO₂ nanocrystals for photocatalytic H₂ production over N-doped TiO₂ under visible light irradiation*. *Int. J. Hydrogen Energy*, 2008. **33**(21): p. 5947-5957.
213. Lu, X.H., et al., *Hydrogenated TiO₂ nanotube arrays for supercapacitors*. *Nano Lett.*, 2012. **12**(3): p. 1690-1696.
214. Naldoni, A., et al., *Effect of nature and location of defects on bandgap narrowing in black TiO₂ nanoparticles*. *J. Am. Chem. Soc.*, 2012. **134**(18): p. 7600-7603.
215. Hu, Y.H., *A highly efficient photocatalyst--hydrogenated black TiO₂ for the photocatalytic splitting of water*. *Angew. Chem. Int. Ed.*, 2012. **51**(50): p. 12410-2.
216. Wang, Z., et al., *H-doped black titania with very high solar absorption and excellent photocatalysis enhanced by localized surface plasmon resonance*. *Adv. Funct. Mater.*, 2013. **23**(43): p. 5444-5450.
217. Yang, C., et al., *Core-shell nanostructured "black" rutile titania as excellent catalyst for hydrogen production enhanced by sulfur doping*. *J. Am. Chem. Soc.*, 2013. **135**(47): p. 17831-17838.
218. Zhou, H., et al., *Three-dimensional nanoporous TiO₂ network films with excellent electrochemical capacitance performance*. *J. Alloys Compd.*, 2014. **597**: p. 1-7.
219. Shahid, M., et al., *Reduced titania films with ordered nanopores and their application to visible light water splitting*. *Bull. Korean Chem. Soc.*, 2013. **34**(8): p. 2271-2275.
220. Lin, X., et al., *Carbon-doped mesoporous TiO₂ film and its photocatalytic activity*. *Microporous Mesoporous Mater.*, 2011. **142**(1): p. 276-281.
221. Chang, P.-y., C.-h. Huang, and R.-a. Doong, *Ordered mesoporous carbon-TiO₂ materials for improved electrochemical performance of lithium ion battery*. *Carbon*, 2012. **50**(11): p. 4259-4268.

222. Wang, T., et al., *Microwave absorption properties and infrared emissivities of ordered mesoporous C-TiO₂ nanocomposites with crystalline framework*. J. Solid State Chem., 2010. **183**(12): p. 2797-2804.
223. Ren, W., et al., *Low temperature preparation and visible light photocatalytic activity of mesoporous carbon-doped crystalline TiO₂*. Appl. Catal., B, 2007. **69**(3-4): p. 138-144.
224. Lin, X.X. and D.G. Fu, *Synthesis of nitrogen-doped mesoporous TiO₂ film and its visible light photocatalytic activity*, in *Sustainable Development of Urban Environment and Building Material, Pts 1-4*, H. Li, et al., Editors. 2012, Trans Tech Publications Ltd: Stafa-Zurich. p. 895-898.
225. Huang, Y., et al., *Effect of carbon doping on the mesoporous structure of nanocrystalline titanium dioxide and its solar-light-driven photocatalytic degradation of NO_x*. Langmuir, 2008. **24**(7): p. 3510-3516.
226. Yu, C., J.C. Yu, and M. Chan, *Sonochemical fabrication of fluorinated mesoporous titanium dioxide microspheres*. J. Solid State Chem., 2009. **182**(5): p. 1061-1069.
227. Pan, J.H., et al., *Self-etching reconstruction of hierarchically mesoporous F-TiO₂ hollow microspherical photocatalyst for concurrent membrane water Purifications*. J. Am. Chem. Soc., 2008. **130**(34): p. 11256-+.
228. Yu, J.C., et al., *Effects of trifluoroacetic acid modification on the surface microstructures and photocatalytic activity of mesoporous TiO₂ thin films*. Langmuir, 2003. **19**(9): p. 3889-3896.
229. Yu, J., et al., *Enhancement of photocatalytic activity of mesoporous TiO₂ powders by hydrothermal surface fluorination treatment*. J. Phys. Chem. C, 2009. **113**(16): p. 6743-6750.
230. Yu, J.C., et al., *Effects of F- doping on the photocatalytic activity and microstructures of nanocrystalline TiO₂ powders*. Chem. Mater., 2002. **14**(9): p. 3808-3816.
231. Park, H. and W. Choi, *Effects of TiO₂ surface fluorination on photocatalytic reactions and photoelectrochemical behaviors*. J. Phys. Chem. B, 2004. **108**(13): p. 4086-4093.
232. Shi, Q., et al., *Preparation and characterization of PVA-I complex doped mesoporous TiO₂ by hydrothermal method*. Appl. Surf. Sci., 2013. **273**: p. 769-775.
233. Liu, G., et al., *Visible light photocatalyst: Iodine-doped mesoporous titania with a bicrystalline framework*. J. Phys. Chem. B, 2006. **110**(42): p. 20823-20828.
234. Guo, S.Y., et al., *Synthesis of phosphorus-doped titania with mesoporous structure and excellent photocatalytic activity*. Mater. Res. Bull., 2013. **48**(9): p. 3032-3036.
235. Yu, J.C., et al., *Synthesis and characterization of phosphated mesoporous titanium dioxide with high photocatalytic activity*. Chem. Mater., 2003. **15**(11): p. 2280-2286.
236. Fan, X., et al., *Role of phosphorus in synthesis of phosphated mesoporous TiO₂ photocatalytic materials by EISA method*. Appl. Surf. Sci., 2008. **254**(16): p. 5191-5198.
237. Feng, H.J., M.H. Zhang, and L.E. Yu, *Phosphorus-doped TiO₂ catalysts with stable anatase-brookite biphasic structure: synthesis and photocatalytic performance*. J. Nanosci. Nanotechnol., 2013. **13**(7): p. 4981-4989.

238. Yu, C.L., et al., *WO₃ coupled P-TiO₂ photocatalysts with mesoporous structure*. Catal. Lett., 2010. **140**(3-4): p. 172-183.
239. Zhang, K., et al., *Preparation and photocatalytic activity of B-N co-doped mesoporous TiO₂*. Powder Technol., 2014. **253**: p. 608-613.
240. He, T.N., et al., *Synthesis and characterization of B-N co-doped mesoporous TiO₂ with enhanced photocatalytic activity*. Rsc Advances, 2014. **4**(12): p. 5880-5886.
241. Lee, J.H., et al., *Photocatalytic characteristics of boron and nitrogen doped titania film synthesized by micro-arc oxidation*. Ceram. Int., 2015. **41**(9): p. 11899-11907.
242. Zhou, X., et al., *Effect of nitrogen-doping temperature on the structure and photocatalytic activity of the B,N-doped TiO₂*. J. Solid State Chem., 2011. **184**(1): p. 134-140.
243. Abdollahi Kakroudi, M., F. Kazemi, and B. Kaboudin, *Highly efficient photodeoximation under green and blue LEDs catalyzed by mesoporous CN codoped nano TiO₂*. J. Mol. Catal. A: Chem., 2014. **392**: p. 112-119.
244. Pan, L., et al., *Enhancement of visible-light-induced photodegradation over hierarchical porous TiO₂ by nonmetal doping and water-mediated dye sensitization*. Appl. Surf. Sci., 2013. **268**: p. 252-258.
245. Xu, J., et al., *Novel N-F-codoped TiO₂ inverse opal with a hierarchical meso-/macroporous structure: synthesis, characterization, and photocatalysis*. J. Phys. Chem. C, 2010. **114**(36): p. 15251-15259.
246. Li, Y., et al., *Mesoporous (N, S)-codoped TiO₂ nanoparticles as effective photoanode for dye-sensitized solar cells*. J. Alloys Compd., 2012. **512**(1): p. 23-26.
247. Li, H., et al., *Photocatalytic activity of (sulfur, nitrogen)-codoped mesoporous TiO₂ thin films*. Res. Chem. Intermed., 2010. **36**(1): p. 27-37.
248. Yu, C., et al., *Sol-gel derived S,I-codoped mesoporous TiO₂ photocatalyst with high visible-light photocatalytic activity*. J. Phys. Chem. Solids, 2010. **71**(9): p. 1337-1343.
249. Hartmann, P., et al., *Mesoporous TiO₂: comparison of classical sol-gel and nanoparticle based photoelectrodes for the water splitting reaction*. ACS Nano, 2010. **4**(6): p. 3147-3154.
250. Sreethawong, T., S. Laehsatee, and S. Chavadej, *Use of Pt/N-doped mesoporous-assembled nanocrystalline TiO₂ for photocatalytic H₂ production under visible light irradiation*. Catal. Commun., 2009. **10**(5): p. 538-543.
251. Fang, J., et al., *One-step synthesis of bifunctional TiO₂ catalysts and their photocatalytic activity*. J. Phys. Chem. C, 2010. **114**(17): p. 7940-7948.
252. Dhakshinamoorthy, A., et al., *Photocatalytic CO₂ reduction by TiO₂ and related titanium containing solids*. Energy Environ. Sci., 2012. **5**(11): p. 9217-9233.
253. Inoue, T., et al., *Photoelectrocatalytic reduction of carbon-dioxide in aqueous suspensions of semiconductor powders*. Nature, 1979. **277**(5698): p. 637-638.
254. Gao, M.Y., et al., *Synthesis of Ag/N-TiO₂/SBA-15 photocatalysts and photocatalytic reduction of CO₂ under visible light irradiation*. Acta Chimica Sinica, 2014. **72**(10): p. 1092-1098.
255. Kim, S., S.-J. Hwang, and W. Choi, *Visible light active platinum-ion-doped TiO₂ photocatalyst*. J. Phys. Chem. B, 2005. **109**(51): p. 24260-24267.

256. You, X., et al., *A novel deposition precipitation method for preparation of Ag-loaded titanium dioxide*. Catal. Lett., 2005. **102**(3-4): p. 247-250.
257. Tian, B., et al., *Preparation of Au/TiO₂ catalysts from Au(I)-thiosulfate complex and study of their photocatalytic activity for the degradation of methyl orange*. Appl. Catal., B, 2008. **79**(4): p. 394-401.
258. Grilli, R., et al., *Surface characterisation and photocatalytic performance of N-doped TiO₂ thin films deposited onto 200 nm pore size alumina membranes by sol-gel methods*. Mater. Chem. and Phys., 2015. **159**: p. 25-37.
259. Yokosuka, Y., et al., *Photocatalytic degradation of trichloroethylene using N-doped TiO₂ prepared by a simple sol-gel process*. Res. Chem. Intermed., 2009. **35**(1): p. 43-53.
260. Wu, Y.C. and L.S. Ju, *Annealing-free synthesis of C-N co-doped TiO₂ hierarchical spheres by using amine agents via microwave-assisted solvothermal method and their photocatalytic activities*. J. Alloys Compd. , 2014. **604**: p. 164-170.
261. Lin, H., et al., *Hydrogen generation under visible light using nitrogen doped titania anodes*. J. Appl. Phys., 2010. **107**(12): p. 124305-6.
262. Pelaez, M., et al., *Microcystin-LR removal from aqueous solutions using a magnetically separable N-doped TiO₂ nanocomposite under visible light irradiation*. Chem. Commun., 2013. **49**(86): p. 10118-20.
263. Nakano, Y., et al., *Deep-level optical spectroscopy investigation of N-doped TiO₂ films*. Appl. Phys. Lett., 2005. **86**(13): p. 132104-3.
264. Hidalgo, D., et al., *Thick mesoporous TiO₂ films through a sol-gel method involving a non-ionic surfactant: characterization and enhanced performance for water photo-electrolysis*. Inter. J. Hydrogen Energ., 2014. **39**(36): p. 21512-21522.
265. Fattakhova-Rohlfing, D., A. Zaleska, and T. Bein, *Three-dimensional titanium dioxide nanomaterials*. Chem. Rev., 2014. **114**(19): p. 9487-558.
266. Li, D., et al., *New synthesis of excellent visible-light TiO_{2-x}N_x photocatalyst using a very simple method*. J. Solid State Chem., 2007. **180**(9): p. 2630-2634.
267. Rane, K.S., et al., *Visible light-sensitive yellow TiO_{2-x}N_x and Fe-N co-doped Ti_{1-y}Fe_yO_{2-x}N_x anatase photocatalysts*. J. Solid State Chem., 2006. **179**(10): p. 3033-3044.
268. Sun, H., et al., *Photocatalytic decomposition of 4-chlorophenol over an efficient N-doped TiO₂ under sunlight irradiation*. J. Photochem. Photobiol., A, 2009. **201**(1): p. 15-22.
269. Selvam, K. and M. Swaminathan, *Nano N-TiO₂ mediated selective photocatalytic synthesis of quinaldines from nitrobenzenes*. RSC Adv., 2012. **2**(7): p. 2848-2855.
270. Duminica, F.D., F. Maury, and R. Hausbrand, *N-doped TiO₂ coatings grown by atmospheric pressure MOCVD for visible light-induced photocatalytic activity*. Surf. Coat. Technol. , 2007. **201**: p. 9349-9353.
271. Gai, L., et al., *Controlled synthesis of nitrogen-doped binary and ternary TiO₂ nanostructures with enhanced visible-light catalytic activity*. J. Solid State Chem., 2013. **199**: p. 271-279.
272. Wu, Q.L., N. Subramanian, and S.E. Rankin, *Hierarchically porous titania thin film prepared by controlled phase separation and surfactant templating*. Langmuir, 2011. **27**(15): p. 9557-9566.

273. Howard, C.J., T.M. Sabine, and F. Dickson, *Structural and thermal parameters for rutile and anatase*. Acta Crystallographica B, 1991. **47**: p. 462-468.
274. Fakhouri, H., et al., *Control of the visible and UV light water splitting and photocatalysis of nitrogen doped TiO₂ thin films deposited by reactive magnetron sputtering*. Appl. Catal., B, 2014. **144**: p. 12-21.
275. Soni, S.S., et al., *Visible-light photocatalysis in titania-based mesoporous thin films*. Adv. Mater. , 2008. **20**(8): p. 1493-1498.
276. Chen, D., et al., *Improving visible-light photocatalytic activity of N-doped TiO₂ nanoparticles via sensitization by Zn porphyrin*. Appl. Surf. Sci., 2008. **255**(5): p. 2879-2884.
277. Wang, J., et al., *Origin of photocatalytic activity of nitrogen-doped TiO₂ nanobelts*. J. Am. Chem. Soc., 2009. **131**: p. 12290-12297.
278. Hernandez, S., et al., *Comparison of photocatalytic and transport properties of TiO₂ and ZnO nanostructures for solar-driven water splitting*. Phys. Chem. Chem. Phys., 2015. **17**(12): p. 7775-86.
279. Zakrzewska, K., et al., *Importance of the electronic structure of modified TiO₂ in the photoelectrochemical processes of hydrogen generation*. Int. J. Hydrogen Energ., 2015. **40**(1): p. 815-824.
280. Spadavecchia, F., et al., *Electronic structure of pure and N-doped TiO₂ nanocrystals by electrochemical experiments and First Principles calculations*. J. Phys. Chem. C, 2011. **115**(14): p. 6381-6391.
281. Bloh, J.Z., A. Folli, and D.E. Macphee, *Adjusting nitrogen doping level in titanium dioxide by codoping with tungsten: properties and band structure of the resulting materials*. J. Phys. Chem. C, 2014. **118**(36): p. 21281-21292.
282. Kisch, H., et al., *A low-band gap, nitrogen-modified titania visible-light photocatalyst*. J. Phys. Chem. C 2007. **111**(30): p. 11445-11449.
283. Beranek, R., *(Photo)electrochemical methods for the determination of the band edge positions of TiO₂-based nanomaterials*. Adv. Phys. Chem., 2011. **2011**: p. 1-20.
284. Sakai, N., et al., *Electronic band structure of titania semiconductor nanosheets revealed by electrochemical and photoelectrochemical studies*. J. Am. Chem. Soc. , 2004. **126**: p. 5851-5858.
285. Hanzu, I., T. Djenizian, and P. Knauth, *Electrical and point defect properties of TiO₂ nanotubes fabricated by electrochemical anodization*. J. Phys. Chem. C, 2011. **115**(13): p. 5989-5996.
286. Zhang, P., et al., *Structure of nitrogen and zirconium co-doped titania with enhanced visible-light photocatalytic Activity*. ACS Appl. Mater. Interfaces, 2014. **6**(7): p. 4622-4629.
287. Siuzdak, K., et al., *Novel nitrogen precursors for electrochemically driven doping of titania nanotubes exhibiting enhanced photoactivity*. New J. Chem., 2015. **39**(4): p. 2741-2751.
288. Qiu, X. and C. Burda, *Chemically synthesized nitrogen-doped metal oxide nanoparticles*. Chem. Phys., 2007. **339**(1-3): p. 1-10.
289. M. Sathish, et al., *Synthesis, characterization, electronic structure, and photocatalytic activity of nitrogen-doped TiO₂ nanocatalyst*. Chem. Mater., 2005. **17**: p. 6349-6353.

290. Boehm, H.P., *Acidic and basic properties of hydroxylated etal oxide surfaces*. Disc. Faraday Soc., 1971. **52**: p. 264-275.
291. Miyauchi, M., et al., *Zeta potential and photocatalytic activity of nitrogen doped TiO₂ thin films*. Phys. Chem. Chem. Phys. , 2004. **6** (4): p. 865-870.
292. Suttiponparnit, K., et al., *Role of surface area, primary particle size, and crystal phase on titanium dioxide nanoparticle dispersion properties*. Nanoscale Res. Lett. , 2011. **6**(27): p. 1-8.
293. Deka, R.C., *Acidity in zeolites and their charactization by different spectroscopic methods*. Indian J. Chem. Technol., 1998. **5**: p. 109-123.
294. Babu, V.J., et al., *Visible light photocatalytic water splitting for hydrogen production from N-TiO₂ rice grain shaped electrospun nanostructures*. Int. J. Hydrogen Energy, 2012. **37**: p. 8897-8904.
295. Hoang, S., et al., *Enhancing visible light photo-oxidation of water with TiO₂ nanowire arrays via cotreatment with H₂ and NH₃: synergistic effects between Ti³⁺ and N*. J. Am. Chem. Soc., 2012. **134**(8): p. 3659-3662.
296. Cao, J., et al., *Selective local nitrogen doping in a TiO₂ electrode for enhancing photoelectrochemical water splitting*. Chem. Commun., 2012. **48**(69): p. 8649-8651.
297. Islam, S.Z., et al., *Synthesis and catalytic applications of non-metal doped mesoporous titania*. Inorganics, 2017. **5**(1): p. 15.
298. Yeh, T.-F., et al., *Roles of graphene oxide in photocatalytic water splitting*. Mater. Today, 2013. **16**(3): p. 78-84.
299. Jiang, Z., et al., *The dedicated high-resolution grazing-incidence X-ray scattering beamline 8-ID-E at the Advanced Photon Source*. J. Synchrotron Radiat., 2012. **19**(4): p. 627-636.
300. Yeh, T.-F., et al., *Elucidating quantum confinement in graphene oxide dots based on excitation-wavelength-independent photoluminescence*. J. Phys. Chem. Lett., 2016. **7**(11): p. 2087-2092.
301. Yu, S., et al., *Graphene quantum dots to enhance the photocatalytic hydrogen evolution efficiency of anatase TiO₂ with exposed {001} facet*. Phys. Chem. Chem. Phys., 2016. **18**: p. 20338--20344.
302. Wu, X., et al., *Fabrication of highly fluorescent graphene quantum dots using L-glutamic acid for in vitro/in vivo imaging and sensing*. J. Mater. Chem. C, 2013. **1**(31): p. 4676-4684.
303. Zor, E., et al., *Graphene quantum dots-based photoluminescent sensor: a multifunctional composite for pesticide detection*. ACS Appl. Mater. Interfaces, 2015. **7**(36): p. 20272-20279.
304. Tang, D., et al., *Graphene oxide derived graphene quantum dots with different photoluminescence properties and peroxidase-like catalytic activity*. RSC Adv., 2016. **6**(56): p. 50609-50617.
305. Taherian, F., et al., *What is the contact angle of water on graphene?* Langmuir, 2013. **29**(5): p. 1457-1465.
306. Hong, K.T., H. Imadojemu, and R. Webb, *Effects of oxidation and surface roughness on contact angle*. Exp. Therm. Fluid Sci, 1994. **8**(4): p. 279-285.

307. Zhang, W.-D., L.-C. Jiang, and J.-S. Ye, *Photoelectrochemical study on charge transfer properties of ZnO nanowires promoted by carbon nanotubes*. J. Phys. Chem. C, 2009. **113**: p. 16247–16253.
308. Spadavecchia, F., et al., *Investigation and optimization of photocurrent transient measurements on nano-TiO₂*. J. Appl. Electrochem., 2013. **43**: p. 217–225.
309. Nemnes, G., et al., *Band alignment and charge transfer in rutile-TiO₂/CH₃NH₃PbI₃-_xCl_x interfaces*. Phys. Chem. Chem. Phys., 2015. **17**(45): p. 30417-30423.
310. Mews, M., et al., *Valence band alignment and hole transport in amorphous/crystalline silicon heterojunction solar cells*. Appl. Phys. Lett., 2015. **107**(1): p. 013902.
311. Xu, Z., et al., *3D periodic multiscale TiO₂ architecture: a platform decorated with graphene quantum dots for enhanced photoelectrochemical water splitting*. Nanotechnology, 2016. **27**(11): p. 115401.
312. Lewis, N.S., *Research opportunities to advance solar energy utilization*. Science, 2016. **351**(6271).
313. Lewis, N.S. and D.G. Nocera, *Powering the planet: chemical challenges in solar energy utilization*. Proc. Natl. Acad. Sci. USA, 2006. **103**(43): p. 15729-35.
314. Sharma, G., et al., *Electronic structure, photovoltage, and photocatalytic hydrogen evolution with p-CuBi₂O₄ nanocrystals*. J. Mater. Chem. A, 2016. **4**: p. 2936–2942.
315. Bagheri, S. and N.M. Julkapli, *Synergistic effects on hydrogenated TiO₂ for photodegradation of synthetic compounds pollutants*. Int. J. Hydrogen energy, 2016. **4**(33): p. 14652-14664.
316. Chen, X., et al., *Properties of disorder-engineered black titanium dioxide nanoparticles through hydrogenation*. Sci. Rep., 2013. **3**:1510.
317. Huo, J., et al., *In situ surface hydrogenation synthesis of Ti³⁺ self-doped TiO₂ with enhanced visible light photoactivity*. Nanoscale, 2014. **6**: p. 9078-9084.
318. Veith, G.M., et al., *Direct determination of solid-electrolyte interphase thickness and composition as a function of state of charge on a silicon anode*. J. Phys. Chem. C 2015. **119**: p. 20339–20349.
319. Marshall, S.T., et al., *Profiling of hydrogen in metal-insulator-semiconductor sensors using neutron reflectivity*. Appl. Phys. Lett., 2008. **92**(15).
320. Kharlampieva, E., et al., *Hydrogen-bonded polymer multilayers probed by neutron reflectivity*. Langmuir, 2008. **24**(20): p. 11346-11349.
321. Vezvaie, M., et al., *Hydrogen absorption into titanium under cathodic polarization: an in-situ neutron reflectometry and EIS study*. J. Electrochem. Soc., 2013. **160**(9): p. C414-C422.
322. Osterloh, F.E., *Inorganic nanostructures for photoelectrochemical and photocatalytic water splitting*. Chem. Soc. Rev., 2013. **42**: p. 2294--2320.
323. Pesci, F.M., et al., *Efficient suppression of electron-hole recombination in oxygen-deficient hydrogen-treated TiO₂ nanowires for photoelectrochemical water splitting*. J. Phys. Chem. C, 2013. **117**(48): p. 25837-25844.
324. Zhang, K., et al., *Large-scale synthesis of stable mesoporous black TiO₂ nanosheets for efficient solar-driven photocatalytic hydrogen evolution via an earthabundant low-cost biotemplate*. RSC Adv., 2016. **6**: p. 50506–50512.

325. Yan, Y., et al., *Slightly hydrogenated TiO₂ with enhanced photocatalytic performance*. J. Mater. Chem. A, 2014. **2**: p. 12708–12716.
326. Yan, Y., *Plasma-assisted synthesis of hydrogenated TiO₂ for energy storage and conversion*. 2015, Universitätsverlag Ilmenau.
327. Xu, J., et al., *Integrated photo-supercapacitor based on bi-polar TiO₂ nanotube arrays with selective one-side plasma-assisted hydrogenation* Adv. Funct. Mater. , 2014. **24**: p. 1840–1846.
328. Veith, G.M., et al., *Direct measurement of the chemical reactivity of silicon electrodes with LiPF₆-based battery electrolytes*. Chem. Commun., 2014. **50**(23): p. 3081-3084.
329. Nelson, A., *Co-refinement of multiple-contrast neutron/X-ray reflectivity data using MOTOFIT*. J. Appl. Crystallogr., 2006. **39**(2): p. 273-276.
330. Heavens, S., *Optical properties of thin films*. 1955: Butterworth: London.
331. Jiang, Z., *GIXSGUI is available for download: <http://www.aps.anl.gov/Sectors/Sector8/Operations/GIXSGUI.html>*. There is no corresponding record for this reference.
332. M, H., S.C. F, and Meagher E P, *Refinement of the structure of anatase at several temperatures*. Zeitschrift fur Kristallographie 1972. **136**: p. 273-281.
333. Guillemot, F., et al., *Ti⁴⁺ to Ti³⁺ conversion of TiO₂ uppermost layer by low-temperature vacuum annealing: interest for titanium biomedical applications*. J. Colloid Interface Sci., 2002. **255**(1): p. 75-78.
334. Lu, J., et al., *Effective increasing of optical absorption and energy conversion efficiency of anatase TiO₂ nanocrystals by hydrogenation*. Phys. Chem. Chem. Phys., 2011. **13**: p. 18063–18068.
335. Wu, H., et al., *Enhanced supercapacitance in anodic TiO₂ nanotube films by hydrogen plasma treatment*. Nanotechnology, 2013. **24**(45): p. 455401.
336. Benkoula, S., et al., *Water adsorption on TiO₂ surfaces probed by soft X-ray spectroscopies: bulk materials vs. isolated nanoparticles*. Sci. Rep., 2014. **5**: p. 15088-15088.
337. Cheng, J. and M. Sprik, *Acidity of the aqueous rutile TiO₂ (110) surface from density functional theory based molecular dynamics*. J. Chem. Theory Comput., 2010. **6**(3): p. 880-889.
338. Mohammadzadeh, M., et al., *Photocatalytic activity of TiO₂ thin films by hydrogen DC plasma*. Appl. Surf. Sci., 2015. **350**: p. 43-49.
339. Zheng, Z., et al., *Hydrogenated titania: synergy of surface modification and morphology improvement for enhanced photocatalytic activity*. Chem. Commun., 2012. **48**: p. 5733–5735.
340. Rajh, T., et al., *Surface restructuring of nanoparticles: an efficient route for ligand–metal oxide crosstalk*. J. Phys. Chem. B, 2002. **106**(41): p. 10543-10552.
341. Moser, J., et al., *Surface complexation of colloidal semiconductors strongly enhances interfacial electron-transfer rates* Langmuir 1991. **7**: p. 3012-3018.
342. Radoičić, M.B., et al., *The role of surface defect sites of titania nanoparticles in the photocatalysis: Aging and modification*. Appl. Catal., B, 2013. **138**: p. 122-127.
343. Rajh, T., et al., *Improving optical and charge separation properties of nanocrystalline TiO₂ by surface modification with vitamin C*. J. Phys. Chem. B, 1999. **103**(18): p. 3515-3519.

Vita

PLACE OF BIRTH: Comilla, Bangladesh

EDUCATION

M.S., Chemical Engineering July 2012
North Carolina A&T State University, Greensboro, NC

B.Sc., Chemical Engineering March 2009
Bangladesh University of Engineering and Technology, Dhaka, Bangladesh

AWARDS, SCHOLARSHIPS AND CERTIFICATES

1. Outstanding Chemical Engineering Graduate Student Award from the department of Chemical and Materials Engineering, University of Kentucky, 2017.
2. Outstanding Poster Presentation Award from Kentucky NSF EPSCoR Super Collider 2017.
3. Dissertation Enhancement Award, University of Kentucky, 2016.
4. NAMS NSF Stipend Award, 2016.
5. Center of Membrane Sciences 2016 Ph.D. Student Fellow Award, University of Kentucky, 2016.
6. Selected to participate in 18th U.S. National School on Neutron and X-ray Scattering, sponsored by Oak Ridge National Laboratory, Argonne National Laboratory and US Department of Energy, 2016.
7. 1st Place Poster Award, Chemical and Materials Engineering Symposium, University of Kentucky, 2015.
8. University of Kentucky Graduate School Travel Award, 2014-2016.
9. UKFCU ScholarConnect Winner, 2014.
10. Six/Sigma Green Belt from Mosescone Heath System, NC, 2012.
11. Certificate for Scholarly Accomplishments and Excellence in Academic Performance at North Carolina A&T State University, 2010-2011.
12. University Technical Scholarship, Bangladesh University of Engineering and Technology, Bangladesh, 2004-2008.

PEER-REVIEWED PUBLICATIONS

Published

1. **Syed Z. Islam**, Suraj Nagpure, Doo-Young Kim, and Stephen E. Rankin, Synthesis and Catalytic Applications of Non-metal Doped Mesoporous Titania, *Inorganics*, **2017**, 5(1), 15.
2. **Syed Z. Islam**, Allen D. Reed, Namal Wanninayake, Doo-Young Kim, and Stephen E. Rankin, Remarkable Enhancement of Photocatalytic Hydrogen Production in N₂/Ar Plasma Treated, Mesoporous TiO₂ Films, *The Journal of Physical Chemistry C*, **2016**, 120(26), 14069–14081.
3. **Syed Z. Islam**, Allen D. Reed, Doo-Young Kim, and Stephen E. Rankin, N₂/Ar Plasma Induced Doping of Ordered Mesoporous TiO₂ Thin Films for Visible Light Active Photocatalysis, *Microporous and Mesoporous Materials*, **2016**, 220, 120-128.

4. **Syed Z. Islam** and Stephen E. Rankin, Hydrazine-Based Synergistic Ti(III)/N Doping of Surfactant-Templated TiO₂ Thin Films for Enhanced Visible Light Photocatalysis, *Materials Chemistry and Physics*, **2016**, 182, 382-393.
5. **Syed Z. Islam**, Vishwanath G. Deshmane, and Shamsuddin Ilias, Thermal Stability Study of Pd-Composite Membrane Fabricated by Surfactant Induced Electroless Plating (SIEP), *Separation Science and Technology*, **2016**, 51(7), 1176-1188.
6. Saikat Das, Suraj Nagpure, Ravinder Garlapalli, Qingliu Wu, **Syed Z. Islam**, Joseph Strzalka, and Stephen E. Rankin, In-Situ GISAXS Study of Pore Orientation Effect on Thermal Transformation Mechanism of Surfactant Templated Mesoporous Titania Thin Films, *Physical Chemistry Chemical Physics*, 2016, 18, 2896-2905 (Featured in ARGONNE TODAY on February 17, 2016).

Submitted

7. **Syed Z. Islam**, Suraj Nagpure, Doo-Young Kim, and Stephen E. Rankin, Plasma Treated Hydrogen Doped Mesoporous Black TiO₂ Thin Films for Water Oxidation Photocatalysis, *Advanced Functional Materials*.

In Preparation for Short-term Submission

8. **Syed Z. Islam**, Namal Wanninayake, Allen Reed, Joseph Strzalka, Doo-Young Kim, and Stephen Rankin, Synergistic Effects of Graphene Quantum Dot Sensitization and Nitrogen Doping of Ordered Mesoporous TiO₂ Thin films for Water Splitting Photocatalysis.
9. **Syed Z. Islam**, M. Arif Khan, Suraj Nagpure, Joseph W. Strzalka, Barbara Knutson and Stephen E. Rankin, Study of Crystallization and Nanostructure of Surfactant Templated Mesoporous Titania Thin Films using Grazing Incidence X-ray Scattering
10. **Syed Z. Islam**, M. Arif Khan, Namal Wanninayake, Suraj Nagpure, Yuxin He, Joseph W. Strzalka, Doo-Young Kim, Barbara Knutson and Stephen E. Rankin, *In Situ* GISAXS Investigation of Low-Temperature Aging of Layer-By-Layer Thick Mesoporous Titania Films with Vertically Oriented 2D-HCP Nanopores.
11. Allen D. Reed, **Syed Z. Islam**, Doo-Young Kim, and Stephen E. Rankin, Hydrogenated Mesoporous TiO₂ Thin Films as an Anode Material for Supercapacitors.
12. Suraj Nagpure, Jiagang Xu, **Syed Z. Islam**, Qinglin Zhang, Yang Tse Cheng, and Stephen Rankin, Synthesis of Layer-By-Layer Thick Mesoporous Titania Films with Vertically Oriented 2D-HCP Nanopores and Their Use in Lithium Ion Batteries As Negative Electrodes.
13. M. Arif Khan, William T. Wallace, **Syed Z. Islam**, Suraj Nagpure, Joseph W. Strzalka, Stephen E. Rankin and Barbara Knutson, Adsorption, Stabilization and Recovery of Polyphenolic Flavonoids Using TiO₂ Functionalized Mesoporous Silica Nanoparticles.

CONFERENCE PRESENTATIONS

Oral Presentations

1. **Syed Z. Islam**, Allen D. Reed, Namal Wanninayake, Doo-Young Kim, and Stephen E. Rankin, Remarkable Enhancement of Photocatalytic Hydrogen Production in Sensitized and N₂/Ar Plasma Treated, Nanoporous TiO₂ Films, AIChE 2016, San Francisco, CA, USA.
2. **Syed Z. Islam**, Allen Reed, Suraj Nagpure, Namal Wanninayake, James F. Browning, Doo Young Kim, and Stephen E. Rankin, Neutron Reflectometry Investigation of Hydrogen in

- Plasma Treated Hydrogen Doped Nanoporous TiO₂ Thin Films for Water Splitting Photocatalysis, AIChE 2016, San Francisco, CA, USA.
3. **Syed Z. Islam**, Namal Wanninayake, Allen D. Reed, Doo-Young Kim, and Stephen E. Rankin, Synergistic Effects of Graphene Quantum Dot Sensitization and Nitrogen Doping of Ordered Mesoporous TiO₂ Thin Films for Water Splitting Photocatalysis, **SPIE** (Solar Hydrogen and Nanotechnology XI), 2016, San Diego, California, USA.
 4. **Syed Z. Islam**, Namal Wanninayake, Allen D. Reed, Doo-Young Kim, and Stephen E. Rankin, Graphene Quantum Dot Sensitization and Nitrogen Doping of Ordered Mesoporous TiO₂ Thin Films for Visible Light Driven Water Splitting, North American Membrane Society Annual Meeting 2016, Bellevue, WA, USA.
 5. **Syed Islam**, Allen Reed, Doo-Young Kim, and Stephen Rankin, Synergistic Effects of Graphene Quantum Dot Sensitization and Nitrogen Doping of Ordered Mesoporous TiO₂ Thin films for Water Splitting Photocatalysis, 2016 TMS Annual Meeting & Exhibition, Nashville, TX, USA.
 6. Suraj Nagpure, **Syed Islam**, and Stephen Rankin, Energy Conversion and Storage Applications of Mesoporous Titania Thin Films with Controlled Pore Orientation, 2016 TMS Annual Meeting & Exhibition, Nashville, TX, USA.
 7. **Syed Z. Islam**, Allen D. Reed, Doo-Young Kim, and Stephen E. Rankin, N₂/Ar-Plasma Assisted Nitrogen Doping of Ordered Mesoporous TiO₂ Thin Films for Water Splitting Photocatalysis, AIChE 2015, Salt Lake City, UT, USA.
 8. **Syed Z. Islam**, Allen D. Reed, Doo-Young Kim, and Stephen E. Rankin, Ordered Mesoporous TiO₂ Thin Films Sensitized with Graphene Quantum Dot for Visible-Light-Driven Photocatalysis, AIChE 2015, Salt Lake City, UT, USA.
 9. Suraj Nagpure, **Syed Z. Islam**, Qinglin Zhang, Yang Tse Cheng, and Stephen Rankin, Synthesis of Layer-By-Layer Thick Mesoporous Titania Films with Vertically Oriented 2D-HCP Nanopores and Their Use in Lithium Ion Batteries As Negative Electrodes, AIChE 2015, Salt Lake City, UT, USA.
 10. **Syed Islam**, and Stephen Rankin, Enhancement of Visible Light Absorption of Ordered Mesoporous Titanium (Ti³⁺) and Nitrogen Doped Titanium Dioxide Thin Films for Solar Energy Conversion, AIChE 2014, Atlanta, GA, USA.
 11. Saikat Das, Suraj Nagpure, Ravinder Garlapalli, **Syed Islam**, Qingliu Wu, Joseph Strzalka and Stephen Rankin, In-Situ GISAXS Study of Pore Orientation Effect on Thermal Transformation Mechanism of Surfactant Templated Mesoporous Titania Thin Films, AIChE 2014, Atlanta, GA, USA.
 12. Shamsuddin Ilias and **Syed Islam**, Thermal Stability of Palladium-Composite Membrane Fabricated By Surfactant Induced Electroless Plating (SIEP), AIChE 2013, San Francisco, CA, USA.

Poster Presentations

13. Christian Rust, Stephen E. Rankin, Barbara L. Knutson and **Syed Z. Islam**, Photocatalytic Mesoporous Titania Thin Films on Porous Substrate through the Evaporation-Induced Self-Assembly Method, AIChE 2016, San Francisco, CA, USA (Submitted).
14. **Syed Z. Islam**, and Stephen E. Rankin, Ordered Nanoporous Titania Thin Films for Energy Conversion and Storage, AIChE 2016, San Francisco, CA, USA.

15. Namal Wanninayake, **Syed Z. Islam**, Allen Reed, Stephen E. Rankin, and Doo Young Kim, Graphene Quantum Dot Immobilized Nanoporous N-TiO₂ Thin Films for Efficient Photocatalytic Water Splitting, Pittcon Conference and Expo 2016, Atlanta, GA, USA.
16. **Syed Islam**, Allen Reed, Namal Wanninayake, Doo-Young Kim, and Stephen Rankin, Synergistic Effects of Graphene Quantum Dot Sensitization and Nitrogen Doping of Ordered Mesoporous TiO₂ Thin Films for Water Splitting Photocatalysis, KY NSF EPSCoR Super Collider Graduate Student Conference 2016, Lexington, KY, USA.
17. **Syed Z. Islam**, Allen D. Reed, Doo-Young Kim, and Stephen E. Rankin, Preparation of N₂-Plasma Assisted Visible Light Active Ordered Mesoporous Nitrogen Doped TiO₂ Thin Films for Solar Energy Conversion, SPIE (Solar Hydrogen and Nanotechnology X), 2015, San Diego, California, USA.
18. **Syed Z. Islam**, Allen D. Reed, Doo-Young Kim, and Stephen E. Rankin, Hydrogen Production By Water Splitting Under Visible Light Using N₂/Ar Plasma Induced Doped Ordered Mesoporous TiO₂ Thin Films, North American Membrane Society Annual Meeting 2015, Boston, MA, USA.
19. **Syed Z. Islam**, Allen D. Reed, Doo-Young Kim, and Stephen E. Rankin, Hydrogen Production By Water Splitting Under Visible Light Using N₂/Ar Plasma Induced Doped Ordered Mesoporous TiO₂ Thin Films, KY NSF EPSCoR conference 2015, Lexington, KY, USA.
20. Allen D. Reed, **Syed Z. Islam**, Doo-Young Kim, and Stephen E. Rankin, Plasma Treated TiO₂ for Photocatalytic and Supercapacitor Applications, RE3 Workshop 2015, Renewable Energy and Energy Efficiency, Louisville, Kentucky, USA.
21. Saikat Das, Suraj Nagpure, Ravinder Garlapalli, **Syed Islam**, Qingliu Wu, Joseph Strzalka and Stephen Rankin, In-Situ GISAXS Kinetic Studies of Surfactant Templated Mesoporous Titania Thin Films: Orientation Effect on Formation and Transformation Mechanism, American Crystallographic Association (ACA) Annual Meeting 2014, At Albuquerque, NM, USA.
22. Karshak Kosaraju, Balaji Tatineni, Michael Duncan, **Syed Zahadul Islam**, Shamsuddin Ilias, Debasish Kuila, Shahrzad Hosseinneshad, and James King, Bimetallic Nanocatalysts in Mesoporous Silica for Steam Reforming of Methanol, 244th ACS National Meeting, 2012, Philadelphia, Pennsylvania, USA.
23. K. M. Tanvir Ahmmmed, **Syed Zahadul Islam** and Syeda R. Sultana, Removal of Dye from Textile Wastewater by Using Activated Carbon in a Fixed Bed Adsorber, 2nd International Conference on Chemical Engineering (ICCHE), 2008, BUET, Bangladesh.